Abstract

The Biophysical Impacts of Aerosols on Surface Climate

Tirthankar "TC" Chakraborty

2021

Aerosols, tiny suspended solid or liquid particles in the atmosphere, are important drivers of atmospheric processes. Aerosols affect the climate as well as local weather by modulating the Earth's energy budget. Previous studies have quantified the impact of aerosols on global climate change, with a focus on the atmospheric radiation budget. However, aerosols have a disproportionately higher impact on the Earth's surface, where we reside. This dissertation isolated this impact of aerosols on the surface climate to better understand the mechanisms that modulate the overall climate response to aerosol loading.

This work developed a surface energy budget perspective to aerosol-climate interactions and quantified the impact of aerosols on surface climate through both radiative and non-radiative pathways. The relative strengths of these pathways depend heavily on both aerosol and land surface properties. Thus, a major emphasis of the dissertation was to investigate the impact of aerosols on the surface energy budget tied to differences in regional aerosol loading and land cover. The research methodology combined data analysis, remote sensing, atmosphere modeling, and land-surface modeling. Both reanalysis datasets with assimilated aerosol observations and atmosphere model runs with radiation diagnostics were used to separate the impact of aerosols on surface climate through the shortwave and longwave radiative effects. To capture the impact of aerosols on surface climate through non-radiative pathways, a global land model was run with and without aerosols. In both cases, a conceptual framework to attribute surface temperature anomalies to its determinants was used to examine the relative impact of each pathway on the local surface temperature. The associated impacts on terrestrial evapotranspiration and land carbon uptake

were also quantified on a global scale using land model runs. Finally, given the importance of diffuse radiation of sunlight on surface processes, a comprehensive evaluation of gridded diffuse radiation in current-generation global products was undertaken. To correct some of the observed biases in these gridded products, a supervised machine learning algorithm was trained to develop a global bias-corrected radiation dataset for future land modeling.

Aerosols lead to one of the largest uncertainties in both diagnostic and prognostic climate simulations. This dissertation advances our understanding of the biophysical mechanisms through which aerosols can impact surface temperature, terrestrial evapotranspiration, and land carbon uptake. It also provides a broader perspective on the importance of the diffuse radiation fertilization effect and the current uncertainties in its representation in Earth System Models.

The Biophysical Impacts of Aerosols on Surface Climate

A Dissertation
Presented to the Faculty of the Graduate School
of
Yale University
in Candidacy for the Degree of
Doctor of Philosophy

by
Tirthankar "TC" Chakraborty

Dissertation Director: Xuhui Lee

Dec 2021

Acknowledgments

This long and exciting journey has been facilitated and guided by many.

First and foremost, I would like to sincerely thank my advisor, Prof. Xuhui Lee, for his counsel and guidance during my time at Yale. I have benefited greatly from his extensive knowledge, valuable insights, and constant encouragement. I am extremely fortunate to have worked with him and learned from him during my PhD. He has driven me to think about the bigger picture and to better contextualize my research and its implications, which has helped me grow as a scientist. He has also given me a lot of freedom to pursue other research interests, which has also been conducive to my success.

I would like to thank my other committee members, Prof. Ron Smith, Prof. Drew Gentner, and Dr. Dave Lawrence, for their guidance and generosity with their time and expertise. Prof. Smith and Prof. Gentner have provided critical feedback during our meetings and Dr. Lawrence's advice was instrumental while I was trying to learn the Community Earth System Model.

A vote of thanks to my fellow students and lab mates, particularly Dr. Natalie Schultz, Yichen Yang, and Keer Zhang.

Beyond the lab, I am grateful to the professors and colleagues who have also made my time at Yale memorable. In particular, I have learned a lot from Profs Dana Tomlin and Angel Hsu during my time here. I thank everyone associated with the geospatial community at Yale, which I have seen grow and prosper during my PhD.

My dissertation would not have been possible without funding support from several organizations, including the Yale School of the Environment, the Yale Institute for Biospheric Studies, the Computational and Information Systems Lab at the National Center for Atmospheric Research, and the Microsoft AI for Earth program.

Last, but certainly not least, I would like to thank my partner, who has been an integral part of this journey, and express my appreciation and gratitude towards my family, who

continue to fully support my decision to pursue a career in scientific research.

Dedicated to the hours spent and the knowledge gained. . .

Contents

List of Figures

xvi

List of Tables

Chapter 1

Introduction

1.1 Research Background

The principal constituents of the Earth system - the atmosphere, the ocean, and the land - show great non-linearity in their interactions (Suni et al., 2015). The interaction between the land and the atmosphere is particularly variable due to the heterogeneity of the land surface (as opposed to the ocean surface). The effect of these interactions on the climate has received much attention in recent years (Seneviratne & Stockli, 2008). In climate and numerical weather prediction models, these interactions determine the lower boundary conditions for the model domain.

The sun's radiation warms the Earth's surface and the net absorbed energy is partitioned into the turbulent fluxes - sensible heat flux and latent heat flux - and ground flux, collectively representing the surface energy balance (Eq. 1.1) (Trenberth et al., 2009). Studies have shown that the heterogeneity of the Earth's land surface makes the feedback between land use and the turbulent fluxes dynamic in space and time (Giorgi & Avissar, 1997; Pielke, 2001; Suni et al., 2015), which, in turn, affects local and regional weather and climate.

The basic surface energy balance is formulated as:

$$K_\downarrow + L_\downarrow - K_\uparrow - L_\uparrow = H + \lambda E + G \tag{1.1}$$

The terms on the left-hand side comprise the net radiative flux (R_n) received by the surface, where $K_\downarrow$ is the incoming shortwave radiative flux, $L_\downarrow$ is the incoming longwave radiative flux, $K_\uparrow$ is the shortwave radiative flux reflected by the surface, and $L_\uparrow$ is the longwave radiative flux emitted by the surface. H is the sensible heat flux and represents the turbulent transfer of heat from the surface to the atmosphere. λE is the latent heat flux or the transfer of moisture from the surface to the atmosphere and G is the ground flux - the energy being transmitted from the surface into the deeper soil layers.

1.1.1 Aerosols: Properties and Impacts

Aerosols are tiny suspended liquid or solid particles that have natural or anthropogenic origins. Naturally, aerosols can be mineral dust (from re-suspension of dust from deserts), sea salt (from sea spray), organic compounds (from forest fires and biogenic emissions), sulphates (from volcanic eruptions), etc. Anthropogenic aerosols can form due to biomass burning, industrial emissions, vehicular emissions, etc. Ultrafine aerosols (<0.01 μm) can be formed by nucleation, or condensation of gaseous pre-cursors. These gradually grow through coagulation into fine aerosols (0.01 - 1 μm) and can then be scavenged by precipitation. The coarser particles (1-10 μm) can be formed due to continued coagulation or due to mechanical re-suspension of dust or evaporation of water droplets. Based on size and chemical nature, aerosols have a wide variety of impacts on both atmospheric processes and human health (Hinds, 1999).

Aerosols interact with radiation in a multitude of ways. These can be grouped into two main processes: scattering and absorption. If, after interaction, the light is re-radiated in the same wavelength, it is termed as scattering. On the other hand, if the light has a

shift in wavelength, it is usually due to absorption. Scattering by a single aerosol particle depends on its size, shape, refractive index, as well as the wavelength of the incident light. For studying earth system processes at synoptic scales, the interactions between aerosol particles and radiation are usually quantified by their bulk properties.

For the atmospheric column, the extinction due to aerosols is given by the Aerosol Optical Depth (AOD), which is:

$$\tau = \int_{SFC}^{TOA} k_e dz \qquad (1.2)$$

Here τ is the AOD, SFC is the surface (z=0) and TOA is the height of the top of the atmosphere. k_e is the extinction coefficient, which is wavelength dependent.

The intensity of radiation of a particular wavelength reaching the surface is then given by:

$$I = I_0 e^{-\tau} \qquad (1.3)$$

where I is the direct radiation intensity received by the surface and I_0 is the TOA radiation.

Aerosol Radiative Effects

As indicated by Eq. 1.3, aerosols can affect the temperature of the surface and near-surface by modifying the radiation received by the planet. The modification of the radiative balance is also termed as radiative effect (or radiative forcing when considering only the anthropogenic contribution). A positive radiative effect means that more radiative flux is being absorbed by the atmosphere or the surface compared to a standard atmosphere or surface, while a negative radiative effect means that less radiative flux is being absorbed. The influence of aerosols on the radiative effect can be divided into two main categories: the direct effect and the indirect effect. Aerosols can directly influence both the incoming

3

solar radiative flux ($K_\downarrow$) and the terrestrial radiative flux through absorption and scattering. This is known as the direct radiative effect of aerosols. Aerosols also affect the formation of clouds, their size and longevity. Since clouds can also interact with the radiative balance of the Earth, this is known as the indirect radiative effect of aerosols.

The Direct Radiative Effect

Aerosols reduce the incoming $K_\downarrow$ from the sun by either scattering it or absorbing it. The ratio of scattering and absorption depends mainly on the concentration, type and vertical profile of aerosols (Forster et al., 2007; Spencer et al., 2008; Boucher et al., 2013). The aerosol-induced longwave radiative effect can be positive - the opposite sign of the short-wave radiative effect (Alizadeh-Choobari et al., 2013) - and depends strongly on particle size (Miller et al., 2006). The relative importance of the direct shortwave and longwave radiative effects depend on aerosol composition. Industrial aerosols (nitrates and sulfates) induce stronger shortwave radiative effect than longwave radiative effect (Haywood et al., 1997; Liao et al., 2004). On the other hand, mineral dust has been shown to have high longwave radiative effect (Hansell et al., 2012; Sicard et al., 2014). Overall, this leads to a change in both the atmospheric and the surface radiative balance. Together, anthropogenic and natural aerosols partially offset the global warming caused by greenhouse gas emissions (Solomon, 2007). However, there are regional differences, with black carbon aerosols warming the atmosphere (Ramanathan & Carmichael, 2008) and sulfate aerosols cooling it (Bellouin et al., 2005; Andreae et al., 2005), though the strength of this cooling is debatable (Harris et al., 2013). Most studies have determined the radiative effect of aerosols at a global scale. However, there are still significant uncertainties at the regional and local scale, where much of the research has been done in recent years (Yu et al., 2001; Verma et al., 2006; Wendisch et al., 2008; Mickley et al., 2012; Han et al., 2012; Zhang et al., 2012).

Except for dust and sulfate aerosols, the direct $K_\downarrow$ radiative effect dominates the direct $L_\downarrow$ radiative effect (Haywood et al., 1997, 2003; Liao et al., 2004). A global modeling study on $K_\downarrow$ and $L_\downarrow$ aerosol forcing found that the $L_\downarrow$ forcing is non-negligible and may be important to reduce uncertainties in climate projections (Reddy et al., 2005). Another modeling study over Australia found that the positive longwave radiative effect due to dust can offset a large portion of the shortwave radiative effect in arid climate (Alizadeh-Choobari et al., 2013). The ratio of the shortwave and longwave radiative effect also has a significant diurnal component. Although shortwave radiative effect may dominate during the day (and on an annual basis), it is not present at night. Given the opposite signs of the two forcings and their diurnal asymmetry, the impact of the aerosol-induced longwave radiative effect is non-negligible for accurate prediction of the diurnal temperature range. A recent study (Cao et al., 2016) on the attribution of causes to the UHI in China found that the nighttime UHI may be enhanced by $L_\downarrow$ forcing due to aerosols. Thus, it is important to disentangle the two components of the aerosol-induced radiative effect and examine how their ratio varies diurnally for different aerosol types, especially at the local and regional scale.

The Indirect Radiative Effect

The indirect effect of aerosols on radiation is manifold and dependent on the interaction of the aerosols with clouds. The major known interactions are:

- The increased reflection of solar radiative flux by clouds, known as the cloud albedo effect or the Twomey effect (Twomey, 1977)

- Prolongation of cloud lifetime by delaying precipitation, known as the cloud lifetime effect (Albrecht, 1989)

- Increase in ice nuclei in mixed-phase clouds, which leads to higher precipitation, as

well as radiative effect, known as the glaciation indirect effect (Lohmann, 2002)

- Delay in freezing of clouds due to smaller droplet size, known as the thermodynamic effect (Matsui et al., 2004)

There are currently significant uncertainties in each of these interactions, particularly in the context of radiative effect (Stocker et al., 2013). Although both the cloud albedo effect and the cloud lifetime effect reduce the incoming radiative flux for both the top of the atmosphere and the surface, the magnitude of reduction depends strongly on the type of cloud and its lifetime. There is also some evidence that aerosols may reduce the lifetime of clouds, for instance, in case of non-precipitating cumulus clouds (Small et al., 2009). Although there is significant observational basis of the aerosol indirect effects on cloud formation (Ramanathan et al., 2001b; Schwartz et al., 2002; Feingold et al., 2003; Kim et al., 2003; Ackerman et al., 2015), the radiative effect due to the indirect effects is hard to quantify (Shao & Liu, 2005). Of the few studies done, one looked at the indirect effect of Saharan dust aerosols on warm clouds and found an indirect $K_\downarrow$ forcing of 29.88 ± 2.42 W m^{-2} per Aerosol Optical Depth (AOD). A study on the $L_\downarrow$ indirect effect due to aerosols for Arctic clouds found a climatologically significant surface forcing of 3.4 W m^{-2} (Lubin & Vogelmann, 2006). Further studies are required on the effect of different aerosols on different types of clouds in various moisture regimes to reach a scientific consensus and hopefully reduce uncertainties in future model projections.

Semi-Direct Effect and Impact on Turbulent Fluxes

There is another group of less studied climatological impacts of aerosols known as the semi-direct effect. The absorption of solar radiative flux by aerosols may lead to a reduction in ambient precipitable water vapor and cause evaporation of clouds, leading to positive radiative effect at the surface (Johnson et al., 2004). Aerosols can also affect

the surface energy budget by influencing the evapo-transpiration from vegetated surfaces (Matsui et al., 2008; Wang et al., 2008). In general, we do not fully understanding the mechanisms involved in the semi-direct radiative effect due to aerosols at different scales (Johnson, 2003).

Aerosols can also change the diffuse radiation ($K_{\downarrow,\mathrm{d}}$), as well as the fraction of diffuse radiation (k_d), received by the surface through scattering (Liepert and Tegen, 2002). The higher $K_{\downarrow,\mathrm{d}}$ allows the sunlight to penetrate the dense canopy and illuminate normally shaded leaves. This impacts ecosystem response, primary productivity, and evapotranspiration (ET) (Niyogi et al., 2004; Mercado et al., 2009) and is known as the diffuse radiation fertilization effect. Thus, other than reducing the incoming radiation at the surface (Zhang et al., 2011), aerosols can also affect the turbulent transfer of heat and moisture (Wang et al., 2008; Urankar et al., 2012).

Previous modeling studies have shown that aerosols, through the diffuse radiation fertilization effect, tends to increase the evaporative fraction, and thus decrease the ratio of the sensible and latent heat fluxes, also known as the Bowen ratio (β) (Wang et al., 2008; Pere et al., 2011; Urankar et al., 2012). Liu et al. (2014) compared the impact of aerosols at a global scale on H and λE and found a proportionally greater decrease in H than would result from just the negative radiative effect. Since the impact of $K_{\downarrow,\mathrm{d}}$ on photosynthesis and transpiration rate depend on vegetation canopy characteristics (Knohl & Baldocchi, 2008), it follows that the aerosol-mediated change in β ($\Delta\beta$) would also be a function of the land cover. The reduction in β due to aerosols has been found to be highest for tropical and temperate broadleaf evergreen forests (Liu et al., 2014) and is positively associated with the Leaf Area Index (LAI) (Matsui et al., 2008). Furthermore, solar radiation may be absorbed or scattered forward, backward or uniformly depending on the chemical and physical characteristics of the aerosol (Hinds, 1999). Thus, aerosol type has a significant influence on how k_d is affected (Cohan et al., 2002). Predominantly scattering aerosols like

sulfate and mineral dust increase the proportion of $K_{\downarrow,\mathrm{d}}$, while predominantly absorbing aerosols like black carbon can slightly reduce it (Kvalevag and Myhre, 2007).

It should be noted that there have not been many systematic investigations of the aerosol-β association over highly polluted regions for different aerosol types. Most importantly, while the impact of aerosols on the turbulent fluxes has been studied, no previous work has examined how that could translate into reductions in surface temperature.

1.1.2 Asymmetric Aerosol Radiative Effect and Temperature Response

Aerosol radiative effect has disproportionately large regional and local impacts, which cannot be captured by the top of the atmosphere radiative effect normally used as a metric in climate studies. Unlike greenhouse gas-induced radiative effect, the impact of aerosols on radiation is different for the surface (large and negative), the atmosphere (large and positive), and the top of the atmosphere (small and negative) (Ramanathan et al., 2001a). Moreover, the ratio of shortwave and longwave radiative effect also depends on the height (Alizadeh-Choobari et al., 2013). For instance, as seen by Alizadeh-Choobari et al. (2013), the TOA longwave forcing is around 4% of the TOA shortwave forcing. However, for the surface, it is close to 20% and in the opposite direction, as in, longwave forcing at the surface is positive, and negates part of the shortwave forcing. Finally, the sensitivity of surface temperature response due to the radiative effect of aerosols is stronger than that due to greenhouse gases (Marvel et al., 2016).

The scientific literature focuses on the top of the atmosphere radiative effect in the context of climate change. However, when trying to elucidate the impact of aerosols on the surface temperature, the surface radiative effect is more important, since the surface temperature directly responds to the change in the incoming radiation at the surface. This is especially true at the regional and local scale since the impact of aerosols on the surface radiation and on the surface feedback through evaporation depend on aerosol type

as well as land cover. Moreover, there is an implicit assumption in the literature that the temperature sensitivity due to aerosol loading is predominantly due to the radiative effect. Since the ecosystem also responds to the aerosol-induced increase in $K_{\downarrow,d}$, which generally increases λE and evaporative cooling, this may not be a correct assumption.

1.1.3 Dearth of Observational Constraints on the Diffuse Radiation Fertilization Effect

$K_{\downarrow,d}$ remains a relatively understudied component of the Earth's radiation budget. The $K_{\downarrow,d}$ fertilization effect, in particular, is poorly constrained by observations due to the dearth of simultaneous measurements of $K_{\downarrow,d}$ and turbulent fluxes across biomes. For instance, only around 50 such sites exist in publicly accessible datasets, namely the FLUXNET (Baldochhi et al., 2001) and AMERIFLUX (Novik et al., 2018) networks (sites shown in Fig. 1.1). When I separate the observed Net Ecosystem Exchange (NEE) and λE into high and low regimes of k_d for different bins of total absorbed shortwave radiation, one can see the expected trends, with both carbon uptake and evapotranspiration increasing for more diffuse conditions (examples shown in Fig. 1.2). This pattern is consistently across most of these sites (not shown).

Sites with simultaneous measurements of diffuse radiation and turbulent fluxes
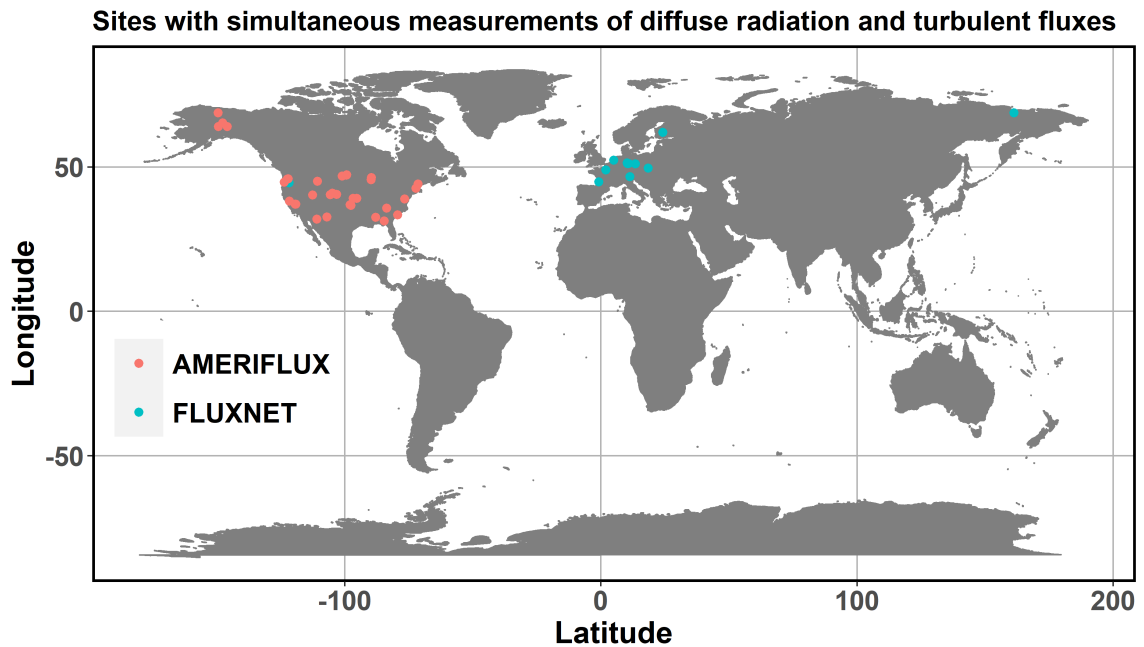
Figure 1.1: Global distribution of sites with simultaneous measurements of diffuse radiation and turbulent fluxes.

However, many of these datasets only contain a couple of months of data, making it hard to generate insights about the global contributions of this effect on the carbon and water budget. Moreover, almost all of these stations are in the northern hemisphere, not in tropical regions, where the $K_{\downarrow,d}$ fertilization effect is expected to be stronger. Thus, our main tool for estimating global impacts of this effect on terrestrial processes is land-surface modeling.
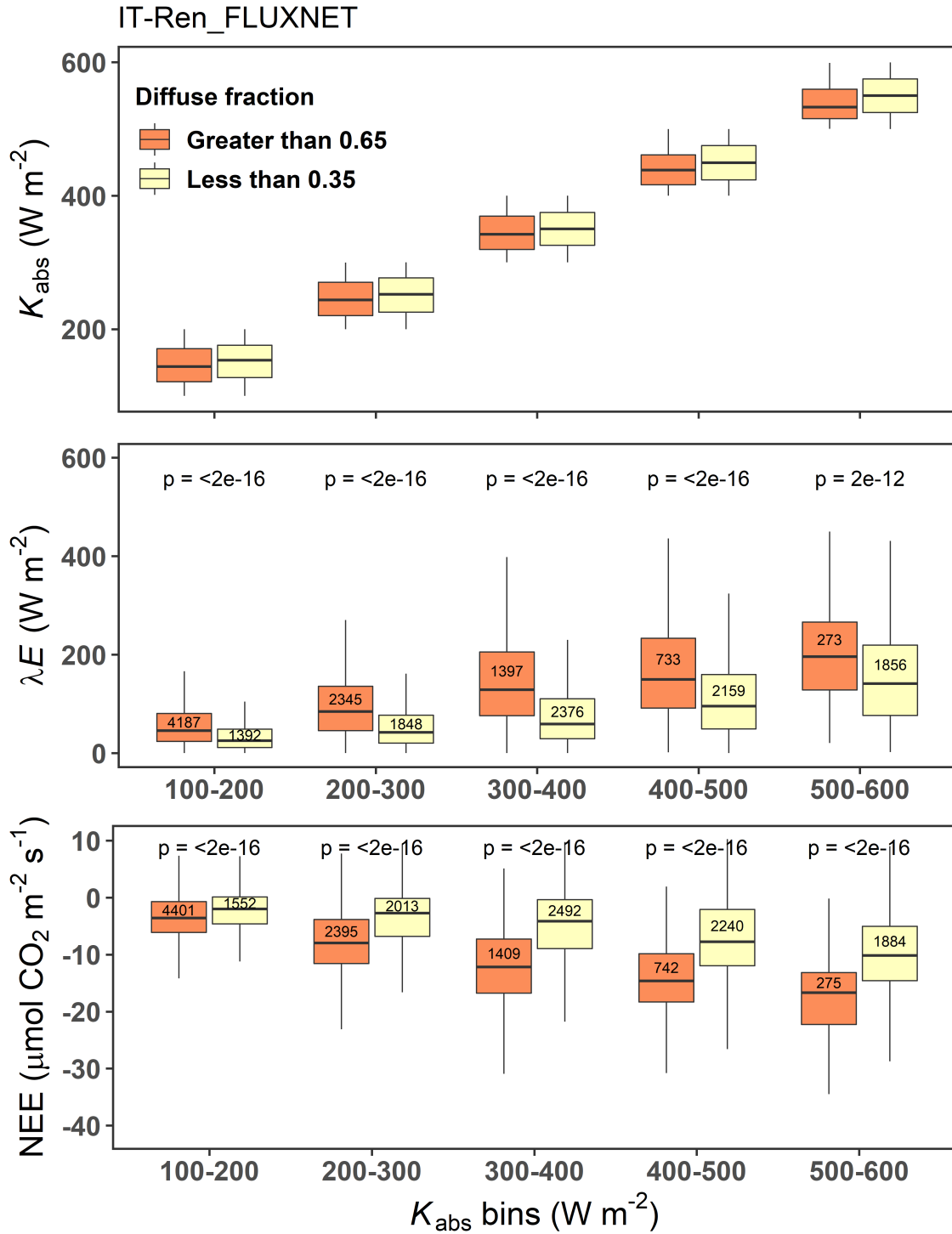
Figure 1.2: Observed latent heat flux and net ecosystem exchange under high and low diffuse fraction regimes for the Renon FLUXNET site in Italy.

1.2 Research Objectives and Dissertation Outline

In my dissertation, I propose to develop a surface energy budget perspective to aerosol-climate interactions and demonstrate that atmospheric aerosols can modify surface climate through both the commonly studied radiative pathways and by enhancing surface evaporative cooling.

This work aims to fill a gap in our scientific understanding of aerosols by isolating the different mechanisms by which aerosols can change the surface temperature at the regional and local scale. The focus is on both aerosol loading and land cover, such that the combined contribution of shortwave radiative effect, longwave radiative effect, and $\Delta\beta$ can be quantified for different ecosystems. In particular, the effect of aerosol-induced β modulation on the surface temperature has not been studied to the best of my knowledge, which is a major gap in our understanding of aerosol influence on the surface energy and carbon budgets. Since the diffuse radiation fertilization effect, one of the main mechanisms by which aerosols can change β, is poorly understood, we discuss potential uncertainties in accurately simulating this effect, both from the perspective of land and atmosphere modeling.

The major objectives and phases of this study are:

- 1) Isolating surface climate response to the shortwave and longwave radiative effects of aerosols

- 2) Isolating the impact of aerosols on surface temperature, terrestrial evapotranspiration, and land carbon uptake through both radiative and non-radiative pathways

- 3) Examining and correcting biases in diffuse solar radiation in global data products

Chapter 2 deals with objective 1 and separates the surface temperature response to aerosols through the shortwave and longwave radiative effects at global to regional scales

for both day and night. This work incorporates the Modern-Era Retrospective analysis for Research and Applications global reanalysis product (version 2; MERRA-2; Gelaro et al., 2017) and using a conceptual surface energy budget framework (Lee et al., 2011).

Chapter 3 deals with objective 2 and expands on **Chapter 1** by including both radiative and non-radiative pathways in the diagnostic calculations. Since MERRA-2 does not provide changes in turbulent fluxes due to aerosols, the latest versions of the Community Atmosphere Model (CAM; Gettelman et al., 2019) and Community Land Model (CLM; Lawrence et al., 2019) are run to calculate them. I also set up modeling experiments to separate the impact of global dimming and the diffuse radiation fertilization effect on surface temperature, terrestrial evapotranspiration, and land carbon uptake.

Chapter 4 deals with part of objective 3. Here I compare the gridded diffuse radiation and diffuse fraction among current-generation reanalysis and satellite-derived products and against ground observations. I also examine the role of aerosols and clouds on long-term trends and biases in diffuse and total incoming solar radiation in the gridded datasets, particularly over Europe and China.

Chapter 5 addresses the biases found in **Chapter 4** by testing different bias-correction techniques for improving the accuracy of gridded datasets and developing a global monthly bias-corrected diffuse radiation product using supervised machine learning.

Appendix A aims to better quantify the impact of urbanization on local climate by developing a new automated algorithm to estimate surface urban heat island (UHI) intensity using satellite remote sensing. The results from the algorithm are validated against previous studies and implemented using over 16-years of satellite observations to create a dataset of surface UHI for over 10000 urban clusters across climate zones. Till date, this remains the most comprehensive quantification of the surface UHI intensity on a global scale using a consistent methodology.

Appendix B uses the COVID-19 lockdown as a perturbation experiment to better un-

derstand human-land-atmosphere coupling in the Indo-Gangetic Basin, one of the most polluted and populated regions of the world. Using some of the methodologies and work-flows developed in **Chapters 1, 2, and 4**, as well as **Appendix A**, this study provides observational evidence of rural control on the UHI, and, more broadly, the strong human influence on surface climate in this region.

Chapter 2

Isolating Surface Climate Response to the Shortwave and Longwave Radiative Effects of Aerosols

2.1 Abstract

Aerosol impact on the surface temperature varies between the shortwave and the longwave components of radiation, depends on the time of the day, and is modulated by underlying biophysical processes. We disentangle these complexities by isolating the direct surface shortwave and longwave radiative effects from a global reanalysis data product and calculating their spatially explicit climate sensitivities. Higher sensitivity is found for the longwave component and is driven by a combination of spatial variability of aerosol species and biophysical control of the underlying surface. The opposing shortwave and longwave effects reduce the global terrestrial mean diurnal temperature range by 0.47 K, with almost half the contribution in the regions of interest considered coming from aerosols of anthropogenic origin. We also find evidence of trend in the local climate sensitivity in the equatorial zone, possibly caused by deforestation. These surface processes can partially explain why the climate forcing efficacy of aerosols exceeds unity.

2.2 Introduction

The impact of aerosols is one the greatest uncertainties in our understanding of the Earth's climate system (Stocker et al., 2013). Aerosols modulate the Earth's radiative budget, either directly through scattering and absorption (Bellouin et al., 2005) or indirectly by influencing the size and longevity of clouds (Li et al., 2011; Twomey, 1991). While several methods can be used to estimate the perturbation to the radiative budget by different forcing agents (Tang et al., 2019), the top of the atmosphere values are traditionally used as a metric for temperature predictions in climate studies. This practice implicitly assumes that the temperature response of the planet is independent of the forcing agent or location of its emission source. While this is defensible for globally homogeneous forcing agents such as well-mixed greenhouse gases, for forcing agents that have significant spatial variability, like land use change, this assumption is insufficient (Bright et al., 2017). Aerosols also fall into this category, due to the significant horizontal and vertical variability of the aerosol radiative effect (RE; Stuber et al., 2005). Because of these spatial heterogeneities, particularly the higher concentration of aerosols over the Northern Hemisphere, the global climate sensitivity to the radiative forcing (RF) of aerosols—the anthropogenic component of the aerosol RE—is higher than to the RF associated with well-mixed greenhouse gases (Hansen et al., 2005; Marvel et al., 2015; Rotstayn et al., 2015; Shindell, 2014).

Both the total aerosol RE (Ramanathan et al., 2001) and the relative roles of shortwave and longwave RE depend on altitude (Choobari et al., 2013), aerosol composition, and aerosol size (Hansell et al., 2012; Haywood et al., 1997; Sicard et al., 2014). Overall, the shortwave RE ($\Delta K_\downarrow$) dominates the longwave RE ($\Delta L_\downarrow$; Haywood et al., 1997; Highwood et al., 2003; Liao et al., 2004). However, $\Delta L_\downarrow$ can offset a large portion of $\Delta K_\downarrow$ in arid and semiarid regions, where coarse-grained mineral dust aerosols are effective emitters of longwave radiation in the atmospheric thermal window (wavelength 4–10 μm; Choobari

et al., 2013).

Moreover, $\Delta L_\downarrow$ exists during both daytime and nighttime unlike $\Delta K_\downarrow$. Further complicating the matter is the fact that the same RE can induce different surface temperature responses because the energy redistribution between the surface and the atmospheric boundary layer varies between time of the day and with the biophysical attributes of the underlying local surface.

Here we deploy the theory of the intrinsic biophysical mechanism (IBPM; Lee et al., 2011) and an atmospheric reanalysis data product to disentangle these synergistic interactions between the aerosol RE and the local biophysical processes. We aim (1) to quantify spatial variations of the surface shortwave and longwave radiative effects under present climate conditions, (2) to calculate the local surface temperature perturbations caused by these effects, and (3) to discuss the contribution of surface-air exchange processes to the long-term change in the climate efficacy of aerosols.

2.3 Methods

2.3.1 The IBPM Theory

The IBPM theory combines the surface energy balance equation with a one-source model of the sensible heat flux to solve for the surface temperature (TS; Lee et al., 2011). This solution expresses T_S as a function of atmospheric forcing and energy redistribution between the surface and the lower atmosphere

$$T_\mathrm{S} = T_\mathrm{b} + \frac{\lambda_0}{1+f}\left(R_n^* - G\right) \tag{2.1}$$

where T_b is the background or blending-height air temperature, λ_0 is the local intrinsic climate sensitivity, f, a dimensionless energy redistribution factor, is a measure of the

efficiency of energy dissipation between the surface and the atmospheric boundary layer, G is ground heat flux, and R_n^* is the apparent net radiation given by

$$R_n^* = K_\downarrow (1 - a) + L_\downarrow - \sigma T_b^4 \qquad (2.2)$$

where $K_\downarrow$ is the incoming shortwave, $L_\downarrow$ is the incoming longwave, a is surface albedo, and σ is the Stefan-Boltzmann constant. The local intrinsic climate sensitivity is essentially the longwave feedback derived by differentiating the Stefan-Boltzmann law and is given by

$$\lambda_0 = \frac{1}{4 \in \sigma T_b^3} \qquad (2.3)$$

Changes to T_S are produced via perturbations to the energy redistribution and to the forcing variables T_b and R_n^*.

The aerosol direct effect changes T_S by perturbing T_b, $K_\downarrow$ and $L_\downarrow$ at the surface, and f. Differentiating Eq. 2.1, we obtain

$$\Delta T_S = \Delta T_b + \Delta T - \frac{\lambda_0}{(1 + f)^2} (R_n^* - G) \Delta f \qquad (2.4)$$

where Δ indicates the perturbation signal. Perturbation to the energy redistribution factor Δf can arise from changes in Bowen ratio as a response to more diffuse radiation under polluted skies or from changes in land use that alters the surface roughness. ΔT can be separated into the contributions from the aerosol surface $\Delta K_\downarrow$ and $\Delta L_\downarrow$ as

$$\Delta T = \frac{\lambda_0}{1 + f} [(1 - a)\Delta K_\downarrow + \Delta L_\downarrow] \qquad (2.5)$$

where the effective local climate sensitivity is given by

$$\lambda^* = \frac{\lambda_0}{1 + f} \qquad (2.6)$$

Note that the local surface temperature perturbation (ΔT), when added to the background temperature change (ΔT_b), gives the total surface temperature change (ΔTS).In this study, we estimate this ΔT from (1) $\Delta K_\downarrow$ and $\Delta L_\downarrow$ derived from the radiation diagnostics with and without aerosols and (2) f from the lowest level modeled temperature and the reanalyzed surface energy balance variables (Bright et al., 2017; Lee et al., 2011) from the Modern-Era Retrospective analysis for Research and Applications global reanalysis product (version 2; MERRA-2; Gelaro et al., 2017).

2.3.2   Reanalysis Data Product

The MERRA-2 data are gridded at a spatial resolution of $0.625°$ by $0.5°$ for every hour. In addition to standard meteorological variables and radiative fluxes under realistic conditions, MERRA-2 calculates the diagnostic radiative flux by assuming no aerosols in the atmosphere. The direct aerosol effect is then determined from these radiation fields. In the case of the shortwave RE, $\Delta K_\downarrow$ is the difference in $K_\downarrow$ between all-sky and polluted conditions versus all-sky and clean conditions (Figs 2.3e and 2.3f). In the case of the longwave RE, $\Delta L_\downarrow$ is the difference in $L_\downarrow$ absorbed by the surface under all-sky and polluted conditions versus clear-sky and clean conditions (Figs 2.3g and 2.4a). This hybrid approach (all-sky for $K_\downarrow$ and clear sky for $L_\downarrow$) is used since MERRA-2 does not provide all-sky incoming $L_\downarrow$ without aerosols.

Additionally, the MERRA-2 dataset is used to compute f by inverting Eq. 2.1

$$f = \frac{\lambda_0}{T_S - T_b} \left(R_n^* - G \right) - 1 \tag{2.7}$$

In this diagnostic calculation, T_b is the air temperature at the lowest model level (985 hPa), and all other variables are obtained from the suite of surface micrometeorological variables produced by the reanalysis. The median f values for each year are calculated

separately for daytime and nighttime for each grid. The annual mean values are averages of the daytime and nighttime values weighted by the daytime and nighttime hours for each grid. For all variables, data from the most recent decade (2008 to 2017) are used to produce mean spatial patterns, and data from the full assimilation period (1980 to 2017) are used to examine temporal trends.

Table 2.1: Summary of mean and standard deviation of the estimated variables for the world's land surfaces and each climate zone for 2008-2017. Here f is the energy redistribution factor (unitless), λ_0 is the intrinsic climate sensitivity (in K W^{-1} m^2), λ^* is the effective local climate sensitivity (in K W^{-1} m^2), RE is the aerosol radiative effect (in W m^{-2}), $\Delta K_\downarrow$ is the aerosol RE in the shortwave band (in W m^{-2}), $\Delta L_\downarrow$ is the aerosol RE in the longwave band (in W m^{-2}), ΔT is the temperature perturbation (in K), and ΔDTR is the diurnal temperature range perturbation (in K).

Variable	Global	Equatorial	Arid	Temperate	Snow	Polar
			Daytime (surface)			
f	6.98 ± 2.53	13.25 ± 7.71	3.47 ± 1.14	7.75 ± 2.99	6.73 ± 1.74	5.12 ± 1.00
λ_0	0.19 ± 0.02	0.16 ± 0.00	0.17 ± 0.01	0.18 ± 0.01	0.21 ± 0.01	0.22 ± 0.01
λ^*	0.029 ± 0.007	0.015 ± 0.007	0.041 ± 0.009	0.022 ± 0.006	0.029 ± 0.006	0.037 ± 0.006
$\Delta K_\downarrow$	-16.40 ± 8.50	-18.31 ± 10.85	-24.94 ± 14.48	-17.40 ± 11.99	-9.62 ± 4.41	-6.44 ± 1.87
$\Delta L_\downarrow$	1.01 ± 1.07	0.77 ± 0.82	2.25 ± 2.30	0.73 ± 0.75	0.26 ± 0.27	0.13 ± 0.14
ΔT (to $\Delta K_\downarrow$)	-0.39 ± 0.24	-0.27 ± 0.24	-0.75 ± 0.47	-0.33 ± 0.28	-0.20 ± 0.12	-0.17 ± 0.08
ΔT (to $\Delta L_\downarrow$)	0.039 ± 0.048	0.015 ± 0.021	0.110 ± 0.119	0.018 ± 0.023	0.007 ± 0.009	0.005 ± 0.007
			Nighttime (surface)			
f	0.90 ± 0.32	0.73 ± 0.73	0.54 ± 0.27	0.62 ± 0.50	1.33 ± 0.62	1.02 ± 0.68
λ_0	0.21 ± 0.03	0.17 ± 0.00	0.20 ± 0.02	0.20 ± 0.01	0.24 ± 0.02	0.27 ± 0.02
λ^*	0.122 ± 0.025	0.115 ± 0.040	0.130 ± 0.023	0.132 ± 0.141	0.113 ± 0.034	0.146 ± 0.043
$\Delta L_\downarrow$	0.99 ± 1.04	0.80 ± 0.84	2.26 ± 2.16	0.75 ± 0.75	0.25 ± 0.28	0.13 ± 0.15
ΔT (to $\Delta L_\downarrow$)	0.126 ± 0.131	0.105 ± 0.138	0.287 ± 0.269	0.107 ± 0.133	0.030 ± 0.042	0.018 ± 0.025
			Annual (surface)			
f	4.21 ± 1.41	7.53 ± 4.42	2.13 ± 0.66	4.50 ± 1.74	4.29 ± 1.12	3.26 ± 0.76
λ^*	0.072 ± 0.013	0.061 ± 0.021	0.081 ± 0.012	0.072 ± 0.065	0.067 ± 0.018	0.087 ± 0.021
ΔT	-0.13 ± 0.06	-0.09 ± 0.08	-0.22 ± 0.10	-0.12 ± 0.10	-0.09 ± 0.05	-0.08 ± 0.03
ΔDTR	-0.47 ± 0.32	-0.36 ± 0.34	-0.93 ± 0.62	-0.42 ± 0.38	-0.22 ± 0.14	-0.18 ± 0.09
RE	-7.94 ± 3.64	-9.17 ± 5.34	-11.25 ± 5.80	-8.74 ± 5.89	-5.01 ± 2.18	-3.39 ± 0.94
			Daytime (top of atmosphere)			
$\Delta K_\downarrow$	-2.99 ± 1.40	-4.85 ± 2.65	-2.73 ± 3.68	-5.12 ± 3.32	-1.88 ± 1.51	-0.34 ± 0.84
$\Delta L_\uparrow$	-0.29 ± 0.27	-0.23 ± 0.22	-0.67 ± 0.56	-0.19 ± 0.21	-0.09 ± 0.09	-0.05 ± 0.05
			Nighttime (top of atmosphere)			
$\Delta L_\uparrow$	-0.10 ± 0.07	-0.12 ± 0.09	-0.18 ± 0.14	-0.08 ± 0.07	-0.04 ± 0.04	-0.02 ± 0.02
			Annual (top of atmosphere)			
Land RE	-1.43 ± 0.71	-2.46 ± 1.32	-1.04 ± 2.06	-2.65 ± 1.71	-0.96 ± 0.77	-0.15 ± 0.44
All RE	(-0.89 ± 0.27)					

The global spatial pattern of daytime f (Fig. 2.1a) is broadly similar to the f map given in Bright et al. (2017) for the period from 2001 to 2011. In Bright et al. (2017), the f value was computed from a satellite- and surface-based observational dataset using the same diagnostic equation (Eq. 2.7). Our global mean f of 4.21 (Table 2.1) compares favorably to the global mean of around 3.67 reported in Bright et al. (2017). As expected, f is lower for smooth surfaces and higher for rough surfaces. Due to the predominance of forested (rougher) areas in tropical latitudes, the f value is much higher near the equator than at other latitudes. A strong diurnal asymmetry exists in f, with much lower values at night resulting from higher static stability and less turbulent mixing than during the day.
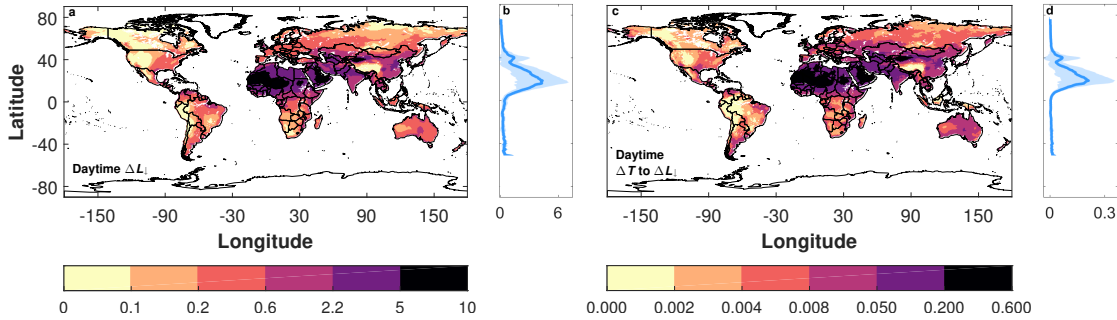
Figure 2.1: Global spatial patterns of daytime **a** and nighttime **c** f (unitless) for 2008-2017. Non-linear color maps are used to better visualize the spatial variations throughout the world. The corresponding zonal characteristics are given in panels **b** (daytime f) and **d** (nighttime f). The solid lines represent the zonal means, while the shaded regions show standard deviations at each degree of latitude.

2.3.3 Isolating the Impact of Aerosols by Climate Zone

Given that we focus on the Earth's land surfaces in this study, all global mean values, unless specified otherwise, refer to the spatial means over the MERRA-2 grids that are predominantly (>90%) land. To investigate the role of surface characteristics on aerosol-surface interactions, we divide the world's land surfaces into the Koppen-Geiger climate classes, namely, equatorial, arid, warm temperate (henceforth, temperate), snow, and po-

lar (Rubel & Kottek, 2010), representing five different regimes of surface characteristics and atmospheric forcing (Fig. 2.2a). Regional mean values are computed from spatial averaging within these regions of interest.
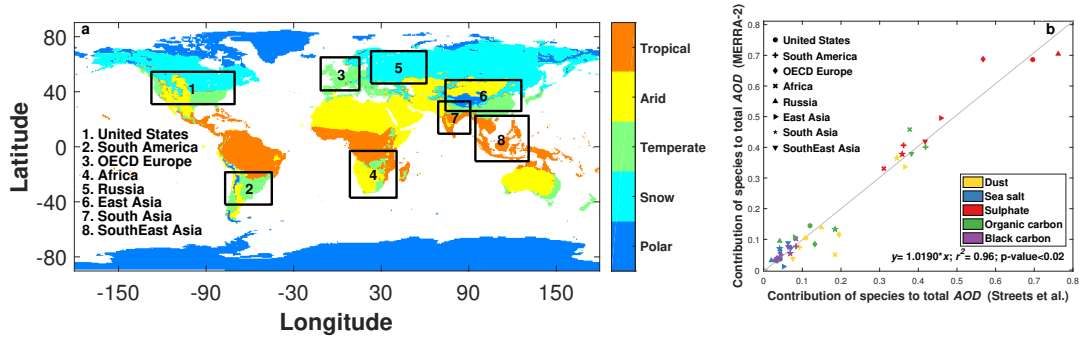
Figure 2.2: a Distribution of Koppen-Geiger climate zones and regions of interest used in this study and **b** comparison of contribution of different species to total AOD for MERRA-2 and Street et al. (2009).

2.3.4 Contribution of Anthropogenic Aerosols to Radiative Effect

A second group of regions of interest are used to estimate the anthropogenic aerosol contribution to the ΔT. They are the following: United States, South America, OECD Europe, Southern Africa, Russia, East Asia, South Asia, and South East Asia. These regions are chosen based on a previous study, in which researchers ran the Goddard Chemistry, Aerosol, Radiation, and Transport (GOCART) model using emission inventories for anthropogenic and natural aerosol sources and quantified the anthropogenic contribution to the aerosol optical depth (AOD) for each aerosol species (Streets et al., 2009).

At the surface, changes in $\Delta K_\downarrow$ are proportional to changes in AOD. Thus, for each region of interest, the fractional contribution of anthropogenic aerosols to $\Delta K_\downarrow$ is equal to the fractional contribution of these aerosols to the total AOD. The anthropogenic AOD fractions for these regions are taken from Streets et al. (2009).

The AOD calculated by MERRA-2 for the five main aerosol species (dust, sea salt, sulphate, organic carbon, and black carbon) is in excellent agreement with the results of

24

Streets et al. (2009; Fig. 2.2b), indicating broad consistence between MERRA-2 and GOCART. The anthropogenic contribution to ΔT for aerosol RE (shortwave) is obtained from Eq. 2.5 using anthropogenic $\Delta K_\downarrow$.

To obtain the anthropogenic contribution to $\Delta L_\downarrow$, we first convert the total assimilated AOD at 550 nm from MERRA-2 to the AOD at 10,000 nm (roughly the middle of the longwave wavelength band) for each aerosol species using the Angstrom power law (Ångström, 1929);

$$\text{AOD}_{10000} = \text{AOD}_{550} \left[\frac{10000}{550} \right]^{\text{Å}} \qquad (2.8)$$

where Å is the Angstrom exponent for the wavelength-dependence of AOD for that species. Of the five aerosol species, we assume that all sulphate, organic carbon, and black carbon aerosols originate from anthropogenic sources and that all dust and sea-salt aerosols originate from natural sources. We then obtain the total fractional contribution of anthropogenic aerosols to the total AOD at 10,000 nm. The anthropogenic contribution to $\Delta L_\downarrow$ is the product of $\Delta L_\downarrow$ and this AOD fraction. Strictly, Å is based on the AOD at two wavelengths and is valid within the range bounded by the two wavelength values used. For instance, MERRA-2's Å is based on the AOD at 470 and 870 nm. Beyond this range, linear extrapolation using Å can lead to uncertainties (Kedia & Ramachandran, 2009). Moreover, some of the sulphate, organic carbon, and black carbon aerosols are produced by natural sources. For these reasons, we consider our estimates of the anthropogenic contribution to $\Delta L_\downarrow$ to be upper bounds of the actual values. The overall results are not affected by these simplifications because the anthropogenic $\Delta L_\downarrow$ fraction is almost negligible, varying from 2% to 6% in the regions of interest, and consistent with previous estimates (Stier et al., 2007).
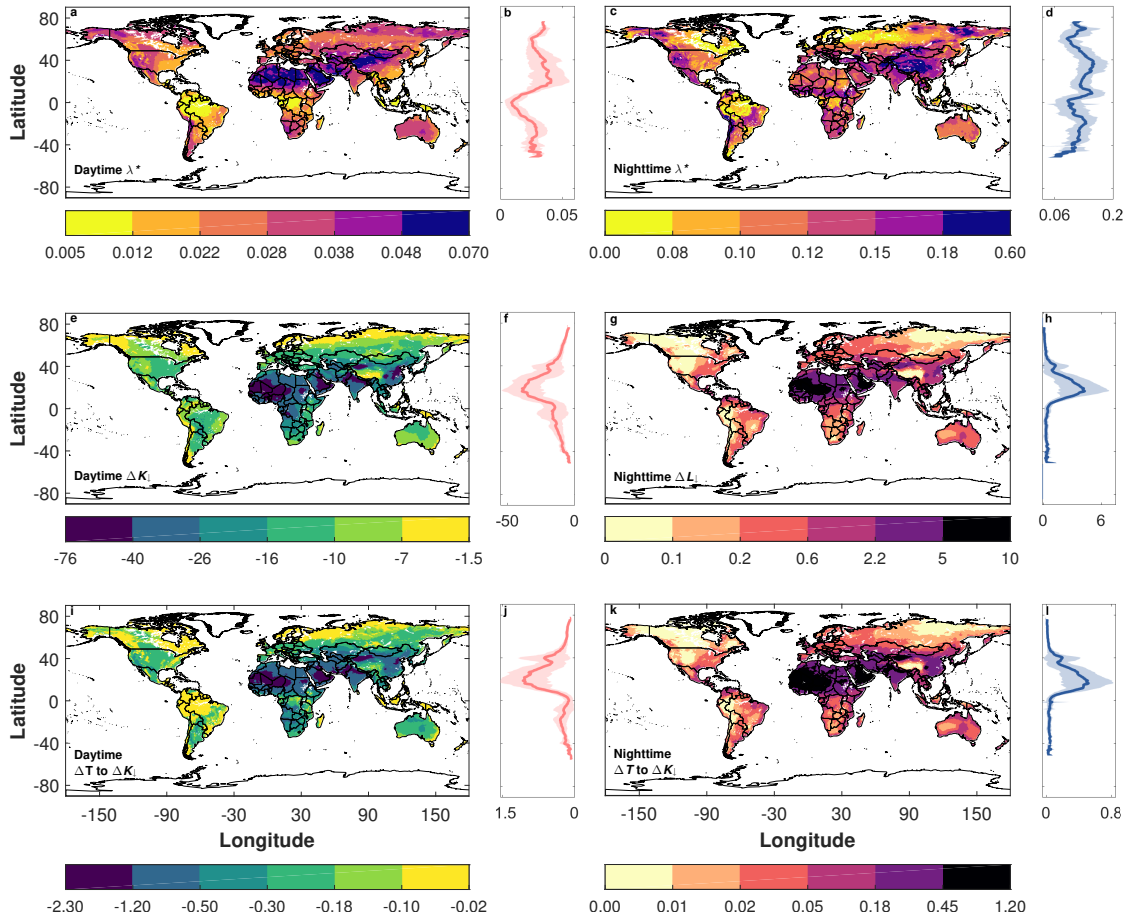
Figure 2.3: Global spatial patterns of daytime **a** and nighttime **c** apparent surface climate sensitivity λ_* (in K W^{-1} m^2), daytime shortwave radiative effect RE (**e** $\Delta K_\downarrow$; in W m^{-2}), nighttime longwave RE (**g** $\Delta L_\downarrow$; in W m^{-2}), daytime temperature perturbation ΔT due to shortwave RE (in K) (i), and nighttime ΔT due to longwave RE (in K) (**k**) for 2008-2017. Non-linear color maps are used to better visualize the spatial variations throughout the world. The corresponding zonal characteristics are also given in panels **b** (daytime λ_*), **d** (nighttime λ_*), f (daytime shortwave RE), **h** (nighttime RE), **j** (daytime ΔT), and l (nighttime ΔT). The solid lines represent the zonal means, while the shaded regions show standard deviations at each degree of latitude.

2.4 Results

2.4.1 Local Temperature Response to Aerosol Direct Radiative Effect

The surface $\Delta K_{\downarrow}$ is most negative over eastern China, North India, and western Africa owing to high pollution and dust emissions (Fig. 2.3e). Due to the strong interaction between dust aerosols and $L_{\downarrow}$, the surface $\Delta L_{\downarrow}$ shows large positive values over arid regions, namely, the Sahara Desert, the Arabian Peninsula, northwestern China, and western India (Figs 2.3g and 2.4a). In heavily polluted parts of eastern China and North India, the daytime $\Delta L_{\downarrow}$ is around 3.5 W m^{-2} or about 30% of the highest value found for Sahara Desert. The global mean daytime $\Delta K_{\downarrow}$ over land is -16.40 W m^{-2}, or 16 times the magnitude of the daytime (1.01 W m^{-2}; Fig. 2.4a) and nighttime $\Delta L_{\downarrow}$ (0.99 W m^{-2}; Fig.2.3g). The annual mean $\Delta K_{\downarrow}$ over the whole planet (land + oceans) is -4.31 W m^{-2}.
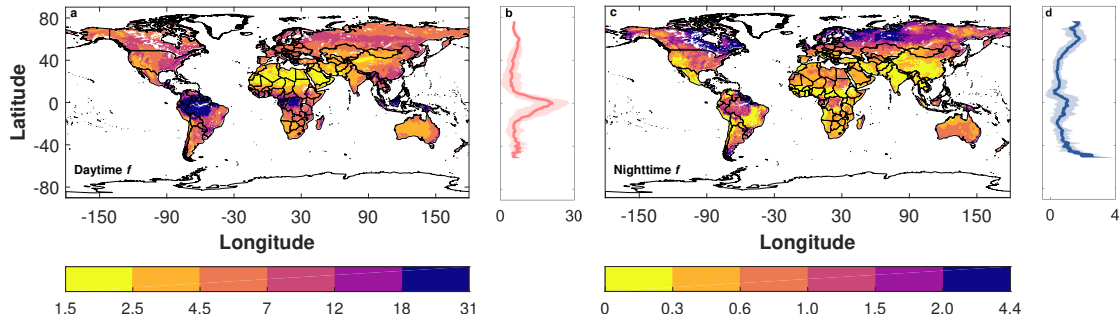
Figure 2.4: a, Global spatial patterns of daytime surface longwave RE ($\Delta L_{\downarrow}$; in W m^{-2}) and **c**, global spatial patterns of daytime temperature perturbation ΔT to daytime longwave RE (in K) for 2008-2017. Non-linear color maps are used to better visualize the spatial variations throughout the world. The corresponding zonal characteristics are given in panels **b** (daytime $\Delta L_{\downarrow}$) and **d** (temperature perturbation to daytime $\Delta L_{\downarrow}$). The solid lines represent the zonal means, while the shaded regions show standard deviations at each degree of latitude.

The surface temperature response to aerosols is controlled by both the local RE and the local climate sensitivity. The daytime local climate sensitivity λ^* is highest over the

27

arid and polar climate zones due to the lack of vegetation and is lowest in the equatorial zone because high surface roughness promotes energy redistribution between the surface and the lower atmosphere (Fig. 2.3a). We have already noted the high RE over the arid zone. λ^* is also high, implying that this zone is most sensitive to aerosol loading. The presence of coarse mode aerosols that strongly affect $L_\downarrow$ over these regions, combined with the overall higher surface reflectivity for $K_\downarrow$, leads to a stronger daytime sensitivity to $\Delta L_\downarrow$ (0.039 K W^{-1} m^2) than to $\Delta K_\downarrow$ (0.024 K W^{-1} m^2) when averaged over the Earth's land surfaces. The nighttime λ^* is more than twice as much as the daytime value, indicating less turbulent mixing during this period and resulting in a much stronger temperature response to the same RE than during the day. There is less variability in λ^* among the different climate zones at night than during the day (Fig. 2.3c). The mean surface climate sensitivity to surface aerosol RE for the Earth's land surface is 0.016 K W^{-1} m^2, estimated by dividing the global mean ΔT of -0.13 K with the global mean surface RE (including both shortwave and longwave) of -7.94 W m^{-2} (Table 2.1). This local surface climate sensitivity is more than an order of magnitude smaller than the global climate sensitivity derived from radiative balance perturbations at the top of the atmosphere (Rotstayn et al., 2015).

The IBPM calculation reveals highly variable but spatially coherent patterns of ΔT across the world (Figs 2.6i, 2.6k, and 2.4c). These spatial patterns are largely controlled by the spatial variabilities of $\Delta K_\downarrow$ and $\Delta L_\downarrow$ and are also influenced by local biophysical processes. The global mean daytime ΔT over land is -0.39 K due to $\Delta K_\downarrow$ and 0.04 K due to $\Delta L_\downarrow$, while the nighttime ΔT is 0.13 K due to $\Delta L_\downarrow$. Regionally, the strongest response is seen in the arid zone, with the daytime ΔT reaching around -2.3 K and nighttime ΔT reaching 1.2 K. The zonal mean ΔT peaks at around 20°N for both shortwave (-1.1 K) and longwave (0.2 K in the daytime and 0.5 K during nighttime) due to the high climate sensitivity (in the daytime; Fig. 2.3b) and the high RE (both daytime and nighttime, Figs

2.3f, 2.3h, and 2.4b). Averaged over the 24-hr cycle, the aerosol direct RE reduces the global surface temperature by 0.13 K during 2008 to 2017 (Table 2.1 and Fig. 2.5). In some regions (like Australia), the nighttime warming due to $\Delta L_\downarrow$ is large enough to almost offset the daytime cooling due to $\Delta K_\downarrow$ (Fig. 2.3).
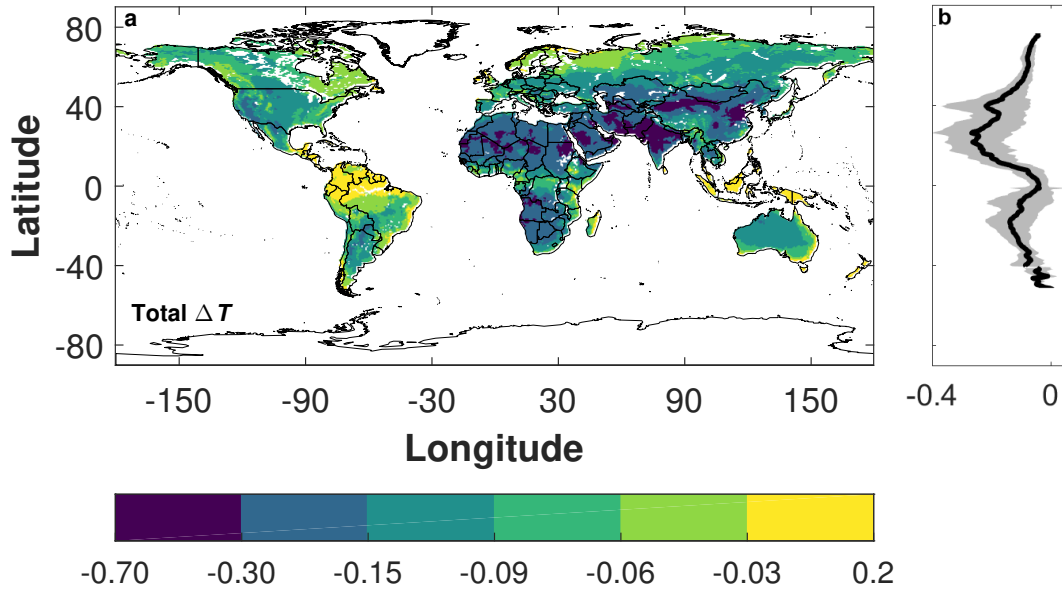
Figure 2.5: a, Global spatial patterns of 24-hour ΔT (in K) and **b**, the zonal characteristics of 24-hour ΔT for 2008-2017. Non-linear color maps are used to better visualize the spatial variations throughout the world. The solid line in panel **b** represents the zonal mean, while the shaded regions show standard deviations at each degree of latitude.

2.4.2 Impact on the Diurnal Temperature Range and Anthropogenic Contributions

The daytime cooling and nighttime warming will reduce the diurnal temperature range (DTR) (Huang et al., 2006; Sarangi et al., 2018). Although this aerosol DTR effect is known conceptually for some time, we lack a detailed assessment of its geographic variation and a quantitative attribution of anthropogenic and natural contributions. Here we find that unsurprisingly, the highest reduction in DTR (around 3 K) occurs over arid regions

with high aerosol loading (Fig. 2.6). In the Amazon basin, because the effective climate sensitivity is low (daytime $\lambda^* = 0.0075$ K W^{-1} m^2), aerosols have little impact on DTR (around -0.09 K) even though $\Delta K_\downarrow$ and $\Delta L_\downarrow$ are moderately strong, at -10.55 and 0.28 W m^{-2}, respectively. For comparison, similar REs ($\Delta K_\downarrow = -9.56$ W m^{-2}; $\Delta L_\downarrow = 0.44$ W m^{-2}) cause a larger reduction in DTR (-0.27 K) in Australia, where smooth landscapes, which are not efficient at dissipating heat from the surface to the atmospheric boundary layer, enhance the climate sensitivity (daytime $\lambda^* = 0.0299$ K W^{-1} m^2).
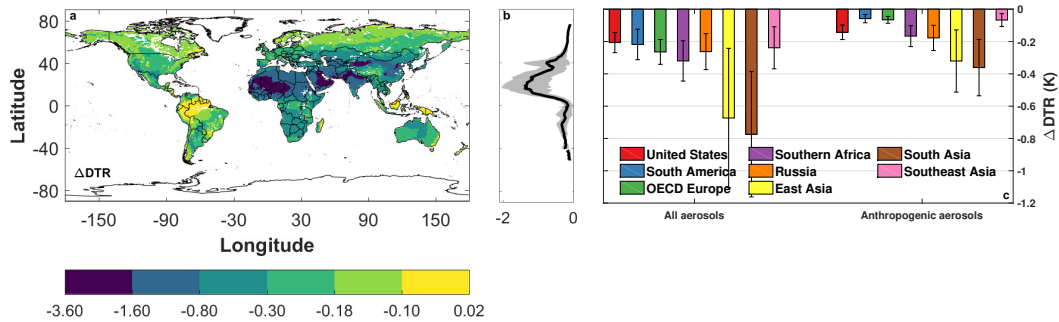
Figure 2.6: a, Global spatial pattern of changes in the diurnal temperature range (DTR; in K) for 2008–2017, **b**, zonal mean change in DTR, and **c**, mean DTR change for each region of interest due to all aerosols and only anthropogenic aerosols. Shaded regions in panel **b** and error bars in panel **c** represent ±1 standard deviation.

Anthropogenic aerosols account for around 10% of the total global aerosol load (Hinds, 1999), but because they have higher scattering efficiencies than natural aerosols, they contribute to almost half the AOD, thus disproportionately modulating the surface temperature response. Averaged over the eight major regions of the world considered here, anthropogenic aerosols reduce the surface $K_\downarrow$ by 8.2 W m^{-2} and increase the surface $L_\downarrow$ by 0.022W m^{-2} (Fig. 2.7) through their direct effect. The anthropogenic contribution to the overall DTR reduction is highest for the Unites States at 68% and lowest for South America at 26%. Aggregating all the eight regions of interest, anthropogenic aerosols lead to about 50% of the total DTR reduction (Fig. 2.6c).
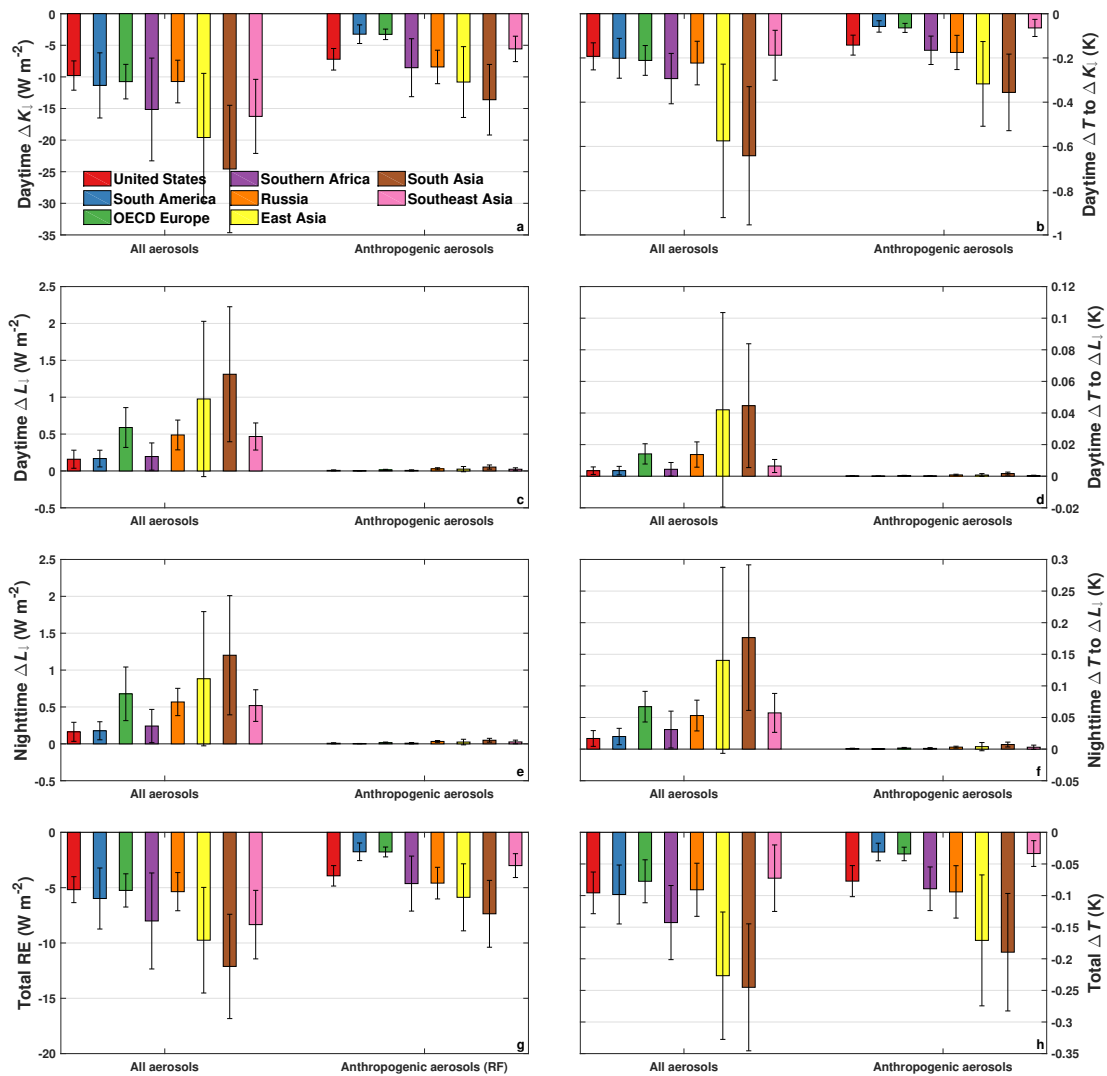
Figure 2.7: a, daytime shortwave RE ($\Delta K_{\downarrow}$), **b**, daytime temperature perturbation due to shortwave RE, **c**, daytime longwave RE ($\Delta L_{\downarrow}$), **d**, daytime temperature perturbation due to longwave RE, **e**, nighttime longwave RE ($\Delta L_{\downarrow}$), f, nighttime temperature perturbation; **g**, total RE at the surface, and **h**, 24-hour mean temperature perturbation for 1980-2006.

2.4.3 Inter-annual Trends

Globally, the ΔT becomes more negative at a rate of -0.014 K per decade in the daytime for shortwave and more positive at a rate of 0.002 K (daytime) and 0.006 K (night) per decade for longwave, from 1980 to 2017 (Fig. 2.8). The combined effect is a decrease

31

of the global DTR by -0.018 K per decade (Fig. 2.9). The primary driver of these global temperature trends is the strengthening of the aerosol RE over time. The mean $\Delta K_\downarrow$ and daytime (nighttime) $\Delta L_\downarrow$ are -16.4 and 1.01 (0.99) W m^{-2} in 2008–2017, respectively, compared to -14.6 and 0.88 (0.88) W m^{-2} in 1980–1989. Note that the differences in the first and last 10-year means are muted due to aerosol loading caused by the volcanic eruption of El Chichón in 1982. Of the five climate zones (Figs 2.8 and 2.10 to 2.13), the temperate zone experiences the largest percentage change between the first and last 10 years for $\Delta K_\downarrow$ (22%) and $\Delta L_\downarrow$ (44% during day, 50% at night).
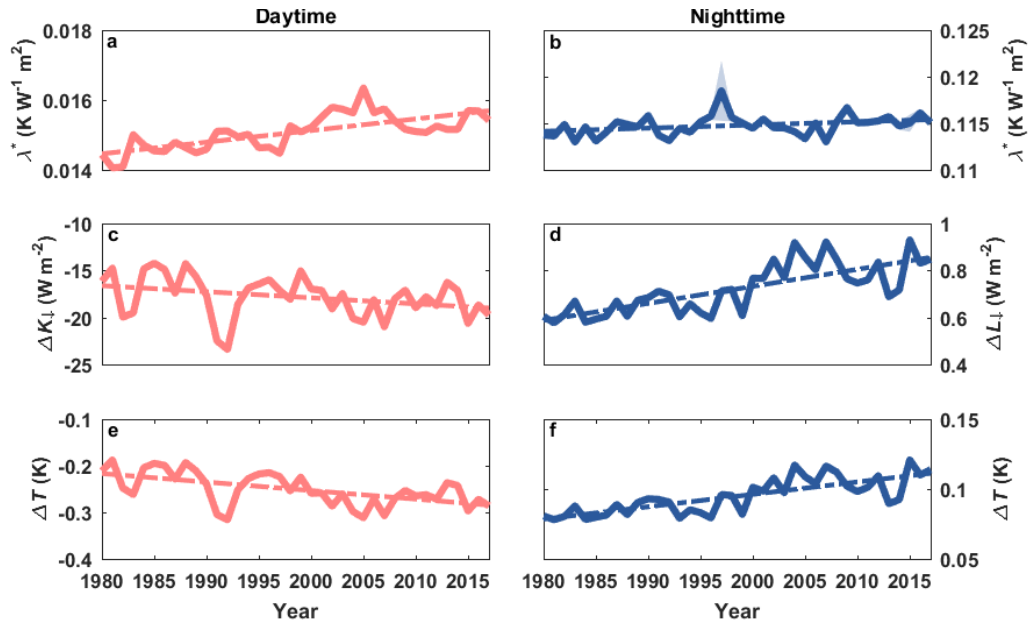
Figure 2.8: Long-term trends in **a**, daytime apparent surface climate sensitivity λ_*, **b** nighttime λ_*, **c** daytime surface shortwave RE ($\Delta K_\downarrow$), **d** nighttime surface longwave RE ($\Delta L_\downarrow$), **e** daytime temperature perturbation, and f nighttime temperature perturbation for the equatorial climate zone. The dashed lines show the linear trends of the temporal variation. All long-term trends are statistically significant (p-value<0.01).
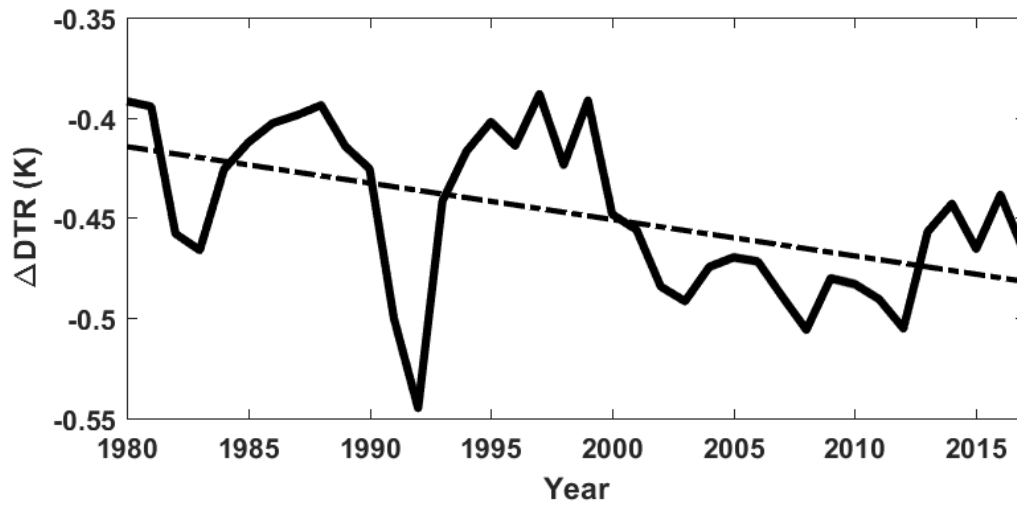
Figure 2.9: Long-term trend of diurnal temperature range perturbation for the world's land surfaces. The solid line shows the mean values while the shaded portion shows the standard error of the means. The standard errors are negligible. The dashed line shows the linear trend of the temporal variation. The long-term trend is statistically significant (p-value<0.01).
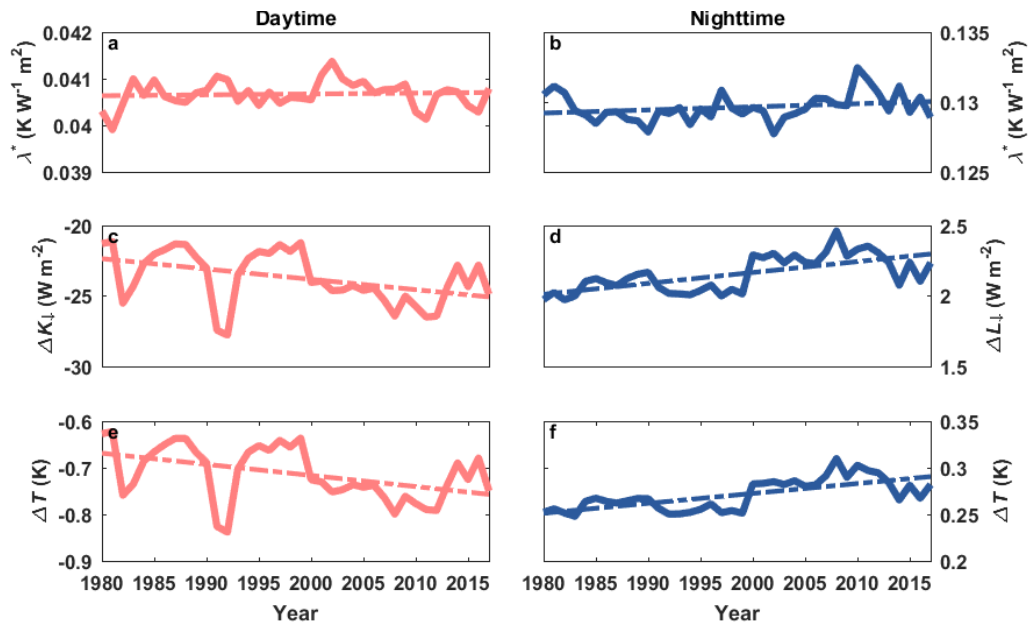
Figure 2.10: Long-term trends in **a**, daytime apparent surface climate sensitivity (λ_*), **b**, nighttime λ_*, **c**, daytime surface shortwave RE ($\Delta K_\downarrow$), **d**, nighttime surface longwave RE ($\Delta L_\downarrow$), **e**, daytime temperature perturbation, and f, nighttime temperature perturbation in the arid climate zone. The dashed lines show the linear trends of the temporal variation. All long-term trends are statistically significant (p-value < 0.01).
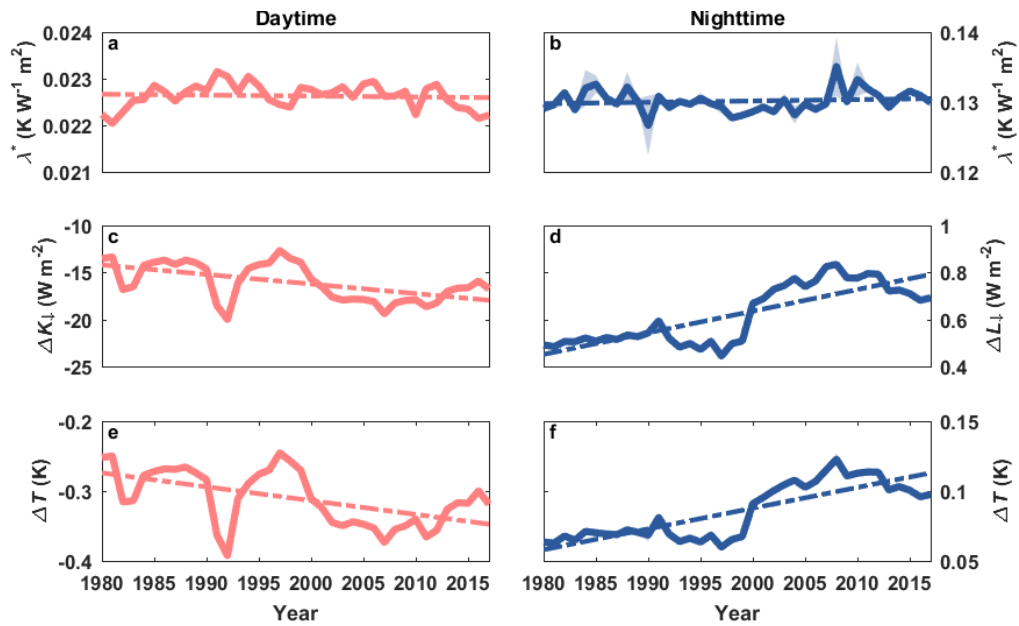
Figure 2.11: Long-term trends in **a**, daytime apparent surface climate sensitivity (λ_*), **b**, nighttime λ_*, **c**, daytime surface shortwave RE ($\Delta K_\downarrow$), **d**, nighttime surface longwave RE ($\Delta L_\downarrow$), **e**, daytime temperature perturbation, and f, nighttime temperature perturbation in the temperate climate zone. The dashed lines show the linear trends of the temporal variation. All long-term trends are statistically significant (p-value < 0.01).
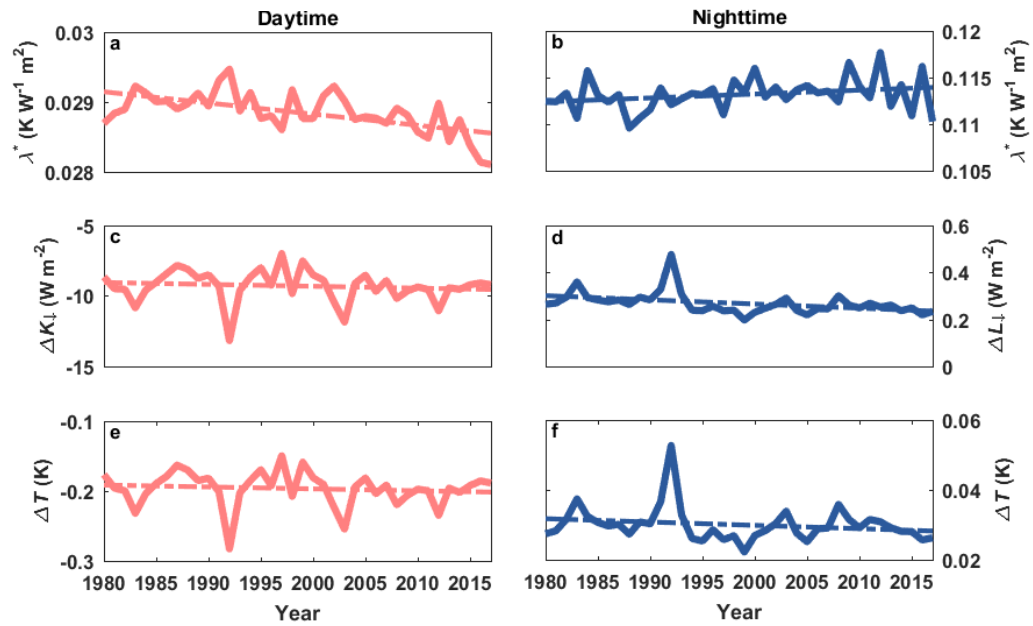
Figure 2.12: Long-term trends in **a**, daytime apparent surface climate sensitivity (λ_*), **b**, nighttime λ_*, **c**, daytime surface shortwave RE ($\Delta K_\downarrow$), **d**, nighttime surface longwave RE ($\Delta L_\downarrow$), **e**, daytime temperature perturbation, and f, nighttime temperature perturbation in the snow climate zone. The dashed lines show the linear trends of the temporal variation. All long-term trends, except for nighttime $\Delta L_\downarrow$, are statistically significant (p-value < 0.01).
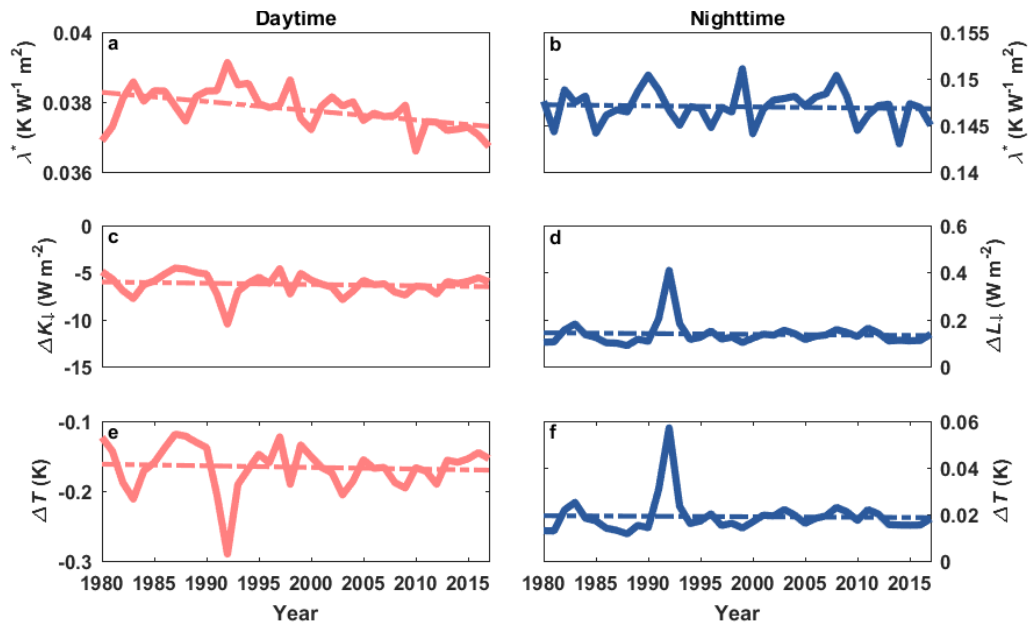
Figure 2.13: Long-term trends in **a**, daytime apparent surface climate sensitivity (λ_*), **b**, nighttime λ_*, **c**, daytime surface shortwave RE ($\Delta K_\downarrow$), **d**, nighttime surface longwave RE ($\Delta L_\downarrow$), **e**, daytime temperature perturbation, and f, nighttime temperature perturbation in the polar climate zone. The dashed lines show the linear trends of the temporal variation. All long-term trends are statistically significant (p-value < 0.01).

Regionally, the most notable feature is a steady increase of daytime λ^*, or a progressive reduction of efficiency of energy redistribution over time, in the equatorial zone (Fig. 2.8a). We attribute this trend to the wide-scale deforestation in the tropics (Achard et al., 2002; Hansen et al., 2013). Although the MERRA-2 modeling system does not explicitly prescribe land use change over time, it uses the observed surface climate variables to constrain the surface energy balance calculation. Tropical deforestation appears to have changed the surface climate so as to result in the diagnosis by the reanalysis of a loss in the efficiency of energy redistribution between the surface and the atmospheric boundary layer. This loss of forest cover serves to amplify the aerosol effect. Sensitivity calculations using Eq. 2.5 show that of the increase of the daytime cooling signal of 0.067 K between 1980 and 2017, about one third is attributed to the reduction in λ^* (and the other two third

to changes in $\Delta K_\downarrow$). Non-radiative surface pathways, such as the energy redistribution efficiency, are shown to dominate the surface temperature change associated with ongoing land cover change and land management activities (Alkama & Cescatti, 2016; Bright et al., 2017; Naudts et al., 2016). Our result suggests that these surface processes can also modify local temperature changes resulting from atmospheric radiative forcing.

2.5 Discussion

Previous studies have shown that the climate sensitivity associated with aerosol RF is greater than that to CO_2 RF (Marvel et al., 2015; Rotstayn et al., 2015; Shindell, 2014). Estimates based on single-forcing model experiments reveal that the former is about 0.55 K W^{-1} m^2 and the latter is 0.40 K W^{-1} m^2 under transient climate conditions (Marvel et al., 2015), giving a sensitivity difference of 0.15 K W^{-1} m^2 and a climate forcing efficacy of 1.4 for aerosols. Geographic variations in aerosols are suggested to play a role in producing this large efficacy (Boucher et al., 2013), but the nature of this role is not well understood. Our study provides a mechanistic explanation for why the efficacy of aerosol RF should exceed unity. In the IBPM framework, the surface temperature perturbation (ΔT) is a signal superimposed on changes in the background atmospheric temperature (ΔT_b, Eq. 2.4). The total surface temperature change is the sum of the two. CO_2, a spatially homogeneous forcing agent, alters the energy balance of the climate system as a whole, leading to changes in the background atmospheric temperature, but it does not change the surface incoming solar radiation in predictable patterns either spatially or temporally (Wild et al., 2015a). In other words, if CO_2 is the only radiative forcing agent, we can omit the surface temperature perturbation due to the surface $K_\downarrow$.

On the other hand, aerosols alter both the whole Earth system energy balance and radiation incident on the surface. We postulate that it is this strong surface RE that results

in the large overall aerosol climate efficacy. In our analysis, we assume that the background temperature change (ΔT_b) can be predicted by the energy imbalance measured at the top of the atmosphere using a standard climate sensitivity value and the additional temperature change (ΔT) is the result of the intrinsic surface biophysical mechanism. It is the latter that explains why the aerosol climate forcing efficacy is greater than unity.

Our calculations suggest that the aerosol direct effect alone can explain the large climate efficacy of aerosols, without consideration of the aerosol indirect effect. The mean surface climate sensitivity to aerosol RE reported above (0.016 K W^{-1} m^2) is based on the surface RE. If we divide the global mean land surface ΔT (-0.13 K) by the combined shortwave and longwave RE at the top of the atmosphere in MERRA-2 (-0.89 W m^{-2}; Table 2.1), we obtain a sensitivity of around 0.15 K W^{-1} m^2 attributed to the intrinsic biophysical mechanism, which is nearly the same as the difference (0.15 W^{-1} m^2) between the aerosol and the CO_2 climate sensitivity (Marvel et al., 2015). Note that accurate calculations of climate sensitivities necessitate examining temperature changes over both land and ocean surfaces. While we only focus on the world's land surfaces, we demonstrate that the local climate response driven by land-atmosphere interactions below the blending height can conceptually explain the higher global climate sensitivity to aerosols.

From this aggregated assessment, we have excluded the temperature perturbation that may arise from changes in the energy redistribution factor f (the last term on the right-hand side of Eq. 2.4). We have already noted that land use change at tropical latitudes has amplified the aerosol effect through reducing f and increasing the local apparent climate sensitivity, although globally, the temporal trend in local apparent climate sensitivity is negligible (Fig. 2.14). A second process that can alter f is changes in the diffuse radiation. Aerosol scattering increases the fraction of diffuse radiation received by the surface, allowing sunlight to penetrate vegetation canopies and increase the gross primary productivity of the land biosphere (Mercado et al., 2009; Rap et al., 2018) and the fraction of heat

transferred through evapotranspiration, thus decreasing the Bowen ratio (Liu et al., 2014). We are unable to isolate this biological response to diffuse radiation from the MERRA-2 dataset since MERRA-2 only provides diffuse radiation under polluted conditions. According to a global modeling study, the presence of aerosols can reduce the land Bowen ratio by 15% to 30% between 20°N and 20°S (Liu et al., 2014). In principle, a reduction in Bowen ratio will generate a negative surface temperature perturbation in the daytime due to changes in f (Lee et al., 2011) in addition to the negative perturbation due to the shortwave RE. An accurate estimate of this Bowen ratio induced signal requires that a land surface model be coupled with an atmospheric radiation transfer model to simultaneously calculate the surface incoming radiation (including changes in the diffuse fraction) and the response of the surface sensible and latent heat fluxes.
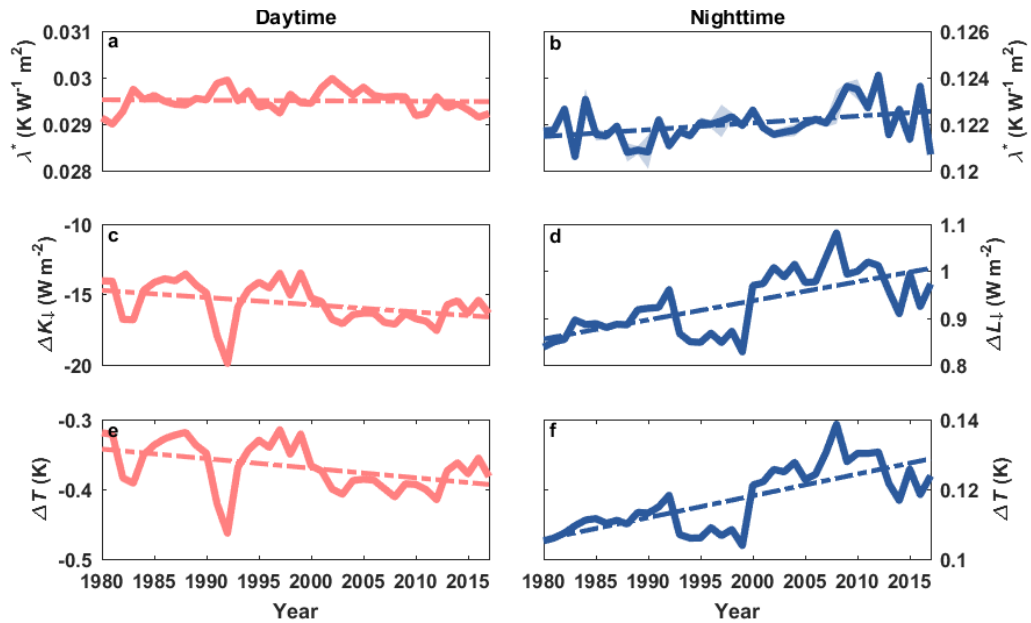
Figure 2.14: Long-term trends in **a**, daytime apparent surface climate sensitivity (λ_*), **b**, nighttime λ_*, **c**, daytime surface shortwave RE ($\Delta K_\downarrow$), **d**, nighttime surface longwave RE ($\Delta L_\downarrow$), **e**, daytime temperature perturbation, and f, nighttime temperature perturbation for the world's land surfaces. The dashed lines show the linear trends of the temporal variation. All long-term trends are statistically significant (p-value < 0.01).

2.6 Conclusions

In this study, we disentangle the local temperature response to the direct surface short-wave and longwave radiative effects of aerosols for the world's land surfaces. We find that the global mean climate sensitivity to the surface longwave effect during the daytime (0.039 K W^{-1} m^2) is 60% stronger than to the daytime surface shortwave effect (0.024 K W^{-1} m^2) and 5 times as strong at night (0.127 K W^{-1} m^2). The former is a consequence of higher emissions of coarse aerosols in regions where the surface energy redistribution is less efficient, and the latter is related to low turbulent mixing in stable nighttime conditions. The opposing longwave and shortwave effects reduce the DTR, particularly in arid regions, with almost half the mean reduction in the aggregated region of interest attributable to anthropogenic aerosols. Finally, we analyze long-term trends in the surface temperature response to aerosol direct radiative effect and find an increase in the local climate sensitivity in the equatorial zone, possible driven by deforestation activities. Our results demonstrate the importance of biophysical processes in modulating the spatial heterogeneity of aerosol-climate interactions. The inclusion of this local climate response to aerosols may explain their higher climate forcing efficacy.

Chapter 3

Isolating the Impact of Aerosols on Surface Temperature, Terrestrial Evapotranspiration, and Land Carbon Uptake Through Both Radiative and Non-Radiative Pathways

3.1 Abstract

Aerosols can enhance terrestrial productivity through increased absorption of solar radiation by the shaded portion of the plant canopy – the diffuse radiation fertilization effect. Although this process can, in principle, alter surface evaporation due to the coupling between plant water loss and carbon uptake, with the potential to change the surface temperature, aerosol-climate interactions have been traditionally viewed in light of the radiative effects within the atmosphere. Here we develop a modeling framework that combines global atmosphere and land model simulations with a conceptual diagnostic tool to investigate these interactions from a surface energy budget perspective. Aerosols increase the terrestrial evaporative fraction, or the portion of net incoming energy consumed by evaporation, by over 4% globally and as much as $\approx$40% regionally. The main mechanism for this is the increase in energy allocation from sensible to latent heat due to global dimming (reduction in global shortwave radiation) and slightly augmented by diffuse radiation fertilization. In regions with moderately dense vegetation (leaf area index > 2), the local surface cooling response to aerosols is dominated by this evaporative pathway, not the reduction in incident radiation. Diffuse radiation fertilization alone has a stronger impact on gross primary productivity (+2.18 Pg C y^{-1} or +1.8%) than on land evaporation (+0.18 W m^{-2} or +0.48%) and surface temperature (-0.01 K). Our results suggest that it is important for land surface models to distinguish between quantity (change in total magnitude) and quality (change in diffuse fraction) of radiative forcing for properly simulating surface climate.

3.2 Introduction

Aerosols modify the Earth's radiative budget through scattering and absorption of solar (shortwave) and terrestrial (longwave) radiation and have large variability in their physical and chemical properties, horizontal and vertical distributions, and feedbacks from other components of the climate system, particularly clouds (Ramanathan 2001; Persad & Caldeira, 2018). Overall, aerosol climatic effects lead to one of the largest uncertainties in future climate projections (Hinds 1999, Stocker 2014). Unlike the effect of well-mixed greenhouse gases, the aerosol radiative effect is stronger at the surface than at the top of the atmosphere (Ramanathan 2001), with aerosols reducing incoming shortwave radiation through scattering and absorption and increasing incoming longwave radiation through re-emission of the absorbed energy (Panicker et al., 2008; Chakraborty & Lee, 2019).

Several past studies have examined the aerosol climatic impacts through the lens of atmospheric energy balance (Ramanathan 2001; Chung et al., 2005; Persad & Caldeira, 2018). In this study, we aim to investigate the global impacts of aerosols from a terrestrial surface energy budget perspective. One outstanding question concerns how the surface sensible heat (H) and latent heat flux (λE) respond differently to the aerosol surface radiative effect. Both regional modeling and observational studies show that aerosols may reduce H more than λE, resulting in an increase of the evaporative fraction (EF), or the proportion of net incoming energy at the surface dissipated through evaporation (Zhang et al., 2008; Matsui et al., 2008; Knohl & Baldocchi, 2008; Steiner et al., 2013; Liu et al., 2014; Wang et al., 2018). Two competing hypotheses are advanced to explain the enhanced EF. First, aerosols alter quality of the shortwave radiation by increasing diffuse radiation ($K_{\downarrow,d}$) at the Earth's surface, which can penetrate deeper into the canopy than direct or beam solar radiation and illuminates normally light-limited portion of the vegetation (Gu et al., 2003). The resulting increase in primary productivity is called the diffuse

radiation fertilization effect (Gu et al., 2002; Niyogi et al., 2004; Mercado et al., 2009; Rap et al., 2015; Rap et al., 2018). Since carbon uptake and water loss are coupled in plants through stomatal conductance, the primary hypothesis is that this increase in diffuse radiation modifies the moisture flux from the surface and therefore EF (Wang et al., 2008). A second hypothesis for the change in EF, implicit in the studies of Gu et al. (2006) and others (Oliveira et al., 2011), is that global dimming, or reduction in quantity of the surface shortwave radiation, is responsible for how the surface available energy is partitioned between H and λE. It is not known which of the two mechanisms – the diffuse radiation fertilization effect or the global dimming effect – dominates the EF response.

A second question of broad interest asks how temperatures respond to aerosol loading. Since the aerosol radiative effect is much larger at the surface than in the atmosphere or at the top of the atmosphere, it follows that aerosols disproportionately affect surface temperature (Ts; Chakrabort & Lee, 2019). A reduction in incoming radiation generally causes surface cooling, but the cooling signal is highly variable in space because land biophysical properties exert a strong control on this local climate response to atmospheric forcing (Luyssaert et al., 2014; Bright et al., 2017) and because the biophysical properties of the surface and the aerosol loading aloft tend to co-vary geographically (Chakraborty & Lee, 2019). In addition, changes in non-radiative processes like convection, evaporation and EF can change T_s, even under a constant amount of incoming radiation (Bonan 2008; Lee et al., 2011). A recent study has examined the T_s response to the direct radiative effect (Chakraborty & Lee, 2019). How aerosols modify T_s via non-radiative pathways, however, remains largely unknown.

This study attempts to address these questions by using a modeling framework that focuses on the modification of the terrestrial surface energy budget by aerosols. We first quantify the perturbations to each component of the surface energy budget using a modeling system consisting of an atmosphere model and a global land model. The atmosphere

model is run with radiation diagnostics to determine the incoming shortwave and longwave radiation fields at the surface with realistic atmospheric aerosol distributions and in a hypothetical atmosphere with aerosols removed but with clouds intact. The remaining components of the surface energy budget are simulated by forcing the land model with the two sets of atmosphere results. In the two simulations, the incoming shortwave (beam and diffuse) and incoming longwave radiation are different, but other forcing variables (air temperature, humidity and wind) at the first grid height and surface variables (precipitation and air pressure) remain the same. A comprehensive evaluation of the simulation results at the appropriate scales using multiple data sources confirms that the modeling setup captures the general direction of these interactions. In parallel, using an offline decomposition analysis of the surface energy budget, we quantify the contributions of aerosol radiative and non-radiative pathways to local surface temperature perturbations (ΔT). Since the non-radiative pathways are expected to be strongly mediated by the biophysical characteristics of the surface (Bonan 2008), we quantify the relative strength of these pathways across different climate and vegetation density zones. Finally, using a third land model run and offline calculations, we isolate the contributions of the aerosol global dimming effect and the diffuse radiation fertilization effect on EF, the carbon budget, and T_s. We find that the aerosol-induced ΔT through the non-radiative pathways is large, especially over vegetated surfaces.

3.3 Materials and Methods

3.3.1 Modeling Framework to Isolate the Impact of Aerosols on the Surface Energy Budget

The Earth's surface energy budget represents the thermodynamic interactions between the surface and the adjacent air layer and is expressed as

$$K_\downarrow + L_\downarrow - K_\uparrow - L_\uparrow = H + \lambda E + G \tag{3.1}$$

where $K_\downarrow$ is the incoming shortwave radiation, $L_\downarrow$ is the incoming longwave radiation, $K_\uparrow$ is the shortwave radiation reflected by the surface, $L_\uparrow$ is the longwave radiation emitted by the surface, H is the sensible heat flux and represents the turbulent transfer of heat from the surface to the atmosphere, λE is the latent heat flux or the transfer of moisture from the surface to the atmosphere, and G is the ground flux. The terms on the left-hand side of Eq. 3.1 comprise the surface net radiation,

$$R_\mathrm{n} = K_\downarrow + L_\downarrow - K_\uparrow - L_\uparrow \tag{3.2}$$

We use the Community Atmosphere Model (CAM, version 6.0 with slab ocean, prescribed sea ice and present-day climatological distribution of aerosols; Gettelman et al., 2019) and the Community Land Model (CLM, version 5.0 with biogeochemistry and prognostic vegetation state turned on; Lawrence et al., 2019) to quantify the impact of aerosols on each component of Eq. 3.1 for the period 2001-2003. We run these models twice at a resolution of $0.9375° \times 1.5°$. The first run, labeled as P, is for the polluted atmosphere. Atmospheric forcing variables produced by CAM at the screen height and at the surface (incoming solar radiation, incoming longwave radiation, air temperature, specific humid-

ity, wind speed, atmospheric pressure, precipitation) are used as inputs to drive CLM. By default, CLM in land-only mode partitions $K_\downarrow$ into the diffuse ($K_{\downarrow,\mathrm{d}}$) and the beam ($K_{\downarrow,\mathrm{b}}$) component using a polynomial fit function of $K_\downarrow$. In the present study, we bypass this default partitioning, and instead use $K_{\downarrow,\mathrm{d}}$ and $K_{\downarrow,\mathrm{b}}$ calculated by CAM. The use of pre-scribed $K_{\downarrow,\mathrm{d}}$ and $K_{\downarrow,\mathrm{b}}$ in CLM instead of its default partitioning scheme has been shown to better capture both the magnitude of GPP and the GPP response to diffuse fraction k_d ($= K_{\downarrow,\mathrm{d}}/K_\downarrow$) for a temperate deciduous forest site (Wozniak et al., 2020). To allow the land processes to adjust to the different forcing sets, the same three years of forcing are looped six times. The results from the final three-year loop are presented. The relatively short time period used is justified since this is a study of perturbation and not change over time. Short periods are also used in other perturbation studies (Matsui et al., 2008; Rap et al., 2018).

In the second run (labeled as C), the incoming solar and incoming longwave radiation are calculated with the diagnostic radiation transfer code of CAM but without aerosols. All other CLM forcing variables (air temperature, specific humidity, wind speed, atmospheric pressure, precipitation) are identical to those in Run P. The results are for a hypothetical atmosphere free of aerosols.

The effect of aerosols on the surface radiation and energy processes is quantified as the difference between Run P and Run C. For example, $K_{\downarrow,\mathrm{d}}$ is 62.88 W m^{-2} in the polluted atmosphere in Run P and 52.09 W m^{-2} in the clean atmosphere in Run C, giving $\Delta K_{\downarrow,\mathrm{d}}$ of 10.79 W m^{-2} (Fig. 3.1). $K_{\downarrow,\mathrm{d}}$ is greater in P than in C because the former in-cludes contributions from scattering by aerosols, gaseous molecules, and clouds whereas the latter include only contributions from scattering by gaseous molecules and clouds. The interaction of aerosols with clouds is simulated by default in CAM and does not affect the diagnostic radiation calculation. Thus, in Run C, the clouds from Run P are preserved. Had all aerosols been removed from the atmosphere in the default CAM setup, practically

all clouds would have disappeared. We perform a third run, labeled as M, to help separate the global dimming and diffuse radiation fertilization effects. In this simulation, $K_\downarrow$ is the same as in the polluted run (P) and k_d is kept the same as in the clean run (C). The overall change in a variable X due to aerosols can then be decomposed as

$$\Delta X = (X_\mathrm{P} - X_\mathrm{M}) + (X_\mathrm{M} - X_\mathrm{C}) \tag{3.3}$$

where subscript M, P, and C denote the three simulations, $(X_\mathrm{P}\text{-}X_\mathrm{M})$ represents the contribution arising from change in radiation quality or the diffuse radiation fertilization effect, and $(X_\mathrm{M}\text{-}X_\mathrm{C})$ represents the contribution arising from change in radiation quantity or the dimming effect. The global (and regional; see next subsection) means, as well as their standard deviations or standard errors (as noted in the corresponding text or figure and table captions), are calculated after weighing the gridded values by the grid areas. A schematic of the modeling setup is in Fig. 3.1.
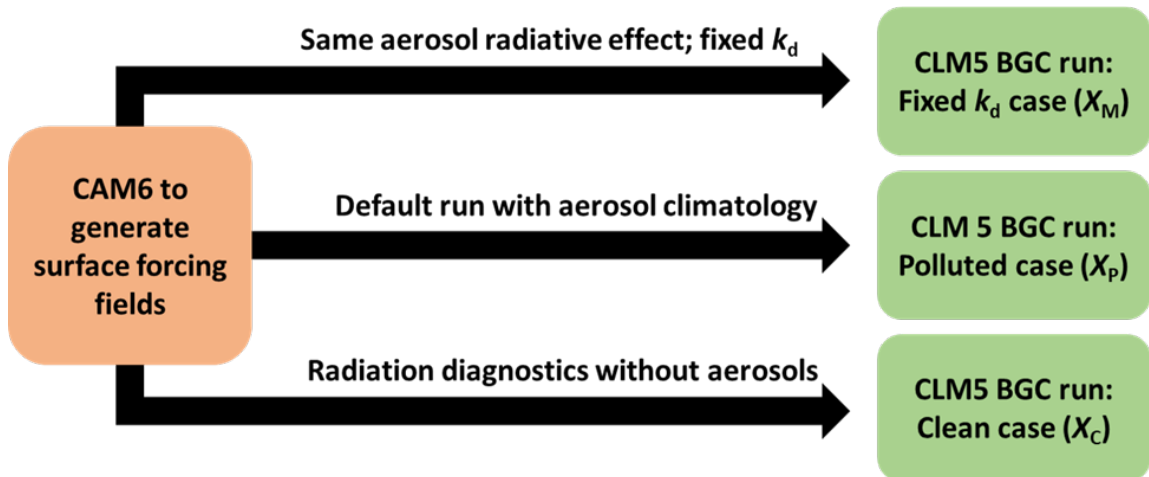
Figure 3.1: Schematic of modeling setup used in the present study. The forcing fields from CAM6 include incoming diffuse radiation, incoming direct beam radiation, incoming longwave radiation, air temperature, specific humidity, wind speed, atmospheric pressure, and precipitation. Only the diffuse radiation, direct beam radiation, and longwave radiation are changed in the different runs to represent the impact of aerosols on the components of the incident radiation at the surface.

Table 3.1: Summary of grid area-weighted annual mean components of the surface radiation energy budgets from CAM and CLM runs for aerosol and no aerosol cases, as well as their changes, for the world's land surface and for each climate zone.

Variable	Case	Regions of interest					
		Global land	Tropical	Arid	Temperate	Boreal	Polar
Incoming shortwave (W m⁻²)	Without aerosols	194.57 ± 59.62	216.35 ± 22.24	257.45 ± 28.76	198.13 ± 33.14	139.83 ± 42.85	140.63 ± 43.72
	With aerosols	185.85 ± 54	206.8 ± 21.14	240.06 ± 26.26	190.4 ± 31.93	135.95 ± 40.55	139.4 ± 42.71
	Change	-8.72 ± 8.98	-9.55 ± 6.76	-17.39 ± 10.65	-7.74 ± 4.55	-3.88 ± 3.17	-1.23 ± 1.99
Reflected shortwave (W m⁻²)	Without aerosols	50.85 ± 32.02	31.68 ± 4.83	64.88 ± 30.47	30.24 ± 7.61	33.35 ± 13.02	94.25 ± 32.3
	With aerosols	49.08 ± 31.05	30.58 ± 4.58	60.46 ± 27.87	29.22 ± 7.33	32.73 ± 12.78	93.78 ± 32.25
	Change	-1.77 ± 2.62	-1.1 ± 0.93	-4.42 ± 3.79	-1.02 ± 0.71	-0.62 ± 0.56	-0.47 ± 0.38
Incoming direct beam (W m⁻²)	Without aerosols	142.48 ± 63.66	148.53 ± 30.55	214.96 ± 33.6	147.13 ± 36.81	89.49 ± 44.58	88.58 ± 46.17
	With aerosols	122.97 ± 49.93	129.53 ± 27.59	172.58 ± 28.3	131.33 ± 32.76	81.94 ± 39.21	85.97 ± 44.14
	Change	-19.51 ± 20.81	-19 ± 12.62	-42.38 ± 24.05	-15.8 ± 8.46	-7.55 ± 6.78	-2.61 ± 4.02
Incoming diffuse (W m⁻²)	Without aerosols	52.09 ± 13.35	67.82 ± 10.09	42.49 ± 8.97	51.01 ± 10.16	50.34 ± 7.29	52.05 ± 15.01
	With aerosols	62.88 ± 14.3	77.27 ± 9.13	67.48 ± 13.63	59.07 ± 8.59	54.01 ± 6.66	53.43 ± 15.3
	Change	10.79 ± 12.22	9.45 ± 6.33	24.99 ± 14	8.06 ± 4.59	3.67 ± 3.7	1.38 ± 2.07
Incoming longwave (W m⁻²)	Without aerosols	305.68 ± 78.83	395.8 ± 16.39	328.73 ± 38.39	338.06 ± 27.78	270.37 ± 21.66	174.98 ± 62.26
	With aerosols	307.8 ± 79.7	396.95 ± 16.1	334.71 ± 39.37	339.08 ± 27.56	270.9 ± 21.82	175.13 ± 62.36
	Change	2.12 ± 3.73	1.16 ± 1.84	5.98 ± 5.18	1.02 ± 1.14	0.53 ± 0.82	0.14 ± 0.6
Emitted longwave (W m⁻²)	Without aerosols	375.03 ± 89.73	452.02 ± 13.36	434.74 ± 38.39	408.34 ± 27.46	324.52 ± 31.73	222.39 ± 63.39
	With aerosols	374.32 ± 89.33	451 ± 12.96	433.69 ± 38.26	407.43 ± 27.1	324.13 ± 31.48	222.28 ± 63.27
	Change	-0.72 ± 0.77	-1.03 ± 0.88	-1.05 ± 0.87	-0.91 ± 0.69	-0.4 ± 0.38	-0.11 ± 0.2
Sensible heat flux (W m⁻²)	Without aerosols	35.64 ± 29.7	46.94 ± 14.24	61.85 ± 15.51	44.78 ± 14.65	21.86 ± 13.24	-9.43 ± 25.45
	With aerosols	32.05 ± 27.86	41.87 ± 14.22	56.22 ± 14.96	40.78 ± 14.59	19.89 ± 12.27	-9.82 ± 24.86
	Change	-3.59 ± 3.03	-5.08 ± 2.97	-5.64 ± 2.95	-4 ± 2.08	-1.97 ± 1.46	-0.39 ± 0.86
Latent heat flux (W m⁻²)	Without aerosols	37.93 ± 29.68	81.5 ± 17.39	24.45 ± 17.82	52.42 ± 17.14	28.24 ± 10.85	7.3 ± 11.33
	With aerosols	37.42 ± 29.23	80.33 ± 17.13	24.18 ± 17.52	51.66 ± 16.8	27.9 ± 10.68	7.19 ± 11.17
	Change	-0.51 ± 0.8	-1.16 ± 1.13	-0.27 ± 0.57	-0.77 ± 0.85	-0.35 ± 0.39	-0.11 ± 0.23
Ground flux (W m⁻²)	Without aerosols	0.8 ± 1.43	0 ± 0.13	0.26 ± 0.5	0.44 ± 0.87	2.24 ± 1.54	1.11 ± 2.04
	With aerosols	0.79 ± 1.43	-0.03 ± 0.12	0.24 ± 0.5	0.42 ± 0.87	2.24 ± 1.54	1.1 ± 2.03
	Change	-0.01 ± 0.03	-0.02 ± 0.02	-0.02 ± 0.02	-0.02 ± 0.02	-0.01 ± 0.04	-0.01 ± 0.04
Imbalance (W m⁻²)	Without aerosols	-0.01 ± 0.03	0 ± 0	0 ± 0.01	-0.02 ± 0.05	-0.01 ± 0.04	0 ± 0.01
	With aerosols	0 ± 0	0 ± 0	0 ± 0	0 ± 0	0 ± 0	0 ± 0
	Change	0 ± 0	0 ± 0	0 ± 0	0 ± 0	0 ± 0	0 ± 0

3.3.2 Model Evaluation

The realism of the CAM and CLM results (Table 3.1) are assessed by comparison with multiple independent data products. The CLM forcing data simulated by CAM are compared with the Global Soil Wetness Project version 3 (GSWP3) dataset (Dirmeyer et al., 2011), the standard atmospheric forcing data used in the Land Model Intercomparison Project (LUMIP) (Lawrence et al., 2016). The components of the surface energy budget

50

from the model runs are also evaluated using NASA's MERRA-2 reanalysis (Gelaro et al., 2017), while the simulated sensible and latent heat fluxes are further evaluated against the FLUXCOM dataset, which merges FLUXNET observations with remote sensing phenology and meteorological data (Jung et al., 2019). We choose the ensemble FLUXCOM estimates from all the machine learning models based on the GSWP3 meteorological forcing for this purpose. We also use observations from the Global Energy Balance Archive (GEBA) (Wild et al., 2017) to evaluate grid-level incoming shortwave and diffuse radiation. Perturbations to the surface radiation budget due to aerosols are compared against the MERRA-2 radiation diagnostics and two previous global studies. The statistical parameters used for model evaluation are the coefficient of determination (r^2), the root-mean-square error (RMSE), and the mean bias error (MBE). For comparisons against the gridded datasets, the same time-period as the model run (2001-2003) is used for all terrestrial surfaces as well as for each individual Koppen-Geiger climate class, namely tropical, arid, temperate, boreal, and polar (Rubel & Kottek, 2010; Fig. 3.2a). For GEBA observations, only the years for which all twelve months of data are available are selected. Since the CAM-CLM run represents the climatological mean of the radiation fields, GEBA sites with at least 3 years of data are averaged to create monthly means. To check how well the aerosol optical depth (AOD) in CAM and leaf area index (LAI) in CLM, two important parameters that modulate aerosol-biosphere-climate interactions, compare to observations, we use 5-year averages (2003-2007) derived from the Moderate Resolution Imaging Spectroradiometer (MODIS) observations (Knyazikhin et al., 1998; Lyapustin et al., 2018) for each climate zone.
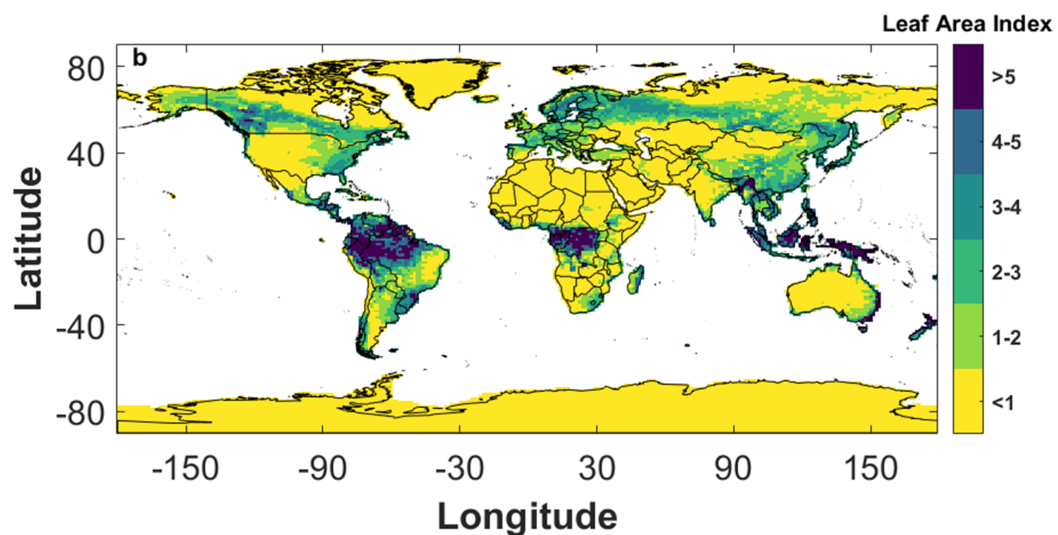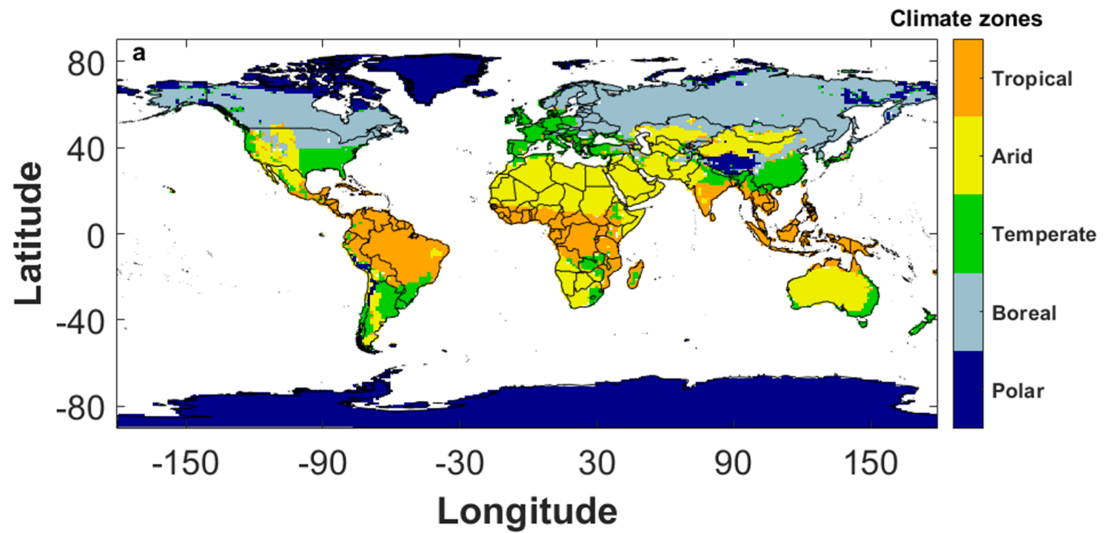
Figure 3.2: Maps of study area. Global distribution of **a** Koppen-Geiger climate zones and **b** leaf area index (LAI) bins.

Table 3.2 shows the evaluation of the forcing fields. We see relatively low r^2 values for almost all the variables for the tropical region. This is probably due to the difference in cloud distribution associated with different parameterizations used in the models. However, overall, our mean forcing fields are comparable to the GSWP3 data, except for wind

speed (RMSE = 2.39 m s^{-1}), though that should not affect our perturbation runs much. Moreover, our overall results are presented at the areally averaged climate zone scale, not for individual grid values.

Table 3.2: Evaluation of the forcing fields from our CAM run against GSWP3 for the period 2001-2003 for the world's land surfaces and for each climate zones. The top two rows for each variable show the grid-area weighted mean and standard deviation from the present study and GSWP3. The statistical parameters for model evaluation are the coefficient of determination (r^2), the weighted root-mean-square error (RMSE), and the mean bias error (MBE).

Variable	Case	Regions of interest					
		Global land	Tropical	Arid	Temperate	Boreal	Polar
Incoming shortwave (W m^{-2})	CAM	186.25 ± 53.6	207.23 ± 20.68	240.05 ± 26.04	191.04 ± 30.84	137.35 ± 40.37	138.87 ± 42.24
	GSWP3	181.95 ± 52.16	213.6 ± 17.55	230.8 ± 29.65	185.58 ± 33.14	134.45 ± 27.83	128.5 ± 37.04
	r^2	0.92	0.53	0.64	0.77	0.94	0.81
	RMSE	17.94	16.02	21.00	18.22	15.39	18.07
	MBE	4.30	-6.37	9.25	5.46	2.90	10.37
Incoming longwave (W m^{-2})	CAM	308.81 ± 79.18	397.29 ± 15.97	335.41 ± 39.36	340.1 ± 27.96	271.7 ± 22.04	177.73 ± 62.74
	GSWP3	309.79 ± 76.79	396.4 ± 15.63	338.88 ± 34.84	338.71 ± 27.03	270.7 ± 22.44	181.84 ± 55.87
	r^2	0.99	0.90	0.94	0.92	0.86	0.98
	RMSE	9.38	5.05	10.99	7.69	8.80	12.39
	MBE	-0.99	0.89	-3.47	1.39	1.00	-4.11
Temperature of lowest atmospheric layer (K)	CAM	281.83 ± 18.34	297 ± 1.88	292.98 ± 6.67	289.31 ± 4.57	273.37 ± 6.63	249.73 ± 16.31
	GSWP3	282.95 ± 18.02	298.79 ± 1.88	293.99 ± 7.46	289.67 ± 4.91	273.27 ± 6.56	252.37 ± 15.35
	r^2	0.99	0.69	0.95	0.91	0.96	0.95
	RMSE	2.52	2.09	2.04	1.57	1.36	4.49
	MBE	-1.13	-1.79	-1.01	-0.35	0.11	-2.64
Specific humidity of lowest atmospheric layer (g kg^{-1})	CAM	6.96 ± 4.83	14.34 ± 2.1	6.44 ± 2.74	8.72 ± 2.66	3.92 ± 1.13	1.37 ± 1.45
	GSWP3	7.34 ± 5.24	15.39 ± 2.65	6.58 ± 2.65	9.32 ± 3.24	3.94 ± 1.21	1.56 ± 1.48
	r^2	0.96	0.50	0.77	0.85	0.90	0.94
	RMSE	1.36	2.21	1.38	1.49	0.41	0.42
	MBE	-0.37	-1.05	-0.14	-0.60	-0.01	-0.19
Surface pressure (hPa)	CAM	925.97 ± 94.86	963.35 ± 37.73	935.23 ± 65.03	943.27 ± 64.66	947.28 ± 71.53	797.89 ± 139.08
	GSWP3	925.44 ± 97.48	962.19 ± 41.08	934.6 ± 66.2	940.99 ± 69.29	947.23 ± 76.87	796.24 ± 142
	r^2	0.98	0.85	0.95	0.91	0.96	0.98
	RMSE	16.45	16.08	14.90	20.65	14.37	20.04
	MBE	0.53	1.16	0.63	2.29	0.05	1.65
Wind speed (m s^{-1})	CAM	5.25 ± 2.07	3.15 ± 1.31	5.38 ± 0.94	4.52 ± 1.24	5.42 ± 1.05	7.86 ± 2.72
	GSWP3	3.26 ± 1.37	2.12 ± 0.96	3.06 ± 0.92	2.97 ± 1.14	3.44 ± 1.03	4.81 ± 1.46
	r^2	0.65	0.38	0.24	0.62	0.54	0.48
	RMSE	2.39	1.51	2.52	1.77	2.13	3.60
	MBE	1.99	1.02	2.32	1.56	1.98	3.04
Precipitation rate (mm hr^{-1})	CAM	0.1 ± 0.1	0.23 ± 0.12	0.05 ± 0.04	0.13 ± 0.07	0.08 ± 0.04	0.05 ± 0.06
	GSWP3	0.09 ± 0.08	0.19 ± 0.09	0.03 ± 0.03	0.13 ± 0.06	0.07 ± 0.03	0.04 ± 0.04
	r^2	0.79	0.57	0.66	0.48	0.53	0.68
	RMSE	0.05	0.09	0.03	0.06	0.03	0.04
	MBE	0.02	0.04	0.02	0.01	0.01	0.01

We evaluate the gridded incoming diffuse radiation and total shortwave radiation against observations, both globally and for each climate zone, and find the results to be reasonable (MBE = 10.20 W m^{-2} for shortwave; -10.52 W m^{-2} for diffuse for all sites; Figs 3.3 and 3.4). Note that the underestimation of k_{d} due to the overestimation of shortwave radiation and underestimation of diffuse radiation will introduce some uncertainties in the magnitude of our results. This underestimation may be due to the lower AOD in CAM compared to MODIS MCD19A2 version 6 observations (Lyapustin et al., 2018), seen for all climate zones except the arid zone (Fig. 3.5b), which is consistent with the results from a recent study (Wang et al., 2021). The evaluation for longwave radiation is not shown since there are very few stations with at least three years of incoming longwave observations in GEBA. The slight difference in incoming shortwave and longwave radiation between Table 3.3 (and 3.1) and Table 3.2 is because they are re-gridded from datasets at different resolution. The MERRA-2 reanalysis assimilates satellite-based observations of aerosols and uses them to isolate the direct radiative effect of aerosols (Gelaro et al., 2017). The magnitude of the shortwave and longwave aerosol radiative effects from our CAM run are similar to the MERRA-2 diagnostics (Table 3.4). Note that MERRA-2 only provides clear-sky $\Delta L_{\downarrow}$ due to aerosols, which contributes to larger relative deviations from CAM (2.12 ± 3.73 W m^{-2} for CAM versus 1.02 ± 1.54 W m^{-2} in MERRA-2).
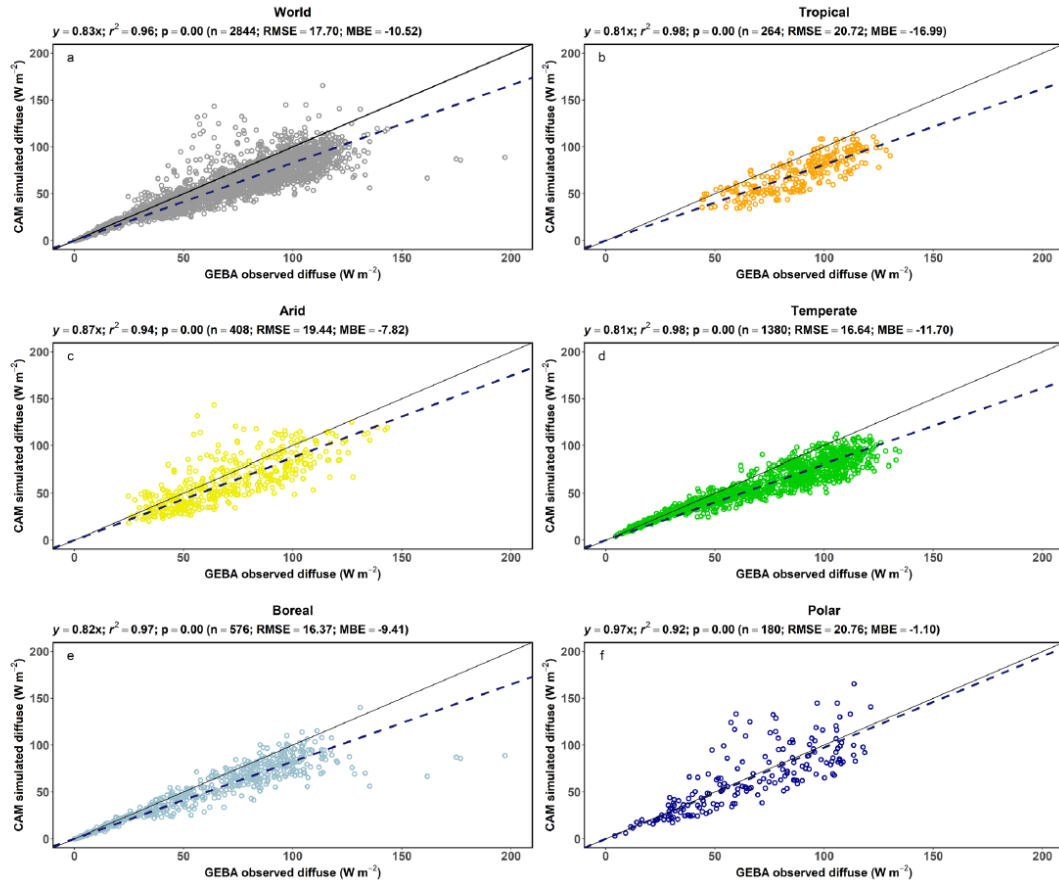
Figure 3.3: Evaluation of diffuse radiation. Grid-level evaluation of monthly incoming diffuse radiation at surface from the CAM run against GEBA observations for **a** all sites, **b** tropical sites, **c** arid sites, **d** temperate sites, **e** boreal sites, and **f** polar sites.
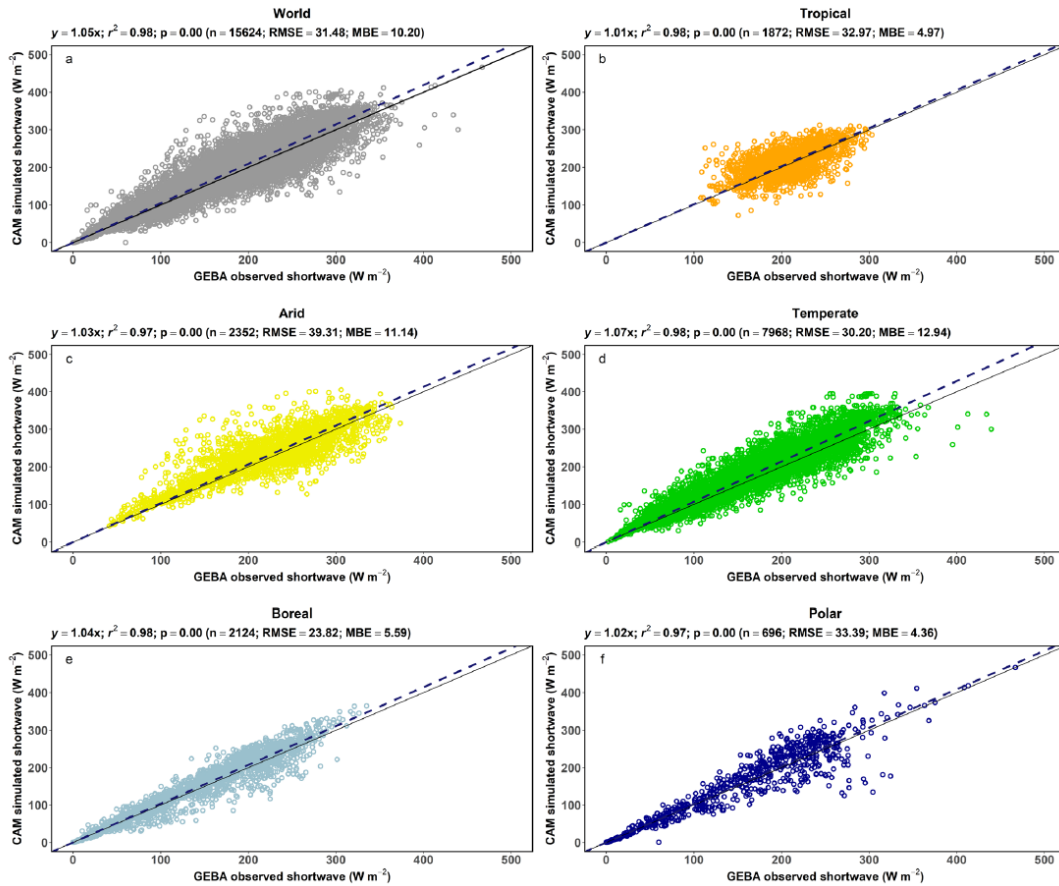
Figure 3.4: Evaluation of shortwave radiation. Grid-level evaluation of monthly incoming shortwave radiation at surface from the CAM run against GEBA observations for **a** all sites, **b** tropical sites, **c** arid sites, **d** temperate sites, **e** boreal sites, and **f** polar sites.

Table 3.3 shows comparison of the simulated surface energy budget components against the MERRA-2 reanalysis dataset. In addition to the expected low explanation of variability in the tropical region, there is a large difference in the magnitude and variability of G between MERRA-2 and CLM ($r^2 = 0.14$; RMSE = 1.53 W m^{-2}).

Table 3.3: Evaluation of the surface radiation and energy budget components simulated by CAM and CLM against MERRA-2 for 2001-2003 for the world's land surfaces and for each climate zone. The top two rows for each variable show the grid-area weighted mean and standard deviation from the present study and MERRA-2. The statistical parameters for model evaluation are the coefficient of determination (r^2), the weighted root-mean-square error (RMSE), and the mean bias error (MBE).

Variable	Case	Regions of interest					
		Global land	Tropical	Arid	Temperate	Boreal	Polar
Incoming shortwave ($W\ m^{-2}$)	CAM-CLM	185.85 ± 54	206.8 ± 21.14	240.06 ± 26.26	190.4 ± 31.93	135.95 ± 40.55	139.4 ± 42.71
	MERRA-2	196.29 ± 59.19	225.38 ± 23.75	252.15 ± 27.63	211.25 ± 31.93	142.54 ± 39	135.4 ± 46.64
	r^2	0.93	0.42	0.67	0.73	0.95	0.91
	RMSE	20.36	25.43	20.99	28.23	11.51	13.40
	MBE	-10.44	-18.58	-12.09	-20.85	-6.59	4.00
Reflected shortwave ($W\ m^{-2}$)	CAM-CLM	49.08 ± 31.05	30.58 ± 4.58	60.46 ± 27.87	29.22 ± 7.33	32.73 ± 12.78	93.78 ± 32.25
	MERRA-2	46.38 ± 27.96	29.21 ± 5.83	62.98 ± 26.7	30.4 ± 7.57	29.71 ± 7.75	79.51 ± 30.93
	r^2	0.92	0.26	0.86	0.54	0.58	0.92
	RMSE	10.44	4.71	9.94	5.24	8.63	17.13
	MBE	2.70	1.37	-2.53	-1.18	3.01	14.27
Incoming longwave ($W\ m^{-2}$)	CAM-CLM	307.8 ± 79.7	396.95 ± 16.1	334.71 ± 39.37	339.08 ± 27.56	270.9 ± 21.82	175.13 ± 62.36
	MERRA-2	294.58 ± 76.46	387.96 ± 19.12	312.93 ± 37.65	321.79 ± 30.58	259.73 ± 20.68	169.94 ± 55.52
	r^2	0.99	0.82	0.94	0.91	0.89	0.98
	RMSE	17.60	12.12	23.85	19.48	13.79	15.17
	MBE	13.22	9.00	21.78	17.30	11.17	5.19
Emitted longwave ($W\ m^{-2}$)	CAM-CLM	374.32 ± 89.33	451 ± 12.96	433.69 ± 38.26	407.43 ± 27.1	324.13 ± 31.48	222.28 ± 63.27
	MERRA-2	365.55 ± 85.49	446.99 ± 11.67	417.39 ± 39.37	394.58 ± 28.46	315.46 ± 26.79	222.16 ± 58.86
	r^2	0.99	0.53	0.96	0.87	0.96	0.97
	RMSE	14.09	10.07	18.16	16.59	11.44	11.56
	MBE	8.77	4.00	16.30	12.85	8.67	0.12
Sensible heat flux ($W\ m^{-2}$)	CAM-CLM	32.05 ± 27.86	41.87 ± 14.22	56.22 ± 14.96	40.78 ± 14.59	19.89 ± 12.27	-9.82 ± 24.86
	MERRA-2	35.37 ± 33.06	41.44 ± 27.67	65.66 ± 18.51	44.51 ± 21.94	18.34 ± 18.32	-3.48 ± 29.89
	r^2	0.78	0.34	0.40	0.32	0.59	0.82
	RMSE	16.74	21.43	16.30	18.43	11.64	12.04
	MBE	-3.33	0.43	-9.44	-3.72	1.55	-6.34
Latent heat flux ($W\ m^{-2}$)	CAM-CLM	37.42 ± 29.23	80.33 ± 17.13	24.18 ± 17.52	51.66 ± 16.8	27.9 ± 10.68	7.19 ± 11.17
	MERRA-2	43.13 ± 37.3	95.02 ± 29.58	18.28 ± 16.94	63.37 ± 24.11	36.31 ± 11.53	9.03 ± 11.72
	r^2	0.81	0.42	0.38	0.38	0.43	0.64
	RMSE	18.44	26.60	14.44	22.08	13.03	7.67
	MBE	-5.71	-14.69	5.90	-11.71	-8.41	-1.84
Ground flux ($W\ m^{-2}$)	CAM-CLM	0.79 ± 1.43	-0.03 ± 0.12	0.24 ± 0.5	0.42 ± 0.87	2.24 ± 1.54	1.1 ± 2.03
	MERRA-2	0.14 ± 0.21	0.1 ± 0.15	0.12 ± 0.15	0.09 ± 0.18	0.26 ± 0.27	0.09 ± 0.23
	r^2	0.14	0.00	0.01	0.02	0.00	0.23
	RMSE	1.53	0.23	0.53	0.92	2.52	2.21
	MBE	0.65	-0.12	0.12	0.33	1.98	1.01

Table 3.4: Comparison of change to the surface energy budget terms due to aerosols with MERRA-2 data and *Chen & Zhuang* (for radiation components) and *Liu et al.* (for turbulent fluxes).

Variable	Case	Source		
		Liu et al.; Chen and Zhuang	**Present study**	**MERRA-2**
Sensible heat flux	Without aerosols	95.26	35.64 ± 29.7	NA
	With aerosols	79.57	32.05 ± 27.86	35.37 ± 33.06
	Change	-15.69	-3.59 ± 3.03	NA
Latent heat flux	Without aerosols	46.00	37.93 ± 29.68	NA
	With aerosols	43.60	37.42 ± 29.23	43.13 ± 37.3
	Change	-2.4	-0.51 ± 0.8	NA
Change in Incoming shortwave		-21.9	-8.72 ± 8.98	-8.49 ± 6.82
Change Incoming longwave		NA	2.12 ± 3.73 (all-sky)	1.02 ± 1.54 (clear-sky)

Table 3.4 shows that the latent heat flux simulated by CLM is in excellent agreement with the FLUXCOM dataset on both the global scale and for individual climate zones with MBE less than 10%. The agreement for sensible heat flux is also quite good except for the boreal and polar climate zones, where CLM shows systematic low biases. The LAI in CLM is slightly higher than the MODIS MCD15A3H version 6 5-year estimates (Fig. 3.5a; Knyazikhin et al., 1998), but the variability between the climate zones is generally captured by the model.

Table 3.5: Evaluation of the sensible and latent heat fluxes simulate by CLM against FLUXCOM data for the world's land surfaces and for each climate zones. The top two rows for each variable show the grid-area weighted mean and standard deviation from the present study and FLUXCOM. The statistical parameters for model evaluation are the coefficient of determination (r^2), the weighted root-mean-square error (RMSE), and the mean bias error (MBE).

Variable	Case	Regions of interest					
		Global land	Tropical	Arid	Temperate	Boreal	Polar
Sensible heat flux (W m^{-2})	CLM	37.42 ± 20.54	41.77 ± 14.21	57.17 ± 14.95	40.78 ± 14.53	19.88 ± 12.27	18.78 ± 23.07
	FLUXCOM	40.87 ± 15.82	44.06 ± 10.47	56.51 ± 12.89	39.09 ± 14.34	28.71 ± 8.01	32.1 ± 19.24
	r^2	0.71	0.32	0.47	0.48	0.44	0.81
	RMSE	12.40	11.99	11.55	11.88	12.94	16.11
	MBE	-3.45	-2.29	0.67	1.69	-8.83	-13.31
Latent heat flux (W m^{-2})	CLM	45.23 ± 26.29	79.81 ± 17	32.12 ± 15.61	51.7 ± 16.74	27.84 ± 10.55	19.2 ± 13.64
	FLUXCOM	48.38 ± 27.49	86.32 ± 18.29	32.3 ± 11.8	56.34 ± 15.05	30.03 ± 8.95	20.29 ± 9.75
	r^2	0.87	0.52	0.42	0.66	0.73	0.62
	RMSE	10.98	14.54	11.92	10.97	6.36	8.11
	MBE	-3.14	-6.51	-0.18	-4.64	-2.20	-1.09
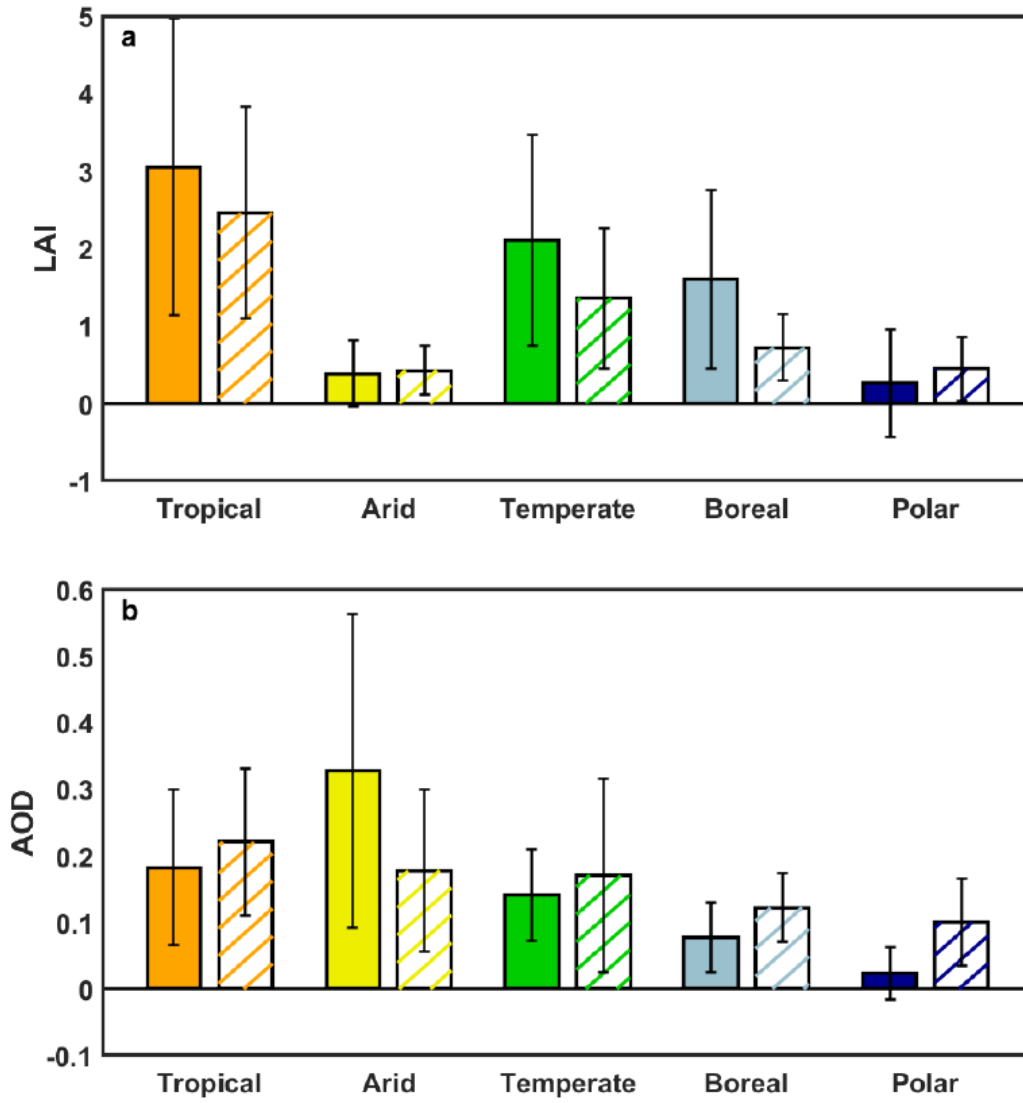
Figure 3.5: Comparison of leaf area index (LAI) and aerosol optical depth (AOD) with satellite observations. Grid-area weighted mean (bars) and standard deviation (error bars) of LAI and AOD from our CLM and CAM runs compared with 5-year averages (2003-2007) observed by satellites for each climate zone are shown. The filled bars are for the parameters in the models, while the hatched bars represent the satellite observations.

We also compare our results with those reported by Liu et al. (2014), which appears to be the only other global study on aerosol impact on turbulent fluxes on land (Table 3.4). Our reductions in H and λE are lower than theirs (Table 3.4). While Liu et al. (2014) did not provide the results for $\Delta K_{\downarrow}$, Chen & Zhuang (2014), who used the same modeling

framework, reported a $\Delta K_\downarrow$ of -21.9 W m^{-2} (global terrestrial mean) due to aerosols, which is higher in magnitude than previous studies (Chung et al., 2005; scaled by AOD over land), as well as MERRA-2 (Table 3.4). Moreover, as also mentioned by the authors, the magnitude of H simulated by their model is significantly higher than other estimates. Since our $\Delta K_\downarrow$ is in good agreement with the MERRA-2 diagnostics and our simulated sensible and latent heat fluxes are much closer to FLUXCOM and MERRA-2 estimates than theirs (Tables 3.4 and 3.5), we are relatively confident about the overall magnitude of the changes in turbulent fluxes in our study.

Davin and Seneviratne (2012) used an older version of CLM (CLM3.5; see changes since then in Oleson et al. (2013) and Lawrence et al. (2019)) with a two-big-leaf canopy structure to demonstrate that it can simulate the enhancement of λE under diffuse light conditions as observed at an evergreen needleleaf forest site. However, a recent study using the multi-layer implementation of CLM at a temperate deciduous forest site suggests an overestimation of the GPP response to k_d at the hourly scale during summer (Wozniak et al., 2020). Our results are less prone to this model uncertainty because the temperature change induced by the fertilization effect is minor in comparison to the change associate with Bowen ratio increase under reduced global radiation which is a robust feature across models (Zhang et al., 2008; Matsui et al., 2008; Mercado et al., 2009; Oliveira et al., 2011; Davin & Seneviratne, 2012; Liu et al., 2014; Rap et al., 2015; Rap et al., 2018) and in observational studies (Wang et al., 2008; Kanniah et al., 2012; Wang et al., 2018).

3.3.3 Terrestrial Evapotranspiration and Its Partitioning

The terrestrial evapotranspiration can be separated into evaporation from the ground (λE_g), evaporation from the canopy (λE_c), transpiration (λE_t) from sunlit leaves ($\lambda E_{t,sun}$), and transpiration from shaded leaves ($\lambda E_{t,sha}$). This separation in CLM is based on the vegetation temperature, ground temperature, surface temperature, and specific humidity. The

method starts with initial guesses for wind speed and Monin-Obukhov length, which are used to iteratively solve for the other components and sub-components of the surface energy budget. More information about this numerical scheme can be found in Oleson et al. (2013).

Of specific importance to the present study, CLM parameterizes photosynthesis and transpiration separately for sunlit and shaded leaves, but it represents the whole canopy with a single foliage temperature (Dai et al., 2004). To determine if this simplification adversely affects our perturbation experiments, we compared the CLM results with the results of the Community Atmosphere–Biosphere Land Exchange model (CABLE version 1.4). Unlike CLM, CABLE solves the energy balance equation and the foliage temperature separately for sunlit and shaded leaves (Wang & Leuining, 1998). The comparison was made for three grid cells where >90% of the grid space is occupied by a single plant functional type (PFT). Two of the grids are occupied by broadleaf evergreen trees, one with the highest (-22.3 W m^{-2}; labeled as BET1, in Congo Basin; 3.3° N, 17.5° E) and the other with the lowest (-1.5 W m^{-2}; labeled as BET2, in Papua New Guinea; 3.3° S, 137.5° E) magnitude of the aerosol shortwave radiative effect $\Delta K_{\downarrow}$, both with a LAI of about 6. The third grid is C3 grass with LAI of 2.1 and $\Delta K_{\downarrow}$ of -6.6 W m^{-2} (labeled as C3, in northern China; 49.5° N, 118.7° E).

For each grid cell, CABLE was prescribed with the corresponding PFT. The default LAI assigned to the relevant PFTs in CABLE was replaced by the monthly LAI calculated by CLM. The CABLE simulations were forced by the same atmospheric variables as in the CLM runs under clean and polluted conditions. To do this, the CABLE model code was modified to use time-dependent beam fraction of radiation from the CAM simulations. Figure 3.6 shows the sensible (H) and latent heat flux (λE), including their components, simulated by the two models for clean sky conditions and their changes due to aerosols, as well as the surface temperature response. The CABLE model confirms that aerosols de-

crease the Bowen ratio and the surface temperature, by amounts similar to those simulated

by CLM. The CABLE simulations also demonstrate broadly similar changes in the sunlit

and shaded components of transpiration due to aerosols compared to the CLM simulations.
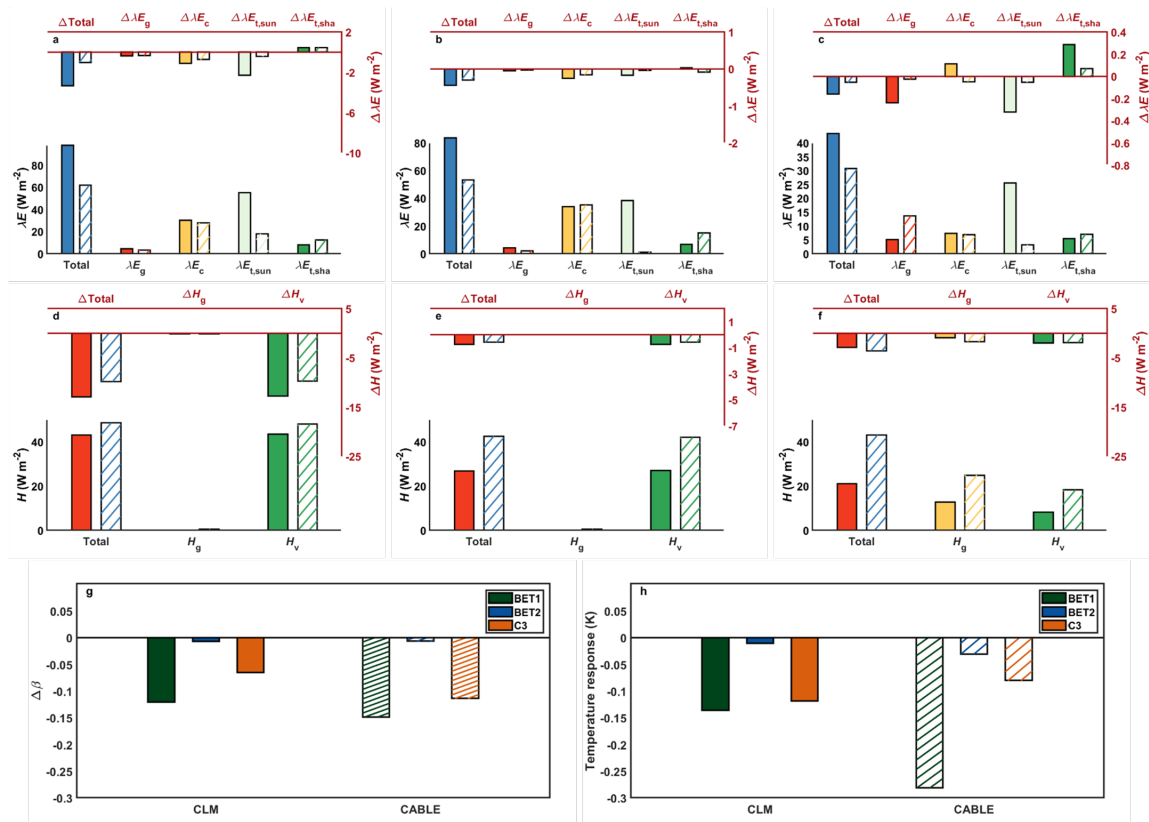
Figure 3.6: Comparisons between CLM and CABLE results. Simulated three-year mean latent heat flux and sensible heat flux, their perturbations, and components for a heavily polluted broadleaf evergreen tree grid (BET1, panels **a** & **d**), a lightly polluted broadleaf evergreen tree grid (BET2, panels **b** & **e**), and a C3 grass grid (C3, panels **c** & **f**). The components for the clean atmosphere are represented by the bars in the lower part of each panel, and the net changes due to aerosols are given by the bars in the upper part. Panel **g** shows the Bowen ratio response to aerosols. Panel **h** shows the surface temperature response to aerosols. CLM is represented by filled bars and CABLE by hatched bars.

3.3.4 Attributing Surface Temperature Perturbations Through Radiative and Non-Radiative Pathways

The total surface temperature change (ΔT_{s}) due to aerosols is the sum of the changes in the blending height temperature (ΔT_{b}) and the local temperature response (ΔT; Chakraborty & Lee, 2019):

$$\Delta T_{\mathrm{s}} = \Delta T + \Delta T_{\mathrm{b}} \tag{3.4}$$

Here ΔT arises from the radiative pathway associated with changes in $K_{\downarrow}$ and $L_{\downarrow}$ and the non-radiative pathway associated with changes in evaporation and in efficiency of convection between the surface and the lower atmosphere. This temperature response can be decomposed according to the theory of intrinsic biophysical mechanism (IBPM) which is a solution of the perturbed form of Eq. 3.1 (Lee et al., 2011),

$$\Delta T = \frac{\lambda_0}{1+f}\Delta K_{\downarrow}(1-a) + \frac{\lambda_0}{1+f}\Delta L_{\downarrow}$$
$$+ \frac{-\lambda_0}{(1+f)^2}\left(R_{\mathrm{n}}^{*} - G\right)\Delta f_1 + \frac{-\lambda_0}{(1+f)^2}\left(R_{\mathrm{n}}^{*} - G\right)\Delta f_2 + \frac{\lambda_0}{1+f}\Delta G \tag{3.5}$$

where a is the surface albedo, R_{n}^{*} is apparent net radiation given by

$$R_{\mathrm{n}}^{*} = K_{\downarrow}(1-a) + L_{\downarrow} - \sigma T_{\mathrm{b}}^{4} \tag{3.6}$$

where σ is the Stefan-Boltzmann constant, λ_0 is the local temperature sensitivity due to longwave radiative feedback given by:

$$\lambda_0 = \frac{1}{4\sigma T_{\mathrm{s}}^{3}} \tag{3.7}$$

and f is a dimensionless energy redistribution factor, a measure of the efficiency of energy dissipation from the surface to the lower atmosphere through convection and evaporation (Lee et al., 2011). A larger f corresponds to a lower effective local climate sensitivity (λ_*) according to the relation $\lambda_* = \lambda_0 / (1+f)$.

The IBPM method is a diagnostic tool grounded on a first principle (the surface energy conservation). It separates the surface temperature perturbation into contributions of different biophysical pathways. Accordingly, the terms on the right-hand side of Eq. 3.5 represent, from left to right, the temperature response due to change in incoming shortwave radiation $\Delta K_\downarrow$ (term 1), change in incoming longwave radiation $\Delta L_\downarrow$ (term 2), change in energy redistribution through evaporation (term 3), change in energy redistribution through convection (term 4), and change in ground heat flux ΔG (term 5). The contribution of the radiative pathway is given by the first two terms, and that of the non-radiative pathway is given by the last three terms. The realism of the IBPM framework has been extensively documented in the past, for example, in studies of temperature perturbation due to urbanization (Zhao et al., 2014), deforestation (Bright et al., 2017; Burokowski et al., 2018), and agricultural activities (Ruehr et al., 2020; Chakraborty et al., 2021), and in a study of lake surface temperature change (Wang et al., 2018).

In this diagnostic calculation, the change terms $\Delta K_\downarrow$, $\Delta L_\downarrow$ and ΔG are given as the difference between the two model runs (P minus C), R_n^* and λ_0 are based on the values of $K_\downarrow$, $L_\downarrow$, α, T_s, and T_b for the clean atmosphere, with T_b being the atmospheric temperature at the first CAM model grid height (average 60 m above the surface). The energy redistribution factor (Lee et al., 2011) is calculated from the following diagnostic equation:

$$f = \frac{\lambda_0}{T_s - T_b} \left(R_n^* - G \right) - 1 \tag{3.8}$$

Only grids with a positive value of f are considered. Contributions due to evaporation

(Δf_1) and convection (Δf_2) are calculated from:

$$\Delta f_1 = -f\frac{\Delta\beta}{\beta(1+\beta)} \tag{3.9}$$

$$\Delta f_2 = -f\frac{\Delta r_a}{r_a} \tag{3.10}$$

where β and r_a are the average Bowen ratio, the ratio of the sensible and latent heat fluxes, and aerodynamic resistance, respectively, from Runs P (or M) and C, while the Δ terms are the changes in the respective variables between the two runs. The role of the EF change is expressed through the β change, noting that a negative $\Delta\beta$ corresponds to a positive ΔEF and vice versa. Changes in β are small (close to zero) for boreal and polar climate, leading to unreasonably high values of the third term in Eq. 3.5. The ΔT through the evaporative pathway is thus set to zero for these grids.
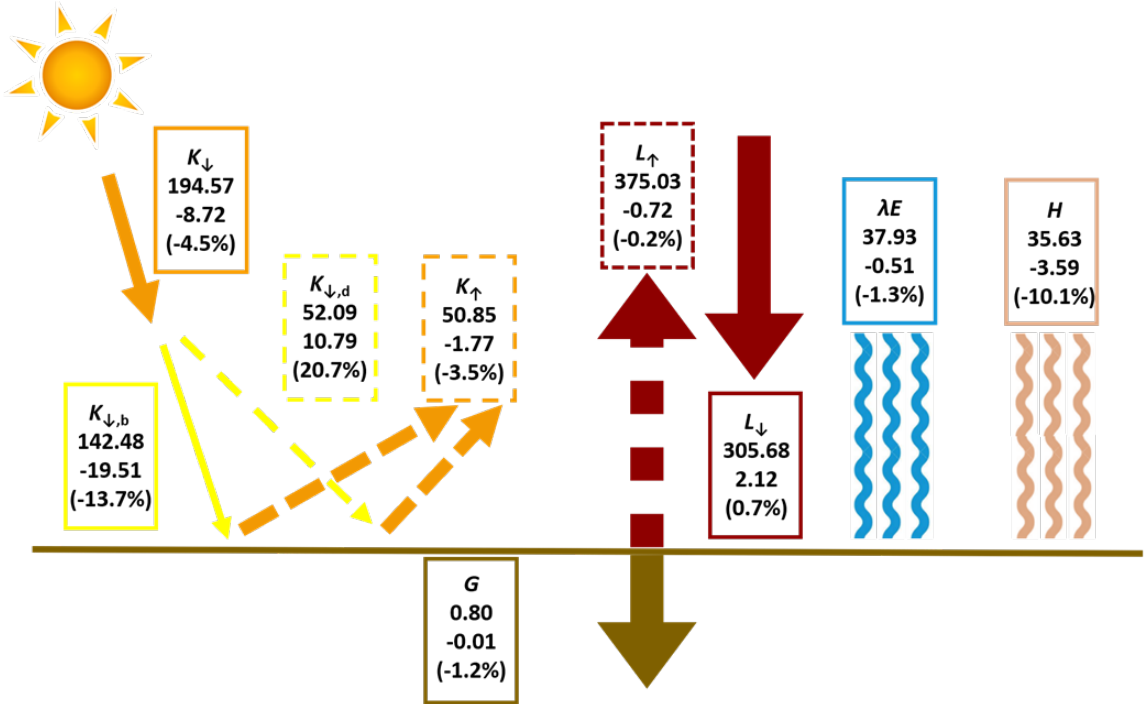
Figure 3.7: Surface energy budget adjustment due to aerosols. Schematic showing grid area-weighted annual mean terrestrial surface energy budget components for a clean atmosphere, namely incoming shortwave radiation ($K_\downarrow$), direct beam radiation ($K_{\downarrow,b}$), diffuse radiation ($K_{\downarrow,d}$), reflected shortwave radiation ($K_\uparrow$), ground heat flux (G), emitted longwave radiation ($L_\uparrow$), incoming longwave radiation ($L_\downarrow$), latent heat flux (λE), and sensible heat flux (H), along with changes (and percentage changes) to each component due to aerosols. In each box, the baseline value is at the top, the change is in the middle and the percentage change is in parentheses at the bottom. All quantities other than the percentage changes are in W m^{-2}.

3.4 Results

3.4.1 Aerosol Impact on the Surface Energy Budget

Unsurprisingly, aerosols decrease the incoming surface shortwave radiation and increase the incoming longwave radiation (Fig. 3.7), whose spatial variations are consistent with the geographic distribution of aerosols (Figs 3.8 and 3.9). The highest changes in incoming radiation are seen over arid regions like the Sahara Desert and the Middle East, and

moderately large changes over heavily polluted regions like northern India and eastern China (Fig. 3.8). The global average reduction in the shortwave radiation $\Delta K_\downarrow$ over land is -8.72 W m^{-2} (-4.5%), from a base $K_\downarrow$ value of 194.57 W m^{-2} for the clean atmospheric state (Fig. 3.7 and Table 3.1). This total $\Delta K_\downarrow$ consists of an increase in the diffuse radiation ($\Delta K_{\downarrow,d}$) by 10.79 W m^{-2} (20.7%) and a decrease in the beam radiation ($\Delta K_{\downarrow,b}$) by 19.51 W m^{-2} (-13.7%). Consequently, the diffuse fraction (k_d) increases by 26%, from 0.268 to 0.338. Because of the large mineral dust aerosol loading and of the low base k_d (0.165) due to low cloud amounts and low zenith angle, the largest percentage increase in k_d ($\approx$70%) is seen for arid regions. Averaged over all land surfaces, increases in $L_\downarrow$ are roughly one-fourth of the decreases in $K_\downarrow$, at 2.12 W m^{-2} (0.7%), almost all of which are attributable to natural absorbing aerosols (Chakraborty & Lee, 2019).
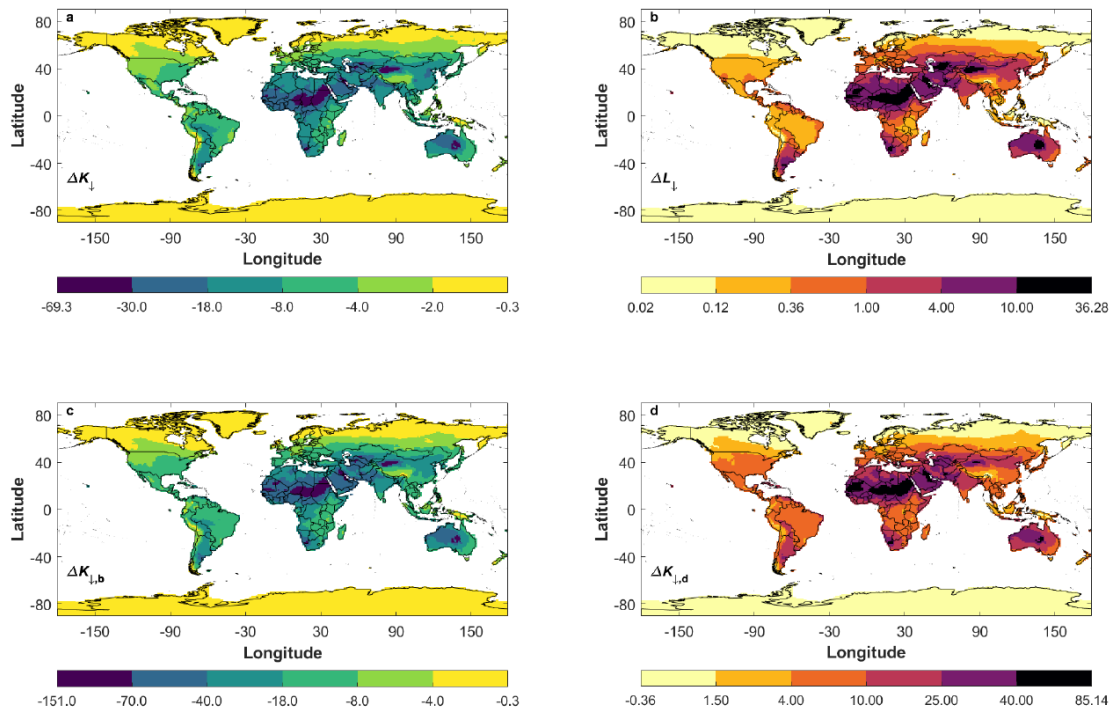
Figure 3.8: Global patterns of changes in incoming radiation at the surface due to aerosols. Global maps of **a**, shortwave radiative effect ($\Delta K_\downarrow$), **b** longwave radiative effect ($\Delta L_\downarrow$), **c** change in beam radiation ($\Delta K_{\downarrow,b}$), and **d** change in diffuse radiation ($\Delta K_{\downarrow,d}$). All quantities are in W m^{-2}. Non-linear color scales are used to better visualize the spatial variations.
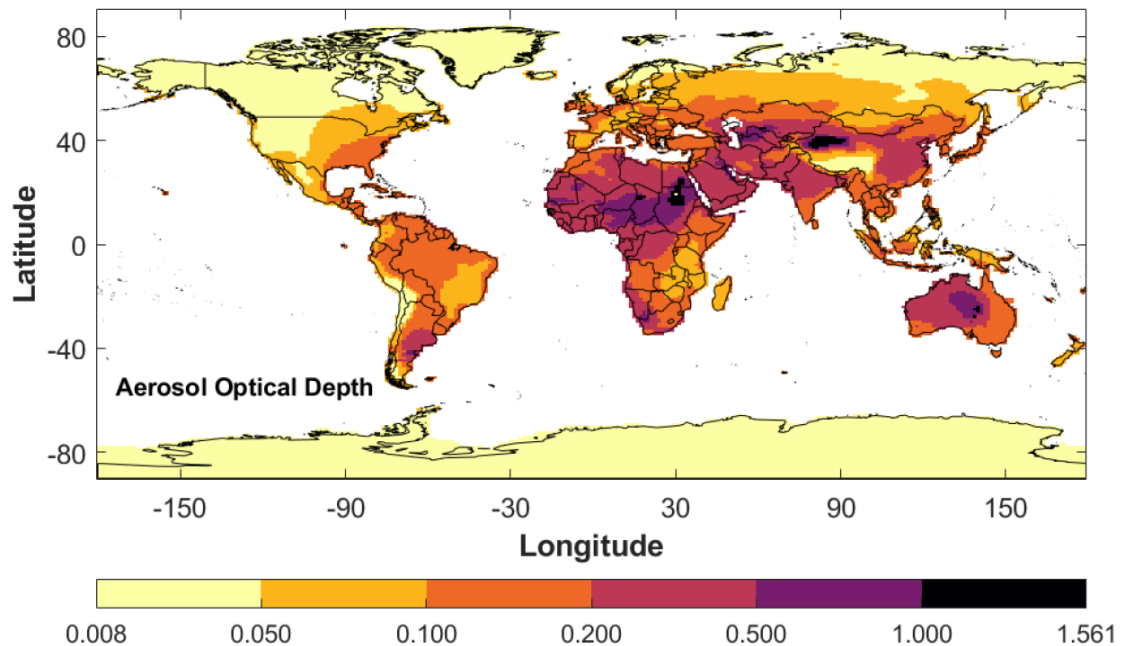
Figure 3.9: Global patterns of aerosol optical depth. Non-linear color scales are used to better visualize the spatial variations.

Aerosols reduce both the terrestrial sensible (H) and the latent heat flux (λE), but by different amounts (Fig. 3.11). H decreases over 7 times as much as λE ($\Delta H =$ -3.59 W m^{-2}, $\Delta\lambda E$ = -0.51 W m^{-2}; Fig. 3.7 and Table 3.1). Separating λE into its components (Fig. 3.10) explains why $\Delta\lambda E$ is smaller than ΔH in magnitude. While λE_g, λE_c, and λE_t decrease, the total decrease in λE_t is partly offset by an increase in $\lambda E_{t,sha}$. Moreover, the percentage increases in $\lambda E_{t,sha}$ are much higher than the percentage decreases in $\lambda E_{t,sun}$. For instance, for the tropical zone (Fig. 3.10b), the increase in $\lambda E_{t,sha}$ is 8.2%, while the decrease in $\lambda E_{t,sun}$ is only 2.4%. In this case, $\lambda E_{t,sha}$ increases by 0.55 W m^{-2}, partly offsetting the decrease in λE_t due to $\Delta\lambda E_{t,sun}$ (-0.83 W m^{-2}). Similar enhancement of $\lambda E_{t,sha}$ is also seen for other biomes.
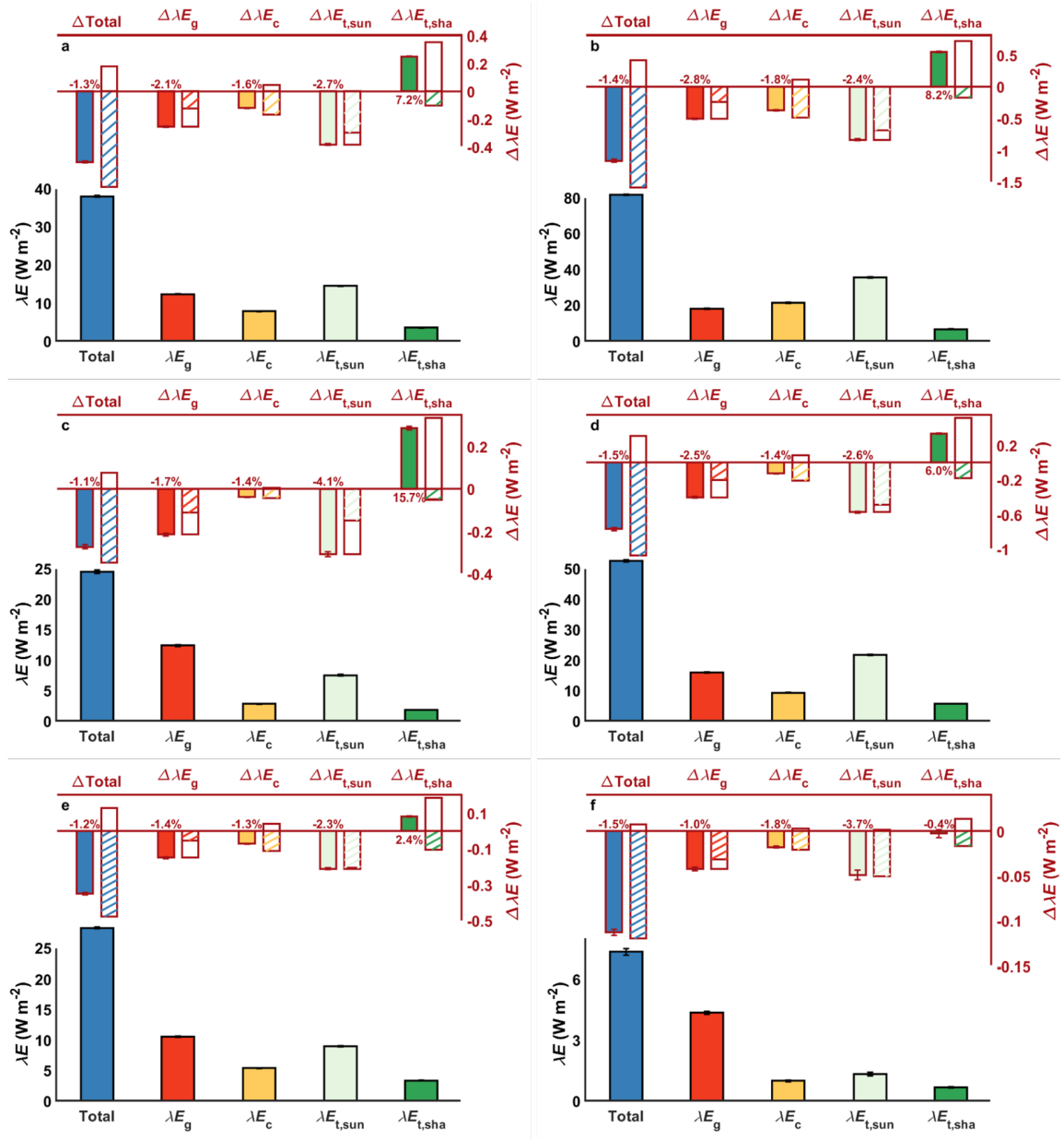
Figure 3.10: Components of latent heat flux and their changes across climate zones. Total grid-area weighted mean latent heat flux (λE) for a clean atmosphere and its change due to aerosols ($\Delta\lambda E$), as well as the corresponding components, namely ground evaporation (λE_{g}), canopy evaporation (λE_{c}), transpiration from sunlit leaves ($\lambda E_{\mathrm{t,sun}}$), and transpiration from shaded leaves ($\lambda E_{\mathrm{t,sha}}$) over **a** all terrestrial surfaces, **b** tropical climate, **c** arid climate, **d** temperate climate, **e** boreal climate, and **f** polar climate. The components for a clean atmosphere are represented by the filled bars in the lower part of each panel. The net changes in the components due to aerosols are given by the filled bars in the upper part of the panel, with the percentage change noted. The net change is further decomposed into contributions from the diffuse radiation fertilization effect (blank) and the dimming effect (hatched). The error bars represent the grid area-weighted standard errors.
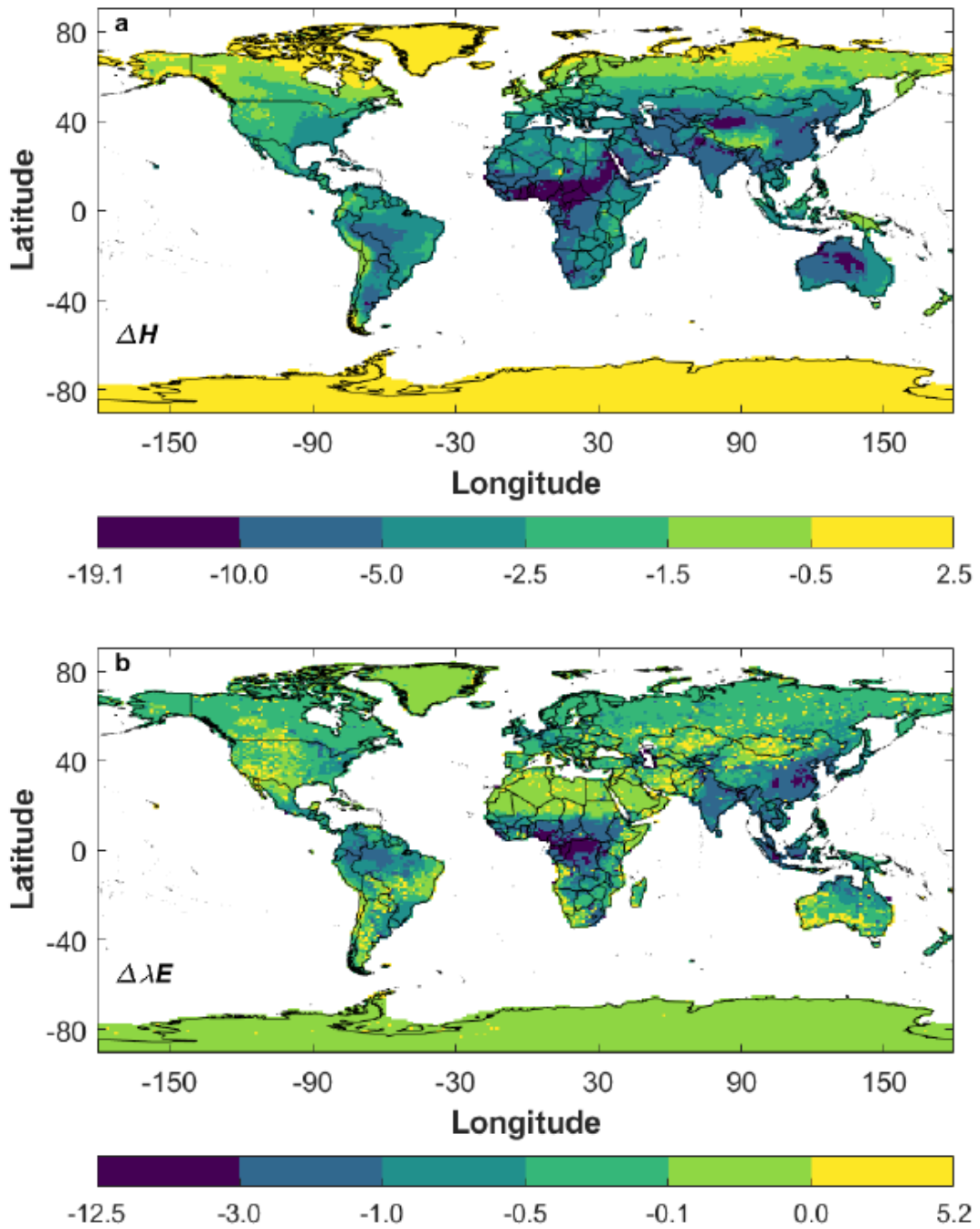
Figure 3.11: Global patterns of changes in turbulent fluxes due to aerosols. Global maps of **a**, change in sensible heat flux (ΔH), and **b** change in latent heat flux ($\Delta \lambda E$). All values are in W m^{-2}. Non-linear color scales are used to better visualize the spatial variations.

According to the hypothesis of diffuse radiation fertilization, efficient penetration of

diffuse radiation through the canopy increases photosynthesis in shaded leaves under pol-
luted conditions. Consequently, this enhances transpiration from shaded leaves and com-
pensates for the lower transpiration from sunlit leaves under the decreased incoming sun-
light ($K_\downarrow$) due to aerosols. Similar patterns are seen for the components of the ecosystem
carbon budget (Fig. 3.12). The net ecosystem productivity (NEP) increases under aerosol
loading in most climate zones, with an average increase of 1.7% for the Earth's land sur-
faces. A similar analysis done for different LAI bins shows that the greatest increase in
NEP (and second highest percentage increase) is for grids with LAI > 5 at 0.46 Pg C y^{-1}
(Fig. 3.13). The overall change in gross primary productivity (GPP) is positive as opposed
to a negative $\Delta\lambda E$, supporting previous finding that aerosol loading enhances ecosystem
water use efficiency (Lu et al., 2017). The diffuse radiation fertilization effect alone has
a stronger impact on GPP (increase of 2.18 Pg C y^{-1} or 1.8% of total terrestrial GPP,
Fig. 3.12a) than on land evaporation (increase of 0.18 W m^{-2} or 0.48% of total terrestrial
evaporation, Fig. 3.10a).
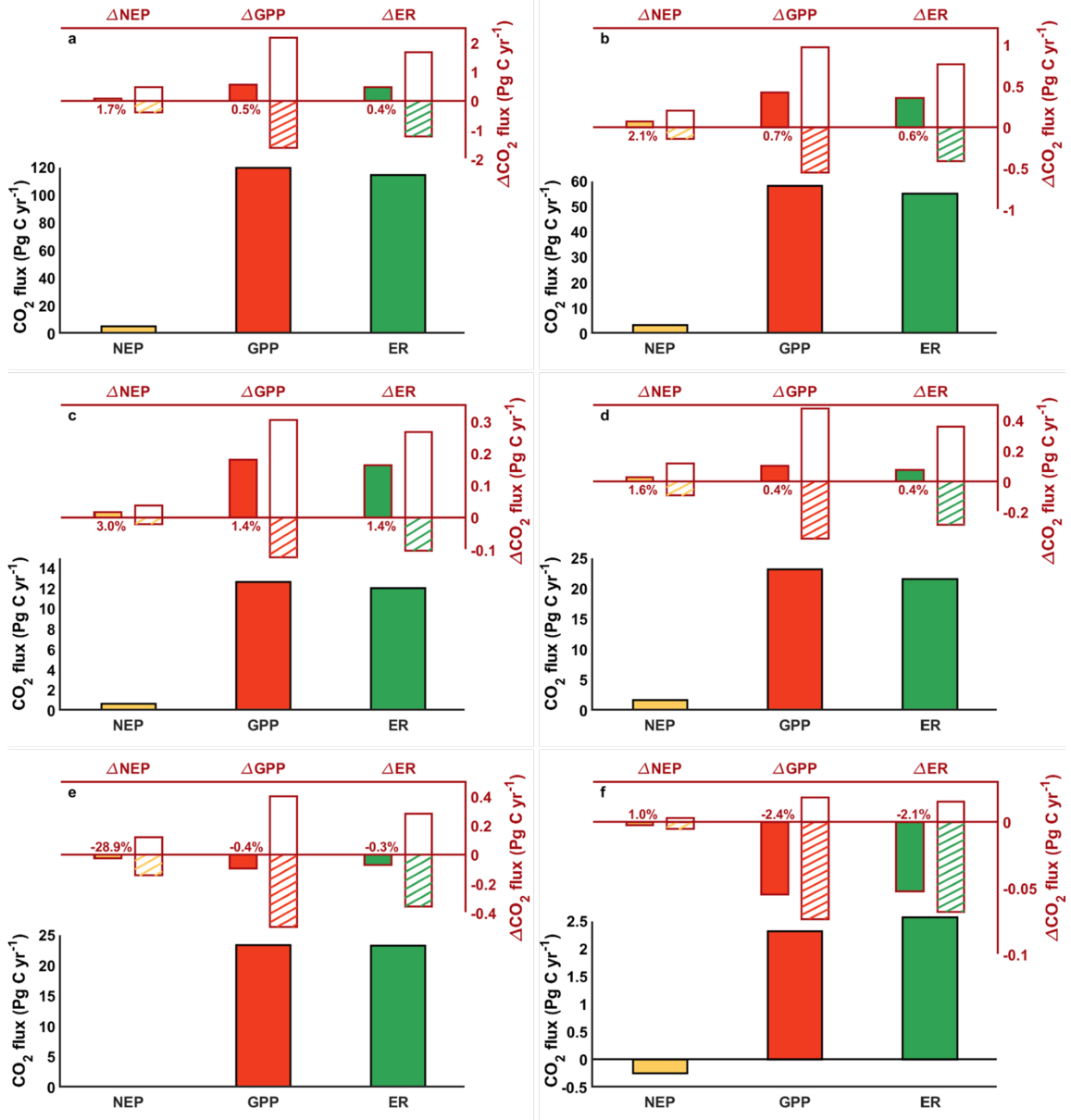
Figure 3.12: Carbon budget across climate zones. Net ecosystem production (NEP, orange bar), gross primary productivity (GPP, red bar), and ecosystem respiration (ER , green bar) over **a** all terrestrial surfaces, **b** tropical climate, **c** arid climate, **d** temperate climate, **e** boreal climate, and **f** polar climate. The carbon flux components for a clean atmosphere are represented by the filled bars in the lower part of each panel. The net changes due to aerosols are given by the filled bars in the upper part of the panel, with the percentage changes noted. The net changes are further decomposed into contributions from the diffuse radiation fertilization effect (blank bar) and the dimming effect (hatched bar).
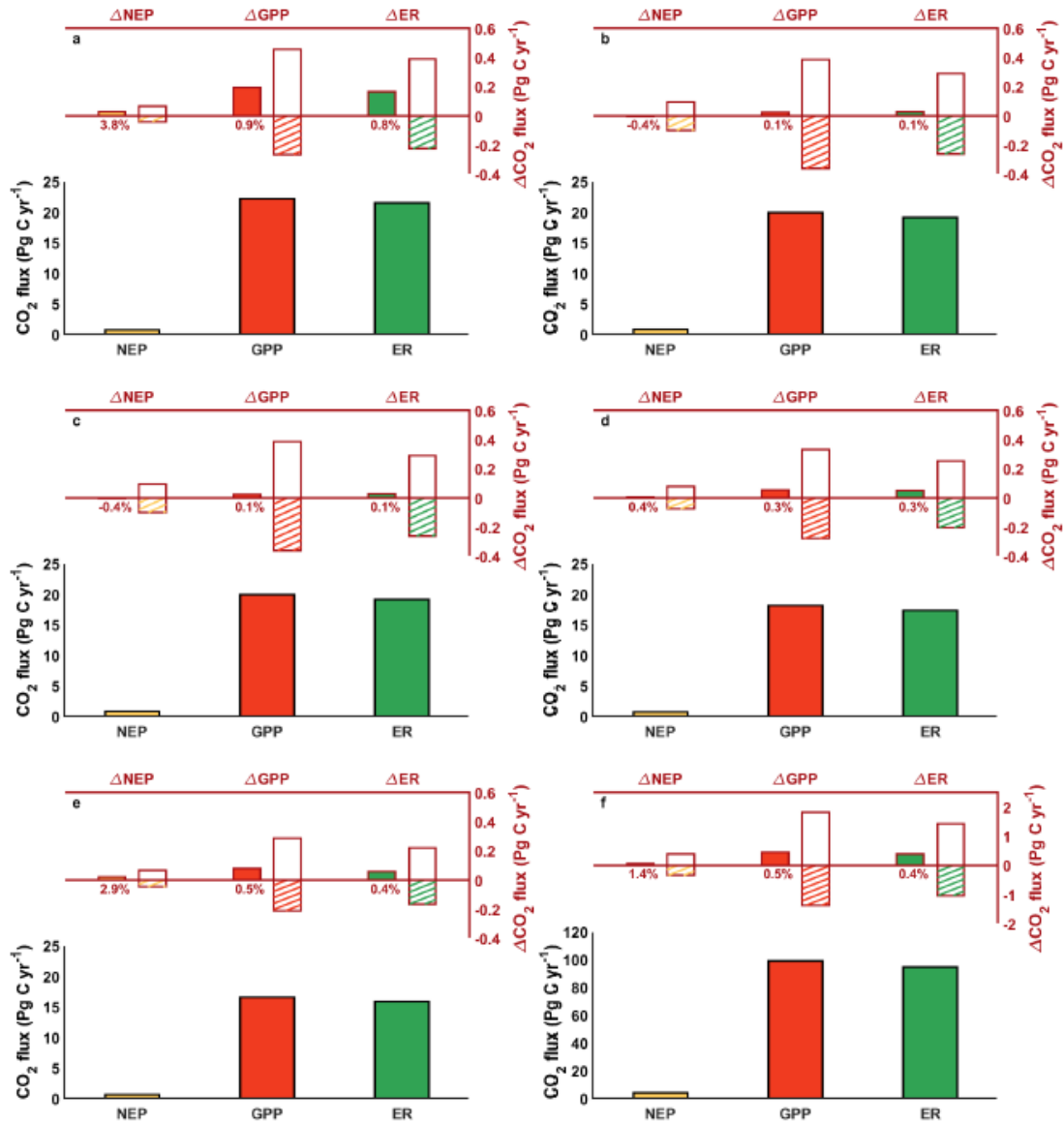
Figure 3.13: Carbon budget across vegetation density zones. Net ecosystem production (NEP, orange bar), gross primary productivity (GPP, red bar), and ecosystem respiration (ER , green bar) over **a** grids with leaf area index (LAI) <1, **b** between 1 to 2, **c** between 2 to 3, **d** between 3 to 4, **e** between 4 to 5, and **f** and above 5. The carbon flux components for a clean atmosphere are represented by the filled bars in the lower part of each panel. The net changes due to aerosols are given by the filled bars in the upper part of the panel, with the percentage changes noted. The net changes are further decomposed into contributions from the diffuse radiation fertilization effect (blank bar) and the dimming effect (hatched bar).

For ΔH, there is no corresponding compensating mechanism; instead H from both

the ground (H_g) and vegetation (H_v) decrease (Fig. 3.14). As a result, EF increases by 0.023 or 4.5% over the global terrestrial surface (Fig. 3.11). Changes in EF reach 0.05 to 0.06 (almost 10%) over the Congo Basin rainforest in central Africa, northern India, and eastern and north-western China. Taklamakan Desert in north-western China shows the highest percentage change in EF (25 to 30%).
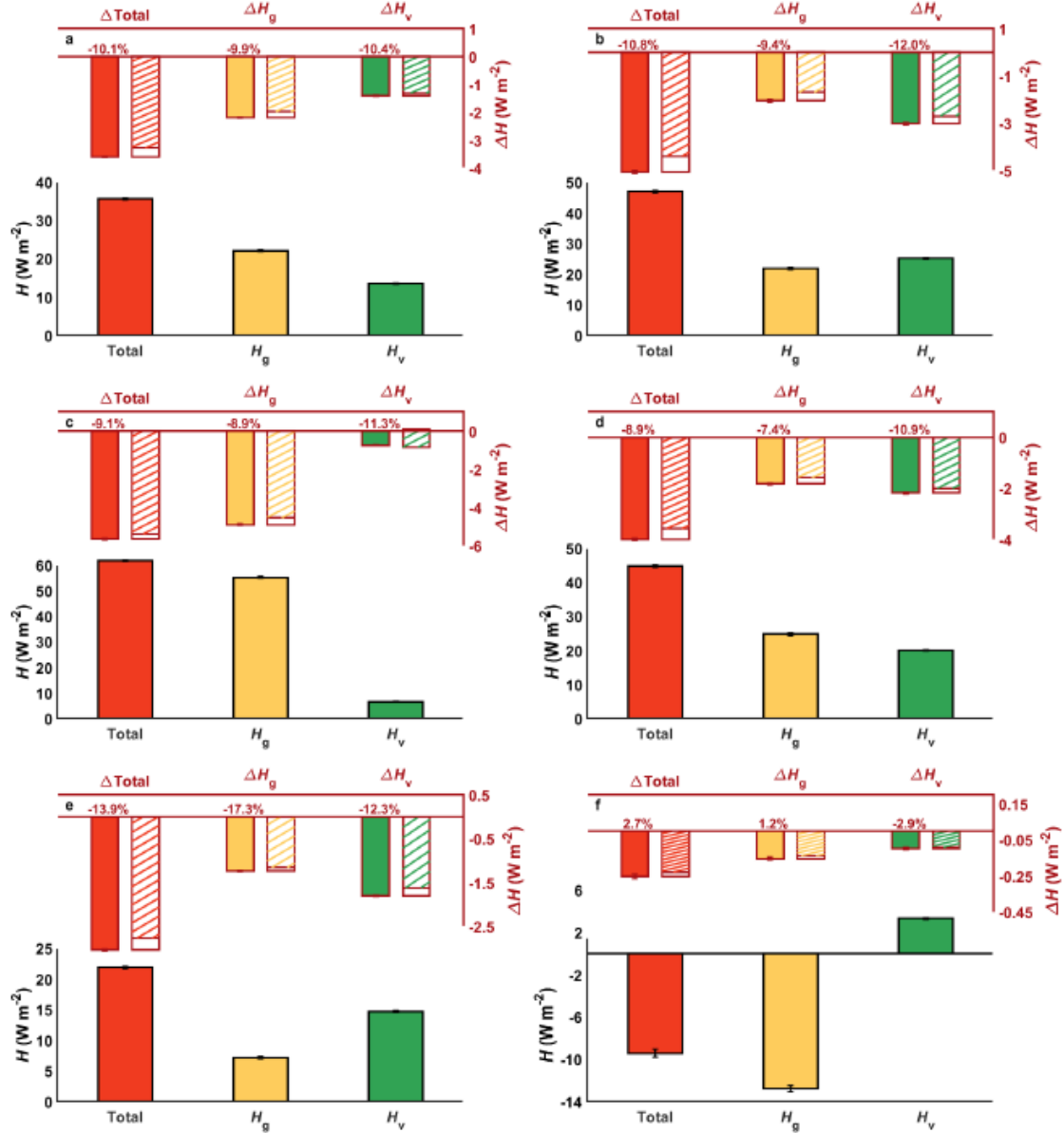
Figure 3.14: Components of sensible heat flux across climate zones. Total grid area-weighted mean sensible heat flux (H, red bar), sensible heat flux from ground (H_g, orange bar), and sensible heat flux from vegetation (H_v, green bar) over **a** all terrestrial surfaces, **b** tropical climate, **c** arid climate, **d** temperate climate, **e** boreal climate, and **f** polar climate. The components for the clean atmosphere are represented by the filled bars in the lower part of each panel. The net changes due to aerosols are given by the filled bars in the upper part of the panel, with the percentage changes noted. The net changes are further decomposed into contributions from the diffuse radiation fertilization effect (blank bar) and the dimming effect (hatched bar). The error bars represent the grid area-weighted standard errors.

The percentage changes in EF are positively correlated with percentage changes in k_d and strongly modulated by vegetation density, as seen from the steeper slopes of the linear fit between them for increasing LAI bins (Fig. 3.15a). The sensitivity of percentage change in EF to percentage changes in k_d increases from 0.14 for grids with an LAI less than 1 to 0.32 for grids with an LAI greater than or equal to 5. Similarly, the actual change in EF shows an increasing trend with increasing Δk_d, though the correlation between the two is weaker (Fig. 3.15b) than between the relative changes since the base available energy varies widely between different grids.
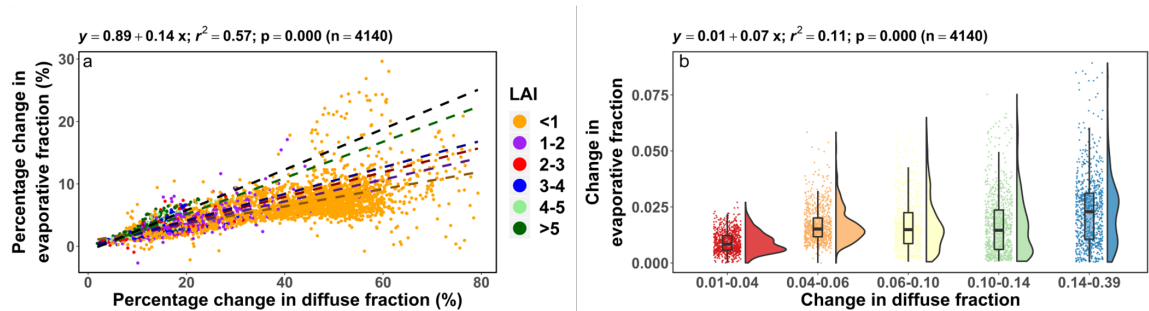
Figure 3.15: Association between diffuse fraction change and evaporative fraction change. **a** Scatter plot of grid-averaged percentage change in diffuse fraction (k_d) versus percentage change in evaporative fraction (EF) between polluted and clean atmosphere. The equation for the linear relationship between the two is given above the figure. The dashed lines, from dark orange to black, are the lines of best fit between the two variables for increasing leaf area index (LAI) bins. **b** Association between grid-averaged changes in EF and in diffuse fraction (Δk_d) between polluted and clean atmosphere. The regression equation between the two is given above the figure, with coefficient of determination r^2, confidence level p, and number of grid points n noted. For each equal-sized Δk_d bin, frequency distributions of ΔEF, as well as box and whisker plots showing the 25th, 50th, and 75th percentile of ΔEF are given.

For this analysis, we used the latest version of CLM with biogeochemistry and prognostic vegetation. To illustrate the validity of our conclusions within the modeling framework, we ran an earlier version of the model (CLM4.5) with the same forcing data and obtained broadly consistent results (Fig. 3.16).
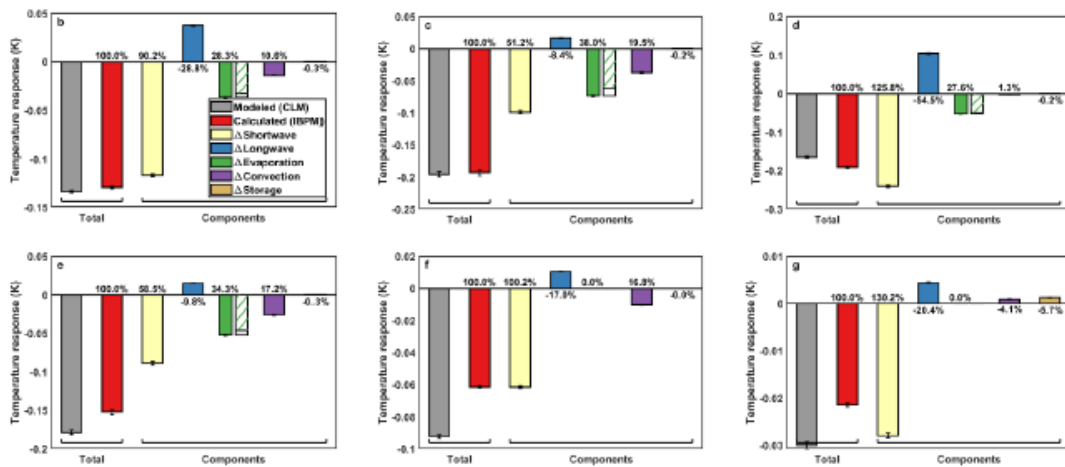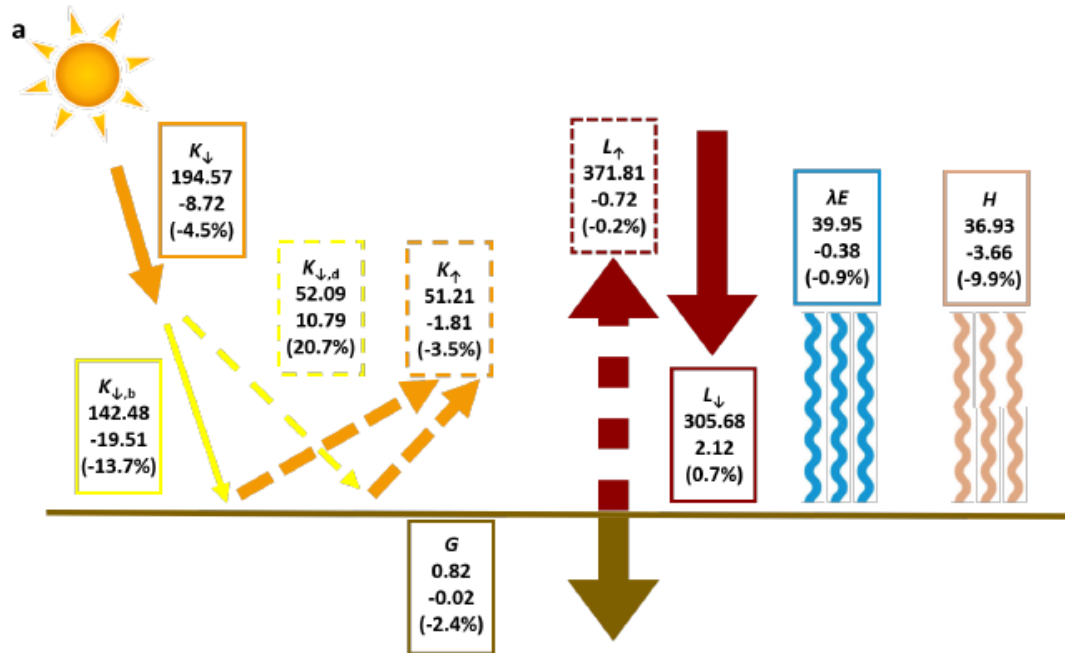
Figure 3.16: Examining consistency of results using CLM4.5. Identical to Fig. 3.7 and Fig. 3.17 but using CLM4.5 results instead of CLM5.0.

3.4.2 Isolating Multiple Pathways of Aerosol-Induced Local Temperature Response

Using the theory of intrinsic bio-physical mechanism (IBPM; Lee et al., 2011), we separate the contributions of different pathways, namely surface shortwave radiative effect, surface

longwave radiative effect, change in EF, change in convection efficiency or aerodynamic resistance, and change in the ground heat flux, to the total surface temperature perturbation (ΔT; Figs 3.17 and 3.18). Note that ΔT only refers to the local temperature response to aerosols. The total aerosol-induced surface temperature change is the sum of this local response and the background atmospheric temperature change (Eq. 3.4). Here the realism of the IBM method is further supported by the good agreement between the temperature perturbation computed online (grey bars, the "truth") and the perturbation calculated with IBPM (red bars, Fig. 3.17).
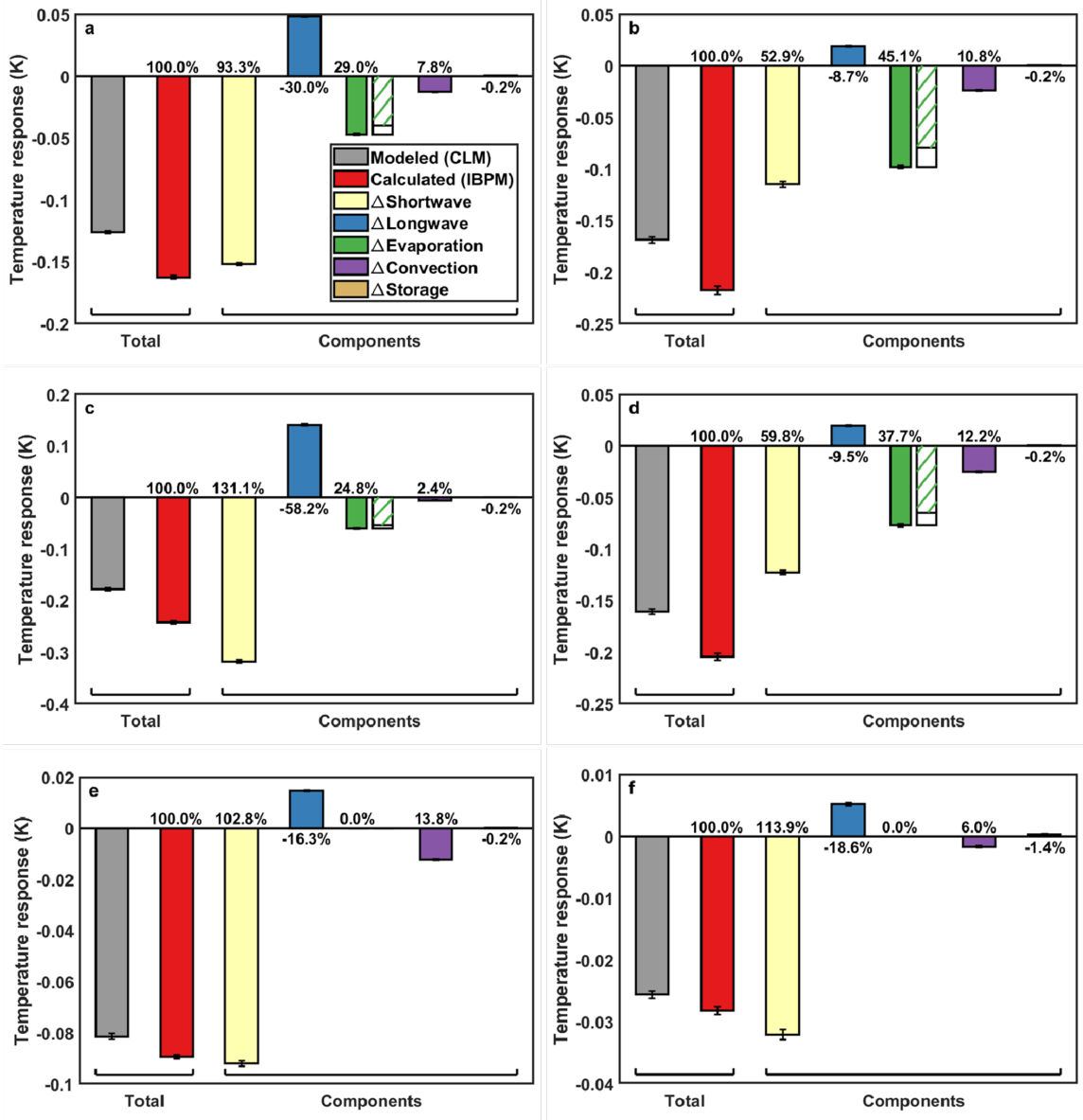
Figure 3.17: Comparing modeled and diagnosed surface temperature response. Total grid-area weighted mean calculated (red, IBPM) and modeled (gray, CLM) temperature response due to aerosols, as well as calculated component contributions from changes in incoming shortwave radiation (light yellow, $\Delta K_{\downarrow}$), incoming longwave radiation (blue, $\Delta L_{\downarrow}$), evaporation (green, ΔEF), convection (purple, Δr_a), and ground heat storage (dark yellow, ΔG) over **a** all terrestrial surfaces, **b** tropical climate, **c** arid climate, **d** temperate climate, **e** boreal climate, and **f** polar climate. The temperature response through evaporation is further decomposed into the contributions from the diffuse radiation fertilization effect (blank bar) and the dimming effect (hatched bar). The percentage value denotes the relative component contribution to the total temperature response. Error bars represent the grid area-weighted standard errors.

The magnitude of $\Delta K_\downarrow$ is higher in regions of higher aerosol loading (Figs 3.8 and 3.9). The highest values are seen in the arid regions. Overall, the surface shortwave radiative effect reduces the global terrestrial surface temperature by 0.15 K, while the longwave radiative effect increases it by 0.05 K. The contributions of these radiative pathways are determined by both the radiation changes and the effective local climate sensitivity (λ_*) - the change in local surface temperature due to a unit surface radiative forcing (Chakraborty & Lee, 2019). The magnitude of λ_* is higher for smooth surfaces, such as deserts and snowpack, and lower for rough surfaces, such as forests (Fig. 3.19). Subsequently, the temperature response to the radiative effect is higher in arid regions and lower in the tropical forests (Fig. 3.18). The highest perturbations ($<$-0.4 K) occur in north-western China, central Australia, and the Middle East, where both the radiation changes and λ_* are high. In comparison, the Amazon rain forest shows low response to the radiative pathways, with decreases of less than 0.1 K (Fig. 3.18a).
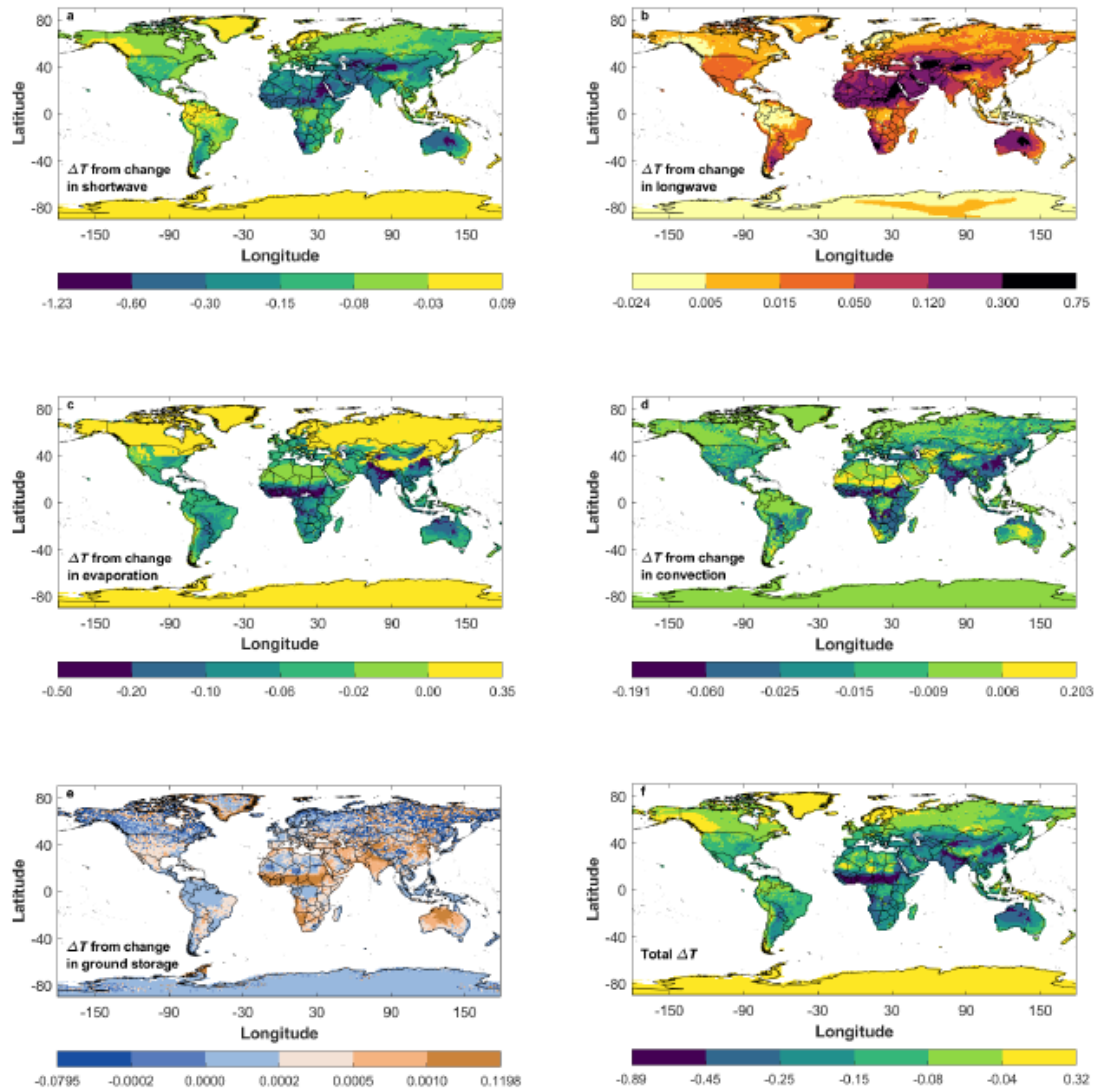
Figure 3.18: Global patterns of different pathways of aerosol-induced temperature response. Global maps of local temperature response (K) from **a** aerosol shortwave radiative effect at surface, **b** aerosol longwave radiative effect at surface, **c** aerosol-induced evaporation change, **d** aerosol-induced convection change, **e** aerosol-induced ground storage change, and **f** the sum of all pathways. Non-linear color scales are used to better visualize the spatial variations.
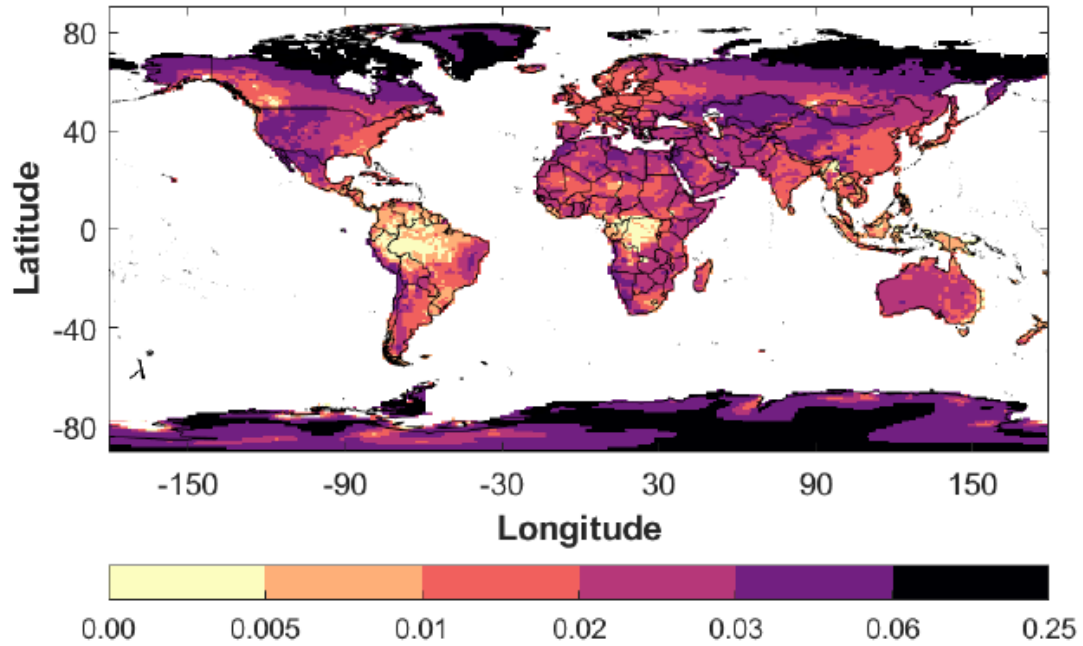
Figure 3.19: Global patterns of effective local climate sensitivity. Values are in K W^{-1} m^2. Non-linear color scales are used to better visualize the spatial variations.

In contrast, the highest perturbations through the non-radiative pathways (sum of evaporation and convection) occur in the Congo Basin (up to -0.6 K), eastern China (up to -0.5 K), and northern India (up to -0.4 K). All of these regions have dense vegetation cover and relatively high aerosol loading. The Amazon basin does not show a high response to the non-radiative pathways (less than 0.05 K) since aerosol loading is relatively low over this region (Figs 3.9 and 3.18d). Taken together, the non-radiative pathways reduce the annual mean terrestrial surface temperature by about 0.06 K. Although aerosols may change r_a through modification of atmospheric stability (Talukdar et al., 2019), we find that the magnitude of this effect is minor compared to the enhancement of evaporative cooling.

The overall change in the annual mean terrestrial surface temperature ΔT is -0.16 K. The highest ΔT is seen in the arid zone, followed by the tropical, temperate, boreal, and polar climate zones (Fig. 3.17). The evaporative pathway accounts for ≈29 % of the total

ΔT globally, and for as much as 45 % in the tropical climate zone. To our knowledge, this is the first isolation of the local temperature response to aerosols through the evaporative pathway. Although it is intuitive that increased water loss in plants will lead to surface cooling, what is surprising is the strength of this pathway.

3.4.3 Dependence on Vegetation Density

The evaporative contribution to the total temperature response increases with increasing LAI, though the total temperature response itself decreases (Fig. 3.20a). At an LAI of around 2, the ΔT via the evaporative pathway exceeds the ΔT due to the surface radiative effect (Fig. 3.20b). At grids with high LAI (> 2), the effective local climate sensitivity is much lower (mean λ_* of 0.013 K W^{-1} m^2 versus global mean of 0.029 K W^{-1} m^2), reducing the surface temperature response through the radiative pathway and thus leading to the relatively large contribution of aerosol-induced evaporation to ΔT. In comparison, arid regions have low LAI (regional mean LAI of 0.39) and high climate sensitivity (regional mean λ_* of 0.026 K W^{-1} m^2), leading to the low contribution of the evaporative pathway to ΔT (Fig. 3.17b). Of the three climate zones considered, LAI is greater than 2 in 58% of the tropical grids, 45% of the temperate grids, and 0.6% of the arid grids (Fig. 3.2b). Overall, high percentage contributions of the evaporative pathway to the aerosol-induced local temperature response are seen over the tropical rainforests in both South America and Africa (Fig. 3.20c).
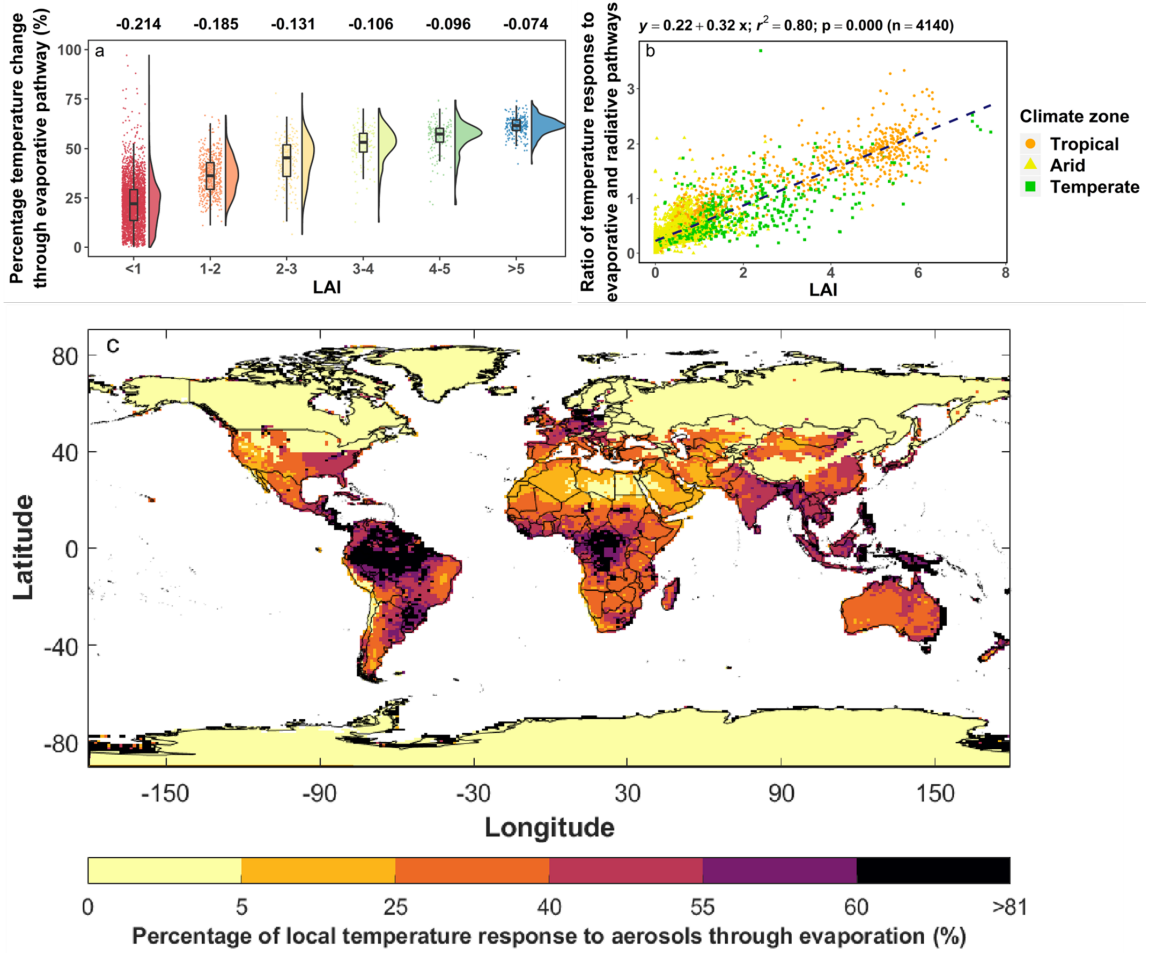
Figure 3.20: Contribution of evaporative pathway to aerosol-induced surface temperature perturbation. **a** Percentage of surface temperature change attributed to the evaporative pathway in increasing leaf area index (LAI) bins. Each data point represents one grid mean value. The box and whisker plot indicates 25th, 50th and 75th percentile values, with the frequency distribution given to the left. The median of the total local surface temperature change in K for each LAI bin is at the top of the figure. **b** Scatter plot of grid-averaged ratio of temperature change attributed to change in evaporation and that attributed to changes in surface shortwave and longwave radiation. The linear regression equation is given above the figure and the dashed line is the line of best fit between the two variables. The three colors represent three climate zones. **c** Global map of percentage contribution of the evaporative pathway to total local temperature response to aerosols.

85

3.4.4 Global Dimming Versus Diffuse Radiation Fertilization

Since aerosols simultaneously reduce $K_\downarrow$ and increase k_d, an open question is whether the aerosol-induced changes in EF, GPP, and surface temperature are caused by changes in the quantity or in the quality of solar radiation (Oliveira et al., 2011). To answer this question, we conducted a third numerical experiment to help separate the total change in a variable into contributions from change in radiation quality or the diffuse radiation fertilization effect and from change in radiation quantity or the dimming effect. Overall, the fertilization effect is more important for gross primary productivity (GPP) and NEP than for λE, increasing the global mean λE by only 0.18 W m^{-2} or 0.48% (Fig. 3.10a) and global annual NEP by 0.49 Pg C and GPP by 2.18 Pg C (1.8 %; Fig. 3.12a). For intensive aerosol emission episodes, such as fires and volcanic eruptions, net reductions in GPP and yield have been demonstrated in previous studies (Yue & Unger, 2018; Proctor et al., 2018). Here we find that for the sum of all aerosols (natural plus anthropogenic), the fertilization effect is stronger than the dimming effect, resulting in a net increase in GPP, which suggests that most ecosystems are light-saturated, although the change is less than half the total change seen in Chen & Zhuang (2014).

In the case of λE, the fertilization effect is much weaker than the dimming effect, resulting in a net reduction in λE (Fig. 3.10). For transpiration, only the shaded canopy shows a positive fertilization effect. That the percentage increase in GPP is higher than the percentage reduction in λE supports the conclusion that diffuse radiation enhances ecosystem water use efficiency (Knohl & Baldocchi, 2008; Kanniah et al., 2012). Dimming dominates the evaporative response to aerosols, contributing 84% to the global EF increase, with the remaining increase (16%) coming from the fertilization effect. Consequently, 84% and 16% of the cooling due to EF change of the terrestrial surface (81% and 19% for tropical areas) are attributed to the dimming and the fertilization effect, respec-

tively (Fig. 3.17). It would not be feasible to obtain the diagnostic insights, such as shown in Fig. 3.20b, using only a fully-coupled simulation because of the interactive nature of different biophysical processes. For example, by perturbing $K_\downarrow$ in the coupled simulation, the evaporative fraction EF will also change, and we would not know whether the surface temperature change is caused by the change in $K_\downarrow$ or by the change in EF.

3.5 Discussion

The results of our global scale modeling are broadly consistent with those reported in ecosystem (Knohl & Baldocchi, 2008) and regional scale studies (Matsui et al., 2008; Davin & Seneviratne, 2012). The stronger effect of diffuse radiation on canopy photosynthesis for higher LAI values (which we see for EF in Fig. 3.15a) was seen using multi-layer model simulations at a deciduous temperate forest (Knohl & Baldocchi, 2008). Matsui et al. (2008) found that H is reduced more than λE by aerosol pollution over eastern United States (ΔH = -8.36 W m^{-2} or -11.3%; $\Delta \lambda E$ = -3.12 W m^{-2} or -2.1%) during summer. Using the same model domain and season, we find similar patterns (ΔH = -4.21 W m^{-2} or -7.5 % and $\Delta \lambda E$ = -0.63 W m^{-2} or -0.8%), though the magnitude of change is lower in our study, which could be due to both the different land-surface model used and the lower value of direct shortwave radiative effect (-16 W m^{-2} in Matsui et al. (2008) versus -6.4 W m^{-2} in present study). Davin and Seneviratne (2012) found that a higher and more realistic diffuse fraction k_d improves the prediction of summertime T_s over Europe than a fixed k_d of 0.30.

Our results highlight the importance of differentiating between total radiative forcing and diffuse radiative forcing at the surface and vegetation responses to these forcings. Currently, $K_{\downarrow,d}$ remains a relatively understudied component of the radiative budget (Halthore & Schwartz, 2000). Although atmospheric reanalysis modeling systems,

such as NCEP/NCAR (Kalnay et al., 1996), MERRA-2 (Gelaro et al., 2017), and ERA5 (Hersbach et al., 2020), have gridded $K_{\downarrow,d}$ values, they have not been rigorously evaluated against field observations, which remain scarce. In the Radiative Forcing Model Intercomparison Project, the primary focus is on the quantity of the radiative forcing compared to the pre-industrial baseline, with a tertiary focus on the aerosol radiative forcing (Pincus et al., 2016). Given the importance of the quality of the radiative forcing demonstrated in the present study, we recommend a coordinated effort to compare $K_{\downarrow,d}$ among the models taking part in CMIP6, which would also constrain climate sensitivity to other climate forcers that change $K_{\downarrow,d}$, like clouds (Wang et al., 2008). Note that to ensure realistic representation of aerosol impact on $K_{\downarrow,d}$, it is important to compare absorbing versus scattering aerosols as prescribed in or simulated by different models. Even identical AOD values can lead to different $K_{\downarrow,d}$. The presence of primarily absorbing aerosols would reduce both $K_{\downarrow,d}$ and $K_{\downarrow,b}$, while primarily scattering aerosols would reduce $K_{\downarrow,b}$ but enhance $K_{\downarrow,d}$ through forward scattering (Gadhavi & Jayaraman, 2010). The present study gives an evaluation of the CAM6-simulated diffuse radiation at the global scale. Although the model has reproduced the observed spatial variations in $K_{\downarrow,d}$ reasonably well on the global scale and also regionally ($r^2 = 0.92$ to 0.98; Fig. 3.3), its diffuse fraction k_d is biased low due to a high bias in $K_{\downarrow}$ (Fig. 3.4) and a low bias in $K_{\downarrow,d}$ (Fig. 3.3). For the 224 model grids that contain GEBA observations for both $K_{\downarrow}$ and $K_{\downarrow,d}$, the modelled k_d is biased low by an average amount of 0.08. In contrast, Mercado et al. (2009) evaluated their modeled k_d using a subset of GEBA observations in Europe, Germany, and China, demonstrating a positive bias in their simulated values for Europe and Germany and comparable values for China. The global land mean k_d (0.34, Run P) is lower than the value of k_d for photosynthetically active radiation of 0.41 reported by Ryu et al. (2018). For reference, the global mean k_d is 0.27 for Run C. If we assume that the model error in k_d is 0.07 and that this error only affects Run P, correcting the model bias would change the diffuse ra-

diation fertilization effect on ΔT from -0.007 K in Fig. 3.17a to -0.014 K, which is still much smaller in magnitude than the global dimming effect (-0.040 K). In other words, the conclusion that the dimming effect dominates the fertilization effect still holds despite the bias error. Furthermore, most of the error will probably cancel out in the perturbation signal (difference between Run P and C) because k_d in Run C is likely biased by a similar amount as both runs incorporate clouds.
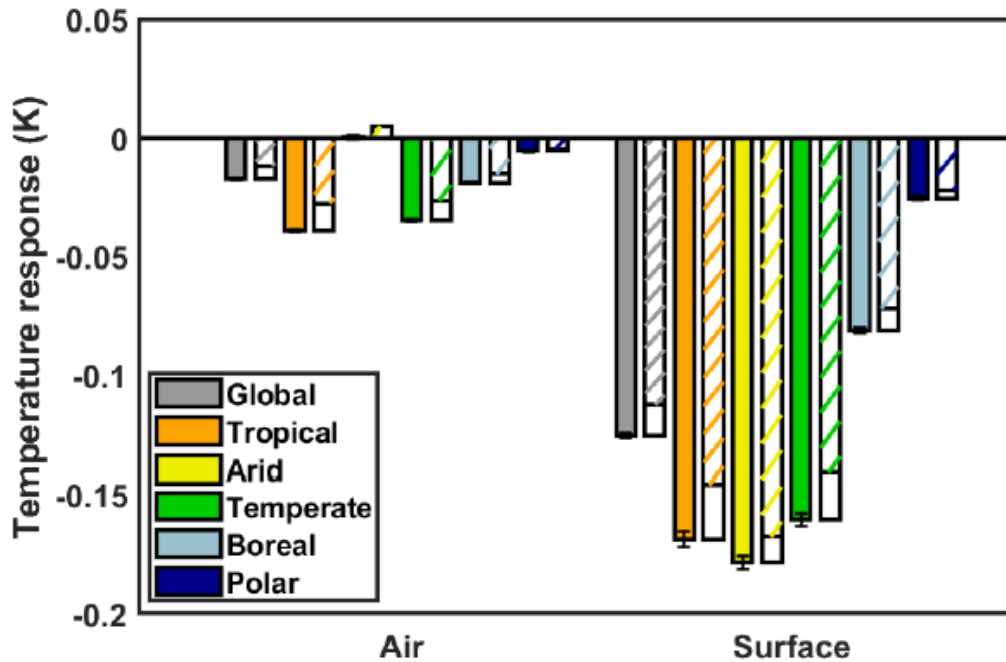
Figure 3.21: Surface and air temperature response to aerosols for all land surfaces and each climate zone. The filled bars represent the net changes. These changes are further decomposed into contributions from the diffuse radiation fertilization effect (blank bar) and the dimming effect (hatched bar). The error bars represent the grid area-weighted standard errors.

On the land-modeling side, there are three broad leaf-to-canopy upscaling schemes (one-big-leaf, two-big-leaf, and multi-layer; Luo et al., 2018). The one-big-leaf models ignore shaded leaves and are thus unable to simulate the diffuse radiation fertilization effect (Lian et al., 2018). On the other hand, CLM uses a two-big-leaf approach for photosynthesis and transpiration, where the carbon and water cycle are separately calculated

for sunlit and shaded parts of the canopy, with sunlit leaves receiving both beam radiation and diffuse radiation and shaded leaves receiving only diffuse radiation, and the LAI dependence captured through the fractional change of shaded versus sunlit leaves (Oliveira et al., 2011; Bonan et al., 2011; Kennedy et al., 2019). Of the land surface models (LSMs) taking part in the Land Model Intercomparison Project as part of CMIP6 activities (LU-MIP; Lawrence et al., 2016), at least three still use the one-big-leaf scheme (Table 3.6). Likewise, the land surface modules in regional weather models usually have the simplistic one-big-leaf type representation of the vegetation (Davin & Seneviratne, 2012) or even combined vegetation and ground surface layers (Chakraborty et al., 2019). Thus, regional studies on aerosol impact on the surface energy budget using these models evidently miss this key mechanism (Pere et al., 2011; Li et al, 2017). Improved representation of canopy architecture to resolve the scale mismatch between leaf and canopy leads to more accurate estimation of radiation transfer through the canopy layer and better agreement between simulated and observed GPP in many cases (Bonan et al., 2012). It is important to stress, however, that these evaluations are based on light-response curves and do not explicitly resolve the response of vegetation to $K_{\downarrow,\mathrm{d}}$. Uncertainties still remain as to how well the CLM model simulates the GPP response to $K_{\downarrow,\mathrm{d}}$ (Wozniak et al., 2020). However, our results are not adversely affected by these uncertainties as the cooling attributed to the diffuse fertilization effect is minor in comparison to the overall Bowen ratio change. Our modeling results regarding the latter are broadly consistent with previous regional (Zhang et al., 2008; Matsui et al., 2008; Davin & Seneviratne, 2012) and global-scale modeling studies on this topic (Table 3.6, Liu et al., 2014), as well as several field-scale observational studies (Gu et al., 2002; Gu et al., 2003; Niyogi et al., 2004; Wang et al., 2008; Kanniah et al., 2012; Wang et al., 2018). On the measurement side, observational constraints on the diffuse radiation fertilization effect are lacking (Steiner et al., 2013). Regions where the magnitude of this signal would be strong, such as heavily polluted tropical areas, have a

dearth of simultaneous measurements of $K_{\downarrow,\mathrm{d}}$ and the surface energy fluxes - an important issue to address in future studies.

Table 3.6: Overview of the land surface models (LSMs) and their parent Earth System models (ESMs) taking part in the Land Model Intercomparison Project (LUMIP), and their canopy representation.

Model		Overview		
ESM	LSM	Canopy representation	Reference	Additional note
CESM2	CLM5.0	Two-big-leaf	Lawrence et al., 2019	Big leaf has one sunlit and one shaded part
CMCC-ESM	CLM4.5	Two-big-leaf	Oleson et al., 2016	Big leaf has one sunlit and one shaded part
CNRM-ESM2	ISBA-CTRIP	Multi-layer	Carrer et al., 2013	10-layer canopy
E3SMv1	ELM (CLM4.5)	Two-big-leaf	Oleson et al., 2016	Big leaf has one sunlit and one shaded part
EC-Earth	LPJ-GUESS	One-big-leaf	Smith et al., 2001	No shaded leaf
GFDL-ESM4	LM4	Multi-layer	Weng et al., 2015	Multi-layer collection of cohort that compete for sunlight
GISS	ModelE	Multi-layer	Spitters et al., 1986	Multi-layer two stream model with direct/diffuse fraction for each layer
MIROC-ES2L	Matsiro/VISIT	One-big-leaf	Takata et al., 2003	No shaded leaf
MPI-ESM1.2-LR	JSBACH3.2	One-big-leaf	Loew et al., 2014	No shaded leaf
NorESM	CLM5.0	Two-big-leaf	Lawrence et al., 2019	Big leaf has one sunlit and one shaded part
UKESM1-0-LL	JULES-ES-1.0	Multi-layer	Clark et al., 2011	Diffuse radiation is fixed as 0.4 of total downwelling in standard configuration; 10-layer canopy

The main limitation of the present study is that the atmosphere is prescribed rather than interactive. In the real world, increases in EF would also lead to local feedback on grid-level forcing variables such as air temperature and humidity and to regional and global feedback via changes in cloud cover and potential changes in aerosol circulation. According to our CLM runs, the local screen-height air temperature is, expectedly, also reduced by aerosols, though the magnitude of decrease is only 0.02 K (global land mean);

much smaller than the reduction in surface temperature (mean reduction of 0.13 K; Fig. 3.21). This stronger sensitivity of surface temperature is similar to the local cooling effect of reforestation (Novick & Katul, 2020). In an idealized numerical experiment in which the surface λE is increased by 1 W m^{-2} and H decreased by 1 W m^{-2} uniformly across the land and the ocean surface (equivalent to an increase of EF by 0.014), the global surface temperature is reduced by 0.54 K due to increases in cloudiness (Ban-Weiss, et al., 2011). In other words, the non-radiative pathway of aerosols (via EF increase) could lead to additional cooling via a cloud feedback, although the feedback strength may have been overestimated by this idealized experiment because the 1 W m^{-2} addition is applied to λE at all times (in day and night and in growing and non-growing season) and over both the land and the ocean surfaces.

With aerosol emissions expected to decrease in future climate scenarios (Westervelt et al., 2015), better constraining aerosol-biosphere-climate interactions will help us isolate regions vulnerable to future warming. In the context of this study, at the local scale, some of the future warming will result from the decrease in the aerosol surface radiative effect and from the decrease in EF due to global brightening. Based on our results, for the highly populated and highly polluted regions of northern India and eastern China, where roughly half of the AOD is from anthropogenic sources (Chakraborty & Lee, 2019), the radiative and non-radiative pathways can lead to an additional annual mean warming of 0.3 K to 0.4 K if all anthropogenic aerosols are removed (Fig. 3.18f). In contrast, the geoengineering scenario of injecting aerosols to the stratosphere to offset greenhouse gas warming will change the surface energy budget and temperature in the opposite direction to pollution abatement. One analog for such a scenario is the eruption of Mount Pinatubo in 1991 (Proctor et al., 2018). According to the MERRA-2 reanalysis, this volcanic eruption reduced the global $K_{\downarrow}$ by about 3.05 W m^{-2} and increased $K_{\downarrow,\mathrm{d}}$ by 3.74 W m^{-2} (year 1992's annual mean minus the mean of 1988 to 1990), or about one-third of the aerosol

surface radiative forcing shown in Fig. 3.7. A similar amount of $K_{\downarrow,d}$ increase is reported from a global model simulation of stratospheric sulfate geoengineering (3.20 W m^{-2}; Xia et al., 2016). These results suggest that aerosols from geoengineering will have a modest non-radiative effect on local temperature.

3.6 Conclusions

We develop a modeling framework for understanding terrestrial aerosol-climate interactions from the surface energy budget perspective. In this framework, aerosols reduce the incoming shortwave radiation four times as much as they increase the incoming longwave radiation, with an overall reduction in the incoming radiation energy of 6.60 W m^{-2} over the global terrestrial surface. Our modeling results demonstrate that the reduction in the incoming radiation is mainly compensated by a reduction in the surface sensible heat flux (ΔH = -3.59 W m^{-2}) and to a lesser extent by a reduction in the surface evaporation ($\Delta \lambda E$ = -0.51 W m^{-2}), leading to an increase in the terrestrial evaporation fraction EF by 0.023. The main mechanism for the EF increase is change in energy allocation due to global dimming (reduction in incoming solar radiation) and augmented by a diffuse radiation fertilization effect or enhanced transpiration from the shaded plant canopy due to the increase of diffuse radiation. We then partition the surface temperature response into contributions from the radiative pathway (reduction in incoming radiation energy) and from the non-radiative pathway (increase in EF). A surprising result is that for grids with LAI $>$ 2, the non-radiative pathway dominates the local temperature response over the radiative pathway. The diffuse radiation fertilization effect alone has a small effect on the terrestrial surface energy budget, increasing evaporation by 0.18 W m^{-2} or 0.48% of total terrestrial evaporation. This contrasts sharply with the terrestrial carbon budget response, with the diffuse radiation fertilization increasing GPP by a much larger amount of 2.18 Pg C y^{-1}

or 1.8% of the total GPP. Given the model-dependent nature of the magnitude of some of these results, we discuss the importance of comprehensive future land model evaluations focused on the diffuse radiation fertilization effect.

Chapter 4

Comparing Diffuse Solar Radiation in Current-Generation Reanalysis and Satellite-Derived Products

4.1 Abstract

Though the partitioning of shortwave radiation ($K_\downarrow$) at the surface into its diffuse ($K_{\downarrow,\mathrm{d}}$) and direct beam ($K_{\downarrow,\mathrm{b}}$) components is relevant for, among other things, the terrestrial energy and carbon budgets, there is a dearth of large-scale comparisons of this partitioning across reanalysis and satellite-derived products. Here we evaluate $K_\downarrow$, $K_{\downarrow,\mathrm{d}}$, and $K_{\downarrow,\mathrm{b}}$, as well as the diffuse fraction (k_d) of solar radiation in four current-generation reanalysis (NOAA-CIRES-DOE, NCEP/NCAR, MERRA-2, ERA5) datasets and one satellite-derived product (CERES) using $\approx$1400 site years of observations. Although the systematic positive biases in $K_\downarrow$ is consistent with previous studies, the biases in gridded $K_{\downarrow,\mathrm{d}}$ and $K_{\downarrow,\mathrm{b}}$ vary in direction and magnitude, both annually and across seasons. The inter-model variability in cloud cover strongly explains the biases in both $K_{\downarrow,\mathrm{d}}$ and $K_{\downarrow,\mathrm{b}}$. Over Europe and China, the long-term (10-year plus) trends in $K_{\downarrow,\mathrm{d}}$ in the gridded products are noticeably differ from corresponding observations and the grid-averaged 35-year trends show an order of magnitude variability. In the MERRA-2 reanalysis, which includes both clouds and assimilated aerosols, the reduction in both clouds and aerosols reinforce each other to establish brightening trends over Europe, while the effect of increasing aerosols overwhelm the effect of decreasing cloud cover over China. The inter-model variability in k_d seen here (0.27 to 0.50 from CERES to MERRA-2) suggests substantial differences in shortwave parameterization schemes and their inputs in climate models and can contribute to inter-model variability in coupled simulations. Based on these results, we call for systematic evaluations of $K_{\downarrow,\mathrm{d}}$ and $K_{\downarrow,\mathrm{b}}$ in CMIP6 models.

4.2 Introduction

Solar radiation is a key driver of the Earth's climate system. During its transmission through the atmosphere, it is scattered and absorbed by aerosols, clouds, and gases. Solar radiation incident on the surface ($K_\downarrow$) consists of beam radiation ($K_{\downarrow,b}$) and diffuse radiation ($K_{\downarrow,d}$). The former follows the original path of the sunlight and the latter is the scattered component that deviates from that path. These components are not routinely measured at weather stations (Stephens et al., 2012). Instead, climatic and ecological studies and solar energy applications generally rely on gridded estimates from atmospheric models, including reanalysis products and global climate models (GCMs). Owing to computational limitations, these models are run at relatively coarse resolutions (50 km to over 200 km). This leads to simplified versions of radiative transfer codes being implemented in these models, as well as differences in input parameters like clouds and aerosols to those codes, both of which influence the estimated radiation fields (Oreopoulos et al., 2012). Systematic biases exist in these model estimates. It is well-known that $K_\downarrow$ is overestimated by most atmospheric models due in large part to the underestimation of cloud cover (Markovic et al., 2009; Bosilovich et al., 2011; Kennedy et al., 2011; Zhao et al., 2013; Wild et al., 2015b; Zhang et al., 2016). This overestimation will lead to surface warming (Chakraborty & Lee 2019) and also increase the energy returned to the atmosphere through heat and moisture fluxes, which may artificially strengthen the hydrological cycle (Wild et al., 1998).

$K_{\downarrow,d}$ remains a relatively understudied component of the Earth's radiation budget. Several studies have demonstrated enhanced carbon uptake and evaporative fraction at various scales with increasing $K_{\downarrow,d}$ (Knohl and Baldocchi 2008; Mercado et al., 2009; Yue and Unger 2017; Rap et al., 2018; Chakraborty et al., 2021). Thus, a better constraint on $K_{\downarrow,d}$ can improve our ability to predict the surface energy, water and carbon budgets. Accu-

rate estimates of the direct/diffuse partitioning of $K_\downarrow$ are also important for solar energy applications, particularly concentrating solar power (Lee et al., 2016).

This study is concerned with biases in surface $K_{\downarrow,d}$ in retrospective analysis or reanalysis datasets, which assimilate observations of some variables to constrain other modeled variables (Kalnay et al., 1996). These observationally constrained datasets represent our best estimates of the current and historical global climate system. Although site-level comparisons of radiation transfer codes that also consider $K_{\downarrow,d}$ have been performed in the past (Oreopoulos et al., 2012), how accurately reanalysis models simulate $K_{\downarrow,d}$ remains largely unknown at the global scale. To our best knowledge, only a couple of regional scale evaluations of $K_{\downarrow,d}$ from reanalysis data are available, both for the ERA5 reanalysis (Jiang et al., 2019b, 2020). The second activity of an ongoing inter-model comparative project called Radiative Forcing Intercomparison Project (RFMIP) requests modeling centers to provide broadband fluxes based on their radiative transfer codes, but does not explicitly require the partitioning of $K_\downarrow$ into $K_{\downarrow,d}$ and $K_{\downarrow,b}$ (Pincus et al., 2016).

The lessons learned about model biases in $K_\downarrow$ are not necessarily applicable to $K_{\downarrow,d}$. $K_{\downarrow,b}$ incident on the surface is controlled by the total extinction of a light beam as it transmits through the atmosphere, while $K_{\downarrow,d}$ is a function of the scattered sunlight (Liu and Jordan 1960). Thus, one can hypothetically fix the overestimation of $K_\downarrow$ in modeled products by increasing aerosols or clouds or through statistical bias-correction algorithms (Zhao et al., 2013), but with unknown individual biases in $K_{\downarrow,d}$ and $K_{\downarrow,b}$. Since aerosols and clouds are parameterized differently in different gridded products, including, but not limited to, prescriptions of cloud droplet size distribution, cloud overlap, and aerosol properties, our hypothesis is that the bias in $K_{\downarrow,d}$ and $K_{\downarrow,b}$ are less systematic in direction than that seen for $K_\downarrow$ in previous studies and strongly controlled by the cloud and aerosol inputs (Wild et al., 2015b). To test these hypotheses, the specific objectives of this study are:

1. To perform a systematic evaluation of the monthly $K_{\downarrow,b}$, $K_\downarrow$, and $K_{\downarrow,d}$ in gridded

data products, including five current-generation reanalysis datasets (NOAA-CIRES-OE, NCEP/NCAR, JRA-55, MERRA-2 and ERA5; only $K_\downarrow$ for JRA-55) and one satellite-derived product (CERES)

2. To examine the differences in these variables between the gridded data products benchmarked against observations at the annual and seasonal time scales

3. To evaluate the ability of the gridded products to capture long-term changes in these variables for Europe and China, two regions which have relatively high densities of ground-based observations and have several previous relevant studies to compare the results

4. To discuss potential sources of biases and inter-model variability, particularly due to cloud cover and also atmospheric aerosols, in these datasets

4.3   Methods

4.3.1   Global Reanalysis Products

We used monthly gridded data from five reanalysis products: (1) NOAA-CIRES-DOE – the Twentieth Century Reanalysis version 3 from National Oceanic and Atmospheric Administration (NOAA), Cooperative Institute for Research in Environmental Science (CIRES), and Department of Energy (DOE), (2) NCEP/NCAR – the 50-year Reanalysis from National Centers for Environmental Prediction (NCEP) and National Center for Atmospheric Research (NCAR), (3) JRA-55 – the Japanese 55-year Reanalysis, (4) MERRA-2 – the Modern-Era Retrospective analysis for Research and Applications, version 2, and (5) ERA5 – the Fifth Generation Reanalysis from the European Centre for Medium-Range Weather Forecasts (ECMWF). They represent the latest iteration of the

major global reanalyses for research and applications. Note that although the Climate Forecast System Reanalysis (CFSR; Saha et al., 2010) is newer than the NCEP/NCAR reanalysis, it does not publicly archive $K_{\downarrow,\mathrm{d}}$. Table 4.1 summarizes the important information about the products considered in the study. Short descriptions of the datasets are given below.

NOAA-CIRES-DOE

This reanalysis assimilates surface pressure observations to provide estimates of the historical climate state (Slivinski et al., 2019). In addition to improvements in the assimilation system, the latest version of the reanalysis includes a higher resolution forecast model, more assimilated pressure observations, and better representation of storm intensity. The radiative transfer model for shortwave in this reanalysis interacts with fractional cloud cover, modeled O_3, time varying CO_2, volcanic aerosols, and solar variations (Hou et al., 2002).

NCEP/NCAR

This reanalysis assimilates data from a wide variety of weather observation including pressure measurements over land, pressure, temperature, and specific humidity measurements over oceans, radiosonde profiles, temperature and wind data observed from aircraft, and satellite-derived cloud-tracked wind data (Kistler et al., 2001). The shortwave parameterization in this reanalysis is based on the work by Lacis and Hansen (1974).

JRA-55

The JRA-55 reanalysis version improves upon the previous JRA-25 product with an updated assimilation system, more ingested observations, a newer longwave radiation scheme, and higher resolution forecasts (Kobayashi et al., 2015). The shortwave radiation is param-

eterized considering random overlap of clouds, H2O absorption based on Briegleb et al. (1992), O_2, O_3, and CO_2 absorption based on Freidenreich & Ramaswamy (1999), and assuming standard atmospheric aerosol profiles with optical depths adjusted using monthly aerosol climatology. It only archives gridded data for $K_\downarrow$.

MERRA-2

The MERRA-2 reanalysis is a recent global reanalysis product that assimilates bias-corrected satellite observations of aerosols and clear-sky irradiances (Randles et al., 2017). It also uses observed precipitation to force the land-surface model. The shortwave radiation scheme is based on Chou and Suarez (1999) and the latest version of the Goddard Earth Observing System (GEOS-5) assimilates newer satellite observations. The total aerosol optical depth (AOD) in MERRA-2 has been evaluated against independent observations (Buchard et al., 2017).

ERA5

The ERA5 reanalysis uses the recently developed Integrated Forecasting System to improve upon its predecessor (Hersbach et al., 2020). In addition to the finer horizontal model resolution, ERA5 has consistent hourly outputs, improvements in the dynamical core, and a four-dimensional variational data assimilation system (like JRA-55). Standardized sets of long-term forcing for aerosols, greenhouse gases, and O_3 are taken from the World Climate Research Programme (WCRP) and the McRad scheme is used to parameterize radiation (Morcrette et al., 2008).

4.3.2 Satellite-Derived Estimates

In addition to the reanalysis products, we used the satellite-derived monthly gridded $K_\downarrow$ and $K_{\downarrow,\mathrm{d}}$ data in the latest version of the Clouds and the Earth's Radiant Energy System

(CERES) synoptic product, (CERES SYN1deg Ed4.1; Rutan et al., 2015). The dataset is well-constrained by observations due to direct measurements of the top of the atmosphere components and the use of aerosol and cloud observations from satellites, including those carrying the Moderate Resolution Imaging Spectroradiometer (MODIS), in the radiative transfer code.

Table 4.1: Summary of the global gridded products considered in the present study. The global means and interannual standard deviations of the variables of interest for Common Period I (2001-2015) are also noted.

Data product	Spatial resolution	Temporal coverage	Reference	Global $K_\downarrow$ (W m^{-2})	Global $K_{\downarrow,d}$ (W m^{-2})	Global $K_{\downarrow,b}$ (W m^{-2})	Global k_d (unitless)
NOAA-CIRES-DOE	1° × 1°	1836 - 2015	Slivinski et al. (2019)	192.9 ± 0.4	92.2 ± 0.2	100.7 ± 0.5	0.478 ± 0.002
NCEP/NCAR	1.85° × 1.85°	1948 - Present	Kistler et al. (2001)	205.3 ± 0.6	81 ± 0.3	124.3 ± 0.6	0.394 ± 0.002
JRA-55	0.562° × 0.562°	1958 - Present	Kobayashi et al. (2015)	189 ± 0.8	NA	NA	NA
MERRA-2	0.5° × 0.625°	1980 - Present	Randles et al. (2017)	185.6 ± 0.7	52.8 ± 0.4	132.8 ± 1	0.284 ± 0.003
ERA5	0.25° × 0.25°	1979 - Present	Hersbach et al. (2020)	187.9 ± 0.4	63.7 ± 0.1	124.2 ± 0.4	0.339 ± 0.001
CERES	1° × 1°	2000 - 2019	Rutan et al. (2015)	185.4 ± 0.3	102.6 ± 0.7	82.8 ± 0	0.553 ± 0.004

4.3.3   Ground-Based Point Observations

The Global Energy Balance Archive (GEBA) is a repository of energy flux measurements at the Earth's surface (Gilgen & Ohmura 1999) and is the most comprehensive global database of observed mean monthly surface radiation components currently available. Here we used the latest iteration of the database (Wild et al., 2017) after removing sites with missing data and applying the following quality control steps:

1. We considered only the observations not flagged as erroneous by the database's quality control procedure (thus, data with flags 5, 6, 7, and 8 were used)

2. Observations for which the monthly means were 0 W m^{-2} were not considered since they are primarily due to either instrument errors or during polar nights.

3. We removed observations if the diffuse fraction, $k_\mathrm{d} = K_{\downarrow,\mathrm{d}}/K_\downarrow$, exceeded one or was 0.

4. Although there are many more stations with $K_\downarrow$ measurements than $K_{\downarrow,\mathrm{d}}$ measurements, to keep the number of sites consistent, we only considered those with simultaneous observations of $K_\downarrow$ and $K_{\downarrow,\mathrm{d}}$ in most cases (except for examining long-term trends; see next subsection).

After data screening, we obtained 221 stations (distribution of stations shown in Fig. 4.1) with a total of 16589 site-months of data between 1980 and 2015. Only a few GEBA sites have direct measurements of $K_{\downarrow,\mathrm{b}}$. For evaluating modeled $K_{\downarrow,\mathrm{b}}$, the observed $K_{\downarrow,\mathrm{b}}$ was computed as the difference between $K_\downarrow$ and $K_{\downarrow,\mathrm{d}}$.
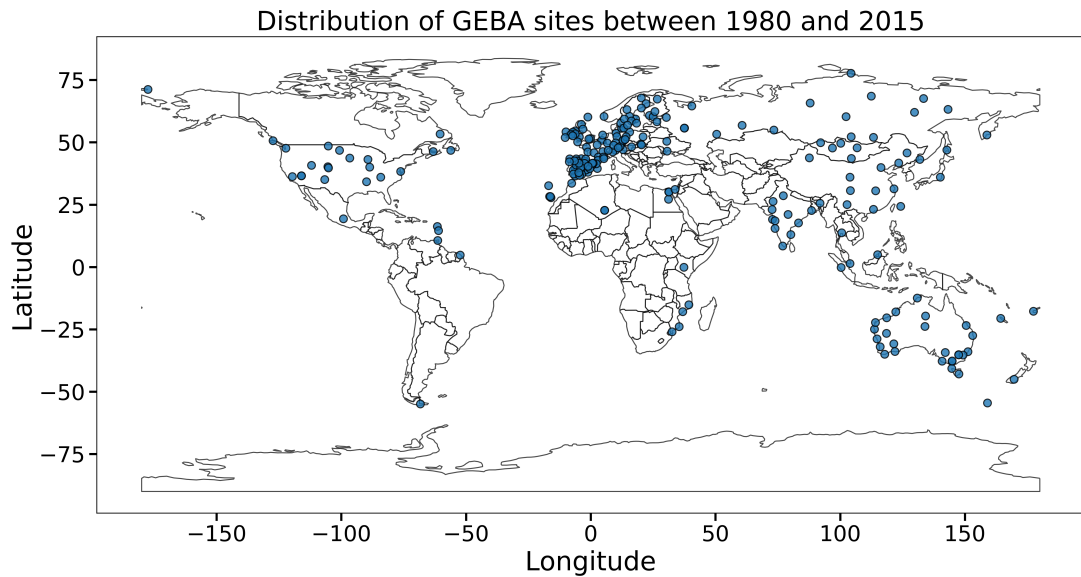
Figure 4.1: Geographic distribution of all the GEBA sites used in this study. The sites used for Common Period I (2001-2015) are shown in Fig. 4.5

4.3.4 Data Processing and Metrices for Evaluation

We extracted monthly $K_{\downarrow,d}$, $K_{\downarrow,b}$, and $K_{\downarrow}$ from the gridded datasets from the start of 1980 to the end of 2019. Only $K_{\downarrow}$ was extracted for JRA-55 since it does not publicly archive $K_{\downarrow,d}$ or $K_{\downarrow,b}$. For the overall evaluation against GEBA, all the grids overlapping the observational sites and months between 2001 to 2015 were used. This period is common to all the six datasets and is referred to as Common Period I. For cases where multiple sites were within one grid box, the same grid value was compared against each of those observations. For NCEP/NCAR, the lowest resolution dataset, roughly 12% of the sites share a common grid with another site, while only 2% of sites share a common grid when using the highest resolution dataset (ERA5). Four metrics were used to evaluate the modeled data, including coefficient of determination (r^2), root mean square error (RMSE), mean bias error (MBE), and mean percentage error (MPE).

To examine inter-model variability at annual and seasonal scales, we chose Common Period I and used the CERES data as reference. To avoid mixing the seasonality of the two hemispheres, we only used sites and grids in the northern hemisphere when examining seasonality. Although point-based observations of surface radiation fields are not always comparable to gridded estimates due to how models represent clouds, at the monthly scale, these uncertainties are reduced (see Limitations subsection).

We restricted our trend analysis to Europe and China between 1980 and 2015. This period, termed here as Common Period II, is longer than the CERES data period but covered by all the five reanalysis products (Table 4.1). These two regions have more sites with continuous data coverage than other regions of the world. We calculated temporal trends for the sites with at least a total of 10 years of data (not necessarily contiguous years). Site-averaged time trends of the gridded model data were based on the same measurement years and the grids containing these GEBA sites. The threshold of 10 years, although somewhat

arbitrary, was used, not to estimate the true 35-year trend but to examine whether the gridded products showed similar trends during the corresponding time-frame. Similar thresholds have been used in other studies that have examined long-term trends in $K_\downarrow$ (Yang et al., 2019; Schwarz et al., 2020). Since few of the sites have both observations of $K_{\downarrow,\mathrm{d}}$ and $K_\downarrow$ that satisfy all the above criteria, we used a different subset of measurements for $K_\downarrow$ and $K_{\downarrow,\mathrm{d}}$ over these regions. This left us with 28 (7) stations over Europe (China) for examining $K_\downarrow$ trends, and 15 (5) sites over Europe (China) for $K_{\downarrow,\mathrm{d}}$ trends. Before using these stations, however, we also tested for change/breakpoints in the time series data using the Standard Normal Homogeneity Test (Alexandersson 1986). Considering only those stations that show no breakpoints at the 95% significance level, we got 24 (4) stations over Europe (China) for $K_\downarrow$ and 8 (4) stations over Europe (China) for $K_{\downarrow,\mathrm{d}}$. We also calculated the grid-averaged modeled trend for the entire period (1980-2015) using all the grids that fall within Europe and China. Before finding the grids intersecting these two regions, the five reanalysis products were re-gridded to $1° \times 1°$ grids, the grid size of CERES, using bilinear interpolation, which is appropriate due to the spatial continuity in these variables at the annual time scale. This re-gridded data were also used to demonstrate grid-by-grid difference in multi-year average values between the products. In all cases, the trends were based on the annual average value regressed against the year of observation, with the statistical significance of the trends calculated. Finally, we also estimated cloud cover, top of the atmosphere $K_\downarrow$ and AOD (from MERRA-2) for Europe, China, and globally to examine the reasons for some of these biases.

4.4 Results

4.4.1 Overall Evaluation and Annual Inter-Comparisons

The global mean $K_\downarrow$ varies from 185.4 W m^{-2} (CERES) to 205.3 W m^{-2} (NCEP/NCAR) for Common Period I (2001-2015), based on all model grids (Table 4.1). In comparison, Wild et al. (2015) found a multi-model mean $K_\downarrow$ of 189.1 W m^{-2} based on 43 CMIP5 models for 2000-2004. For the grid-years that coincide with the GEBA observations, the modeled mean $K_\downarrow$ varies from 165.2 W m^{-2} (CERES) to 208.1 W m^{-2} (NCEP/NCAR), and the observed mean $K_\downarrow$ is 162.5 W m^{-2}. All the reanalysis datasets capture the seasonal (Fig. 4.7) and geographic distributions of the GEBA-observed $K_\downarrow$ relatively well, with the overall r^2 varying from 0.9 for NOAA-CIRES-DOE and NCEP/NCAR to 0.96 for CERES (Table 4.2). As expected, CERES performs better than all the reanalysis products, both in terms of variability ($r^2 = 0.97$) and bias (MBE=2.6 W m^{-2}).

The global mean $K_{\downarrow,\mathrm{b}}$ varies from 82.8 W m^{-2} (CERES) to 132.8 W m^{-2} (MERRA-2) during Common Period I, based on all model grids. The sign of the error in $K_{\downarrow,\mathrm{b}}$ is less consistent across the different products than the error in $K_\downarrow$ (Fig. 4.2). While NCEP/NCAR, MERRA-2, and ERA5 overestimate $K_{\downarrow,\mathrm{b}}$ (MBE = 36.8, 39.9, and 17.4 W m^{-2}, respectively), NOAA-CIRES-DOE and CERES underestimate it (MPE = -4.3 and -16.8 W m^{-2}, respectively; Table 4.2). Among the reanalyses, ERA5 performs the best at capturing the global variability in $K_{\downarrow,\mathrm{b}}$ ($r^2 = 0.9$), and NCEP/NCAR perform the worst ($r^2 \approx 0.73$).

Table 4.2: Evaluations of monthly mean incoming shortwave radiation ($K_\downarrow$), direct beam radiation ($K_{\downarrow,b}$), diffuse radiation ($K_{\downarrow,d}$), and diffuse fraction (k_d) at the surface against the common GEBA observations for Common Period I (2001-2015). Statistical summaries of the evaluations include the intercept and slope of the line of best fit, coefficient of determination (r^2), Mean Bias Error (MBE), and Mean Percentage Error (MPE). The sample size is 14155 in all cases.

	Slope	Intercept	r2	RMSE	MBE	MPE	Slope	Intercept	r2	RMSE	MBE	MPE
	Total shortwave radiation ($K_\downarrow$)						Direct beam radiation ($K_{\downarrow,b}$)					
NOAA-CIRES-DOE	1	8.82	0.9	30.16	9.52	5.9	0.89	6.15	0.75	34.66	-4.28	-4.4
NCEP/NCAR	1.01	43.91	0.9	53.45	45.56	28	0.89	47.59	0.73	51.43	36.79	38.2
JRA-55	0.98	18.25	0.93	26.71	15.27	9.4	NA	NA	NA	NA	NA	NA
MERRA-2	1.03	13.06	0.94	28.22	18.54	11.4	1.08	32.11	0.86	49.44	39.9	41.5
ERA5	0.99	9.72	0.96	18.04	7.51	4.6	0.99	18.15	0.9	27.17	17.38	18.1
CERES	0.98	6.45	0.97	15.72	2.65	1.6	0.8	2.7	0.88	28.32	-16.82	-17.5
	Diffuse radiation ($K_{\downarrow,d}$)						Diffuse fraction (k_d)					
NOAA-CIRES-DOE	0.94	17.68	0.75	21.67	13.8	20.8	0.7	0.21	0.41	0.16	0.08	16.4
NCEP/NCAR	0.73	26.91	0.66	20.01	8.77	13.2	0.41	0.2	0.36	0.14	-0.07	-14.5
MERRA-2	0.61	4.84	0.83	25.84	-21.36	-32.2	0.56	0.03	0.62	0.2	-0.18	-38.4
ERA5	0.7	9.86	0.86	16	-9.87	-14.9	0.72	0.05	0.72	0.11	-0.08	-17.5
CERES	1.28	0.89	0.86	26.61	19.47	29.4	0.76	0.2	0.67	0.13	0.09	19.8

The global mean $K_{\downarrow,d}$ varies from 52.8 W m^{-2} (MERRA-2) to 102.6 W m^{-2} (CERES), and diffuse fraction k_d varies from 0.28 (MERRA-2) to 0.55 (CERES) during Common Period I based on all model grids (Table 4.1). For the grid-years that coincide with the GEBA observations, k_d ranges from 0.28 (MERRA-2) to 0.55 (CERES), and the observed mean k_d for the quality-controlled GEBA dataset is 0.46. NOAA-CIRES-DOE, NCEP/NCAR and CERES have positive biases in $K_{\downarrow,d}$ (MBE = 13.8, 8.77, and 19.5 W m^{-2}, respectively; Table 4.2), and MERRA-2 and ERA5 have negative biases (MBE = -21.4 and -9.9

W m^{-2}, respectively; Table 4.2). Bias errors in k_{d} depends on errors in $K_{\downarrow,\mathrm{d}}$ and $K_{\downarrow}$. For MERRA-2 and ERA5, $K_{\downarrow}$ is positively biased, and $K_{\downarrow,\mathrm{d}}$ is negatively biased (Table 4.2). Consequently, these two reanalyses underestimate k_{d}, with MERRA-2 performing the worst among the datasets, with an MBE of -0.18 for all sites. NCEP/NCAR underestimates k_{d} (MBE = -0.07) because it overestimates $K_{\downarrow}$ more (relatively speaking) than it overestimates $K_{\downarrow,\mathrm{d}}$ (Table 4.2). Even though NCEP/NCAR and NOAA-CIRES-DOE show smaller MBE than MERRA-2, they do not capture the observed variability in k_{d} well (r^2 = 0.36 to 0.41). ERA5 captures the variability in k_{d} the best (r^2 = 0.72), even better than CERES (r^2 = 0.67). CERES overestimates k_{d} (MBE = 0.09) as it underestimates $K_{\downarrow,\mathrm{b}}$ and overestimates $K_{\downarrow,\mathrm{d}}$.
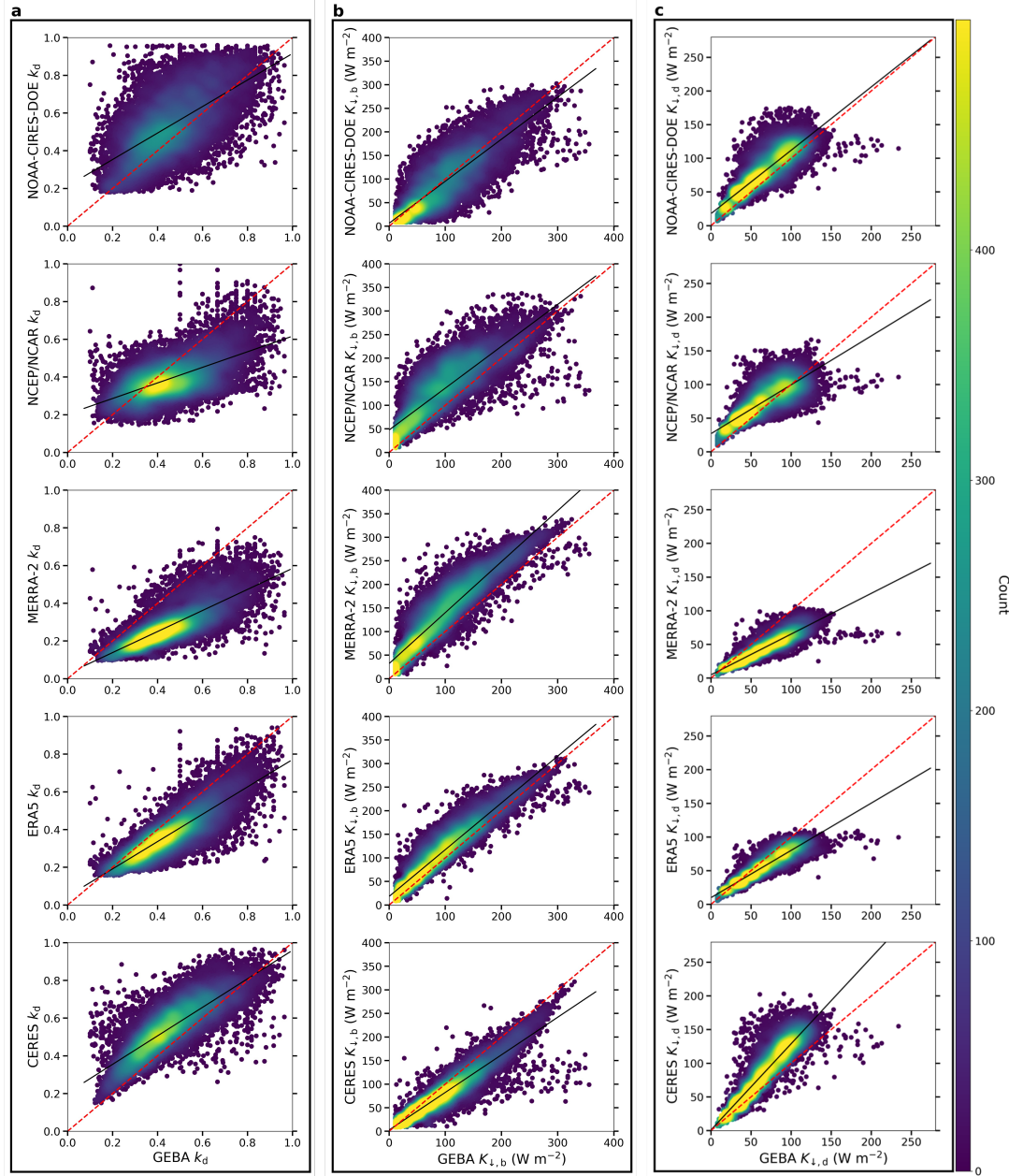
Figure 4.2: Evaluations of monthly mean incoming **a** diffuse fraction (k_d), **b** beam radiation ($K_{\downarrow,b}$), and **c** diffuse radiation ($K_{\downarrow,d}$) at the surface of gridded reanalysis and CERES products against the common GEBA observations for Common Period I (2001-2015). The red dashed lines represent the 1:1 relationship. Color indicates data density. Statistical summaries of the evaluations are in Table 4.2.

Figure 4.2 shows the scatter plots between gridded and observed k_d, $K_{\downarrow,d}$, and $K_{\downarrow,b}$ for all common GEBA site-months, with each data point representing a monthly mean and

the color representing the density of data. Fig. 4.3 shows the scatter plots for total $K_\downarrow$. The scatter is a result of both natural (seasonal and geographic) variations and measurement and model errors. As discussed earlier, the gridded data show larger variability than observations, and the biases in gridded $K_{\downarrow,d}$ and $K_{\downarrow,b}$ across products is less systematic in sign than the consistent overestimation seen for $K_\downarrow$ (Fig. 4.1 and Table 4.1). This lack of consistency is evident in the scatter plot. For instance, although the line of best fit for the gridded $K_{\downarrow,b}$ data is ERA5 is almost identical to the 1:1 line, the slope is only 0.7 for $K_{\downarrow,d}$ since the intercept. For CERES, the line of best fit is less than the 1:1 line for $K_{\downarrow,b}$, but is greater than 1:1 for $K_{\downarrow,d}$, demonstrating the underestimation of $K_{\downarrow,b}$ and overestimation of $K_{\downarrow,d}$ by this dataset with an intercept close to zero. In general, more scatter is seen for NOAA-CIRES-DOE and NCEP/NCAR data and the least for ERA5 and CERES. For NOAA-CIRES-DOE, the large scatter for k_d suggests that the dataset cannot adequately capture the spatiotemporal distribution of this variable.

4.4.2   Site-level Evaluation and Spatial Patterns

Figure 4.4a and 4.4b map the MBE in $K_\downarrow$ at individual GEBA sites for NCEP/NCAR and CERES, respectively, for Common Period I. Similarly, Figs 4.4c and 4.4d display the site-level MBE in NCEP/NCAR and CERES for $K_{\downarrow,d}$. Bias maps for the other data products can be found in Fig. 4.5.
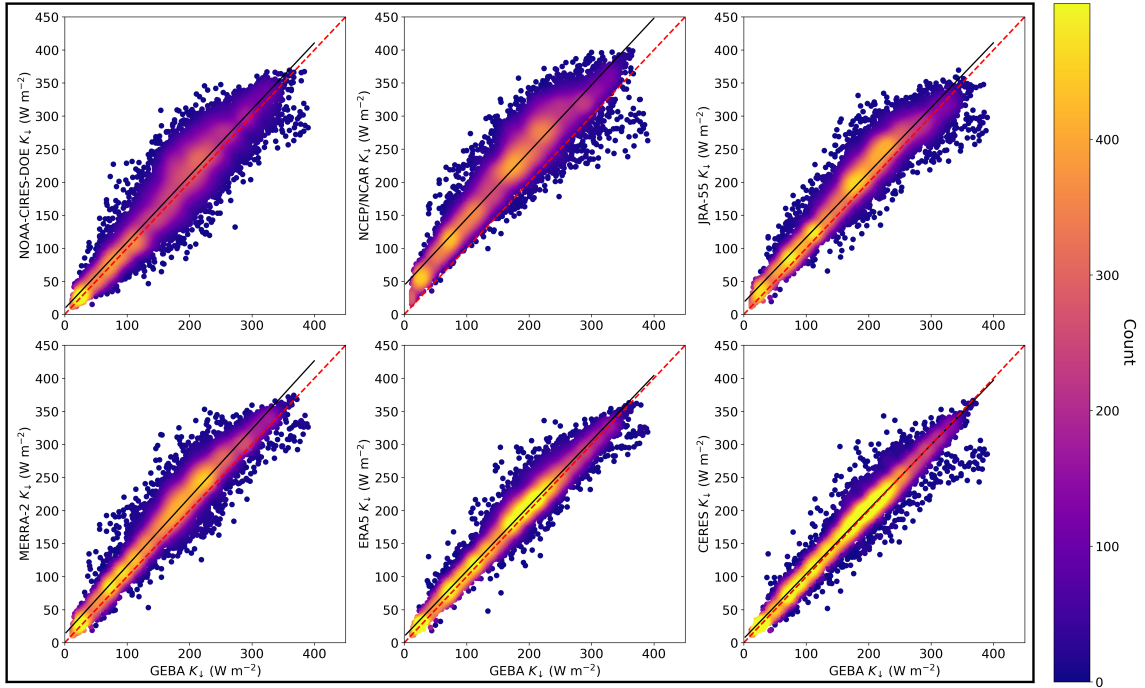
Figure 4.3: Evaluations of monthly mean incoming shortwave radiation ($K_\downarrow$) at the surface of gridded reanalysis and CERES products using all common GEBA observations for Common Period I (2001-2015). The red dashed lines represent the 1:1 relationship. Color indicates data density. Statistical summaries of the evaluations are in Table 4.2 of the main text.
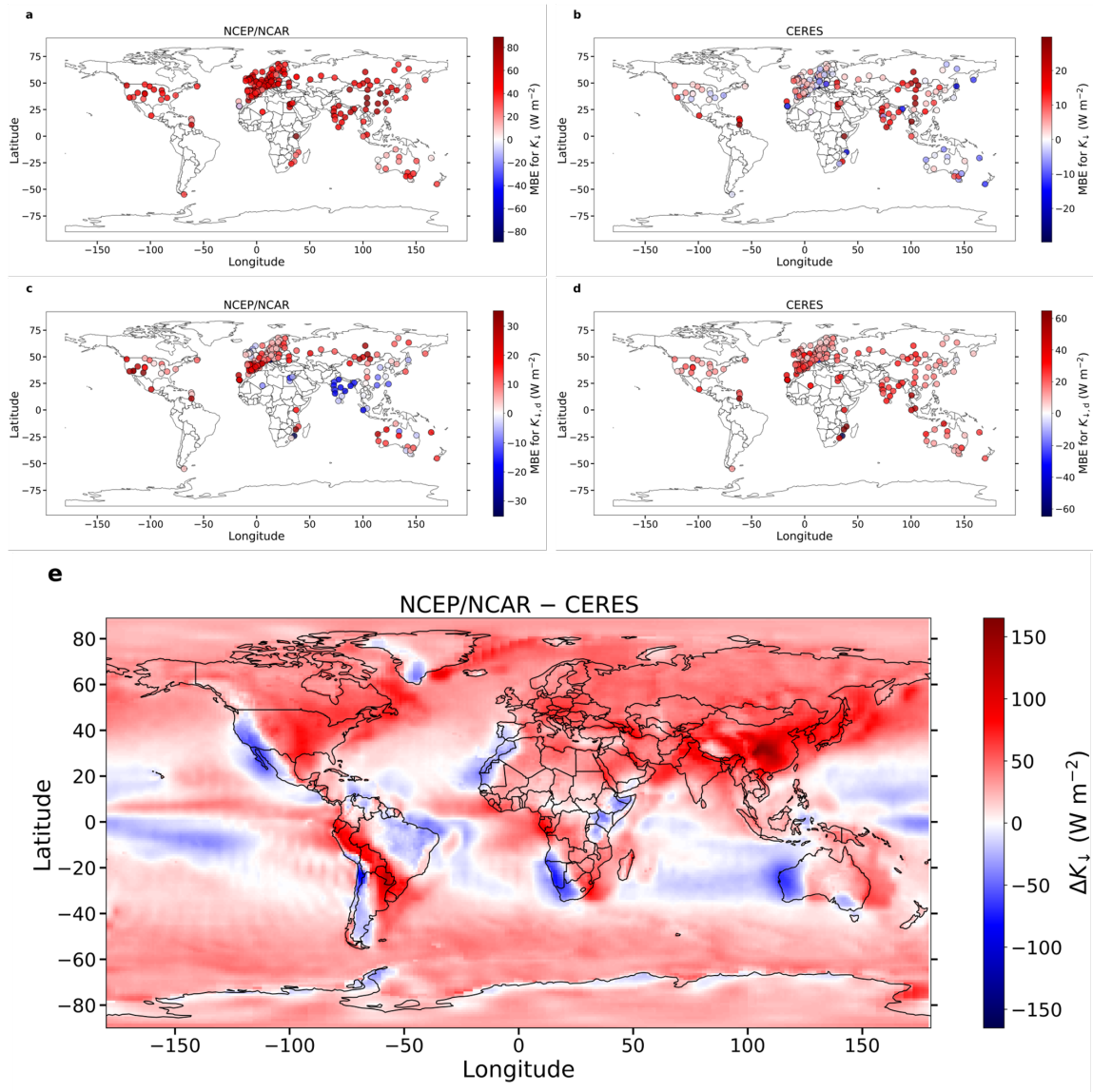
Figure 4.4: Site-level mean bias error (MBE) in incoming shortwave radiation ($K_\downarrow$) at the surface for **a** NCEP/NCAR and **b** CERES data compared to common GEBA observations for Common Period I (2001-2015). Sub-figures **c** and **d** show mean bias error in incoming diffuse radiation ($K_{\downarrow,d}$) at the surface for NCEP/NCAR and CERES, respectively. Finally, sub-figure **e** shows the grid-wise difference in $K_\downarrow$ between NCEP/NCAR and CERES data.
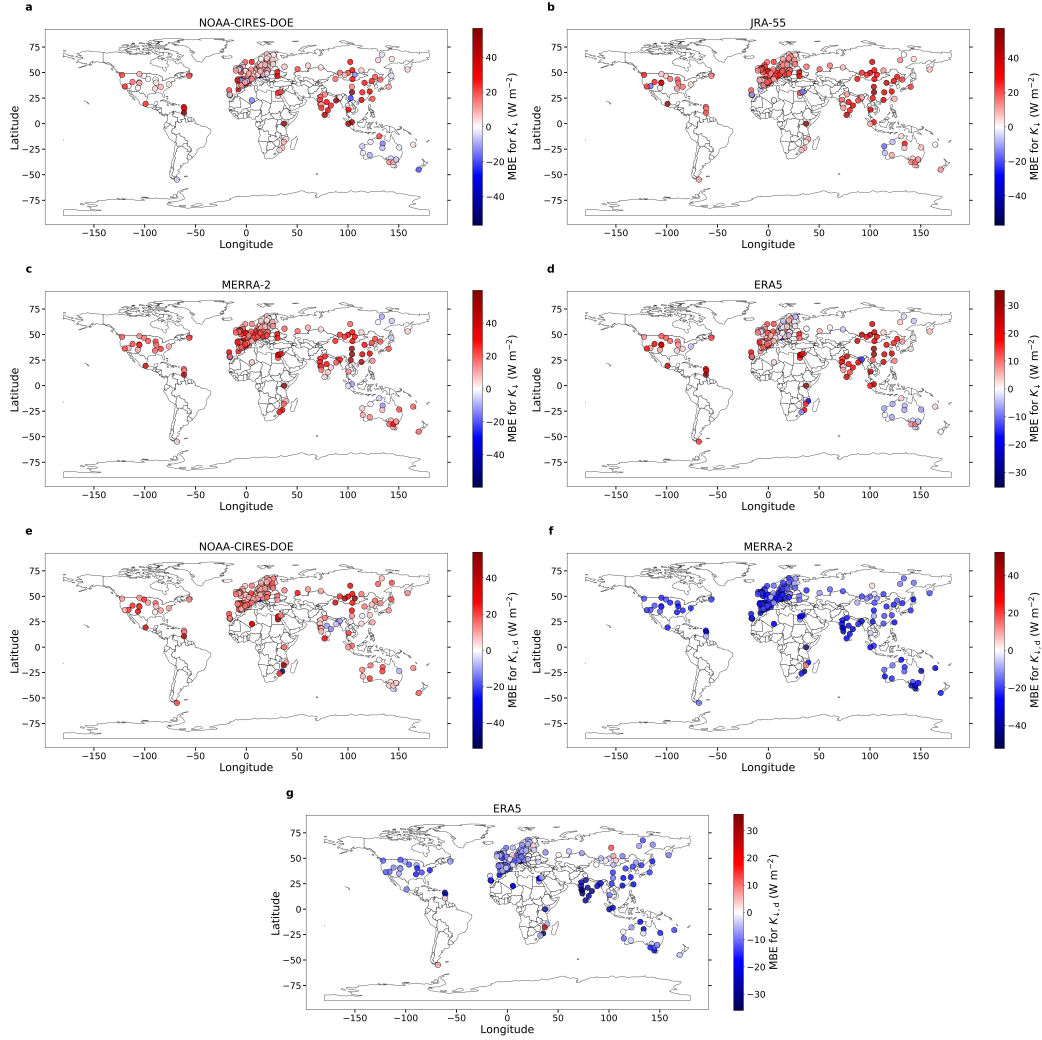
Figure 4.5: Site-level mean bias error (MBE) in incoming shortwave radiation ($K_\downarrow$) at the surface for **a** NOAA-CIRES-DOE, **b** JRA-55, **c** MERRA-2, and **d** ERA5 gridded data compared to common GEBA observations for Common Period I (2001-2015). Sub-figures **e**, **f**, and **g** show the corresponding MBE in incoming diffuse radiation ($K_{\downarrow,\text{b}}$) at the surface for NOAA-CIRES-DOE, MERRA-2, and ERA5, respectively.

The site-level MBE patterns of $K_\downarrow$ and $K_{\downarrow,\text{d}}$ are consistent with the overall evaluation in the previous subsection. The reanalysis products show a positive $K_\downarrow$ bias for the majority of the GEBA sites (80.5% for NOAA-CIRES-DOE, 98.9% for NCEP/NCAR, 90% for JRA-55, 94.7% for MERRA-2, and 78.9% for ERA5). The NCEP/NCAR reanalysis has the highest $K_\downarrow$ MBE among the datasets considered, and ERA5 and CERES have

low biases. MERRA-2 underestimates $K_{\downarrow,d}$ for almost all the sites (99.7%; Fig. 4.1f) and ERA5 underestimates $K_{\downarrow,d}$ for 91.9% of the sites (Fig. 4.5g). NOAA-CIRES-DOE, NCEP/NCAR, and CERES overestimate $K_{\downarrow,d}$ for 93.6%, 76.5%, and 98% of the sites, respectively (Figs 4.5c, 4.5e, and 4.7d).

Since CERES captures both the magnitude and variability of $K_{\downarrow}$ more accurately than the reanalyses (Table 4.2), here we use CERES as the reference to examine anomaly hot spots of the reanalysis products for Common Period I (Figs 4.7c and 4.6). All the reanalysis products show qualitatively similar positive biases from CERES over southern China and along the western coast of South America. NOAA-CIRES-DOE shows some of the largest localized anomalies; positive biases as much as 100 W m^{-2} are evident over eastern China. Overall, the differences are lower over Europe (0.0 ± 1.2 W m^{-2} for ERA5 to 46.6 ± 2.0 W m^{-2} for NCEP/NCAR; mean $\pm$ standard deviation) than over China (12.3 ± 1.4 W m^{-2} for NOAA-CIRES-DOE to 65.6 ± 2.1 W m^{-2} for NCEP/NCAR) for all the reanalysis products, a pattern consistent with site-level evaluations using GEBA observations (Figs 4.4 and 4.5). The closer value between CERES and the reanalyses over Europe could be due to stronger constraints on the energy budget due to more quality-assured assimilated meteorological observations over this region. For reference, the number of common GEBA stations over Europe for Common Period I is 93, while there are only 10 over China; with similar sampling biases expected for assimilated variables. Another potential factor is the influence of higher aerosol loading over China, which is not explicitly represented in most of these datasets.
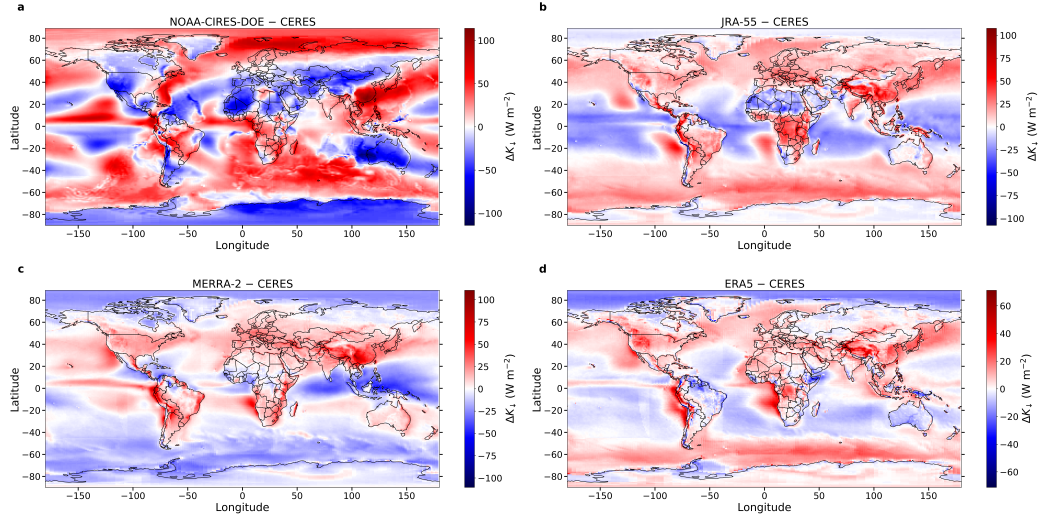
Figure 4.6: Grid-wise difference in incoming shortwave radiation ($K_\downarrow$) at surface between CERES data and **a** NOAA-CIRES, **b** JRA-55, **c** MERRA-2, and **d** ERA5, respectively for Common Period I (2001-2015).

4.4.3 Annual Cycle

Figure 4.7 compares the northern hemisphere seasonal patterns in $K_{\downarrow,d}$, $K_\downarrow$, and k_d among the datasets and the GEBA observations in the northern hemisphere, using the site-months common to the datasets and the GEBA observations for Common Period I. The complete northern hemispheric mean seasonal patterns are given in Figs 4.7b, 4.7d, and 4.7f using all the model grids. The GEBA observations are skewed towards middle to high latitudes; thus Figs 4.7a and 4.7b shows a stronger $K_\downarrow$ and $K_{\downarrow,d}$ seasonality than Figs 4.7b and 4.7d. For instance, the inter-seasonal range of $K_\downarrow$, or the difference between the monthly maximum and monthly minimum $K_\downarrow$ for the average year, is 134.4 W m^{-2} in Fig. 4.7b and 178.8 W m^{-2} in Fig. 4.7a for CERES. The data products generally capture the observed seasonality, showing much higher $K_\downarrow$ and $K_{\downarrow,d}$ values in the summer than in the winter (Figs 4.7a and 4.7c). Among the datasets, the inter-seasonal range in site-corresponding $K_\downarrow$ varies from 178.8 W m^{-2} in CERES and ERA5 (181 W m^{-2} for GEBA) to 207.7 W

m^{-2} in NCEP/NCAR according to Fig. 4.7a.
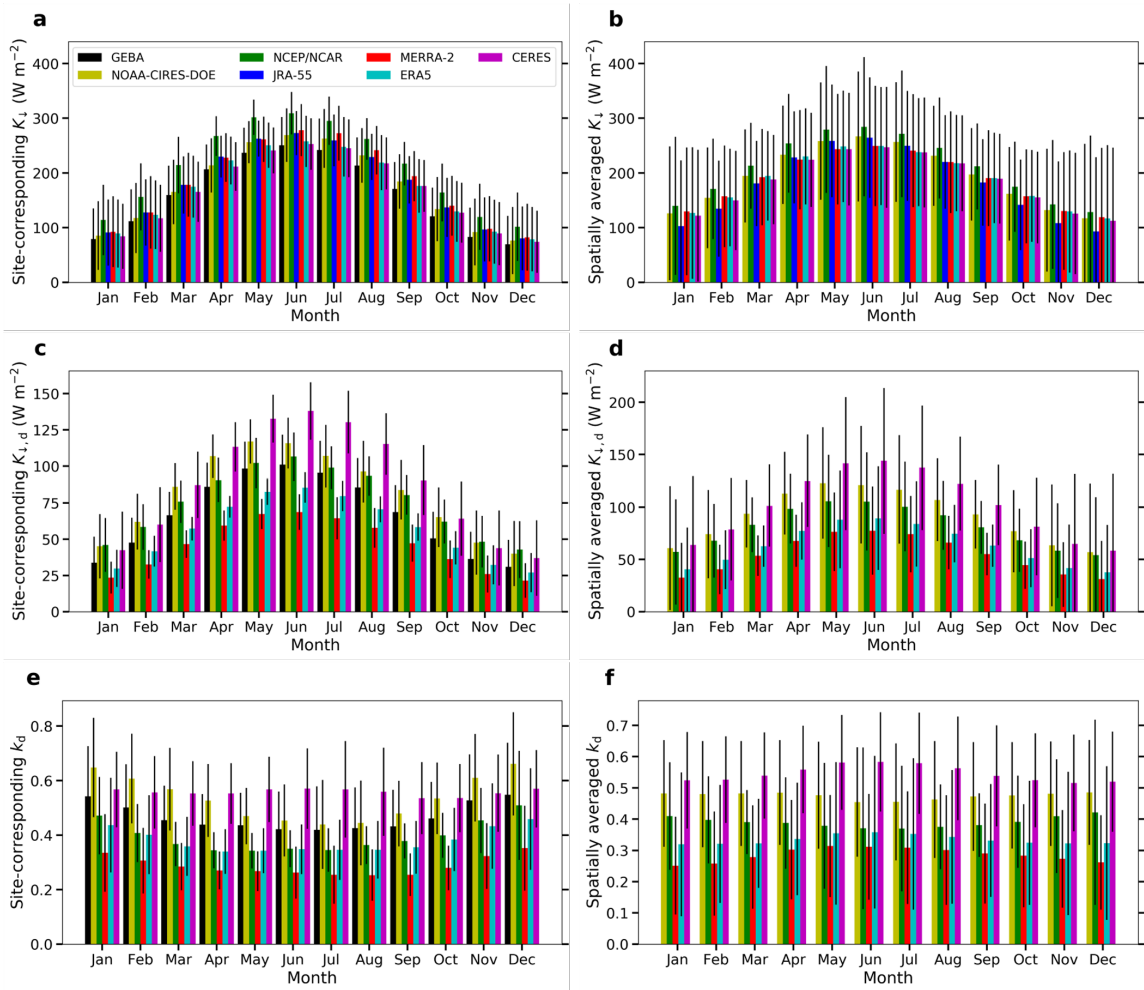
Figure 4.7: Seasonal variation in **a** incoming shortwave radiation ($K_\downarrow$), **c** incoming diffuse radiation ($K_{\downarrow,d}$), and **e** diffuse fraction (k_d) at the surface for all northern Hemisphere common GEBA sites and the grids overlaying the sites for Common Period I (2001-2015). Sub-figures **b**, **d**, and **f** show the corresponding northern hemisphere means from the gridded products for the same period. In all cases, the black lines show the standard deviations (of the site-level data for **a**, **c**, and **e** and the spatial variability of the grid values for **b**, **d**, and **f**).

Generally, there is a larger inconsistency in the $K_{\downarrow,d}$ seasonal variations than the $K_\downarrow$ seasonal variations among the datasets. Particularly, the CERES data shows a more pronounced $K_{\downarrow,d}$ seasonality (inter-seasonal range = 101 W m^{-2}) than the GEBA observations (inter-seasonal range = 70 W m^{-2}) and the other data products (average inter-seasonal

range of 61.6 W m^{-2} for the other products; Fig. 4.7c).

Globally, the observed k_d is higher in winter and lower in the summer (Fig. 4.7e). The inter-seasonal range in k_d varies substantially between the products, with CERES showing the lowest range of 0.03 and NOAA-CIRES-DOE showing the highest range of 0.22 (Fig. 4.7e). In comparison, the inter-seasonal range in the corresponding GEBA observations is 0.13. The muted seasonality in CERES is evidently driven by the stronger seasonality for $K_{\downarrow,\mathrm{d}}$ in this dataset. Combining all the gridded products, for the northern hemisphere, the spatially averaged inter-seasonal range in k_d is only 0.05 (Fig. 4.7f), compared to 0.13 for the grids corresponding to the GEBA observations; evidently due to the higher frequency of GEBA observations in the higher latitudes.

4.4.4 Long-term Trends over Europe and China

We analyze the long-term trends in $K_\downarrow$ and $K_{\downarrow,\mathrm{d}}$ in Europe and China in two ways. First, we calculate the trends using the reanalysis products for Common Period II (1980-2015) and all grid cells in these two regions. The results are presented as solid bars in Fig. 4.8 with the statistical significance of the trends noted. Over Europe, NOAA-CIRES-DOE shows a slightly negative trend and the other four reanalysis products show clearly positive trends in $K_\downarrow$, with the rate of change varying from -0.07 W m^{-2} per decade in NOAA-CIRES-DOE to 2.02 W m^{-2} per decade in ERA5 (Fig. 4.8a). The average trend of the five products is 0.80 ± 0.74 W m^{-2} per decade (mean $\pm$ standard deviation; here standard deviation indicates variation among the five products). The regional mean $K_{\downarrow,\mathrm{d}}$ shows an increasing trend according to NCEP/NCAR and decreasing trends according to the other three products (NOAA-CIRES-DOE, MERRA-2, and ERA5), with the rate of change ranging from 0.39 W m^{-2} per decade in NCEP/NCAR to -1.6 W m^{-2} per decade in MERRA-2 (Fig. 4.8b), with a four-product mean value of -0.86 ± 0.75 W m^{-2} per decade. JRA-55 does not provide $K_{\downarrow,\mathrm{d}}$ data.
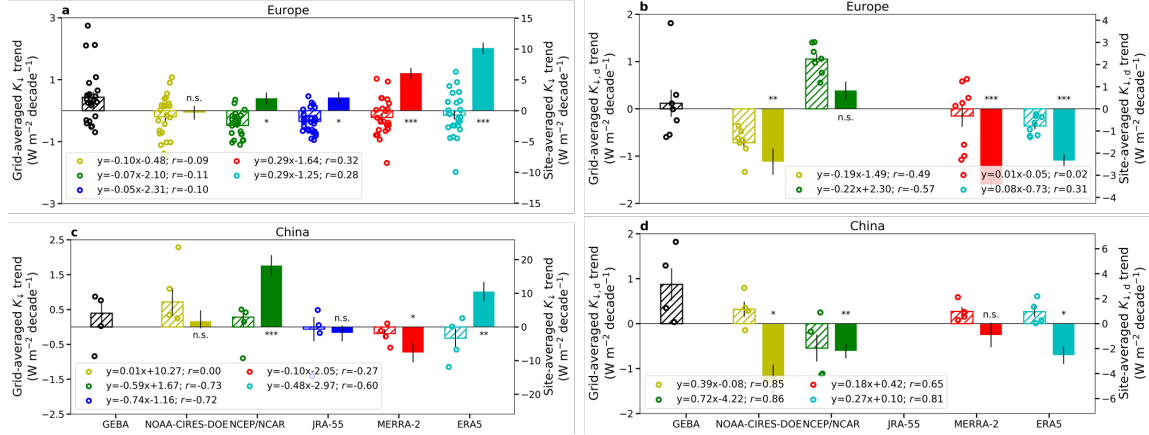
Figure 4.8: Long-term trends from gridded and observed data. Sub-figures **a** and **b** show trends in incoming shortwave radiation ($K_{\downarrow}$) and incoming diffuse radiation ($K_{\downarrow,\mathrm{d}}$) at the surface over Europe. The long-terms trends in the GEBA observations with at least 10 years of data in Common Period II (1980-2015), as well as the corresponding trends for the overlapping grids from the gridded products, are shown with circles. The hatched bars show the mean ($\pm$ standard error) of the trends based on these circles. Equations of lines representing the associations between the observed and the corresponding modeled trends are in the legends. The solid bars show the grid-area averaged regional values for the gridded reanalysis products for the entire period (1980-2015), and the error bars represent the standard errors. Sub-figures **c** and **d** are similar, but for China. The p-values of the grid-averaged trends are indicated by asterisks, with three asterisks representing p<0.0001, two for p<0.001, and one for p<0.05.

Over China, the trends in $K_{\downarrow}$ are less consistent than those over Europe. Two products (MERRA-2 and JRA-55) show decreasing trends, and three (NOAA-CIRES-DOE, NCEP/NCAR, and ERA5) show increasing trends. The rate of change varies from -0.73 W m^{-2} per decade (MERRA-2) to 1.76 W m^{-2} per decade (NCEP/NCAR), giving a five-product mean of 0.41 ± 0.88 W m^{-2} per decade. In contrast, all products show decreasing trends in $K_{\downarrow,\mathrm{d}}$, giving a four-product mean rate of change of -0.72 $\pm$ 0.39 W m^{-2} per decade (Fig. 4.8d).

Second, we analyze the time trends using the GEBA data and the reanalysis data from the grids containing these GEBA sites and for the same measurement years. Since the number of sites which fulfill all the quality-control criteria, including the homogeneity test, are small (see Methods section), we stress that these do not necessarily represent

regional trends. Instead, we examine whether the gridded products capture the observed trends for the corresponding periods. The trends for the individual stations included for each region are represented by the circles in Fig. 4.8, with the overall mean and standard errors for these shown as hatched bars. For 62.5% (15 of 24) of the GEBA sites considered over Europe, we see a positive trend, with an average increasing trend in $K_\downarrow$ (2.18 W m^{-2} per decade), which is consistent with existing studies (Wild 2012, 2016; Schwarz et al., 2020). None of the reanalysis products capture the direction of the mean brightening trend for the corresponding grids and years, though the regressions between the observed and modeled trends in $K_\downarrow$ are positive for ERA5 ($r = 0.28$) and MERRA-2 ($r = 0.32$). For $K_{\downarrow,d}$, only half of the six GEBA sites show decreasing trends. Among the reanalysis products, only ERA5 captures (weakly) the corresponding trends ($r = 31$).

Over China, 3 of the 4 GEBA sites show a brightening trend (Fig. 4.8c), with none of the corresponding reanalysis products capturing the variability of trends between the sites. On the contrary, for $K_{\downarrow,d}$, all the four considered GEBA sites show an increase over time, with all the reanalysis products other than NCEP/NCAR capturing the positive direction of the mean trend.

Several previous studies have examined the long-term trends in $K_\downarrow$ over Europe and China owing to the larger data coverage and strong temporal trends in these regions (Samukova et al., 2014; Lorenzo et al., 2015; Feng et al., 2018; Schwarz et al., 2020). Although the magnitude of the trends varies across studies depending on quality control of the data and the selection of the observation sites and the time periods of interest, most studies have found strong brightening over Europe and weak to negligible brightening over China since the 1980s. For Europe, Lorenzo et al. (2015) found an increasing trend of 3.2 W m^{-2} per decade for $K_\downarrow$ between 1986 and 2012. Similarly, Pfeifroth et al. (2018) found increasing trends between 1.9 W m^{-2} and 2.4 W m^{-2} per decade for 1983-2015. Most recently, Schwarz et al. (2020) found an increase in the $K_\downarrow$ absorbed by the surface at a

rate of 1.7 W m^{-2} per decade in Europe for the 31-year period between 1985 and 2015. For the time periods corresponding to the three studies mentioned above, we calculate the five-product mean brightening trends of 0.63 W m^{-2} per decade, 0.68 W m^{-2} per decade, and 0.57 W m^{-2} per decade, respectively. Over China, strong brightening trends (by 10.6 W m^{-2} per decade) have been seen for clear-sky conditions between 2006-2018 (Yang et al., 2019). For all-sky conditions, the absorbed $K_{\downarrow}$ at the surface showed a dimming trend of -0.7 W m^{-2} per decade between 1985 and 2009 and a brightening trend of 1.4 W m^{-2} per decade between 2011 and 2015 (Schwarz et al., 2020). We find a five-product mean increase in $K_{\downarrow}$ by 0.41 W m^{-2} per decade for Common Period II in China. The observed increase in $K_{\downarrow}$ for the subset of GEBA sites in China is not captured by the reanalyses over the corresponding sites. The overall regional brightening has also been found to be missing in unconstrained CMIP5 model simulations (Moseid et al., 2020).

Observational constraints on long-term trends in $K_{\downarrow,d}$ are much rarer, partly because of the lack of sufficient ground stations that measure this variable, as well as higher uncertainties in these measurements. For Europe, a couple of studies show decreasing trend in $K_{\downarrow,d}$ since the 1980s (Samukova et al., 2014; Wild et al., 2017). We also find a decreasing four-product mean trend of -0.86 W m^{-2} per decade for Common Period II. For China, there are more studies on long-term trends in $K_{\downarrow,d}$, generally showing a decrease in $K_{\downarrow,d}$ till the 1990s, followed by an increase till 2010 (Wang & Yang, 2014). For northern China, $K_{\downarrow,d}$ showed an increasing tendency from 1959 to 2016 according to a recent study (Feng et al., 2018), but a strong decreasing tendency for the Beijing and Shenyang stations, both in the northern China, according to another study (Wang et al., 2020). We find a decreasing four-product mean trend in $K_{\downarrow,d}$ of -2.93 (-0.72) W m^{-2} per decade for Common Period II.

4.4.5 Role of Clouds and Aerosols on Inter-Model Variability in Gridded Products

Previous studies show overestimation of $K_\downarrow$ in reanalysis datasets due to the underestimation of clouds (Zhao et al., 2013; Wild et al., 2015b; Loeb et al., 2019). Here, we separately analyze the correlation of $K_{\downarrow,d}$ and $K_{\downarrow,b}$ with percentage cloud cover at the global scale, both within the gridded products using annual averages and between the products using multi-year averages for Common Period I (Fig. 4.9). The datasets show similar spatial patterns in cloud cover (Fig. 4.10), but large differences in global mean values, ranging from 52.3% in NCEP/NCAR to 66.5% in CERES. In general, products with lower cloud cover have higher average $K_{\downarrow,b}$ and lower $K_{\downarrow,d}$, which makes sense mechanistically. The exception to this strong linear relationship (r^2 = 0.96 for $K_{\downarrow,b}$ and 0.92 for $K_{\downarrow,d}$; Fig. 4.9) is NCEP/NCAR, which has the lowest cloud cover, but not the lowest $K_{\downarrow,d}$ or the highest $K_{\downarrow,b}$. Note that NCEP/NCAR does have the highest $K_\downarrow$ (Table 4.1). Thus, the issue is the partitioning of $K_{\downarrow,d}$ in the product. The underestimation of $K_{\downarrow,b}$ and overestimation of $K_{\downarrow,d}$ in CERES may be due to the positive bias in not just percentage cloud cover (Kato et al., 2018), but the well-known systematic overestimation in MODIS-derived cloud droplet size (Painemal & Zuidema 2011). Larger particles lead to more forward scattering (Plass and Kattawar 1968), which could contribute to the positive bias in $K_{\downarrow,d}$ at the surface while simultaneously reducing $K_{\downarrow,b}$.
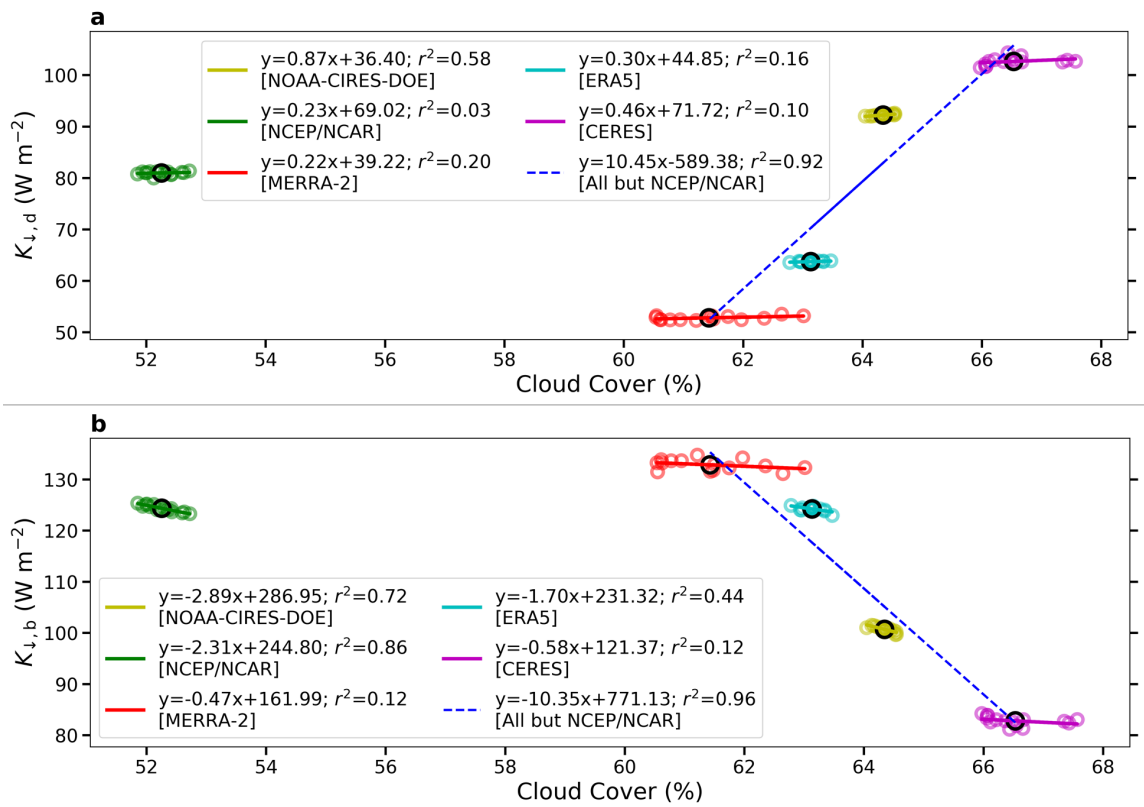
Figure 4.9: Associations between percentage cloud cover and incident **a** diffuse radiation ($K_{\downarrow,\text{d}}$) and **b** direct beam radiation ($K_{\downarrow,\text{b}}$) for Common Period I (2001-2015). Each colored circle represents an annual mean value, while the black circle shows the multi-year average for the gridded product. The lines of best fit and their equations are shown, both for individual gridded products and across products (not considering NCEP/NCAR).
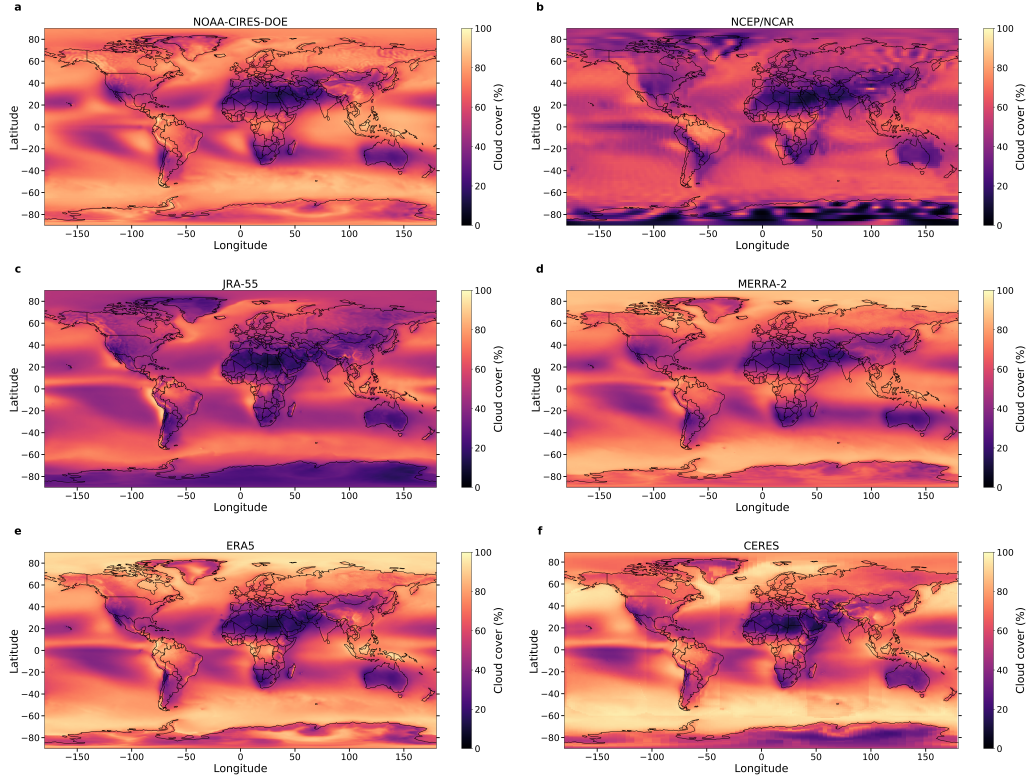
Figure 4.10: Spatial distribution of cloud cover in **a** NOAA-CIRES, **b** NCEP/NCAR, **c** JRA-55, **d** MERRA-2, **e** ERA5, and **f** CERES for Common Period I (2001-2015).

Although the relationships between annual cloud cover and annual $K_{\downarrow,b}$ (and $K_{\downarrow,d}$) for each gridded product are not consistently strong, we find the expected direction of sensitivity to cloud cover in all the datasets. The sensitivities are positive for $K_{\downarrow,d}$, ranging from 0.22 W m^{-2} per cloud cover percentage in MERRA-2 to 0.87 W m^{-2} per cloud cover percentage in NOAA-CIRES-DOE, and negative for $K_{\downarrow,b}$, ranging from -0.47 W m^{-2} per cloud cover percentage in MERRA-2 to -2.89 W m^{-2} per cloud cover percentage in NOAA-CIRES-DOE. Overall, the collinearity between cloud cover and $K_{\downarrow,b}$ is higher than for $K_{\downarrow,d}$. The individual scatterplots between $K_{\downarrow,d}$ (and $K_{\downarrow,b}$) and cloud cover percentage are also in Fig. 4.11. Although there are large uncertainties in both cloud and aerosol representation in coarse-gridded models, that the inter-product variability of these atmospheric constituents controls the inter-product variability in the surface radiation fields is

a reasonable assumption. This is because the top of the atmosphere incoming $K_\downarrow$ has strong theoretical constraints and varies between 340.3 W m^{-2} in NOAA-CIRES-DOE to 341.9 W m^{-2} in NCEP/NCAR for Common Period I. It is harder to separate the relative importance of the individual constituents due to the structural and parametric differences between these products. Cloud-radiation interactions depend not only on aerial coverage of clouds, but also on cloud thickness and cloud optical properties, usually represented by the cloud optical depth (COD). For instance, an underestimation of cloud cover and an overestimation of COD can lead to a positive bias in $K_{\downarrow,b}$ and a negative bias in $K_{\downarrow,d}$ with minimal impact on overall $K_\downarrow$, which is seen in ERA5 (Table 4.2). In contrast, CERES, which has much higher cloud cover than ERA5 (Fig. 4.9), shows a negative bias in $K_{\downarrow,b}$ and a positive bias in $K_{\downarrow,d}$, which may be due to either the larger cloud droplet size or underestimated COD or a combination of both (Minnis et al., 2011). The overestimation of optically thick clouds in models compared to satellite observations has been known for a while (Zhang et al., 2005) but has not been used to specifically examine the differences in direct/diffuse partitioning among models. Although COD is not publicly archived in most of these reanalysis products, preventing such an analysis in the present study, accurately representing both overall cloud cover and COD might reduce this large variability in direct/diffuse partitioning across these products. The reanalysis products also have large differences in aerosol representation. The NOAA-CIRES-DOE and NCEP/NCAR reanalysis do not include tropospheric aerosols (although NOAA-CIRES-DOE has volcanic aerosols), ERA5 and JRA-55 consider aerosol climatology, and MERRA-2 includes time-varying assimilated aerosols and is the only one of these products that archive AOD. Thus, a similar analysis using all gridded products is not possible for the inter-product variability in aerosols.
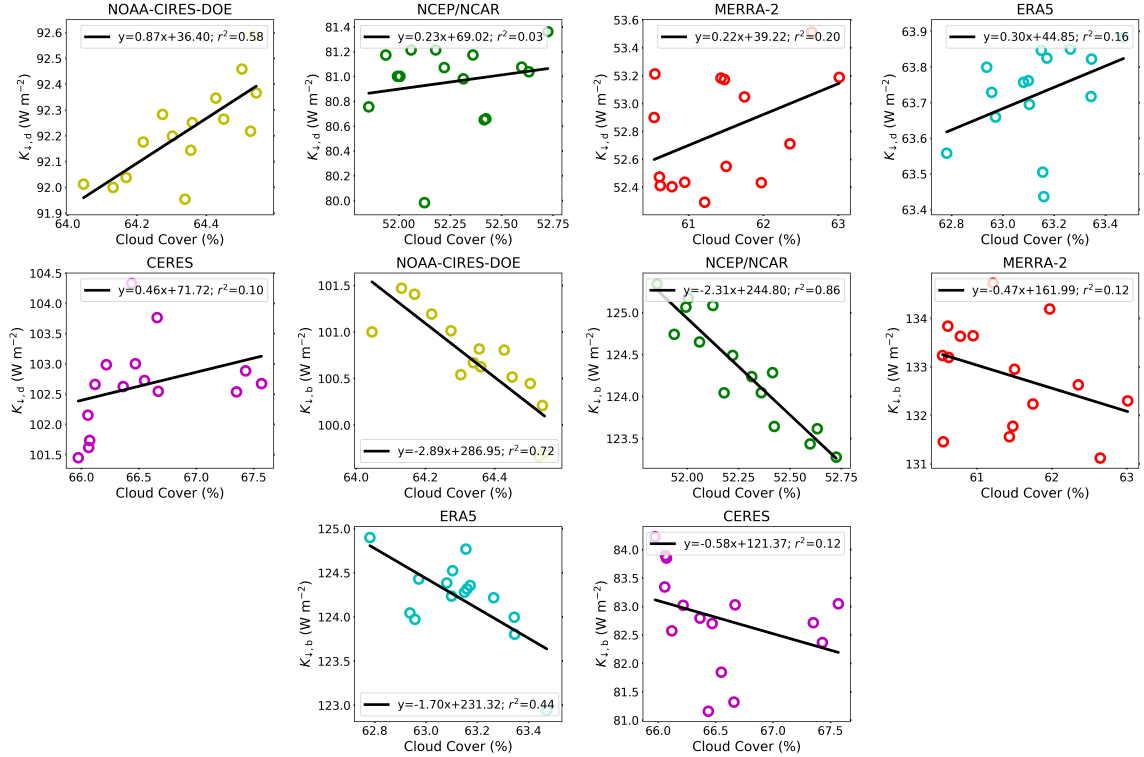
Figure 4.11: Associations between annual average percentage cloud cover and surface radiation fields (incident diffuse radiation $K_{\downarrow,d}$ and direct beam radiation $K_{\downarrow,b}$) for Common Period I (2001-2015) for each of the gridded products. The lines of best fit and their equations are shown.

We also examined the long-term trends in clouds and aerosols for Europe and China. Figure 4.12 (a to f) shows the correlation between the trends in cloud cover and the trends in $K_{\downarrow}$ and $K_{\downarrow,d}$ for Europe and China among the six datasets. Common Period I is used for CERES and Common Period II for the reanalysis products. For Europe in particular, these correlations are strong ($r^2 = 0.92$ for $K_{\downarrow,b}$ and 0.80 for $K_{\downarrow,d}$; Figs 4.12c and 4.12e), suggesting that the strength of the brightening over these regions in the gridded data is primarily a function of the trends in the modeled cloud cover. All the datasets other than JRA-55 show a decrease in cloud cover over this region between 1980 and 2015 (Common Period II). We also calculate the trend in AOD for Europe from the MERRA-2 data (Fig. 4.12g), showing a decreasing trend of 0.04 per decade during the same period. The

decrease in aerosol for Europe has been previously seen using both observations and models (Yang et al., 2020). Since aerosols generally increase $K_{\downarrow,\mathrm{d}}$, keeping all other factors constant, this would explain the simultaneous decadal increase in $K_\downarrow$ and decrease in $K_{\downarrow,\mathrm{d}}$ over Europe. For China, cloud cover decreases in most of the gridded products (other than JRA-55), with the magnitudes of change roughly half of that seen over Europe. The correlation between trends in cloud cover and trends in $K_\downarrow$ is relatively weak, though this is primarily driven by MERRA-2 being an outlier (r^2 increases to 0.88 if MERRA-2 is not used in this regression). Incidentally, only MERRA-2 assimilates observations of aerosols, showing an increase in AOD by 0.03 per decade over this region (Fig. 4.12h). Moreover, according to the grid-averaged trends, $K_{\downarrow,\mathrm{d}}$ decreased during this period over China. This pattern could be due to the relative change in absorbing and scattering aerosols over the region during this time period. MERRA-2 data shows a stronger increase in absorbed AOD compared to scattered AOD over China during Common Period II, suggesting a relative enhancement in absorbing aerosols (Fig. 4.12h). Even though the absorbing component of total AOD in MERRA-2 is modeled, not assimilated, observations bear out the increase in absorbing aerosols over China during this period (Schwarz et al., 2020).
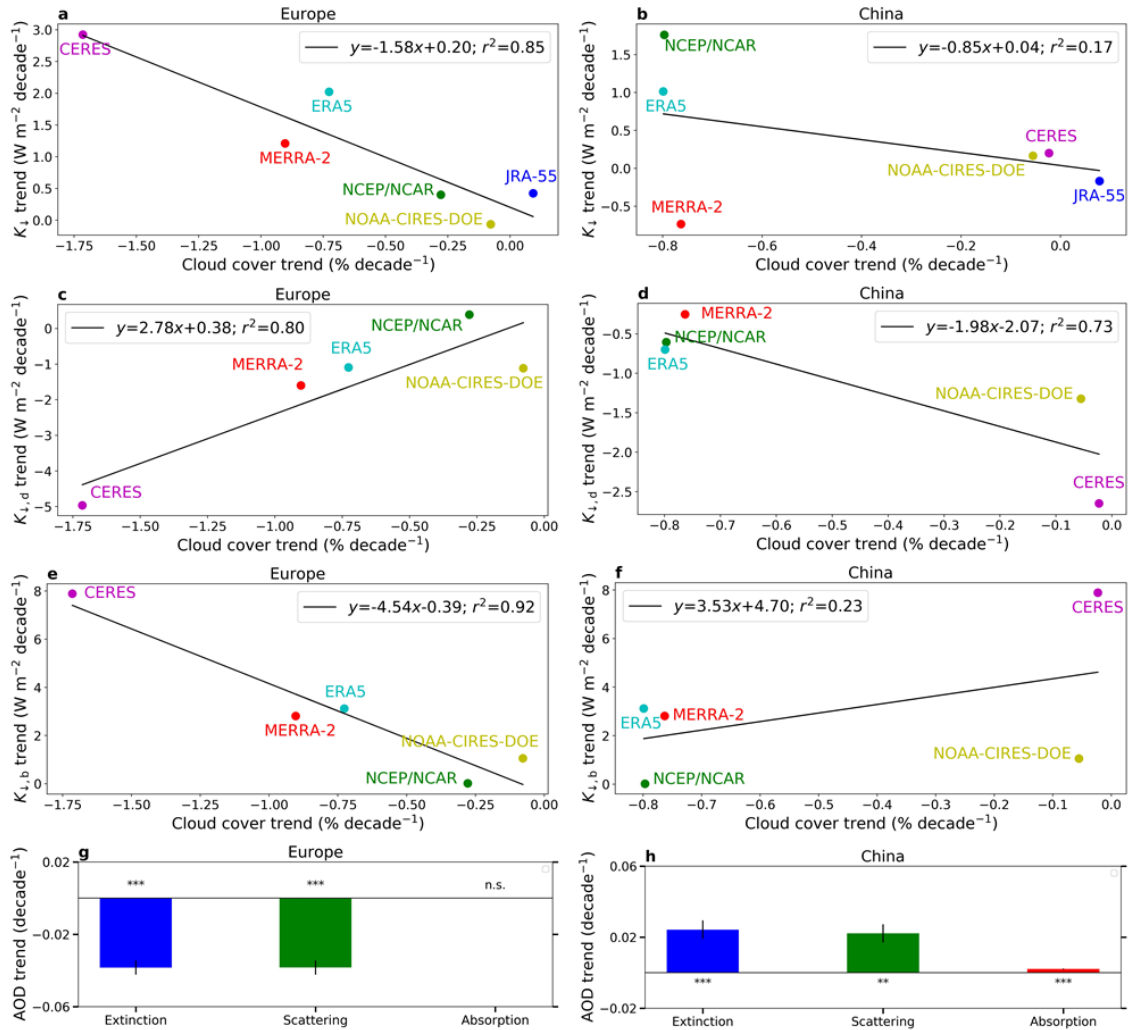
Figure 4.12: Linear regressions between trends in grid-area averaged percentage cloud cover and trends in **a** incoming shortwave radiation ($K_\downarrow$) over Europe, **b** $K_\downarrow$ over China, **c** incoming diffuse radiation ($K_{\downarrow,d}$) over Europe, **d** $K_{\downarrow,d}$ over China, **e** direct beam radiation ($K_{\downarrow,b}$) over Europe, and **f** $K_{\downarrow,b}$ over China for all the gridded products during Common Period II (1980-2015) for the reanalysis products and Common Period I (2001-2015) for CERES. The equations for the lines of best fit are annotated. Sub-figures **g** and **h** show the trends in grid-area averaged aerosol optical depth (AOD), separated into the scattering and absorbing components, for Common Period II as assimilated by MERRA-2. For **g** and **h**, the black lines show the standard errors. The p-values are indicated for **g** and **h** by asterisks, with three asterisks representing p<0.0001, two for p<0.001, and one for p<0.05.

Since in addition to cloud cover, MERRA-2 assimilates gridded AOD, we can estimate the sensitivity of the trends in $K_\downarrow$ and $K_{\downarrow,d}$ due to the trends in cloud cover and aerosols

by solving this system of two equations:

$$\frac{K_{\mathrm{R,Tr,Eu}}}{K_{\mathrm{R,80,Eu}}} = a\frac{\mathrm{CLD_{R,Tr,Eu}}}{\mathrm{CLD_{R,80,Eu}}} + b\frac{\mathrm{AOD_{R,Tr,Eu}}}{\mathrm{AOD_{R,80,Eu}}} \tag{4.1}$$

$$\frac{K_{\mathrm{R,Tr,Ch}}}{K_{\mathrm{R,80,Ch}}} = a\frac{\mathrm{CLD_{R,Tr,Ch}}}{\mathrm{CLD_{R,80,Ch}}} + b\frac{\mathrm{AOD_{R,Tr,Ch}}}{\mathrm{AOD_{R,80,Ch}}} \tag{4.2}$$

Here subscripts $K_{\mathrm{R,Tr,Eu}}$ and $K_{\mathrm{R,Tr,Ch}}$ represent the trends in the MERRA-2 gridded products for Europe and China, respectively. The variables considered are the incoming radiation (K_{R}; either $K_{\downarrow}$ or $K_{\downarrow,\mathrm{d}}$), the cloud cover (CLD), and AOD. Since these variables have different ranges, they are normalized by the value of the variable for the base year (1980; denoted by subscripts $\mathrm{R, 80, Eu}$ and $\mathrm{R, 80, Ch}$) to represent the fractional rates of change. For reference, $\mathrm{CLD_{R,80,Eu}}$ and $\mathrm{CLD_{R,80,Ch}}$ are 63.56% and 47.95%, respectively, while $\mathrm{AOD_{R,80,Eu}}$ and $\mathrm{AOD_{R,80,Ch}}$ are 0.26 and 0.18. Finally, a and b are the unitless coefficients that give the sensitivity of the fraction rate of change in the radiation components to the fractional rate of change in CLD and AOD, respectively. Simultaneously solving these two equations, we find that both a and b are negative for fractional rate of change in $K_{\downarrow}$ (a = -0.184, b = -0.037) and positive for the corresponding fractional rate of change in $K_{\downarrow,\mathrm{d}}$ (a = 1.074, b = 0.124). These values make sense physically since an increase in aerosols and clouds tends to decrease $K_{\downarrow}$ and increase $K_{\downarrow,\mathrm{d}}$. In terms of magnitude, clouds play a stronger role than aerosols; with the sensitivity being almost 9 times higher for clouds for $K_{\downarrow,\mathrm{d}}$ and 5 times stronger for $K_{\downarrow}$. Over Europe, the effect of clouds and aerosols reinforce each other, with both decreasing, thereby increasing $K_{\downarrow}$ and decreasing $K_{\downarrow,\mathrm{d}}$. Over China, the total effect of aerosols, controlled by both the lower sensitivity to aerosols and the much higher fractional rate of change in AOD, overwhelm the impact of clouds, with $K_{\downarrow}$ decreasing in spite of a decrease in cloud cover.

We use this framework to constrain the sensitivity of $K_{\downarrow}$ and $K_{\downarrow,\mathrm{d}}$ to CLD and AOD in the MERRA-2 dataset because of its conceptual simplicity. For comparison, we also used

multi-linear regressions to examine the trend in $K_\downarrow$ and $K_{\downarrow,\mathrm{d}}$ as a function of grid-averaged CLD and AOD separately for Europe and China, given by the equation:

$$\frac{K_\mathrm{R}}{K_{\mathrm{R},80}} = \beta_0 + \beta_1 \frac{\mathrm{CLD_R}}{\mathrm{CLD_{R,80}}} + \beta_2 \frac{\mathrm{AOD_R}}{\mathrm{AOD_{R,80}}} \tag{4.3}$$

Here the annual average values of $K_\downarrow$ and $K_{\downarrow,\mathrm{d}}$ (K_R), CLD (CLD_R), and AOD (AOD_R) are normalized by their 1980 values and β_0, β_1, and β_2 are the coefficients of regression. Although the results are different over the two regions since they are not mathematically constrained by the same sensitivity as done for Eqs 4.1 and 4.2, we get the same signs and similar relative magnitudes of the regression coefficients. β_1 and β_2 are always positive for $K_{\downarrow,\mathrm{d}}$ and always negative for $K_\downarrow$. Clouds play a stronger role in both Europe and China for $K_\downarrow$ (β_1/β_2 = 14.52 and 6.26, respectively) and $K_{\downarrow,\mathrm{d}}$ (β_1/β_2 = 3.57 and 8.03, respectively).

4.5 Discussion and Summary

4.5.1 Comparison with Other Modeled and Satellite-Derived Estimates

We are not aware of any formalized attempts to evaluate $K_{\downarrow,\mathrm{d}}$ in current-generation CMIP6 models or their previous iterations. Although operational GCMs may sometimes lead re-analysis products in model development efforts (for instance, frequently using prognostic aerosols instead of prescribed aerosol distributions), many of the radiation codes and cloud parameterizations used to generate the reanalysis products are also implemented in those models. Additionally, that GCMs are run with less constraints on the atmospheric and sur-face variables than reanalysis products suggests that there may also be wide disparities in the $K_{\downarrow,\mathrm{d}}$ modeled by GCMs. We see evidence of this from two studies that have evaluated $K_{\downarrow,\mathrm{d}}$ at larger scales. Mercado et al. (2009) used radiative transfer calculations to simulate $K_{\downarrow,\mathrm{b}}$ and $K_{\downarrow,\mathrm{d}}$ globally. Using a subset of GEBA observations over Europe, Germany,

and China, they evaluated their modeled $K_\downarrow$ and k_d. For GEBA stations in Germany and Europe, they found an underestimation in $K_\downarrow$ and an overestimation in k_d. Over China, their model overestimated $K_\downarrow$, but correctly simulated k_d, suggesting an overestimation in $K_{\downarrow,\mathrm{d}}$. More recently, Chakraborty et al. (2021) used the latest version (version 6) of the Community Atmosphere Model (CAM6; Gettelman et al., 2019) to simulate $K_{\downarrow,\mathrm{d}}$ and $K_{\downarrow,\mathrm{b}}$ and evaluated the modeled values using all available GEBA observations. CAM6 overestimated $K_\downarrow$ and underestimated $K_{\downarrow,\mathrm{d}}$, leading to an MBE of -0.08 for k_d for all GEBA sites.

Our evaluation of the CERES dataset shows that, while CERES does a great job at capturing both the magnitude and variability in $K_\downarrow$ (Table 4.2), there are issues with the direct/diffuse partitioning. CERES overestimates $K_{\downarrow,\mathrm{d}}$ and underestimates $K_{\downarrow,\mathrm{b}}$, leading to an overestimation in k_d (roughly 0.09 for all GEBA sites; Table 4.2), potentially caused by higher cloud fraction and cloud droplet size in satellite-derived products (Painemal & Zuidema 2011; Kato et al., 2018). In this context, a few other satellite-derived $K_{\downarrow,\mathrm{d}}$ products also warrant discussion. Recently, Jiang et al. (2020) evaluated the $K_{\downarrow,\mathrm{d}}$ in a recent dataset (JiEA) created using a deep learning algorithm and geostationary satellite measurements (Jiang et al., 2019a). Using 39 observation sites over East Asia, they found much better performance of the JiEA product compared to ERA5. Consistent with our results, ERA5 underestimated $K_{\downarrow,\mathrm{d}}$ (MBE=-17.2 W m^{-2}; -1.2 W m^{-2} for JiEA) over their study area. The grid-area averaged k_d over East Asia was 0.42 for JiEA and 0.35 for ERA5. For China, which covers a large part of their study area, the grid-averaged k_d for the same time period (2007-2014) varies from only 0.27 in the MERRA-2 dataset to roughly double that value (0.56) in the CERES data. Over Europe and Africa, the Copernicus Atmosphere Monitoring Service (CAMS) provides $K_\downarrow$, $K_{\downarrow,\mathrm{d}}$, and $K_{\downarrow,\mathrm{b}}$ estimates every 15 minutes based on the Heliosat-4 method using Meteosat geostationary satellite observations (Qu et al., 2017). We estimated $K_{\downarrow,\mathrm{d}}$ over the region of Europe ('AGATE') covered by these satel-

lites for Common Period I and found the regional average $K_{\downarrow,\text{d}}$ to range from 52.8 W m^{-2} in MERRA-2 to 102.6 in CERES versus a value of 65.4 W m^{-2} in CAMS. Another recent study produced global datasets of $K_{\downarrow}$, total photosynthetically active radiation (PAR) and its diffuse component from 2000 to 2016 by combining a radiative transfer model with an artificial neural network trained using MODIS data (Ryu et al., 2018). They calculated a global average ratio of 0.41 for diffuse PAR to total PAR and 0.46 for total PAR to $K_{\downarrow}$.

Of the data products we consider, only MERRA-2, NOAA-CIRES-DOE, and NCEP/NCAR publicly archive the diffuse portion of PAR. For Common Period I, we find large differences in these estimates for the three datasets for both diffuse PAR to total PAR (0.37 for MERRA-2; 0.54 for NOAA-CIRES-DOE; 0.46 for NCEP/NCAR) and for total PAR to $K_{\downarrow}$ (0.44 for MERRA-2; 0.52 for NOAA-CIRES-DOE; 0.61 for NCEP/NCAR). In comparison, the diffuse PAR to total PAR and total PAR to $K_{\downarrow}$ in the CAM simulations by Chakraborty et al. (2021) were 0.41 and 0.51, respectively.

4.5.2 Limitations

Point observations have been frequently used to compare against gridded estimates of surface radiation (Markovic et al., 2009; Zhao et al., 2013; Wild et al., 2015b). However, radiation transfer calculations in GCMs and reanalyses are based on the plane-parallel approximation, the assumption of one-dimensional atmospheric grids with horizontal planes as the upper and lower bounds, for computational efficiency. The real atmosphere has 3D cloud structures, particularly relevant for cloud-radiation interactions. For instance, cloud side illumination is the interception of radiation due to the existence of cloud sides in the real atmosphere, which are not captured by their plane-parallel approximations; a major issue at high solar zenith angles (Schäfer et al., 2016). Similarly, for low zenith angles, cloud side leakage causes more radiation to pass through the edges of clouds and reach the surface, which would be blocked in a plane-parallel representation (Ham et al., 2014).

The overall result of these two mechanisms is generally an underestimation in simulated $K_\downarrow$ even when the cloud fraction is correctly captured by the approximation (Okata et al., 2017). Thus, these two effects on their own cannot explain the systematic overestimation in $K_\downarrow$ we find in the gridded products (Table 4.2). Cloud sky leakage would normally lead to more forward scattering, and may thus increase $K_{\downarrow,d}$ in regions with low zenith angle, which we do find in the GEBA observations compared to the MERRA-2 and ERA5 datasets. The effect of cloud side illumination, on the other hand, primarily blocks $K_{\downarrow,b}$ (Hogan & Shonk 2013), which would overestimate $K_{\downarrow,b}$ in GCMs, which is seen in all reanalysis products other than NOAA-CIRES-DOE (Table 4.2).

These problems are most serious at shorter time scales, as patchy clouds can cause large fluctuations in the observations at individual sites. Thus, since the signs of these 3D effects largely depend on zenith angle, the errors are reduced substantially when using monthly means since it averages over the various zenith angles (as was done here) and by combining the biases over multiple sites in a region. Note that the bias errors found here may also be related to other aspects of the 3D cloud structure, such as how overlap of clouds at various heights is represented (Wang et al., 2016). However, the inter-model variability is not affected by these issues since all the products considered use similar approximations. We find that this variability for both $K_{\downarrow,d}$ and $K_{\downarrow,b}$ is strongly controlled by cloud fraction (Fig. 4.8). Additional differences are also expected due to the shortwave parameterizations used in these datasets that convert the cloud representations to the radiances across wavelength channels. However, such an evaluation requires a modeling setup that controls for the different inputs to the radiative transfer models used in the gridded products and hyperspectral observations for validation (Aumann et al., 2018).

A quantitative comparison of the long-term trends using observations requires consistent data coverage. The GEBA data are not always appropriate for this purpose because the trends in $K_{\downarrow,d}$ and $K_\downarrow$ (circles and hatched bars, Fig. 4.8) are derived from two different

subsets of the data (there are more $K_\downarrow$ observations than $K_{\downarrow,d}$ observations). Moreover, even within Common Period II, the data coverage changes over time. This lack of consistent data coverage is particularly relevant for China since many studies find a reversal of the trends somewhere between 1990 and 2000, potentially influenced by the instrument changes after 1993 (Wang & Yang, 2014). We try to account for potential breakpoints in the trends by testing for homogeneity of the time-series. However, this reduces the number of available stations substantially, particularly over China (Fig. 4.8). As such, although the inter-model variability in long-term trends in the gridded datasets illustrates the differences between these models, we advise caution when talking about the 'real' regional trends using GEBA observations, particularly for $K_{\downarrow,d}$ given the dearth of available observations. For China, one alternative is to use data from the China Meteorological Data Service Center (http://data.cma.cn). However, as seen in Wang et al. (2020), after testing for homogeneity, only 12 stations are available with long-term observations of both $K_\downarrow$ and $K_{\downarrow,d}$. An in-depth analysis of the influence of station and year range selection on these trends is in Schwarz et al. (2020), though they do not focus on $K_{\downarrow,d}$. Given that we find that the gridded data cannot generally capture either the direction or the variability in trends across the available GEBA sites for the corresponding time-periods, further work is necessary to evaluate long-term trends in $K_{\downarrow,d}$ across CMIP6 models with consolidated observational databases that include both regional and global networks.

4.5.3 Summary

We find large differences in $K_{\downarrow,d}$, $K_{\downarrow,b}$, and k_d across current-generation gridded products. The variability is evident from the monthly to the annual scales and show large biases from observational benchmarks. For 2001-2015, the range of variability is 10.7% for global mean $K_\downarrow$ (185.4 to 205.3 W m^{-2}), 60.4% for global mean $K_{\downarrow,b}$ (82.8 to 132.8 W m^{-2}), 94.3% for global mean $K_{\downarrow,d}$ (52.8 to 102.6 W m^{-2}), and 96.4% for global mean k_d (0.28

to 0.55). The variability between these products is statistically explained by the biases in modeled cloud fraction. Long-term (1980-2015) trends in the two variables also differ over Europe and China and are not captured well by the gridded products. These inter-model differences in $K_{\downarrow,\mathrm{d}}$ would affect Earth system simulations, particularly relevant for surface climate and for estimating solar energy potential. Thus, we suggest comprehensive comparisons of simulated k_d in the CMIP6 models to better identify potential deficiencies in current-generation atmosphere models.

Chapter 5

Developing a Bias-Corrected Global Radiation Dataset Using Supervised Learning

5.1 Abstract

Diffuse solar radiation is an important, but understudied, component of the Earth's surface radiation budget, with most global climate models not archiving this variable and a dearth of ground-based observations. Here we describe a global 40-year (1980 - 2019) monthly database of total shortwave radiation, including its diffuse and direct beam components, called BaRAD (Bias-adjusted RADiation dataset). The dataset is based on a random forest algorithm trained using Global Energy Balance Archive (GEBA) observations and applied to the Modern-Era Retrospective analysis for Research and Applications, Version 2 (MERRA-2) dataset at the native MERRA-2 resolution ($0.5° \times 0.625°$). The dataset preserves seasonal, latitudinal, and long-term trends in the MERRA-2 data, but with reduced biases than MERRA-2. The mean bias error is close to 0 (root mean square error = 10.1 W m^{-2}) for diffuse radiation and -0.2 W m^{-2} (root mean square error = 19.2 W m^{-2}) for the total shortwave. Studies on atmosphere-biosphere interactions, especially those on the diffuse radiation fertilization effect, can benefit from this dataset.

5.2 Background & Summary

The Earth's climate is driven by solar (shortwave) radiation and its interactions with the different components of the Earth system. The shortwave radiation is attenuated by scattering and absorption by atmospheric aerosols, clouds, and gases, with the remaining portion reaching the Earth's surface as direct beam radiation ($K_{\downarrow,b}$). A portion of the scattered radiation also reaches the surface, which deviates from its original path and is known as diffuse radiation ($K_{\downarrow,d}$). The sum of $K_{\downarrow,b}$ and $K_{\downarrow,d}$, or the total incident shortwave radiation at the surface ($K_{\downarrow}$), influences local weather and climate, the hydrological cycle, and the carbon budget. There is also strong scientific interest in $K_{\downarrow,d}$ because a high diffuse

136

fraction can increase agricultural and ecosystem productivity and enhance the terrestrial water flux to the atmosphere through increased photosynthesis in normally shaded parts of the plant canopy, a phenomenon known as the diffuse radiation fertilization effect (Gu et al., 2003; Mercado et al., 2009; Rap et al., 2018).

Current Earth System Models (ESMs) generally overestimate $K_\downarrow$ compared to observations, primarily due to errors associated with parameterizations of clouds and aerosols (Markovic et al., 2009; Bosilovich et al., 2011; Kennedy et al., 2011; Zhang et al., 2016). This overestimation would cause artificial surface warming, with undesired consequences on atmosphere-biosphere interactions (Wild et al., 2016; Chakraborty & Lee, 2019). Although similar evaluations of ESM $K_{\downarrow,\mathrm{d}}$ are not available, large differences are reported for $K_{\downarrow,\mathrm{d}}$ between reanalysis datasets and observations (Chakraborty et al., 2021). The bias in $K_{\downarrow,\mathrm{d}}$ in these gridded datasets is not consistent in direction, unlike that for $K_\downarrow$. Such biases may contribute to uncertainties in modelling surface energy and carbon budgets and impact optimum placement of concentrating solar power systems (Oliveira et al., 2011; Lee et al., 2016).

Several previous studies have examined the biases in modeled $K_\downarrow$ using the clearness index (k_t). This index, defined as the ratio between surface incident and extraterrestrial radiation, captures the combined impact of aerosols, clouds, and gases on atmospheric transmittance on solar radiation (Zhao et al. 2013; Boilley et al., 2015; Trolliet et al., 2018). These atmospheric constituents attenuate solar radiation as it moves through the atmospheric column. Although k_t, a measure of the total light extinction, directly affects $K_{\downarrow,\mathrm{b}}$ and therefore exerts a strong control on $K_\downarrow$, it is only tangentially related to $K_{\downarrow,\mathrm{d}}$. It is known that $K_{\downarrow,\mathrm{d}}$ is primarily controlled by the abundance of scattering agents in the atmosphere, as well as their degree of forward scattering (Plass and Kattawar, 1968). An atmospheric scattering agent that reduces $K_{\downarrow,\mathrm{b}}$ may actually increase $K_{\downarrow,\mathrm{d}}$. Thus, a new approach is required to correct biases in $K_{\downarrow,\mathrm{d}}$.

In recent years, machine learning algorithms have been used to reduce biases in radiation fields derived from reanalysis products or derive the fields from satellite observations (Zhou et al., 2017; Frank et al., 2018; Yang et al., 2018; Wei et al., 2019; Hao et al., 2020; Peng et al., 2021). By training against observed data, these algorithms can capture previously unknown relationships between actual and gridded variables, generally leading to improvements over traditional parametric and multi-ensemble averaging techniques22. However, the majority of these algorithms have been implemented at the regional scale, particularly over China, Europe, and the US, with a focus on the total $K_\downarrow$. For reasons briefly described above, it is also important to develop a generalizable bias-correction algorithm for $K_{\downarrow,\mathrm{d}}$. Of note, a recent study developed a global hourly $K_{\downarrow,\mathrm{d}}$ dataset using a random forest algorithm on satellite retrievals from the Earth Polychromatic Imaging Camera (EPIC)21, although this focused on a short period from June 2015 to June 2019. A gridded data product after proper bias correction is especially welcome for tropical regions where $K_{\downarrow,\mathrm{d}}$ measurements are rare but the diffuse fertilization effect is strong due to high vegetation densities (Rap et al., 2018; Chakraborty et al., 2021).

In this paper, we describe the development of a new dataset of monthly gridded radiation fields, including $K_\downarrow$, $K_{\downarrow,\mathrm{b}}$, and $K_{\downarrow,\mathrm{d}}$, from 1980 to 2019. We attempt to improve historical global gridded estimates of $K_{\downarrow,\mathrm{d}}$. through three major steps:

1. Examine the control of k_t on biases in $K_\downarrow$, $K_{\downarrow,\mathrm{b}}$, and $K_{\downarrow,\mathrm{d}}$ separately

2. Test bias-correction algorithms for $K_\downarrow$ and $K_{\downarrow,\mathrm{d}}$, including a method based on k_t, a multiple linear regression (MLR) and a random forest (RF) model

3. Implement the best performing bias-correction algorithm to create a global 40-year Bias-adjusted RADiation dataset, or BaRAD.

5.3 Methods

5.3.1 Reanalysis Data

The gridded data reported here is based on the Modern-Era Retrospective analysis for Research and Applications, version 2 (MERRA-2) global reanalysis dataset (Randles et al., 2017). MERRA-2 improves upon the original MERRA dataset in several ways. It adds an extensive aerosol assimilation by using bias-adjusted aerosol optical depth (AOD) from satellite observations24. Unlike MERRA, MERRA-2 uses observed precipitation to force the land-surface model (Reichle and Liu, 2014). It uses a newer version of the Goddard Earth Observing System (GEOS-5) and assimilates newer satellite observations of aerosols, clouds, and precipitation (Reichle et al., 2017). MERRA-2 is available from 1980 to present day at a grid resolution of $0.5°$ latitude and $0.625°$ longitude. The variables we wish to correct are monthly mean $K_\downarrow$ and $K_{\downarrow,d}$ using predictors that physically control transmitted radiation. They include estimates of atmospheric clouds and aerosols, as well information about the position of the Sun, which controls energy input to the atmospheric column.

5.3.2 Ground-Based Observations for Training and Validation

We used the Global Energy Balance Archive (GEBA) for training and validation of bias correction algorithms. GEBA is a comprehensive observational data repository of the components of the Earth's surface energy budget (Gilgen & Ohmura, 1999). The latest version of the database has roughly 2500 unique stations (Wild et al., 2017). Here we used the monthly mean $K_\downarrow$ and $K_{\downarrow,d}$ stored in the database. The data were screened with several quality control steps. We only selected the monthly mean values lower than 600 W m^{-2} for $K_\downarrow$ and 250 W m^{-2} for $K_{\downarrow,d}$. Cases where the ratio of modeled to observed monthly

means exceed 5 were ignored. Finally, only sites with all 12 months of available data were selected to avoid biased representation across seasons. After these data screening steps, we obtained 935 unique sites with 134541 site-months of data for $K_\downarrow$ and 290 unique sites with 28880 site-months for $K_{\downarrow,d}$ between 1980 and 2017 (Fig. 5.1). Monthly mean $K_{\downarrow,b}$ was computed as the difference between $K_\downarrow$ and $K_{\downarrow,d}$.
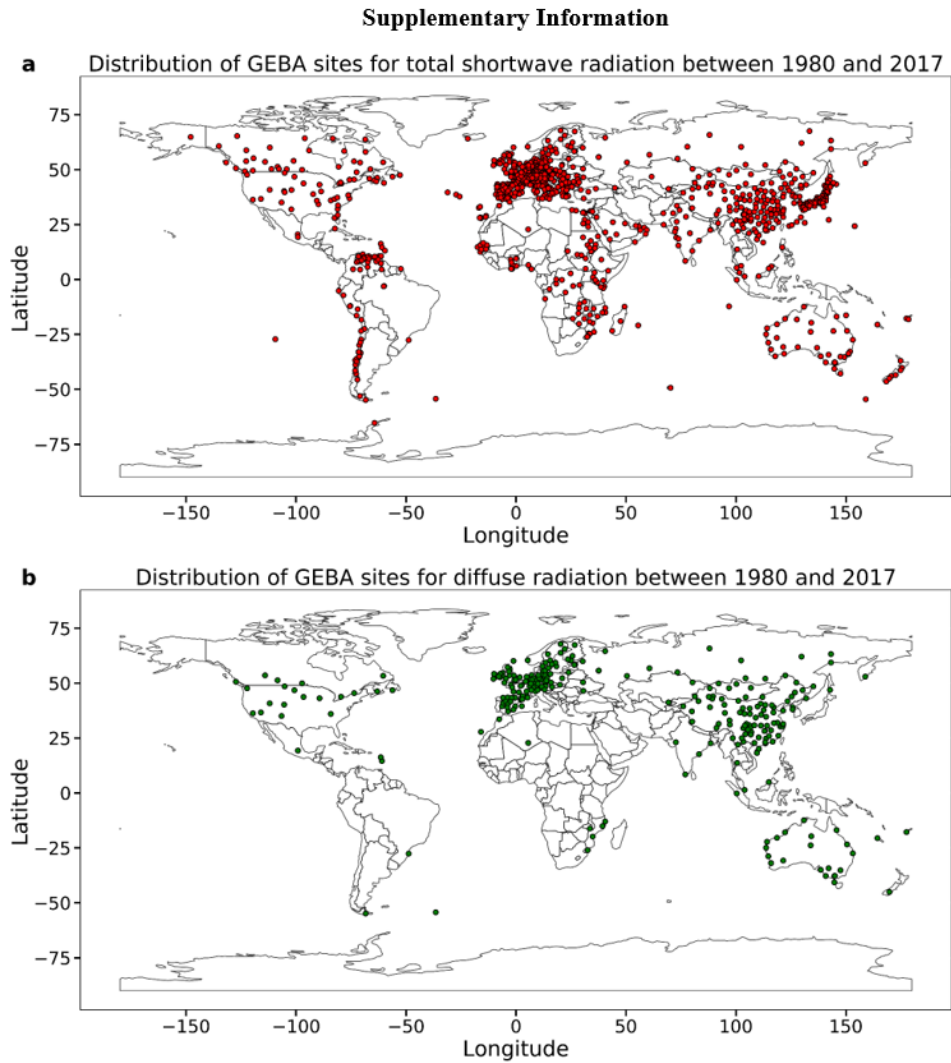
Figure 5.1: Distribution of GEBA sites used for evaluating and training bias-correction algorithms in the present study for **a** shortwave radiation and **b** diffuse radiation.

5.3.3 Bias-Correction Algorithms

We tested three bias correction algorithms, including a technique based on clearness index and two data-driven algorithms. Several studies have used clearness index k_t as a threshold for designating sky condition or for estimating $K_\downarrow$ (Iziomon et al., 2000; Zhao et al., 2013; Jiang et al., 2015). In Zhao et al. (2013), the bias in $K_\downarrow$ (b_m) is related to k_t in a linear fashion:

$$b_m = b_0.k_t + b_1 \qquad (5.1)$$

Here b_0 is the sensitivity of b_m to k_t, and b1 is the model bias ratio under completely cloudy conditions. In their study, b_m is given as

$$b_m = \frac{K_R - K_O}{K_R} \qquad (5.2)$$

where K_R and K_O are modeled and observed values, respectively. Clearness index is given by

$$k_t = \frac{K_{\downarrow,o}}{K_{TOA}} \qquad (5.3)$$

where K_{TOA} is the extra-terrestrial radiation at the top of the atmosphere and $K_{\downarrow,O}$ is the observed $K_\downarrow$ value. Their method also accounts for site elevation H. Here we used a linear model as a function of k_t and H to correct $K_\downarrow$

$$K_\downarrow = \beta_0 k_t + \beta_1 H + \beta_2 \qquad (5.4)$$

where β_0, β_1, and β_2 are empirical coefficients. A linear model of the same form was also used to correct $K_{\downarrow,d}$. Since k_t involves observed $K_\downarrow$ (Eq. 5.1), Eq. 5.5 cannot be used

to correct biases in gridded data when observations are not available. Thus, we considered two variations of this algorithm, one using observed $K_\downarrow$ ($K_{\downarrow,\mathrm{O}}$) and site elevation to calculate clearness index, called the $k_{\mathrm{t,O}}$ model, and the other using grid-averaged terrain elevation (H_R) and the clearness index calculated from modeled $K_\downarrow$ ($K_{\downarrow,\mathrm{R}}$), given by:

$$k_\mathrm{t} = \frac{K_{\downarrow,\mathrm{R}}}{K_{\mathrm{TOA}}} \tag{5.5}$$

which we call the $k_{\mathrm{t,R}}$ model.

The second algorithm, a multi-linear regression (MLR), expresses the dependent variable as a linear combination of predictors. In the case of $K_\downarrow$, it takes the following form

$$K_{\downarrow,\mathrm{O}} = \beta_0 K_{\downarrow,\mathrm{R}} + \beta_1 \mathrm{SAOD} + \beta_2 \mathrm{AAOD} + \beta_3 \mathrm{COD} + \beta_4 \mathrm{CF} + \beta_5 \theta_\mathrm{z} + \beta_6 H_\mathrm{R} + \beta_7 \tag{5.6}$$

where β_0 to β_7 are regression coefficients, $K_{\downarrow,O}$ is the observed (or bias corrected) $K_\downarrow$, $K_{\downarrow,\mathrm{R}}$ is the $K_\downarrow$ from the reanalysis without correction, SAOD is scattering aerosol optical depth (AOD), AAOD is absorption AOD, COD is cloud optical depth, CF is cloud fraction, and θ_z is mean zenith angle. The MLR procedure with the same set of predictors was also applied to $K_{\downarrow,\mathrm{d}}$. These predictors provide strong physical constraints on atmospheric radiative transfer (Schwarz et al., 2020) with both COD and AOD being direct measures of light extinction along the atmospheric column. The separation of AOD into SAOD and AAOD is more important for $K_{\downarrow,\mathrm{d}}$ than for $K_\downarrow$ since while absorption of solar radiation by aerosols would reduce both $K_{\downarrow,\mathrm{d}}$ and $K_{\downarrow,\mathrm{b}}$, forward scattering would reduce $K_{\downarrow,\mathrm{b}}$ and increase $K_{\downarrow,\mathrm{d}}$. With the intent of developing a generalized algorithm, one regression is used for the entire dataset. Since θ_z is one of the predictors, seasonal and latitudinal effects is accounted for to some extent. The algorithm was implemented using the stats package on the R programming language.

The third algorithm is a random forest (RF) regression technique (Breiman et al. 2001). Unlike the MLR model, the RF regression does not assume a standard linear structure of the relationship; instead it derives the relationship from the training data using an ensemble of decision trees. This relationship (for the total incoming radiation) can be expressed in a generic form as:

$$K_{\downarrow,O} = f(K_{\downarrow,R}, \text{SAOD}, \text{AAOD}, \text{COD}, \text{CF}, \theta_z, H_R). \qquad (5.7)$$

This random forest regression was implemented using the R Random Forest package. The default minimum size of terminal nodes (5) was used, but the maximum number of trees to generate was set to 2000. In most folds, the models converged before reaching this limit.

We used a 10-fold cross-validation technique to evaluation the performance of these algorithms. The entire GEBA dataset was randomly partitioned into 10 equal subsets. One of the ten subsets was used for validation and the other nine for training. The process was repeated 10 times. The accuracy was quantified using the coefficient of determination (r^2), the root mean square error (RMSE), and the mean bias error (MBE). Cross-validation is desired for the RF algorithm because it is prone to overfitting and using multiple folds allows us to examine the consistency of the results across different training/validation splits. The two linear models (Eqs 5.4 and 5.6) are not prone to overfitting. However, because they are sensitive to outliers, cross-validation was also done to estimate the influence of the training data selection on their performance.

The final data product (BaRAD) consists of monthly $K_\downarrow$, $K_{\downarrow,b}$, and $K_{\downarrow,d}$ corrected with the best performing algorithm at the native MERRA-2 resolution. Here the algorithm was trained on the whole quality screened GEBA dataset.
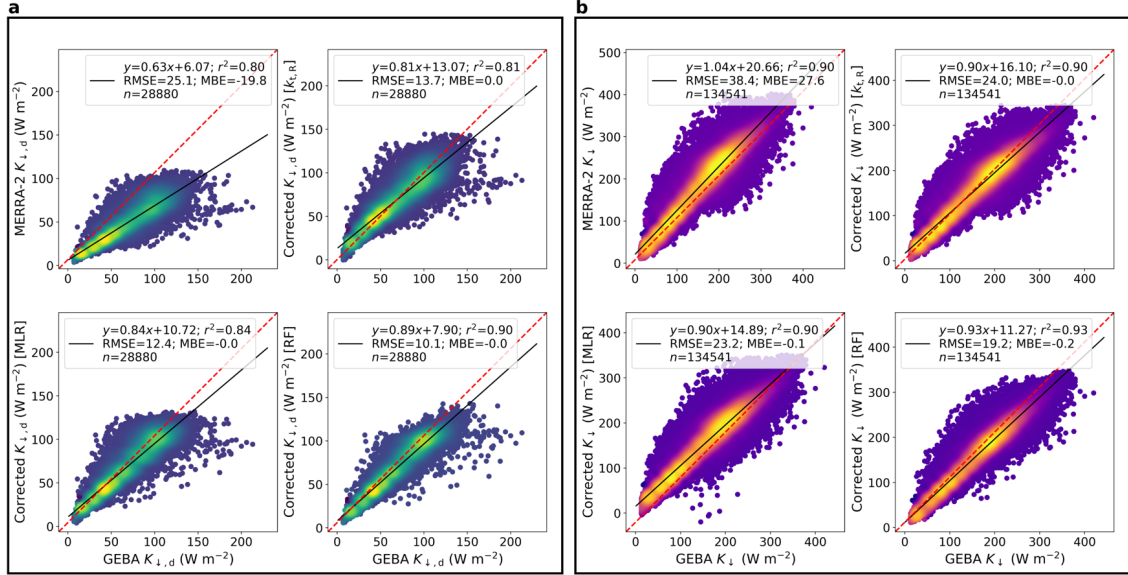
Figure 5.2: Comparison of original and bias-adjusted MERRA-2 data with GEBA observations. **a** monthly mean diffuse radiation ($K_{\downarrow,\mathrm{d}}$) and **b** total shortwave radiation ($K_{\downarrow}$,) from MERRA-2 as well as the bias-adjusted estimates from the $k_{\mathrm{t,R}}$, MLR, and RF models. For the bias-adjusted estimates, the consolidated test data from all 10 folds are shown. The red dashed lines represent the 1:1 relationship. Color indicates data density and the statistical summaries of the evaluations are noted.

5.3.4 Clearness Index as a Predictor of Bias

Zhao et al. (2013) found systematic overestimation of $K_{\downarrow}$ in two reanalysis datasets. To correct these model biases, they utilized the empirical relationship between the sensitivity of b_{m} to the observed k_{t}. Here the sensitivity is the slope of the linear regression between b_{m} and $k_{\mathrm{t,O}}$. To illustrate how this sensitivity varies between $K_{\downarrow}$, $K_{\downarrow,\mathrm{d}}$, and $K_{\downarrow,\mathrm{b}}$, we separately examined the associations between b_{m} and $k_{\mathrm{t,O}}$.

Unsurprisingly, b_{m} for $K_{\downarrow}$ and $k_{\mathrm{t,O}}$ are negatively correlated, both overall and for the common sites (Figs 5.3b and 5.3d). Here the common sites are those with simultaneous measurements of $K_{\downarrow}$ and $K_{\downarrow,\mathrm{d}}$. The sensitivity of b_{m} to $k_{\mathrm{t,O}}$ is -0.76 for all sites and -0.8 for common sites, which are close to the value of -0.82 found by Zhao et al. (2013) for MERRA in North America. Similarly, b_{m} for $K_{\downarrow,\mathrm{b}}$ is also negatively correlated with

$k_{t,O}$, with the sensitivity being higher in magnitude (-1.23; Fig. 5.3c) than that for $K_\downarrow$, suggesting that total atmospheric transmittance has a stronger effect on the biases in $K_{\downarrow,b}$ than on the biases in $K_\downarrow$. For $K_{\downarrow,d}$, the sensitivity of b_m to $k_{t,O}$ is strong (-0.89; Fig. 5.3a), but the variability in the bias is not explained well by it ($r^2 = 0.15$). Overall, the coefficient of determination (r^2) is highest for $K_{\downarrow,b}$ and smallest for $K_{\downarrow,d}$, indicating that clearness index is a poor predictor of model bias in $K_{\downarrow,d}$.

It is also important to note the intercept of the equations shown in Fig. 5.3. This intercept represents the b_m for a completely non-transmissive atmosphere (i.e. when $k_{t,O}$ = 0). For both $K_\downarrow$ and $K_{\downarrow,b}$, this value is positive (0.96 for $K_{\downarrow,b}$; 0.5 to 0.53 for $K_\downarrow$). This implies that the reanalysis overestimates $K_\downarrow$ under non-overcast skies, and its estimates improve for clearer conditions. On the other hand, the intercept for the regression line between the b_m for $K_{\downarrow,d}$ and $k_{t,O}$ is close to zero and the slope is negative, suggesting that MERRA-2 $K_{\downarrow,d}$ is underestimated even under completely clear conditions.

5.3.5 Comparing Bias-Correction Algorithms

Figure 5.2 shows the comparison of the original MERRA-2 and bias-adjusted values with the GEBA observations. MERRA-2 underestimates $K_{\downarrow,d}$ (MBE = -19.8 W m^{-2}; Fig. 5.7a) and overestimates $K_\downarrow$ (MBE = 27.6 19.8 W m^{-2}; Fig. 5.7b). Consistent with the $K_\downarrow$ overestimation, the modeled clearness index $k_{t,R}$ (0.54 $\pm$ 0.11) is higher than the observed index $k_{t,O}$ (0.45 $\pm$ 0.12). This increased transmissivity may be caused by underestimation of both clouds and aerosols, although clouds probably play a greater role since MERRA-2 has assimilated observations of AOD. Although an underestimation in clouds would also explain the underestimation in $K_{\downarrow,d}$, the intercept of the equation in Fig. 5.3a (see previous subsection) suggests that clouds are not the primary factor.

All the three algorithms reduce the MBE and RMSE of $K_\downarrow$, $K_{\downarrow,b}$, and $K_{\downarrow,d}$ in comparison to the original MERRA-2 values. The RF model performs the best overall, minimizing

the RMSE and maximizing r^2 for both $K_\downarrow$ (RMSE = 19.2 W m^{-2}; $r^2 = 0.93$) and $K_{\downarrow,\mathrm{d}}$ (RMSE = 10.1 W m^{-2}; $r^2 = 0.90$). The Taylor diagrams for each individual fold (from the 10-fold cross-validation), along with the results for both the $k_{\mathrm{t,O}}$ and $k_{\mathrm{t,R}}$ models, are in Figs. 5.4 and 5.5. The RF model consistently outperforms the others for every fold (with one exception; see below). For $K_{\downarrow,\mathrm{d}}$, the MLR model is not as good as the RF model but is better than the $k_{\mathrm{t,R}}$ and $k_{\mathrm{t,O}}$ models (Fig. 5.4). For $K_\downarrow$, the $k_{\mathrm{t,O}}$ model performs slightly better than the RF model (Fig. 5.5), which makes sense since $k_{\mathrm{t,O}}$ includes the observed $K_\downarrow$, and thus this model, not useable to correct global datasets, is not shown in Fig. 5.2. That the $k_{\mathrm{t,O}}$ model outperforms the other models for $K_\downarrow$ but not for $K_{\downarrow,\mathrm{d}}$ confirms our hypothesis that the k_{t} model is not appropriate to address biases in $K_{\downarrow,\mathrm{d}}$.
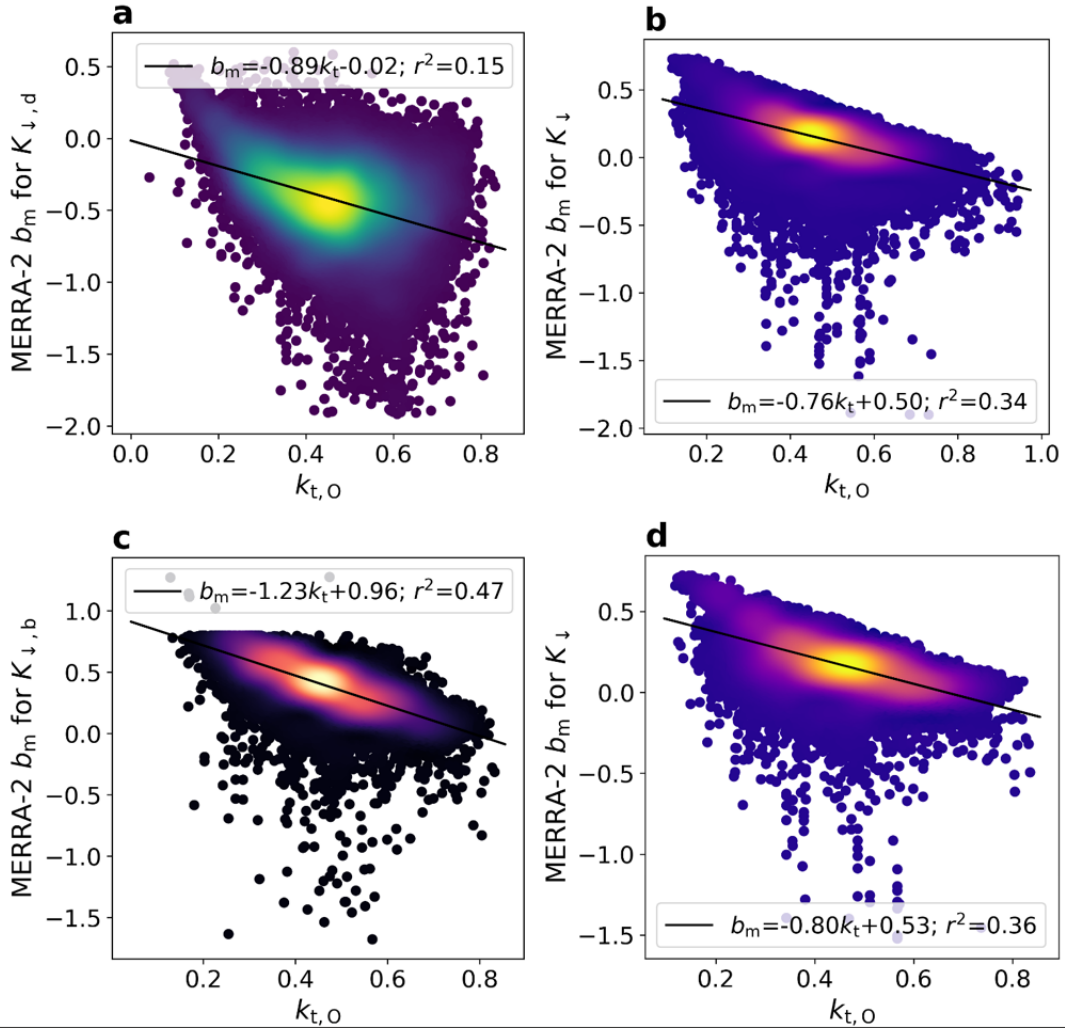
Figure 5.3: Control of clearness index on biases in the MERRA-2 dataset. **a** Bias in diffuse radiation ($K_{\downarrow,\mathrm{d}}$), **b** bias in total shortwave radiation ($K_{\downarrow}$), **c** bias in direct beam radiation ($K_{\downarrow,\mathrm{b}}$), and **d** bias total shortwave radiation ($K_{\downarrow}$) for the sites that also have $K_{\downarrow,\mathrm{b}}$ measurements. Statistical summaries of the associations are noted. Color indicates data density.

Physically, the monthly average radiation components cannot be negative. However, both the $k_{\mathrm{t,R}}$ and MLR models predict a small fraction of negative values for $K_{\downarrow}$ (0.15% for $k_{\mathrm{t,R}}$ and 0.10% for MLR) and $K_{\downarrow,\mathrm{d}}$ (0.24% for $k_{\mathrm{t,R}}$ and 0.01% for MLR). The RF corrected values do not suffer from this drawback.
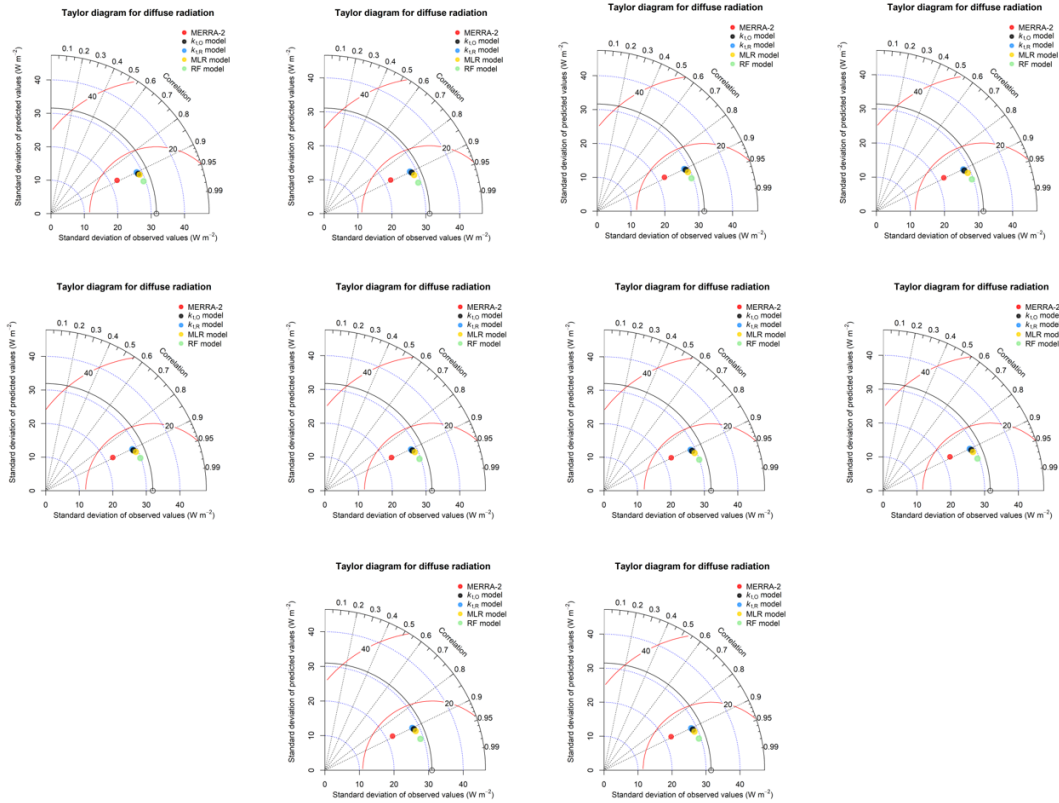
Figure 5.4: Taylor diagrams for diffuse radiation. The 10 Taylor diagrams represent the observed diffuse radiation ($K_{\downarrow,d}$) values and predicted values from MERRA-2, the $k_{t,O}$ models, the $k_{t,R}$ models, the MLR models, and the RF models for all the folds used in the cross-validation.
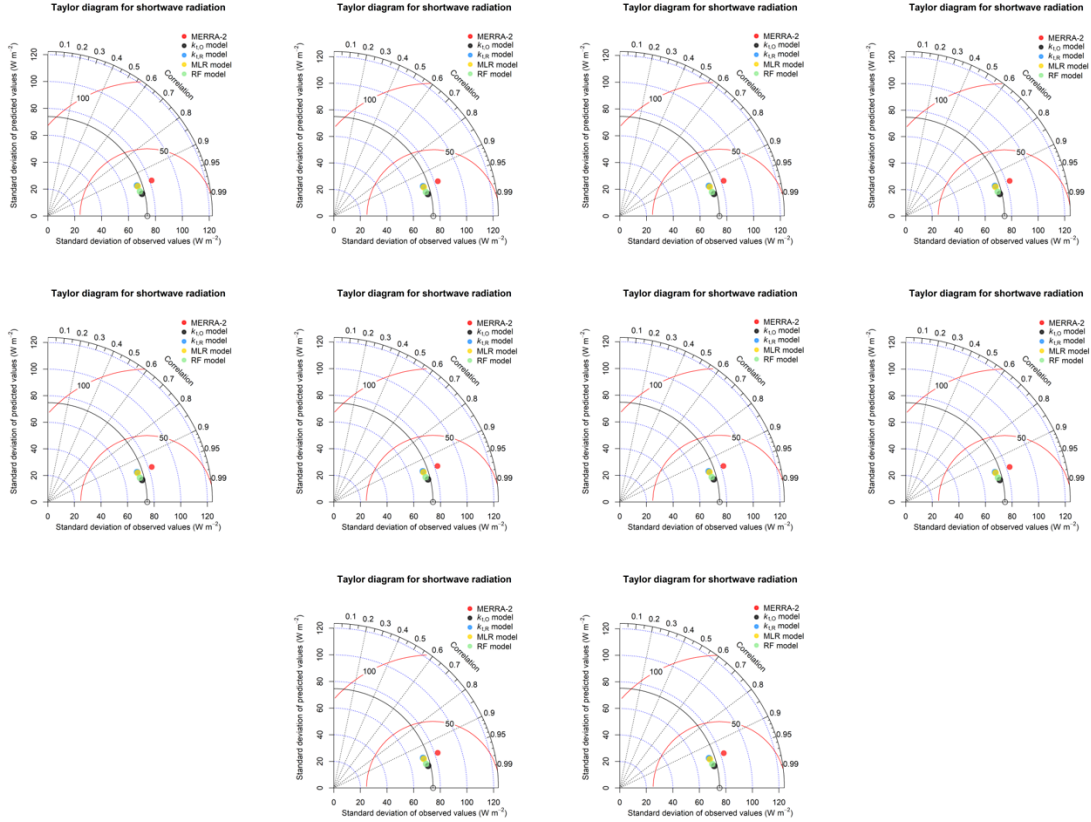
Figure 5.5: Taylor diagrams for total shortwave radiation. The 10 Taylor diagrams represent the total shortwave radiation ($K_\downarrow$) values and predicted values from MERRA-2, the $k_{t,O}$ models, the $k_{t,R}$ models, the MLR models, and the RF models for all the folds used in the cross-validation.

MLR and RF use the same gridded variables as predictors. Fig.5.6 presents the relative importance of each variable. For the MLR model, the importance score was obtained with the method proposed by Lindeman et al. (1980). Briefly, since the stepwise addition of predictors in the MLR model leads to different fractional contributions to the total r^2 for different permutations, this method considers all possible sequences of predictors and then averages the fractional contributions across all the sequences to get the final importance scores. The resulting fractional importance scores add up to unity. For the RF model, a variable importance is the increase in mean square error (MSE) of the predicted values if the same variable is removed from the model. A higher increase in MSE indicates that the variable is more important to the performance of the RF model. For the MLR model, the

most important predictors are the original MERRA-2 radiation value (relative importance of 0.49 ± 0.0 for $K_\downarrow$; 0.46 ± 0.0 for $K_{\downarrow,\mathrm{d}}$) and the solar zenith angle θ_z (relative importance of 0.42 ± 0.0 for $K_\downarrow$; 0.45 ± 0.0 for $K_{\downarrow,\mathrm{d}}$; Figs 5.6a and 5.9b). For the RF model, the two best predictors are different for $K_{\downarrow,\mathrm{d}}$ and for $K_\downarrow$: For $K_{\downarrow,\mathrm{d}}$, COD and CF have the highest importance scores ($224.4 \pm 3.3\%$ for COD; $138.2 \pm 3.1\%$ for CF), and for $K_\downarrow$, AAOD and SAOD have the highest importance scores ($223.6 \pm 16.5\%$ for AAOD; $206.5 \pm 7.5\%$ for SAOD).
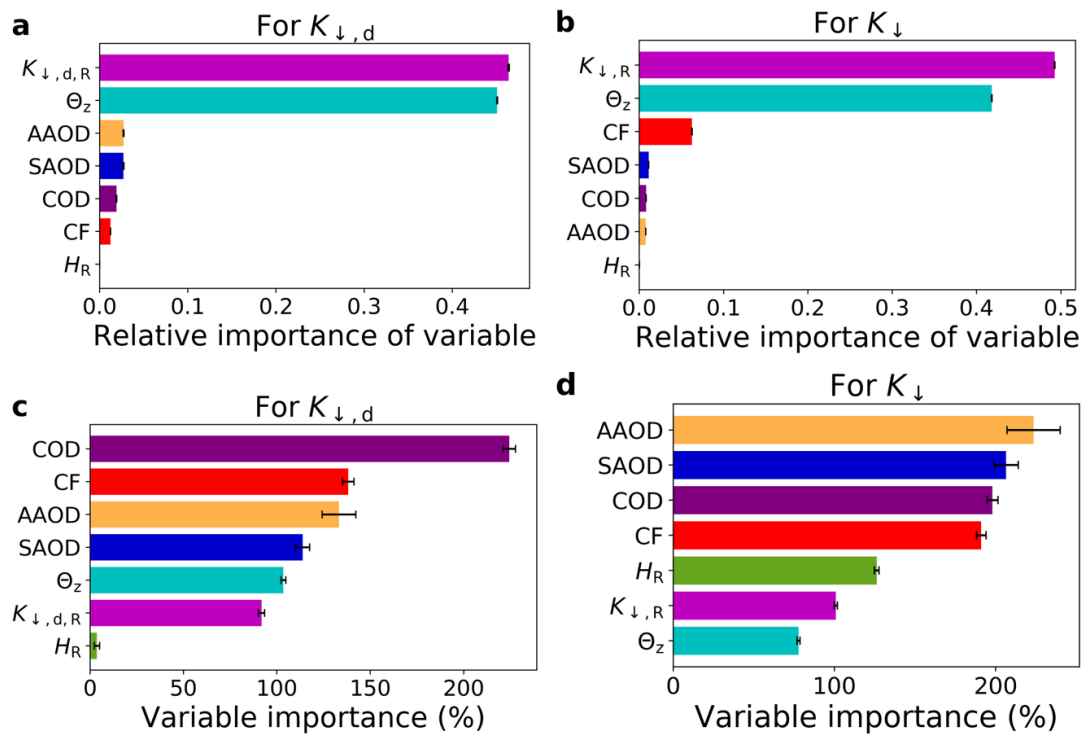
Figure 5.6: Rank of variable importance for bias-correction. **a** and **b**: Variable importance scores for the MLR model; **c** and **d**: permutation importance scores for the RF model.

5.3.6 The BaRAD Dataset

Based on our cross-validation results, we choose the RF model to adjust the biases in the MERRA-2 $K_\downarrow$ and $K_{\downarrow,\mathrm{d}}$. We re-trained the model twice, one for $K_\downarrow$ and the other for $K_{\downarrow,\mathrm{d}}$, using the same predictors and all available GEBA observations. The trained model

was used to bias-adjust the corresponding gridded monthly MERRA-2 fields from 1980 to 2019. The bias-adjusted dataset is referred to as BaRAD. The final BaRAD data deposited in the public archive has gone through two additional post-correction adjustments. First, because of lack of training data in polar regions, there exist a few positive values at some polar grids during polar nights; these positive values constitute 6.5% of the entire dataset for $K_\downarrow$. Here we have forced the bias-corrected $K_\downarrow$ and $K_{\downarrow,d}$ to zero when the corresponding MERRA-2 values are zero in those grids. Second, since $K_{\downarrow,d}$ and $K_\downarrow$ were trained separately, there is a small fraction of gridded data (less than 0.5%) where $K_{\downarrow,d}$ exceeds $K_\downarrow$, which is physically impossible. For these cases, we have set the $K_{\downarrow,d}$ value equal to $K_\downarrow$.

5.4 Data Records

The BaRAD dataset is available in netCDF format and includes the monthly values of $K_\downarrow$ (variable name: K_down), $K_{\downarrow,d}$ (variable name: K_diff), and $K_{\downarrow,b}$ (K_dir) starting from January, 1980. All variables have the unit of W m^{-2}. The dataset can be accessed at Figshare.

5.5 Technical Validation

5.5.1 Comparison of BaRAD Dataset with Other Data Products

In Figs 5.9, 5.8, and 5.9, we compare the spatial, zonal, and seasonal patterns in the BaRAD dataset with the original MERRA-2 dataset. We also compare these patterns with the latest version of the Clouds and the Earth's Radiant Energy System (CERES) surface radiation product (Kato et al., 2018). The CERES dataset provides satellite-based estimates of the Earth's radiative budget (from the surface to the top of the atmosphere)

and clouds. The data are available globally at $1° \times 1°$ resolution from 2000 onwards. The latest version (CERES_SYN1deg_Ed4.1) of the dataset includes monthly estimates of both $K_{\downarrow,\mathrm{d}}$ and $K_{\downarrow}$.
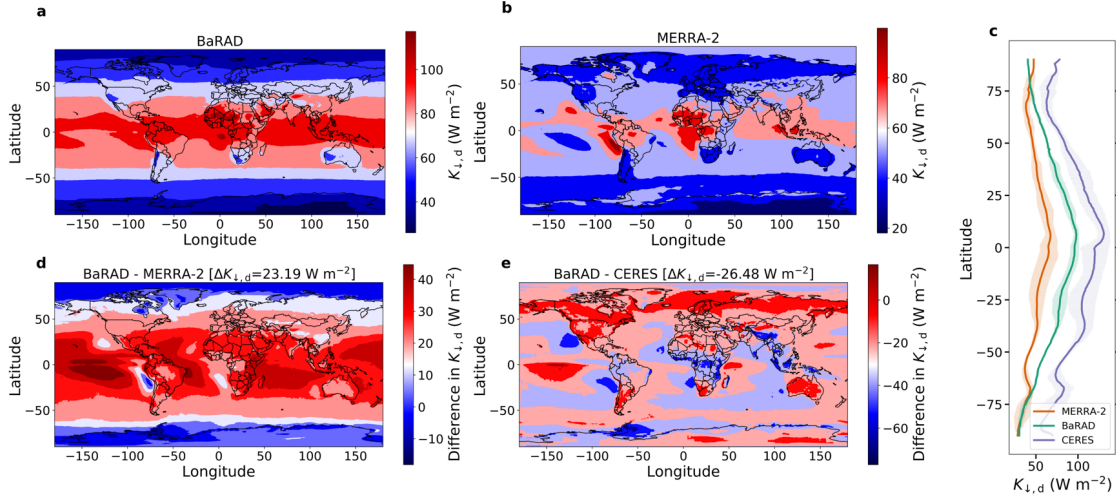
Figure 5.7: Spatial and latitudinal variability in diffuse radiation. Global pattern of diffuse radiation ($K_{\downarrow,\mathrm{d}}$) in **a** the BaRAD product, **b** the MERRA-2 dataset, and **c** the CERES dataset. The grid-wise difference between BaRAD and **e** MERRA-2 and **f** CERES are also shown. Sub-figure **b** shows the mean latitudinal variability of $K_{\downarrow,\mathrm{d}}$ in all three products. The shaded areas represent the standard deviation. The area-weighted mean difference in $K_{\downarrow,\mathrm{d}}$ ($\Delta K_{\downarrow,\mathrm{d}}$) between the BaRAD data and the MERRA-2 and CERES products, respectively, are shown at the top of sub-figures **d** and **e**, respectively.

Although the three datasets show broadly similar latitudinal (Figs 5.7c and 5.8c) and spatial patterns (Figs 5.7d, 5.7e, 5.86d, and 5.8e), $K_{\downarrow,\mathrm{d}}$ in the BaRAD dataset is higher than in MERRA-2 over the Sahara and India and higher than the CERES data over Australia. For $K_{\downarrow}$, BaRAD shows a lower value than both MERRA-2 and CERES over the tropical region. Figures 5.7 and 5.8 also show the mean area-weighted difference ($\Delta K_{\downarrow}$ and $\Delta K_{\downarrow,\mathrm{d}}$) between the BaRAD data and the MERRA-2 and CERES products, respectively. The global mean $K_{\downarrow}$ and $K_{\downarrow,\mathrm{d}}$ are 167.9 and 75.8 W m^{-2}, respectively, according to BaRAD. In comparison, the global mean $K_{\downarrow}$ is higher at 185.4 W m^{-2} and 185.9 W m^{-2} according to MERRA-2 and CERES respectively, and the global mean $K_{\downarrow,\mathrm{d}}$ is lower at 52.6 W m^{-2} according to MERRA-2 and higher at 102.4 W m^{-2} according to CERES.
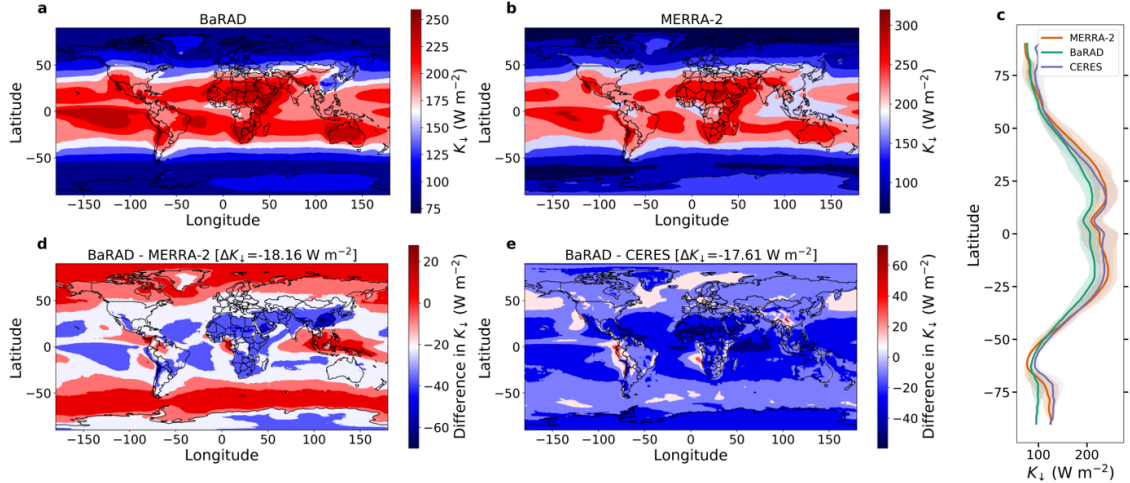
Figure 5.8: Spatial and latitudinal variability in shortwave radiation. Global pattern of shortwave radiation ($K_\downarrow$) in **a** the BaRAD product, **b** the MERRA-2 dataset, and **c** the CERES dataset. The grid-wise difference between BaRAD and **e** MERRA-2 and **f** CERES are also shown. Sub-figure **b** shows the mean latitudinal variability of $K_\downarrow$ in all three products. The shaded areas represent the standard deviation. The area-weighted mean difference in $K_\downarrow$ (ΔK) between the BaRAD data and the MERRA-2 and CERES products, respectively, are shown at the top of sub-figures **d** and **e**, respectively.

We calculate the seasonal trends of $K_{\downarrow,d}$ and $K_\downarrow$ in the northern and southern hemisphere grids (Fig. 5.9). We show the seasonality separately for the two hemispheres. Although there are large differences in the magnitude of the three datasets the seasonal variation is captured by the BaRAD dataset compared to the other two. For instance, the highest northern hemisphere averages are during the boreal summer and the lowest values are during the winter; vice versa for the southern hemisphere. These patterns are evident in all the datasets.
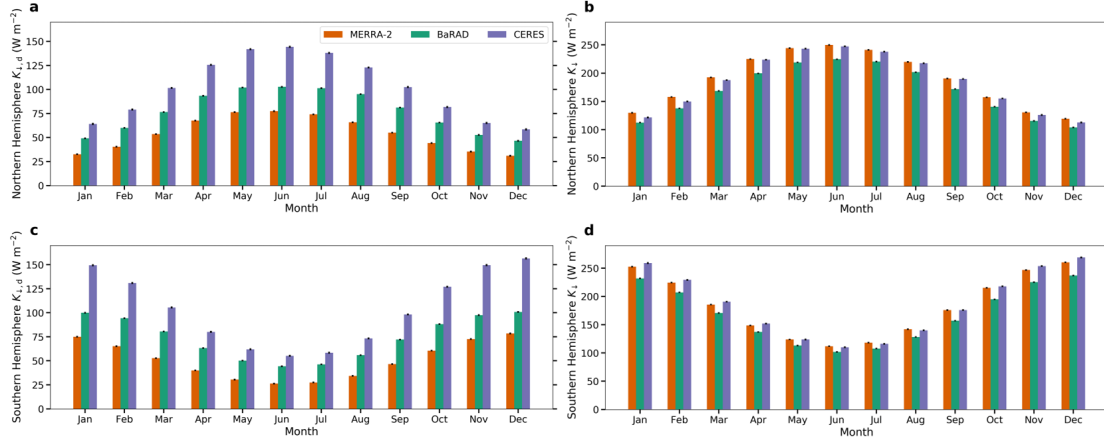
Figure 5.9: Seasonal variability in all products. Monthly variability in diffuse radiation ($K_{\downarrow,\mathrm{d}}$) in MERRA-2, BaRAD, and CERES for **a** the northern hemisphere and **c** the southern hemisphere. Sub-figures **b** and **d** are the same, but for total shortwave radiation ($K_{\downarrow}$). The error bars show the standard errors for each month.

We also compare the BaRAD dataset with the newly developed $K_{\downarrow}$ and $K_{\downarrow,\mathrm{d}}$ datasets from the EPIC measurements between 2016 and 201921. The EPIC instrument housed on the Deep Space Climate Observatory (DSCOVR) satellite, takes narrow band spectral images of the sunlit face of Earth for 10 channels every 60 to 100 min. The dataset generated by Hao et al. (2020) is available at $0.1° \times 0.1°$ resolution and is based on a random forest algorithm trained using in situ observations and the EPIC-derived variables (Hao et al., 2019). Here we compare the available observations with the BaRAD data for the same period. Although the EPIC-based dataset has several advantages over many existing global estimates of $K_{\downarrow,\mathrm{d}}$, namely the much higher spatial and temporal (up to hourly) resolution, it is not ideal for studying climatological trends. The EPIC instrument is affected by cloud cover and downtime. Thus, the EPIC data are interrupted by data gaps, with 5.1% of days missing between 2016 and 2019. Moreover, the product is only available over land. We regridded the EPIC-derived data to the native MERRA-2 resolution using a nearest neighbor interpolation and compared the spatial and latitudinal trends in the $K_{\downarrow,\mathrm{d}}$ and $K_{\downarrow}$ with the BaRAD values (Fig. 5.10). Overall, the global mean $K_{\downarrow,\mathrm{d}}$ in BaRAD is

close to the EPIC-derived values, with the MBE of only -0.72 W m^{-2}. Greater differences are seen for $K_\downarrow$ with BaRAD underestimating it by 22.55 W m^{-2}. Many of the differences between the two products occur over Africa, as also seen from the latitudinal trends (Figs 5.10b and 5.10d). It is important to note that the in situ observations used in Hao et al. (2020) to evaluate the product lacks spatial representation over central Africa, while the GEBA observations are much more frequent here, at least for $K_\downarrow$ (Fig. 5.1). For $K_{\downarrow,\mathrm{d}}$, both GEBA and the datasets used in Hao et al. (2020) are sparse, which could explain the low $\Delta K_{\downarrow,\mathrm{d}}$ for this variable.
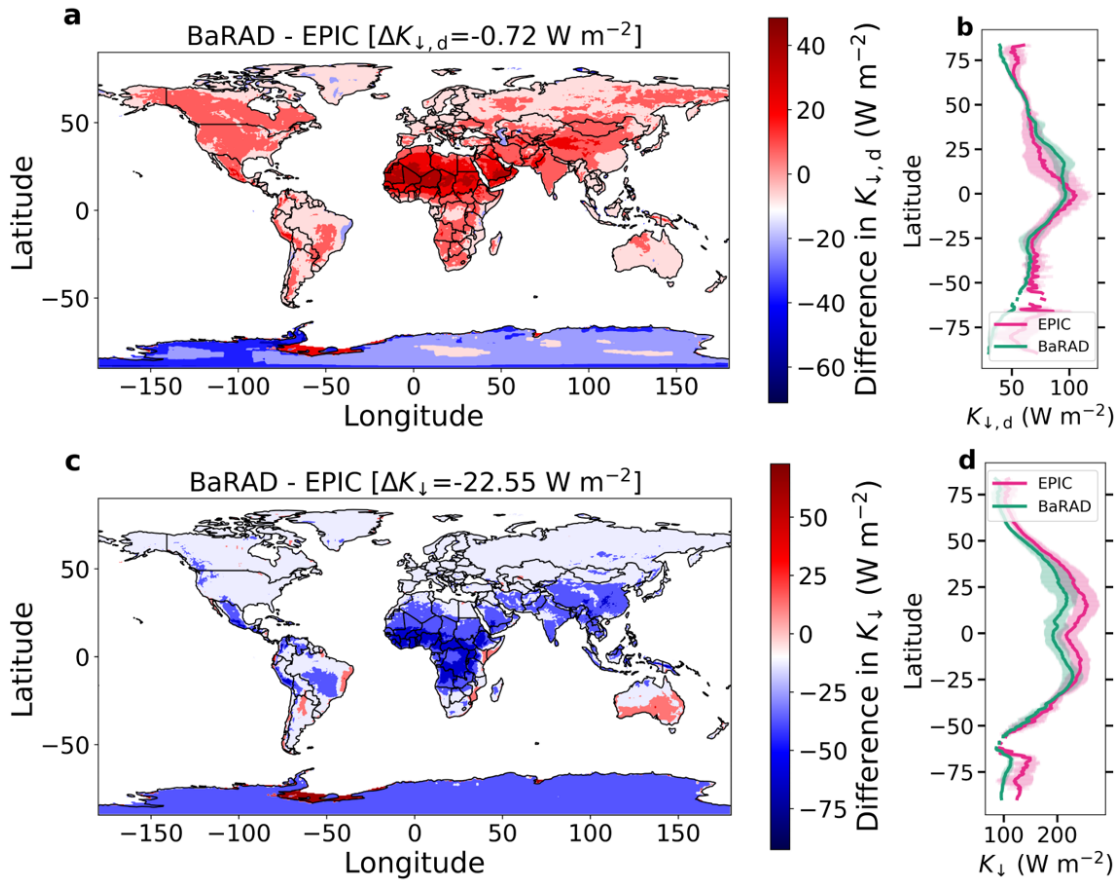
Figure 5.10: Comparison of spatial and latitudinal variability in total shortwave radiation and diffuse radiation between the BaRAD product and EPIC-derived estimates. Spatial patterns of the grid-wise difference in **a** diffuse radiation ($K_{\downarrow,d}$) and **b** total shortwave radiation ($K_{\downarrow}$) over land. Sub-figure **b** and **d** show the mean latitudinal variability of $K_{\downarrow,d}$ and $K_{\downarrow}$ over land for the two products. The shaded areas represent the standard deviation. The area-weighted difference in $K_{\downarrow,d}$ ($\Delta K_{\downarrow,d}$) and $K_{\downarrow}$ ($\Delta K_{\downarrow}$) between the BaRAD product and the EPIC-derived dataset are shown at the top of sub-figures **a** and **c**, respectively.

5.5.2 Long-term Trends

Figures S7a, S7b, S7c, and S7d show the 40-year trend in $K_{\downarrow}$ and $K_{\downarrow,d}$ in the MERRA-2 and the BaRAD dataset for the two hemispheres. The two datasets show similar trends for $K_{\downarrow}$ and $K_{\downarrow,d}$, but they are offset by about 20 W m^{-2} for both $K_{\downarrow}$ and $K_{\downarrow,d}$. More importantly, the BaRAD dataset captures the impacts of the two large volcanic eruptions, El Chichón in 1982 and Mount Pinatubo in 1991, on $K_{\downarrow,d}$, particularly in the northern

hemisphere (Fig. 5.12), which is also seen in the MERRA-2 dataset36. For the northern hemisphere, the anomaly in $K_\downarrow$ from the mean of the previous and subsequent years (1981 and 1983) due to the El Chichón eruption was -1.95 W m^{-2} in MERRA-2 versus 2.81 W m^{-2} in the BaRAD dataset. For the Mount Pinatubo eruption, the $K_\downarrow$ anomaly was -1.28 W m^{-2} in MERRA-2 versus -1.39 W m^{-2} in the BaRAD dataset. For northern hemisphere $K_{\downarrow,d}$, there was an increase by 2.67 W m^{-2} in 1982 compared to the average of the values in 1981 and 1983 in MERRA-2 and 2.13 W m^{-2} for BaRAD. Similarly, in 1991, the northern hemisphere $K_{\downarrow,d}$ was higher by 1.75 W m^{-2} compared to 1990 and 1992 in MERRA-2 versus 1.14 W m^{-2} in BaRAD.
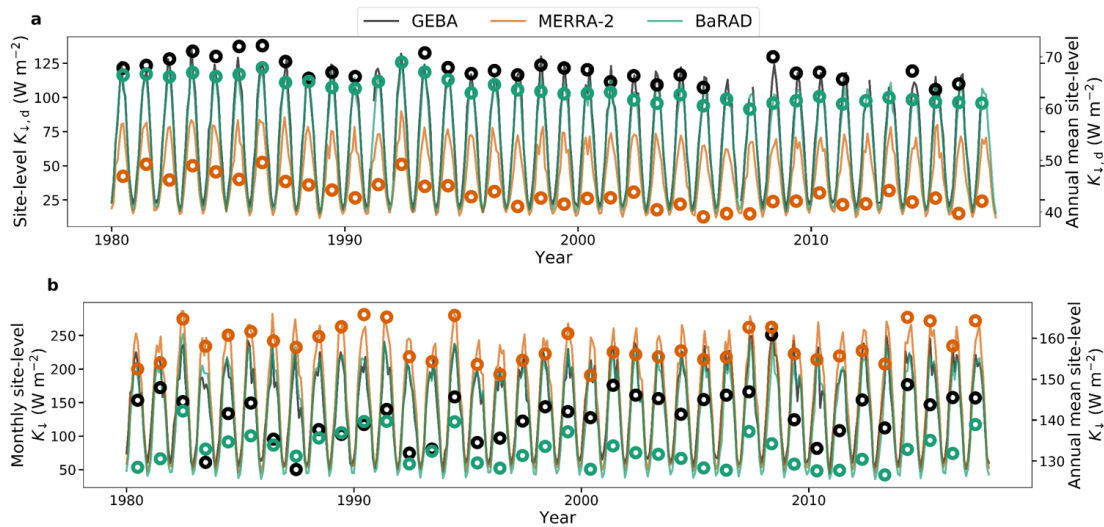
Figure 5.11: Long-term trends at site scale. Long-term trends in **a** diffuse radiation ($K_{\downarrow,d}$) and **b** total shortwave radiation ($K_\downarrow$) for GEBA site with longest archival history, along with corresponding gridded values from MERRA-2 and BaRAD. The monthly values are plotted on the left y-axes and the annual averages are on the right y-axes.

Figures 5.11a and 5.11b are two examples of site-level comparison with observations made at Sapporo, Japan (43.05° N, 141.33° E for $K_\downarrow$) and Würzburg, Germany (49.77° N, 9.97° E for $K_{\downarrow,d}$). These two sites are chosen because they have the longest data availability. The BaRAD dataset replicates both the magnitude and long-term variability of the site observations ($r^2 = 0.99$ and MBE = -3.65 W m^{-2} for $K_{\downarrow,d}$; $r^2 = 0.97$ and MBE = -8.64 W

m^{-2} for $K_\downarrow$). On the other hand, MERRA-2 captures the variability ($r^2 = 0.98$ for $K_{\downarrow,\text{d}}$; 0.97 for $K_\downarrow$), but has larger biases for both $K_{\downarrow,\text{d}}$ (MBE = -22.95 W m^{-2}) and $K_\downarrow$ (MBE = 16.85 W m^{-2}).
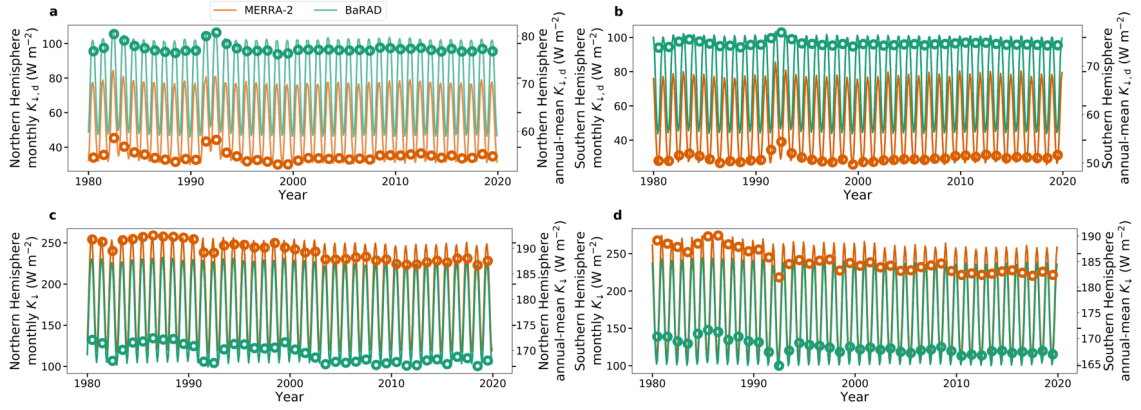
Figure 5.12: Long-term trends at regional scale. Sub-figures **a**, **b**, **c**, and **d** show the long-term regional trends in $K_{\downarrow,\text{d}}$ and $K_\downarrow$ for northern and southern hemispheres, respectively. The monthly values are plotted on the left y-axes and the annual averages are on the right y-axes.

5.6 Usage Notes

The BaRAD dataset developed here performs well when compared to the GEBA dataset and captures the seasonal, latitudinal, and long-term trends in $K_\downarrow$ and $K_{\downarrow,\text{d}}$. However, the dataset can be affected by bias sampling in the GEBA dataset. The GEBA dataset is overrepresented in the global north, especially in Europe and China (Wild et al., 2017). A second source of bias is associated with the lack of training data over ocean surfaces. Finally, polar regions are under-sampled by GEBA as noted above. We urge caution when using this dataset over polar regions and ocean surfaces. For land grids in the southern hemisphere, although there are many observations for $K_\downarrow$, there are fewer stations with $K_{\downarrow,\text{d}}$ measurements. As such, when possible, we suggest independent validation of the BaRAD $K_{\downarrow,\text{d}}$ data before its applications for southern hemisphere land grids.

Chapter 6

Major Results and Future Work

6.1 Major Results

Chapter 2 of the dissertation found large asymmetries in the shortwave and longwave radiative effects of aerosols, both regionally and diurnally. During daytime, both the shortwave and longwave radiative effects are active and the shortwave effect is much stronger than the longwave effect. During night, only the longwave radiative effect of aerosols is active during a period of higher near-surface stability, leading to disproportionately larger temperature response than during daytime. Overall, the climate sensitivity to the longwave radiative effect is higher than that for the shortwave radiative effect. This is true when averaged for the whole day due to the day-night assymetry and also due to the incidental co-location of regions of high climate sensitivity with regions with high dust aerosol loading, which have a strong interaction with longwave radiation.

Chapter 3 showed that in addition to the generally known impact of aerosol diffuse radiation fertilization on terrestrial evapotranspiration and land carbon uptake, aerosols can also cool down the surface through non-radiative means. The evaporative cooling due to aerosols is stronger than the local temperature response through the radiative pathways for landscapes with medium to high vegetation density. When separating the impact of the

global dimming and diffuse radiative fertilization effect of aerosols, the fertilization effect showed a stronger impact on gross primary productivity and the global dimming was more important for latent heat flux and surface temperature within the Community Earth System Modeling framework.

Chapter 4 showed large discrepancies in the diffuse radiation fields among the current-generation global gridded products. When moving from the MERRA-2 reanalysis to the CERES dataset, the global mean diffuse fraction almost doubles. A strong correlation is seen between biases in cloud cover and the difference in diffuse radiation among the products. Although aerosols have a smaller impact on the overall biases, they do strongly influence the long-term trends in diffuse radiation, particularly over China.

Chapter 5 tests different algorithms, both conceptual and data-driven ones, to reduce the biases in the radiation fields of the MERRA-2 reanalysis. It was found that clearness index based correction algorithms cannot account for the diffuse/direct partitioning, but purely data-driven algorithms perform quite well. Using such an algorithm, a 40-year monthly gridded dataset at the MERRA-2 native resolution that includes both total incoming shortwave and diffuse radiation at the surface was developed.

6.2 Future Work

6.2.1 Confirming Influence of Surface Radiative Effect on Global Climate Sensitivity to Aerosols

The reason for the higher climate sensitivity to aerosols compared to greenhouse gases has been an open question (Marvel et al., 2015; Rotstayn et al., 2015; Shindell, 2014). In **Chapter 2**, I showed that the difference in climate sensitivity between aerosols and well-mixed greenhouse gases can be explained by the additional local surface temperature

perturbation due to the high surface radiative effect of aerosols. However, this diagnosis was done offline by comparing the overall temperature response to aerosols due to the surface radiative forcing with values found in a previous study (Marvel et al., 2015). Although the conceptual argument is valid, these values are not directly comparable since they come from different models. There is a need to further examine this using perturbation experiments by turning on and off anthropogenic aerosols and greenhouse gases. Doing so using different Earth System Models can tell us about the generalizability of this theory and improve our understanding of aerosol impact on the Earth system.

6.2.2 Comparing Impact of Diffuse Radiation on Terrestrial Processes Across Different Leaf-to-Canopy Upscaling Schemes

I used the Community Land Model in **Chapter 3** to estimate the impact of the diffuse radiation fertilization effect on terrestrial processes. This model uses a two-big-leaf approach to scaling energy and carbon fluxes from the leaf to the vegetation canopy. There are currently several other upscaling schemes used in CMIP6 model. It is necessary to compare the sensitivity of the terrestrial water and carbon budgets to diffuse radiation fertilization across these models. Quantifying the range of this sensitivity can provide better constrains on modeled terrestrial evapotranspiration and carbon sink in Earth System Models (ESMs), which currently show large inter-model variability. A good start may be to compare the corresponding sensitivities within CLM using the recently developed multi-layer plant canopy model (Bonan et al., 2018) and the default two-big-leaf approach.

6.2.3 Examining Long-Term Feedback Between Diffuse Radiation and Surface Vegetation Cover

An important question that arises from the results in **Chapter 3** is whether there is any possible feedback between vegetation state and incoming diffuse radiation. The few studies which have attempted to answer this question have not done so using dynamic vegetation schemes (Rap et al., 2018; Wang et al., 2019). With aerosol loading expected to change drastically under most future scenarios (Westervelt et al., 2015), with reduced aerosols under most IPCC scenarios due to clean-up efforts and potential increases in stratospheric aerosols in proposed geoengineering schemes, we need to better constrain this feedback for a more complete understanding of the role of aerosols on current and future surface climate. Evidently, this feedback will also depend on model parameterization of vegetation-radiation interactions, and thus requires coordinated efforts across modeling groups. For CLM, running the model in land-only mode, once using satellite phenology and once while turning biogeochemistry on, would allow one to isolate how the canopy state responds to this potential feedback.

6.2.4 Improving Observational Constraints on Diffuse Radiative Fertilization Effect

Earth system models were used for the majority of this dissertation work since there is a lack of simultaneous observations of turbulent fluxes, aerosols, and diffuse radiation (Fig. 1.1). Although I comprehensively evaluate the bulk simulations against available satellite and ground-based observations, the perturbation signals due to aerosols are much harder to isolate in observations. A concentrated effort is needed to set up measurement platforms in regions with both high aerosol loading and high vegetation density, such as in

the Amazon, in the Congo Basin, and parts of south Asia. We would expect stronger signal to noise ratios in these regions, which would give us improved observational constraints on the diffuse radiation fertilization effect; also relevant for model evaluation.

6.2.5 Updating Internal Diffuse/Direct Partitioning Schemes for Land-Only Model Simulations

In **Chapter 3**, I forced the Community Land Model with the diffuse/direct partitioning from the Community Atmosphere Model. This is done since, by default, the land model has an internal partitioning scheme based on a multregression fit that only depends on total irradiance. Evidently, this not an explicit function of aerosols or clouds. Different land models have different partitioning schemes when diffuse radiation is not provided, from assumptions of constant diffuse fraction to the use of simple linear estimates. Given the importance of diffuse radiation on surface processes, it is necessary to update these internal partitioning schemes when the models are run in land-only mode without explicit representation of diffuse radiation, such as in the Land Use Model Intercomparison Project. Doing so in a consistent manner can remove one source of uncertainty for multi-model comparisons.

6.2.6 Better Constraining Diffuse Radiation Across Atmosphere Models

In **Chapter 4**, I found that clouds strongly influenced the difference in diffuse radiation in global gridded products (Fig. 4.9). Since a lot of the radiation schemes used in these products are also used in operational Earth System Models, one would expect similar variability in diffuse radiation in them. Future atmosphere model development should consider how well diffuse radiation is captured by these models, through both radiative

transfer parameterization and cloud and aerosol inputs to the radiation codes.

6.2.7 Understanding Potential Biophysical Impacts of Aerosols Through Indirect Effect

All of the results in **Chapters 2 and 3** focus on the direct effect of aerosols. The radiation diagnostics used assume the indirect effect for both aerosol and non-aerosol cases. However, the influence of aerosols on clouds would contribute to both the surface radiative effect and changes in diffuse fraction of sunlight. Future research should attempt to separate the direct and indirect effects of aerosols on surface climate through both radiative and non-radiative pathways. Since clouds and the land carbon sink are the two largest sources of uncertainty in future projections of climate change, better examining the magnitude and direction of these biophysical processes can help us predict more realistic scenarios and enhance our overall understanding of the Earth system.

6.3 References

1. Achard, F., Eva, H. D., Stibig, H. J., Mayaux, P., Gallego, J., Richards, T., & Malingreau, J. P. (2002). Determination of Deforestation Rates of the Worlds Humid Tropical Forests. Science 297, 999–1002.

2. Ackerman, A. S., Toon, O. B., Taylor, J. P., Johnson, D. W., Hobbs, P. V., & Ferek, R. J. (2015). Effects of aerosols on cloud albedo: Evaluation of twomey's parameterization of cloud susceptibility using measurements of ship tracks. Journal of the Atmospheric Sciences, 72(9).

3. Albrecht, B. A. (1989). Aerosols, cloud microphysics, and fractional cloudiness. Science, 245(4923):1227–1231.

4. Alexandersson, Hans. (1986). A homogeneity test applied to precipitation data. Journal of climatology, 6, no. 6, 661-675.

5. Alizadeh Choobari, O., Zawar-Reza, P., & Sturman, A. (2013). Simulation of the spatial distribution of mineral dust and its direct radiative forcing over australia. Tellus B: Chemical and Physical Meteorology, 65(1):19856.

6. Alkama, R. & Cescatti, A. (2016). Biophysical climate impacts of recent changes in global forest cover. Science, 351, 600–604.

7. Andreae, M. O., Jones, C. D., & Cox, P. M. (2005). Strong present-day aerosol cooling implies a hot future. Nature, 435(7046):1187–1190.

8. Ångström, A. (1929). On the atmospheric transmission of sun radiation and on dust in the air. Geografiska Annaler, 11(2), 156-166.

9. Aumann, H. H., Chen, X., Fishbein, E., Geer, A., Havemann, S., Huang, X., ... & Yung, Y. L. (2018). Evaluation of radiative transfer models with clouds. Journal of Geophysical Research: Atmospheres, 123(11), 6142-6157.

10. Baldocchi, D., Falge, E., Gu, L., Olson, R., Hollinger, D., Running, S., ... & Wofsy, S. (2001). FLUXNET: A new tool to study the temporal and spatial variability of ecosystem-scale carbon dioxide, water vapor, and energy flux densities. Bulletin of the American Meteorological Society, 82(11), 2415-2434.

11. Ban-Weiss, G. A., Bala, G., Cao, L., Pongratz, J., & Caldeira, K. (2011). Climate forcing and response to idealized changes in surface latent and sensible heat. Environmental Research Letters, 6(3), 034032.

12. Bellouin, N., Boucher, O., Haywood, J., & Reddy, M. S. (2005). Global estimate of aerosol direct radiative forcing from satellite measurements. Nature, 438, 1138–1141.

13. Boilley, A. & Wald, L. (2015). Comparison between meteorological re-analyses from ERA-Interim and MERRA and measurements of daily solar irradiation at surface. Renewable Energy, 75, 135–143.

14. Bonan, G. B. (2008). Forests and Climate Change: Forcings, Feedbacks, and the Climate Benefits of Forests. Science, 320, 1444–1449.

15. Bonan, G. B., Lawrence, P. J., Oleson, K. W., Levis, S., Jung, M., Reichstein, M., ... & Swenson, S. C. (2011). Improving canopy processes in the Community Land Model version 4 (CLM4) using global flux fields empirically inferred from FLUXNET data. Journal of Geophysical Research: Biogeosciences, 116(G2).

16. Bonan, G. B., Oleson, K. W., Fisher, R. A., Lasslop, G., & Reichstein, M. (2012). Reconciling leaf physiological traits and canopy flux data: Use of the TRY and

FLUXNET databases in the Community Land Model version 4. Journal of Geophysical Research: Biogeosciences, 117(G2).

17. Bonan, G. B., Patton, E. G., Harman, I. N., Oleson, K. W., Finnigan, J. J., Lu, Y., & Burakowski, E. A. (2018). Modeling canopy-induced turbulence in the Earth system: a unified parameterization of turbulent exchange within plant canopies and the roughness sublayer (CLM-ml v0). Geoscientific Model Development, 11(4), 1467-1496.

18. Bosilovich, M. G., Robertson, F. R., & Chen, J. (2011). Global energy and water budgets in MERRA. Journal of Climate, 24(22), 5721-5739.

19. Boucher, O., Randall, D., Artaxo, P., Bretherton, C., Feingold, G., Forster, P., ... & Zhang, X. Y. (2013). Clouds and aerosols. In Climate change 2013: the physical science basis. Contribution of Working Group I to the Fifth Assessment Report of the Intergovernmental Panel on Climate Change (pp. 571-657). Cambridge University Press.

20. Breiman, L. (2001). Random forests. Machine learning, 45, 5–32.

21. Briegleb, B. P. (1992). Delta-Eddington approximation for solar radiation in the NCAR Community Climate Model. Journal of Geophysical Research: Atmospheres, 97(D7), 7603-7612.

22. Bright, R. M., Davin, E., O'Halloran, T., Pongratz, J., Zhao, K., & Cescatti, A. (2017). Local temperature response to land cover and management change driven by non-radiative processes. Nature Climate Change, 7, 296–302.

23. Buchard, V., Randles, C. A., Da Silva, A. M., Darmenov, A., Colarco, P. R., Govindaraju, R., ... & Yu, H. (2017). The MERRA-2 aerosol reanalysis, 1980 onward. Part II: Evaluation and case studies. Journal of Climate, 30(17), 6851-6872.

24. Burakowski, E., Tawfik, A., Ouimette, A., Lepine, L., Novick, K., Ollinger, S., ... & Bonan, G. (2018). The role of surface roughness, albedo, and Bowen ratio on ecosystem energy balance in the Eastern United States. Agricultural and Forest Meteorology, 249, 367-376.

25. Cao, C., Lee, X., Liu, S., Schultz, N., Xiao, W., Zhang, M., & Zhao, L. (2016). Urban heat islands in china enhanced by haze pollution. Nature Communications, 7(1), 1-7.

26. Carrer, D., Roujean, J. L., Lafont, S., Calvet, J. C., Boone, A., Decharme, B., ... & Gastellu-Etchegorry, J. P. (2013). A canopy radiative transfer scheme with explicit FAPAR for the interactive vegetation model ISBA-A-gs: Impact on carbon fluxes. Journal of Geophysical Research: Biogeosciences, 118(2), 888-903.

27. Chakraborty, T. & Lee, X. (2019). Land Cover Regulates the Spatial Variability of Temperature Response to the Direct Radiative Effect of Aerosols. Geophysical Research Letters, 46, 8995–9003.

28. Chakraborty, T. & Lee, X. (2021). Large Differences in Diffuse Solar Radiation Among Current-Generation Reanalysis and Satellite-Derived Products. Journal of Climate.

29. Chakraborty, T., Lee, X. & Lawrence, D. (2021). Strong Local Evaporative Cooling Over Land Due to Atmospheric Aerosols. Journal of Advances in Modeling Earth Systems, 13, e2021MS002491.

30. Chakraborty, T., Sarangi, C., & Lee, X. (2021). Reduction in human activity can enhance the urban heat island: insights from the COVID-19 lockdown. Environmental Research Letters, 16(5), 054060.

31. Chakraborty, T., Sarangi, C., Krishnan, M., Tripathi, S. N., Morrison, R., & Evans, J. (2019). Biases in model-simulated surface energy fluxes during the Indian monsoon onset period. Boundary-Layer Meteorology, 170(2), 323-348.

32. Chen, M., & Zhuang, Q. (2014). Evaluating aerosol direct radiative effects on global terrestrial ecosystem carbon dynamics from 2003 to 2010. Tellus B: Chemical and Physical Meteorology, 66(1), 21808.

33. Choobari, O. A., Zawar-Reza, P. & Sturman, A. (2013). Simulation of the spatial distribution of mineral dust and its direct radiative forcing over Australia. Tellus B: Chemical and Physical Meteorology, 65, 19856.

34. Chou, M. D., & Suarez, M. J. (1999). A solar radiation parameterization for atmospheric studies (Vol. 15, p. 38). National Aeronautics and Space Administration, Goddard Space Flight Center, Laboratory for Atmospheres, Climate and Radiation Branch.

35. Chung, C. E., Ramanathan, V., Kim, D., & Podgorny, I. A. (2005). Global anthropogenic aerosol direct forcing derived from satellite and ground-based observations. Journal of Geophysical Research: Atmospheres, 110(D24).

36. Clark, D. B., Mercado, L. M., Sitch, S., Jones, C. D., Gedney, N., Best, M. J., ... & Cox, P. M. (2011). The Joint UK Land Environment Simulator (JULES), model description–Part 2: carbon fluxes and vegetation dynamics. Geoscientific Model Development, 4(3), 701-722.

37. Cohan, D. S., Xu, J., Greenwald, R., Bergin, M. H., & Chameides, W. L. (2002). Impact of atmospheric aerosol light scattering and absorption on terrestrial net primary productivity. Global Biogeochemical Cycles, 16(4).

38. Dai, Y., Dickinson, R. E., & Wang, Y. P. (2004). A two-big-leaf model for canopy temperature, photosynthesis, and stomatal conductance. Journal of Climate, 17(12), 2281-2299.

39. Davin, E. L., & Seneviratne, S. I. (2012). Role of land surface processes and diffuse/direct radiation partitioning in simulating the European climate. Biogeosciences, 9(5), 1695-1707.

40. Dirmeyer, P. A. (2011). A history and review of the Global Soil Wetness Project (GSWP). Journal of Hydrometeorology, 12(5), 729-749.

41. Feingold, G., Eberhard, W. L., Veron, D. E., and Previdi, M. (2003). First measurements of the twomey indirect effect using ground-based remote sensors. Geophysical Research Letters, 30(6).

42. Feng, Y., D. Chen, & X. Zhao, (2018). Estimated long-term variability of direct and diffuse solar radiation in North China during 1959–2016. Theoretical and Applied Climatology, 137, 153–163.

43. Forster, P., Ramaswamy, V., Artaxo, P., Berntsen, T., Betts, R., Fahey, D. W., ... & Van Dorland, R. (2007). Changes in atmospheric constituents and in radiative forcing. Chapter 2. In Climate Change 2007. The Physical Science Basis.

44. Frank, C. W., Wahl, S., Keller, J. D., Pospichal, B., Hense, A., & Crewell, S. (2018). Bias correction of a novel European reanalysis data set for solar energy applications. Solar Energy, 164, 12-24.

45. Freidenreich, S. M., & Ramaswamy, V. (1999). A new multiple-band solar radiative parameterization for general circulation models. Journal of Geophysical Research: Atmospheres, 104(D24), 31389-31409.

46. Gadhavi, H., & Jayaraman, A. (2010). Absorbing aerosols: contribution of biomass burning and implications for radiative forcing. Annales Geophysicae, 28, 103-111.

47. Gelaro, R., McCarty, W., Suárez, M. J., Todling, R., Molod, A., Takacs, L., ... & Wargan, K. (2017). The Modern-Era Retrospective Analysis for Research and Applications, Version 2 (MERRA-2). Journal of Climate, 30, 5419–5454.

48. Gettelman, A., Mills, M. J., Kinnison, D. E., Garcia, R. R., Smith, A. K., Marsh, D. R., ... & Randel, W. J. (2019). The whole atmosphere community climate model version 6 (WACCM6). Journal of Geophysical Research: Atmospheres, 124(23), 12380-12403.

49. Gilgen, H., & Ohmura, A. (1999). The global energy balance archive. Bulletin of the American Meteorological Society, 80(5), 831-850.

50. Giorgi, F. & Avissar, R. (1997). Representation of heterogeneity effects in earth system modeling: Experience from land surface modeling. Rev Geophys, 35(4):413–437.

51. Gu, L. (2003). Response of a Deciduous Forest to the Mount Pinatubo Eruption: Enhanced Photosynthesis. Science, 299, 2035.

52. Gu, L., Baldocchi, D. D., Wofsy, S. C., Munger, J. W., Michalsky, J. J., Urbanski, S. P., & Boden, T. A. (2003). Response of a deciduous forest to the Mount Pinatubo eruption: Enhanced photosynthesis. Science, 299(5615), 2035-2038.

53. Gu, L., Baldocchi, D., Verma, S. B., Black, T. A., Vesala, T., Falge, E. M., & Dowty, P. R. (2002). Advantages of diffuse radiation for terrestrial ecosystem productivity. Journal of Geophysical Research: Atmospheres, 107(D6), ACL-2.

54. Gu, L., Meyers, T., Pallardy, S. G., Hanson, P. J., Yang, B., Heuer, M., ... & Wullschleger, S. D. (2006). Direct and indirect effects of atmospheric conditions

and soil moisture on surface energy partitioning revealed by a prolonged drought at a temperate forest site. Journal of Geophysical Research: Atmospheres, 111(D16).

55. Halthore, R. N., & Schwartz, S. E. (2000). Comparison of model-estimated and measured diffuse downward irradiance at surface in cloud-free skies. Journal of Geophysical Research: Atmospheres, 105(D15), 20165-20177.

56. Ham, S. H., Kato, S., Barker, H. W., Rose, F. G., & Sun-Mack, S. (2014). Effects of 3-D clouds on atmospheric transmission of solar radiation: Cloud type dependencies inferred from A-train satellite data. Journal of Geophysical Research: Atmospheres, 119(2), 943-963.

57. Han, Z., Li, J., Xia, X., & Zhang, R. (2012). Investigation of direct radiative effects of aerosols in dust storm season over east asia with an online coupled regional climatechemistry-aerosol model. Atmospheric environment, 54:688–699.

58. Hansell, R. A., Tsay, S. C., Hsu, N. C., Ji, Q., Bell, S. W., Holben, B. N., ... & Li, Z. (2012). An assessment of the surface longwave direct radiative effect of airborne dust in Zhangye, China, during the Asian Monsoon Years field experiment (2008). Journal of Geophysical Research: Atmospheres 117, D00K39.

59. Hansell, R. A., Tsay, S. C., Hsu, N. C., Ji, Q., Bell, S. W., Holben, B. N., ... & Chen, H. (2012). An assessment of the surface longwave direct radiative effect of airborne dust in Zhangye, China, during the Asian Monsoon Years field experiment (2008). Journal of Geophysical Research: Atmospheres, 117(D16).

60. Hansen, J. E., Sato, M. K. I., Ruedy, R., Nazarenko, L., Lacis, A., Schmidt, G. A., ... & Bell, N. (2005). Efficacy of climate forcings. Journal of Geophysical Research: Atmospheres, 110, D18104.

61. Hansen, M. C., Potapov, P. V., Moore, R., Hancher, M., Turubanova, S. A. A., Tyukavina, A., ... & Kommareddy, A. (2013). High-Resolution Global Maps of 21st-Century Forest Cover Change. Science, 342, 850–853.

62. Hao, D., Asrar, G. R., Zeng, Y., Zhu, Q., Wen, J., Xiao, Q., & Chen, M. (2020). DSCOVR/EPIC-derived global hourly & daily downward shortwave and photosynthetically active radiation data at $0.1° \times 0.1°$ resolution. Earth System Science Data, 12(3), 2209-2221.

63. Hao, D., Asrar, G. R., Zeng, Y., Zhu, Q., Wen, J., Xiao, Q., & Chen, M. (2019). Estimating hourly land surface downward shortwave and photosynthetically active radiation from DSCOVR/EPIC observations. Remote Sensing of Environment, 232, 111320.

64. Harris, E., Sinha, B., Van Pinxteren, D., Tilgner, A., Fomba, K. W., Schneider, J., ... & Herrmann, H. (2013). Enhanced role of transition metal ion catalysis during in-cloud oxidation of SO2. Science, 340(6133), 727-730.

65. Haywood, J. M., Roberts, D. L., Slingo, A., Edwards, J. M. & Shine, K. P. (1997). General Circulation Model Calculations of the Direct Radiative Forcing by Anthropogenic Sulfate and Fossil-Fuel Soot Aerosol. Journal of Climate, 10, 1562–1577.

66. Haywood, J., Francis, P., Osborne, S., Glew, M., Loeb, N., Highwood, E., Tanre, D., Myhre, G., Formenti, P., & Hirst, E. (2003). Radiative properties and direct radiative effect of Saharan dust measured by the c-130 aircraft during shade: 1. solar spectrum. Journal of Geophysical Research: Atmospheres, 108(D18).

67. Hersbach, H., Bell, B., Berrisford, P., Hirahara, S., Horányi, A., Muñoz-Sabater, J., & Simmons, A. (2020). The ERA5 global reanalysis. Quarterly Journal of the Royal Meteorological Society.

68. Hersbach, H., Bell, B., Berrisford, P., Hirahara, S., Horányi, A., Muñoz-Sabater, J., ... & Thépaut, J. N. (2020). The ERA5 global reanalysis. Quarterly Journal of the Royal Meteorological Society, 146(730), 1999-2049.

69. Highwood, E. J., Haywood, J. M., Silverstone, M. D., Newman, S. M., & Taylor, J. P. (2003). Radiative properties and direct effect of Saharan dust measured by the C-130 aircraft during Saharan Dust Experiment (SHADE): 2. Terrestrial spectrum. Journal of Geophysical Research, 108, 8578.

70. Hinds, C. W. (1999). Aerosol Technology: Properties, Behavior, and Measurement of Airborne Particles A Wiley-Interscience Publication 2.

71. Hogan, R. J., & Shonk, J. K. (2013). Incorporating the effects of 3D radiative transfer in the presence of clouds into two-stream multilayer radiation schemes. Journal of the atmospheric sciences, 70(2), 708-724.

72. Hou, Y. T., Moorthi, S., & Campana, K. (2002). Parameterization of solar radiation transfer in the NCEP models.

73. Huang, Y., Dickinson, R. E. & Chameides, W. L. (2006). Impact of aerosol indirect effect on surface temperature over East Asia. Proceedings of the National Academy of Sciences, 103, 4371–4376.

74. Iziomon, M., Mayer, H. & Matzarakis, A. (2000). Empirical models for estimating net radiative flux: A case study for three mid-latitude sites with orographic variability. Astrophysics and Space Science, 273, 313–330.

75. Jiang, B., Zhang, Y., Liang, S., Wohlfahrt, G., Arain, A., Cescatti, A., ... & Zhang, X. (2015). Empirical estimation of daytime net radiation from shortwave radiation and ancillary information. Agricultural and Forest Meteorology, 211, 23-36.

76. Jiang, H., N. Lu, J. Qin, W. Tang, & L. Yao, 2019a: A deep learning algorithm to estimate hourly global solar radiation from geostationary satellite data. Renewable and Sustainable Energy Reviews, 114, 109327.

77. Jiang, H., Yang, Y., Wang, H., Bai, Y., & Bai, Y. (2020). Surface Diffuse Solar Radiation Determined by Reanalysis and Satellite over East Asia: Evaluation and Comparison. Remote Sensing, 12(9), 1387.

78. Jiang, H., Yang, Y., Bai, Y., & Wang, H. (2019). Evaluation of the total, direct, and diffuse solar radiations from the ERA5 reanalysis data in China. IEEE Geoscience and Remote Sensing Letters, 17(1), 47-51.

79. Johnson, B. T. (2003). The semi direct aerosol effect. The University of Reading, Department of Meteorology.

80. Kim, B. G., Schwartz, S. E., Miller, M. A., & Min, Q. (2003). Effective radius of cloud droplets by ground-based remote sensing: Relationship to aerosol. Journal of Geophysical Research: Atmospheres, 108(D23).

81. Johnson, B., Shine, K., & Forster, P. (2004). The semi-direct aerosol effect: Impact of absorbing aerosols on marine stratocumulus. Quarterly Journal of the Royal Meteorological Society, 130(599):1407–1422.

82. Jung, M., Koirala, S., Weber, U., Ichii, K., Gans, F., Camps-Valls, G., ... & Reichstein, M. (2019). The FLUXCOM ensemble of global land-atmosphere energy fluxes. Scientific data, 6(1), 1-14.

83. Kalnay, E., Kanamitsu, M., Kistler, R., Collins, W., Deaven, D., Gandin, L., ... & Joseph, D. (1996). The NCEP/NCAR 40-year reanalysis project. Bulletin of the American meteorological Society, 77(3), 437-472.

84. Kanniah, K. D., Beringer, J., North, P., & Hutley, L. (2012). Control of atmospheric particles on diffuse radiation and terrestrial plant productivity: A review. Progress in Physical Geography, 36(2), 209-237.

85. Kato, S., Rose, F. G., Rutan, D. A., Thorsen, T. J., Loeb, N. G., Doelling, D. R., ... & Ham, S. H. (2018). Surface irradiances of edition 4.0 Clouds and the Earth's Radiant Energy System (CERES) Energy Balanced and Filled (EBAF) data product. Journal of Climate, 31(11), 4501-4527.

86. Kedia, S. & Ramachandran, S. (2009). Variability in aerosol optical and physical characteristics over the Bay of Bengal and the Arabian Sea deduced from Ångström exponents. Journal of Geophysical Research: Atmospheres 114, D14207.

87. Kennedy, A. D., Dong, X., Xi, B., Xie, S., Zhang, Y., & Chen, J. (2011). A comparison of MERRA and NARR reanalyses with the DOE ARM SGP data. Journal of Climate, 24(17), 4541-4557.

88. Kennedy, D., Swenson, S., Oleson, K. W., Lawrence, D. M., Fisher, R., Lola da Costa, A. C., & Gentine, P. (2019). Implementing plant hydraulics in the community land model, version 5. Journal of Advances in Modeling Earth Systems, 11(2), 485-513.

89. Kistler, R., Kalnay, E., Collins, W., Saha, S., White, G., Woollen, J., ... & Fiorino, M. (2001). The NCEP–NCAR 50-year reanalysis: monthly means CD-ROM and documentation. Bulletin of the American Meteorological society, 82(2), 247-268.

90. Knohl, A. & Baldocchi, D. D. (2008). Effects of diffuse radiation on canopy gas exchange processes in a forest ecosystem. Journal of Geophysical Research: Biogeosciences, 113(G2).

91. Knyazikhin, Y., Martonchik, J. V., Myneni, R. B., Diner, D. J., & Running, S. W. (1998). Synergistic algorithm for estimating vegetation canopy leaf area index and fraction of absorbed photosynthetically active radiation from MODIS and MISR data. Journal of Geophysical Research: Atmospheres, 103(D24), 32257-32275.

92. Kobayashi, S., Ota, Y., Harada, Y., Ebita, A., Moriya, M., Onoda, H., ... & Takahashi, K. (2015). The JRA-55 reanalysis: General specifications and basic characteristics. Journal of the Meteorological Society of Japan. Ser. II, 93(1), 5-48.

93. Kokhanovsky, A. & Zege, E. (1997). Optical properties of aerosol particles: A review of approximate analytical solutions. Journal of aerosol science, 28(1):1–21.

94. Kowalczyk, E. A., Wang, Y. P., Law, R. M., Davies, H. L., McGregor, J. L., & Abramowitz, G. (2006). The CSIRO Atmosphere Biosphere Land Exchange (CABLE) model for use in climate models and as an offline model. CSIRO Marine and Atmospheric Research Paper, 13, 42.

95. Kvalevag, M. M. & Myhre, G. (2007). Human impact on direct and diffuse solar radiation during the industrial era. Journal of Climate, 20(19):4874–4883.

96. Lacis, A. A., & Hansen, J. (1974). A parameterization for the absorption of solar radiation in the earth's atmosphere. Journal of Atmospheric Sciences, 31(1), 118-133.

97. Lawrence, D. M., Fisher, R. A., Koven, C. D., Oleson, K. W., Swenson, S. C., Bonan, G., ... & Zeng, X. (2019). The Community Land Model version 5: Description of new features, benchmarking, and impact of forcing uncertainty. Journal of Advances in Modeling Earth Systems, 11(12), 4245-4287.

98. Lawrence, D. M., Hurtt, G. C., Arneth, A., Brovkin, V., Calvin, K. V., Jones, A. D., ... & Shevliakova, E. (2016). The Land Use Model Intercomparison Project

(LUMIP) contribution to CMIP6: rationale and experimental design. Geoscientific Model Development, 9(9), 2973-2998.

99. Lee, K. T., Yao, Y., He, J., Fisher, B., Sheng, X., Lumb, M., ... & Rogers, J. A. (2016). Concentrator photovoltaic module architectures with capabilities for capture and conversion of full global solar radiation. Proceedings of the National Academy of Sciences, 113(51), E8210-E8218.

100. Lee, X., Goulden, M. L., Hollinger, D. Y., Barr, A., Black, T. A., Bohrer, G., ... & Katul, G. (2011). Observed increase in local cooling effect of deforestation at higher latitudes. Nature 479, 384–387.

101. Li, M., Wang, T., Xie, M., Zhuang, B., Li, S., Han, Y., & Chen, P. (2017). Impacts of aerosol-radiation feedback on local air quality during a severe haze episode in Nanjing megacity, eastern China. Tellus B: Chemical and Physical Meteorology, 69(1), 1339548.

102. Li, Z., Niu, F., Fan, J., Liu, Y., Rosenfeld, D., & Ding, Y. (2011). Long-term impacts of aerosols on the vertical development of clouds and precipitation. Nature Geoscience 4, 888–894.

103. Lian, X., Piao, S., Huntingford, C., Li, Y., Zeng, Z., Wang, X., ... & Wang, T. (2018). Partitioning global land evapotranspiration using CMIP5 models constrained by observations. Nature Climate Change, 8(7), 640-646.

104. Liao, H., Seinfeld, J. H., Adams, P. J., & Mickley, L. J. (2004). Global radiative forcing of coupled tropospheric ozone and aerosols in a unified general circulation model. Journal of Geophysical Research 109, D16207.

105. Liao, H., Seinfeld, J. H., Adams, P. J., & Mickley, L. J. (2004). Global radiative

forcing of coupled tropospheric ozone and aerosols in a unified general circulation model. Journal of Geophysical Research: Atmospheres, 109(D16).

106. Liepert, B. & Tegen, I. (2002). Multidecadal solar radiation trends in the United States and Germany and direct tropospheric aerosol forcing. Journal of Geophysical Research: Atmospheres, 107(D12).

107. Lindeman, R. H. (1980). Introduction to bivariate and multivariate analysis tech. rep.

108. Liu, B. Y., & Jordan, R. C. (1960). The interrelationship and characteristic distribution of direct, diffuse and total solar radiation. Solar energy, 4(3), 1-19.

109. Liu, S., Chen, M. & Zhuang, Q. (2014). Aerosol effects on global land surface energy fluxes during 2003-2010. Geophysical Research Letters 41, 7875–788.

110. Loeb, N. G., Wang, H., Rose, F. G., Kato, S., Smith, W. L., & Sun-Mack, S. (2019). Decomposing shortwave Top-of-Atmosphere and surface radiative flux variations in terms of surface and atmospheric contributions. Journal of Climate, 32(16), 5003-5019.

111. Loew, A., Van Bodegom, P. M., Widlowski, J. L., Otto, J., Quaife, T., Pinty, B., & Raddatz, T. (2014). Do we (need to) care about canopy radiation schemes in DGVMs? Caveats and potential impacts. Biogeosciences, 11(7), 1873-1897.

112. Lohmann, U. (2002). A glaciation indirect aerosol effect caused by soot aerosols. Geophysical Research Letters, 29(4).

113. Lu, X., Chen, M., Liu, Y., Miralles, D. G., & Wang, F. (2017). Enhanced water use efficiency in global terrestrial ecosystems under increasing aerosol loadings. Agricultural and Forest Meteorology, 237, 39-49.

114. Lubin, D. & Vogelmann, A. M. (2006). A climatologically significant aerosol long-wave indirect effect in the arctic. Nature, 439(7075):453–456.

115. Luo, X., Chen, J. M., Liu, J., Black, T. A., Croft, H., Staebler, R., ... & McCaughey, H. (2018). Comparison of big-leaf, two-big-leaf, and two-leaf upscaling schemes for evapotranspiration estimation using coupled carbon-water modeling. Journal of Geophysical Research: Biogeosciences, 123(1), 207-225.

116. Luyssaert, S., Jammet, M., Stoy, P. C., Estel, S., Pongratz, J., Ceschia, E., ... & Dolman, A. J. (2014). Land management and land-cover change have impacts of similar magnitude on surface temperature. Nature Climate Change, 4(5), 389-393.

117. Lyapustin, A., Wang, Y., Korkin, S., & Huang, D. (2018). MODIS collection 6 MAIAC algorithm. Atmospheric Measurement Techniques, 11(10), 5741-5765.

118. Markovic, M., Jones, C. G., Winger, K. & Paquin, D. (2009). The surface radiation budget over North America: gridded data assessment and evaluation of regional climate models. International Journal of Climatology: A Journal of the Royal Meteorological Society 29. 2226–2240.

119. Marvel, K., Schmidt, G. A., Miller, R. L. & Nazarenko, L. S. (2015). Implications for climate sensitivity from the response to individual forcings. Nature Climate Change 6, 386–389.

120. Matsui, T., Beltrán-Przekurat, A., Niyogi, D., Pielke, R. A., & Coughenour, M. (2008). Aerosol light scattering effect on terrestrial plant productivity and energy fluxes over the eastern United States. Journal of Geophysical Research: Atmospheres, 113(D14).

121. Matsui, T., Masunaga, H., Pielke, R. A., & Tao, W.-K. (2004). Impact of aerosols

and atmospheric thermodynamics on cloud properties within the climate system. Geophysical Research Letters, 31(6).

122. Mercado, L. M., Bellouin, N., Sitch, S., Boucher, O., Huntingford, C., Wild, M., & Cox, P. M. (2009). Impact of changes in diffuse radiation on the global land carbon sink. Nature, 458(7241), 1014-1017.

123. Mickley, L., Leibensperger, E., Jacob, D., & Rind, D. (2012). Regional warming from aerosol removal over the United States: Results from a transient 2010–2050 climate simulation. Atmospheric Environment, 46:545–553.

124. Miller, R. L., Cakmur, R. V., Perlwitz, J., Geogdzhayev, I. V., Ginoux, P., Koch, D., ... & Tegen, I. (2006). Mineral dust aerosols in the NASA Goddard Institute for Space Sciences ModelE atmospheric general circulation model. Journal of Geophysical Research: Atmospheres, 111(D6).

125. Minnis, P., Sun-Mack, S., Young, D. F., Heck, P. W., Garber, D. P., Chen, Y., ... & Yang, P. (2011). CERES edition-2 cloud property retrievals using TRMM VIRS and Terra and Aqua MODIS data—Part I: Algorithms. IEEE Transactions on Geoscience and Remote Sensing, 49(11), 4374-4400.

126. Morcrette, J. J., Barker, H. W., Cole, J. N. S., Iacono, M. J., & Pincus, R. (2008). Impact of a new radiation package, McRad, in the ECMWF Integrated Forecasting System. Monthly weather review, 136(12), 4773-4798.

127. Moseid, K. O., Schulz, M., Storelvmo, T., Julsrud, I. R., Olivie, D., Nabat, P., ... & Takemura, T. (2020). Bias in CMIP6 models compared to observed regional dimming and brightening trends (1961–2014). Atmospheric Chemistry and Physics, 20(24), 16023-16040.

128. Naudts, K., Chen, Y., McGrath, M. J., Ryder, J., Valade, A., Otto, J., & Luyssaert, S. (2016). Europe's forest management did not mitigate climate warming. Science 351, 597–600.

129. Niyogi, D., Chang, H. I., Saxena, V. K., Holt, T., Alapaty, K., Booker, F., ... & Xue, Y. (2004). Direct observations of the effects of aerosol loading on net ecosystem CO_2 exchanges over different landscapes. Geophysical Research Letters, 31(20).

130. Novick, K. A., Biederman, J. A., Desai, A. R., Litvak, M. E., Moore, D. J., Scott, R. L., & Torn, M. S. (2018). The AmeriFlux network: A coalition of the willing. Agricultural and Forest Meteorology, 249, 444-456.

131. Novick, K. A., & Katul, G. G. (2020). The duality of reforestation impacts on surface and air temperature. Journal of Geophysical Research: Biogeosciences, 125(4).

132. Okata, M., Nakajima, T., Suzuki, K., Inoue, T., Nakajima, T. Y., & Okamoto, H. (2017). A study on radiative transfer effects in 3-D cloudy atmosphere using satellite data. Journal of Geophysical Research: Atmospheres, 122(1), 443-468.

133. Oleson, K. W., Lawrence, D. M., Bonan, G. B., Drewniak, Huang, B. M., Koven, C. D., ... & Thornton, P. E. (2013). Technical description of version 4.5 of the Community Land Model (CLM) (No. NCAR/TN-503+STR).

134. Oliveira, P. J. C., Davin, E. L., Levis, S., & Seneviratne, S. I. (2011). Vegetation-mediated impacts of trends in global radiation on land hydrology: a global sensitivity study. Gloal. Change Biology, 17, 3453–3467.

135. Oreopoulos, L., Mlawer, E., Delamere, J., Shippert, T., Cole, J., Fomin, B., ... & Rossow, W. B. (2012). The continual intercomparison of radiation codes: Results from phase I. Journal of Geophysical Research: Atmospheres, 117(D6).

136. Painemal, D., & Zuidema, P. (2011). Assessment of MODIS cloud effective radius and optical thickness retrievals over the Southeast Pacific with VOCALS-REx in situ measurements. Journal of Geophysical Research: Atmospheres, 116(D24).

137. Panicker, A. S., Pandithurai, G., Safai, P. D., & Kewat, S. (2008). Observations of enhanced aerosol longwave radiative forcing over an urban environment. Geophysical Research Letters, 35(4).

138. Peng, L., Wei, Z., Zeng, Z., Lin, P., Wood, E. F., & Sheffield, J. (2021). Reducing Solar Radiation Forcing Uncertainty and Its Impact on Surface Energy and Water Fluxes. Journal of Hydrometeorology, 22(4), 813-829.

139. Pere, J. C., Mallet, M., Pont, V., & Bessagnet, B. (2011). Impact of aerosol direct radiative forcing on the radiative budget, surface heat fluxes, and atmospheric dynamics during the heat wave of summer 2003 over western Europe: A modeling study. Journal of Geophysical Research: Atmospheres, 116(D23).

140. Persad, G. G., & Caldeira, K. (2018). Divergent global-scale temperature effects from identical aerosols emitted in different regions. Nature communications, 9(1), 1-9.

141. Pfeifroth, U., Sanchez-Lorenzo, A., Manara, V., Trentmann, J., & Hollmann, R. (2018). Trends and variability of surface solar radiation in Europe based on surface- and satellite-based data records. Journal of Geophysical Research: Atmospheres, 123(3), 1735-1754.

142. Pielke, R. A. (2001). Influence of the spatial distribution of vegetation and soils on the prediction of cumulus convective rainfall. Rev Geophys, 39(2):151–177.

143. Pincus, R., Forster, P. M., & Stevens, B. (2016). The Radiative forcing model intercomparison project (RFMIP): experimental protocol for CMIP6. Geoscientific

Model Development, 9(9), 3447-3460.

144. Plass, G. N., & Kattawar, G. W. (1968). Monte Carlo calculations of light scattering from clouds. Applied optics, 7(3), 415-419.

145. Proctor, J., Hsiang, S., Burney, J., Burke, M., & Schlenker, W. (2018). Estimating global agricultural effects of geoengineering using volcanic eruptions. Nature, 560(7719), 480-483.

146. Qu, Z., Oumbe, A., Blanc, P., Espinar, B., Gesell, G., GSCHwIND, B., ... & Wald, L. (2017). Fast radiative transfer parameterisation for assessing the surface solar irradiance: The Heliosat-4 method. Meteorologische Zeitschrift, 26(1), 33-57.

147. Ramanathan, V. & Carmichael, G. (2008). Global and regional climate changes due to black carbon. Nature geoscience, 1(4):221–227.

148. Ramanathan, V., Crutzen, P., Kiehl, J., & Rosenfeld, D. (2001a). Aerosols, climate, and the hydrological cycle. science, 294(5549):2119–2124.

149. Ramanathan, V., Crutzen, P. J., Lelieveld, J., Mitra, A. P., Althausen, D., Anderson, J., ... & Valero, F. P. J. (2001b). Indian Ocean Experiment: An integrated analysis of the climate forcing and effects of the great Indo-Asian haze. Journal of Geophysical Research: Atmospheres, 106(D22), 28371-28398.

150. Randles, C. A., Da Silva, A. M., Buchard, V., Colarco, P. R., Darmenov, A., Govindaraju, R., ... & Flynn, C. J. (2017). The MERRA-2 aerosol reanalysis, 1980 onward. Part I: System description and data assimilation evaluation. Journal of climate, 30(17), 6823-6850.

151. Rap, A., Scott, C. E., Reddington, C. L., Mercado, L., Ellis, R. J., Garraway, S., ... & Spracklen, D. V. (2018). Enhanced global primary production by biogenic aerosol

via diffuse radiation fertilization. Nature Geoscience, 11(9), 640-644.

152. Rap, A., Spracklen, D. V., Mercado, L., Reddington, C. L., Haywood, J. M., Ellis, R. J., ... & Butt, N. (2015). Fires increase Amazon forest productivity through increases in diffuse radiation. Geophysical Research Letters, 42(11), 4654-4662.

153. Reddy, M. S., Boucher, O., Balkanski, Y., & Schulz, M. (2005). Aerosol optical depths and direct radiative perturbations by species and source type. Geophysical research letters, 32(12).

154. Reichle, R. H., & Liu, Q. (2014). Observation-corrected precipitation estimates in GEOS-5.

155. Reichle, R. H., Draper, C. S., Liu, Q., Girotto, M., Mahanama, S. P., Koster, R. D., & De Lannoy, G. J. (2017). Assessment of MERRA-2 land surface hydrology estimates. Journal of Climate, 30(8), 2937-2960.

156. Rotstayn, L. D., Collier, M. A., Shindell, D. T. & Boucher, O. (2015). Why Does Aerosol Forcing Control Historical Global-Mean Surface Temperature Change in CMIP5 Models? Journal of Climate 28, 6608–6625.

157. Rubel, F., & Kottek, M. (2010). Observed and projected climate shifts 1901-2100 depicted by world maps of the Köppen-Geiger climate classification. Meteorologische Zeitschrift, 19(2), 135.

158. Ruehr, S., Lee, X., Smith, R., Li, X., Xu, Z., Liu, S., ... & Zhou, Y. (2020). A mechanistic investigation of the oasis effect in the Zhangye cropland in semiarid western China. Journal of Arid Environments, 176, 104120.

159. Rutan, D. A., Kato, S., Doelling, D. R., Rose, F. G., Nguyen, L. T., Caldwell, T. E., & Loeb, N. G. (2015). CERES synoptic product: Methodology and validation

of surface radiant flux. Journal of Atmospheric and Oceanic Technology, 32(6), 1121-1143.

160. Ryu, Y., Jiang, C., Kobayashi, H., & Detto, M. (2018). MODIS-derived global land products of shortwave radiation and diffuse and total photosynthetically active radiation at 5 km resolution from 2000. Remote Sensing of Environment, 204, 812-825.

161. Saha, S., Moorthi, S., Pan, H. L., Wu, X., Wang, J., Nadiga, S., ... & Goldberg, M. (2010). The NCEP climate forecast system reanalysis. Bulletin of the American Meteorological Society, 91(8), 1015-1058.

162. Samukova, E. A., Gorbarenko, E. V., & Erokhina, A. E. (2014). Long-term variations of solar radiation in Europe. Russian Meteorology and Hydrology, 39(8), 514-520.

163. Sanchez-Lorenzo, A., Wild, M., Brunetti, M., Guijarro, J. A., Hakuba, M. Z., Calbó, J., ... & Bartok, B. (2015). Reassessment and update of long-term trends in downward surface shortwave radiation over Europe (1939–2012). Journal of Geophysical Research: Atmospheres, 120(18), 9555-9569.

164. Sarangi, C., Kanawade, V. P., Tripathi, S. N., Thomas, A., & Ganguly, D. (2018). Aerosol-induced intensification of cooling effect of clouds during Indian summer monsoon. Nature Communications 9, 3754.

165. Schäfer, S. A., Hogan, R. J., Klinger, C., Chiu, J. C., & Mayer, B. (2016). Representing 3-D cloud radiation effects in two-stream schemes: 1. Longwave considerations and effective cloud edge length. Journal of Geophysical Research: Atmospheres, 121(14), 8567-8582.

166. Schwartz, S. E., & Benkovitz, C. M. (2002). Influence of anthropogenic aerosol on cloud optical depth and albedo shown by satellite measurements and chemical transport modeling. Proceedings of the National Academy of Sciences, 99(4), 1784-1789.

167. Schwarz, M., Folini, D., Yang, S., Allan, R. P., & Wild, M. (2020). Changes in atmospheric shortwave absorption as important driver of dimming and brightening. Nature Geoscience, 13(2), 110-115.

168. Seinfeld, J. & Pandis, S. (1998). Atmospheric chemistry and physics, 1326 pp.

169. Seneviratne, S. I. & Stockli, R. (2008). The role of land-atmosphere interactions for climate variability in Europe. In Climate Variability and Extremes during the Past 100 years, pages 179–193. Springer.

170. Shao, H. & Liu, G. (2005). Why is the satellite observed aerosol's indirect effect so variable? Geophysical research letters, 32(15).

171. Shindell, D. T. (2014). Inhomogeneous forcing and transient climate sensitivity. Nature Climate Change 4, 274–277.

172. Sicard, M., Bertolın, S., Mallet, M., Dubuisson, P., & Comeron, A. (2014). Estimation of mineral dust long-wave radiative forcing: sensitivity study to particle properties and application to real cases in the region of Barcelona. Atmospheric Chemistry and Physics, 14(17):9213–9231.

173. Sicard, M., Bertolín, S., Mallet, M., Dubuisson, P. & Comerón, A. (2014). Estimation of mineral dust long-wave radiative forcing: sensitivity study to particle properties and application to real cases in the region of Barcelona. Atmospheric Chemistry and Physics 14, 9213–9231.

174. Slivinski, L. C., Compo, G. P., Whitaker, J. S., Sardeshmukh, P. D., Giese, B. S., McColl, C., ... & Wyszyński, P. (2019). Towards a more reliable historical reanalysis: Improvements for version 3 of the Twentieth Century Reanalysis system, QJ Roy. Meteorol. Soc., 145, 2876–2908.

175. Small, J. D., Chuang, P. Y., Feingold, G., & Jiang, H. (2009). Can aerosol decrease cloud lifetime? Geophysical Research Letters, 36(16).

176. Smith, B., Prentice, I. C., & Sykes, M. T. (2001). Representation of vegetation dynamics in the modelling of terrestrial ecosystems: comparing two contrasting approaches within European climate space. Global ecology and biogeography, 621-637.

177. Solomon, S. (2007). Climate change 2007-the physical science basis: Working group I contribution to the fourth assessment report of the IPCC, volume 4. Cambridge University Press.

178. Spencer, M., Holecek, J., Corrigan, C., Ramanathan, V., & Prather, K. (2008). Sizeresolved chemical composition of aerosol particles during a monsoonal transition period over the Indian ocean. Journal of Geophysical Research: Atmospheres, 113(D16).

179. Spitters, C. J. T., Toussaint, H. A. J. M., & Goudriaan, J. (1986). Separating the diffuse and direct component of global radiation and its implications for modeling canopy photosynthesis Part I. Components of incoming radiation. Agricultural and Forest Meteorology, 38(1-3), 217-229.

180. Steiner, A. L., Mermelstein, D., Cheng, S. J., Twine, T. E., & Oliphant, A. (2013). Observed impact of atmospheric aerosols on the surface energy budget. Earth Interactions, 17(14), 1-22.

181. Stephens, G. L., Li, J., Wild, M., Clayson, C. A., Loeb, N., Kato, S., ... & Andrews, T. (2012). An update on Earth's energy balance in light of the latest global observations. Nature Geoscience, 5(10), 691-696.

182. Stier, P., Seinfeld, J. H., Kinne, S. & Boucher, O. (2007). Aerosol absorption and radiative forcing. Atmospheric Chemistry and Physics Discussions 7, 5237-5261.

183. Stocker, T. F., Qin, D., Plattner, G.-K., Tignor, M., Allen, S. K., Boschung, J., Nauels, A., Xia, Y., Bex, B., & Midgley, B. (2013). IPCC, 2013: climate change 2013: the physical science basis. contribution of working group I to the fifth assessment report of the Intergovernmental Panel on Climate Change (Cambridge University Press, Cambridge, United Kingdom, 2014).

184. Streets, D. G., Yan, F., Chin, M., Diehl, T., Mahowald, N., Schultz, M., ... & Yu, C. (2009). Anthropogenic and natural contributions to regional trends in aerosol optical depth, 1980–2006. Journal of Geophysical Research 114, D00D18.

185. Stuber, N., Ponater, M. & Sausen, R. (2005). Why radiative forcing might fail as a predictor of climate change. Climate Dynamics 24, 497–510.

186. Suni, T., Guenther, A., Hansson, H. C., Kulmala, M., Andreae, M. O., Arneth, A., ... & Seneviratne, S. (2015). The significance of land-atmosphere interactions in the Earth system–iLEAPS achievements and perspectives, Anthropocene, 12, 69–84.

187. Trenberth, K. E., Fasullo, J. T., & Kiehl, J. (2009). Earth's global energy budget. Bull Am Meteor Soc, 90(3):311–323.

188. Takata, K., Emori, S., & Watanabe, T. (2003). Development of the minimal advanced treatments of surface interaction and runoff. Global and planetary Change, 38(1-2), 209-222.

189. Talukdar, S., Venkat Ratnam, M., Ravikiran, V., & Chakraborty, R. (2019). Influence of black carbon aerosol on the atmospheric instability. Journal of Geophysical Research: Atmospheres, 124(10), 5539-5554.

190. Tang, T., Shindell, D., Faluvegi, G., Myhre, G., Olivié, D., Voulgarakis, A., ... & Smith, C. (2019). Comparison of Effective Radiative Forcing Calculations Using Multiple Methods, Drivers, and Models. Journal of Geophysical Research: Atmospheres 124(8), 4382-4394.

191. Trolliet, M., Walawender, J. P., Bourlès, B., Boilley, A., Trentmann, J., Blanc, P., ... & Wald, L. (2018). Downwelling surface solar irradiance in the tropical Atlantic Ocean: a comparison of re-analyses and satellite-derived data sets to PIRATA measurements. Ocean Science, 14(5), 1021-1056.

192. Twomey, S. (1977). Atmospheric aerosols.

193. Twomey, S. (1991). Aerosols, clouds, and radiation. Atmos. Environ. A 25, 2435–2442

194. Urankar, G., Prabha, T., Pandithurai, G., Pallavi, P., Achuthavarier, D., & Goswami, B. (2012). Aerosol and cloud feedbacks on surface energy balance over selected regions of the Indian subcontinent. Journal of Geophysical Research: Atmospheres, 117(D4).

195. Verma, S., Boucher, O., Upadhyaya, H., & Sharma, O. (2006). Sulfate aerosols forcing: An estimate using a three-dimensional interactive chemistry scheme. Atmospheric environment, 40(40):7953–7962.

196. Wang, K., Dickinson, R. E., & Liang, S. (2008). Observational evidence on the effects of clouds and aerosols on net ecosystem exchange and evapotranspiration. Geophysical Research Letters, 35(10).

197. Wang, S., Ibrom, A., Bauer-Gottwein, P., & Garcia, M. (2018). Incorporating diffuse radiation into a light use efficiency and evapotranspiration model: An 11-year study in a high latitude deciduous forest. Agricultural and Forest Meteorology, 248, 479-493.

198. Wang, W., Lee, X., Xiao, W., Liu, S., Schultz, N., Wang, Y., ... & Zhao, L. (2018). Global lake evaporation accelerated by changes in surface energy allocation in a warmer climate. Nature Geoscience, 11(6), 410-414.

199. Wang, X., Liu, Y., & Bao, Q. (2016). Impacts of cloud overlap assumptions on radiative budgets and heating fields in convective regions. Atmospheric Research, 167, 89-99.

200. Wang, Y. P., & Leuning, R. (1998). A two-leaf model for canopy conductance, photosynthesis and partitioning of available energy I:: Model description and comparison with a multi-layered model. Agricultural and Forest Meteorology, 91(1-2), 89-111.

201. Wang, Y. W., & Yang, Y. H. (2014, January). China's dimming and brightening: evidence, causes and hydrological implications. In Annales Geophysicae (Vol. 32, No. 1, pp. 41-55). Copernicus GmbH.

202. Wang, B., Shugart, H. H., & Lerdau, M. T. (2019). Complexities between plants and the atmosphere. Nature Geoscience, 12(9), 693-694.

203. Wang, Y., Yang, S., Sanchez-Lorenzo, A., Yuan, W., & Wild, M. (2020). A revisit of direct and diffuse solar radiation in China based on homogeneous surface observations: climatology, trends, and their probable causes. Journal of Geophysical Research: Atmospheres, 125(9), e2020JD032634.

204. Wang, Y., Xia, W., Liu, X., Xie, S., Lin, W., Tang, Q., ... & Zhang, G. J. (2021). Disproportionate control on aerosol burden by light rain. Nature Geoscience, 14(2), 72-76.

205. Wei, Y., Zhang, X., Hou, N., Zhang, W., Jia, K., & Yao, Y. (2019). Estimation of surface downward shortwave radiation over China from AVHRR data based on four machine learning methods. Solar Energy, 177, 32-46.

206. Wendisch, M., Hellmuth, O., Ansmann, A., Heintzenberg, J., Engelmann, R., Althausen, D., ... & Mao, J. (2008). Radiative and dynamic effects of absorbing aerosol particles over the Pearl River Delta, China. Atmospheric Environment, 42(25), 6405-6416.

207. Weng, E. S., Malyshev, S., Lichstein, J. W., Farrior, C. E., Dybzinski, R., Zhang, T., ... & Pacala, S. W. (2015). Scaling from individual trees to forests in an Earth system modeling framework using a mathematically tractable model of height-structured competition. Biogeosciences, 12(9), 2655-2694.

208. Westervelt, D. M., Horowitz, L. W., Naik, V., Golaz, J. C., & Mauzerall, D. L. (2015). Radiative forcing and climate response to projected 21st century aerosol decreases. Atmospheric Chemistry and Physics, 15(22), 12681-12703.

209. Wild, M., Ohmura, A., Gilgen, H., & Morcrette, J. J. (1998). The distribution of solar energy at the Earth's surface as calculated in the ECMWF re-analysis. Geophysical research letters, 25(23), 4373-4376.

210. Wild, M. (2012). Enlightening global dimming and brightening. Bulletin of the American Meteorological Society, 93(1), 27-37.

211. Wild, M., Folini D., Henschel, F., Fischer, N., Müller, B. (2015a). Projections of

long-term changes in solar radiation based on CMIP5 climate models and their influence on energy yields of photovoltaic systems. Solar Energy, 116, 12–24.

212. Wild, M., Folini, D., Hakuba, M. Z., Schär, C., Seneviratne, S. I., Kato, S., ... & König-Langlo, G. (2015b). The energy balance over land and oceans: an assessment based on direct observations and CMIP5 climate models. Climate Dynamics, 44(11-12), 3393-3429.

213. Wild, M. (2016). Decadal changes in radiative fluxes at land and ocean surfaces and their relevance for global warming. Wiley Interdisciplinary Reviews: Climate Change, 7(1), 91-107.

214. Wild, M., Ohmura, A., Schär, C., Müller, G., Folini, D., Schwarz, M., ... & Sanchez-Lorenzo, A. (2017). The Global Energy Balance Archive (GEBA) version 2017: A database for worldwide measured surface energy fluxes. Earth System Science Data, 9(2), 601-613.

215. Wozniak, M. C., Bonan, G. B., Keppel-Aleks, G., & Steiner, A. L. (2020). Influence of Vertical Heterogeneities in the Canopy Microenvironment on Interannual Variability of Carbon Uptake in Temperate Deciduous Forests. Journal of Geophysical Research: Biogeosciences, 125(8).

216. Xia, L., Robock, A., Tilmes, S., & Neely Iii, R. R. (2016). Stratospheric sulfate geoengineering could enhance the terrestrial photosynthesis rate. Atmospheric Chemistry and Physics, 16(3), 1479-1489.

217. Yang, L., Zhang, X., Liang, S., Yao, Y., Jia, K., & Jia, A. (2018). Estimating surface downward shortwave radiation over china based on the gradient boosting decision tree method. Remote Sensing, 10(2), 185.

218. Yang, S., X. L. Wang, X. L. & M. Wild, (2019). M. Causes of Dimming and Brightening in China Inferred from Homogenized Daily Clear-Sky and All-Sky in situ Surface Solar Radiation Records (1958–2016). Journal of Climate 32, 5901–5913.

219. Yang, Y., Lou, S., Wang, H., Wang, P., & Liao, H. (2020). Trends and source apportionment of aerosols in Europe during 1980–2018. Atmospheric Chemistry and Physics, 20(4), 2579-2590.

220. Yu, S., Zender, C. S., & Saxena, V. (2001). Direct radiative forcing and atmospheric absorption by boundary layer aerosols in the southeastern us: model estimates on the basis of new observations. Atmospheric Environment, 35(23):3967–3977.

221. Yue, X., & Unger, N. (2017). Aerosol optical depth thresholds as a tool to assess diffuse radiation fertilization of the land carbon uptake in China. Atmospheric Chemistry and Physics, 17(2), 1329-1342.

222. Yue, X., & Unger, N. (2018). Fire air pollution reduces global terrestrial productivity. Nature communications, 9(1), 1-9.

223. Zhang, H., Shen, Z., Wei, X., Zhang, M., & Li, Z. (2012). Comparison of optical properties of nitrate and sulfate aerosol and the direct radiative forcing due to nitrate in china. Atmospheric Research, 113:113–125.

224. Zhang, M. H., Lin, W. Y., Klein, S. A., Bacmeister, J. T., Bony, S., Cederwall, R. T., ... & Zhang, J. H. (2005). Comparing clouds and their seasonal variations in 10 atmospheric general circulation models with satellite measurements. Journal of Geophysical Research: Atmospheres, 110(D15).

225. Zhang, M., Yu, G. R., Zhuang, J., Gentry, R., Fu, Y. L., Sun, X. M., ... & Li, Y. N. (2011). Effects of cloudiness change on net ecosystem exchange, light use

efficiency, and water use efficiency in typical ecosystems of China. Agricultural and Forest Meteorology, 151(7), 803-816.

226. Zhang, X., Liang, S., Wang, G., Yao, Y., Jiang, B., & Cheng, J. (2016). Evaluation of the reanalysis surface incident shortwave radiation products from NCEP, ECMWF, GSFC, and JMA using satellite and surface observations. Remote Sensing, 8(3), 225.

227. Zhang, Y., Fu, R., Yu, H., Dickinson, R. E., Juarez, R. N., Chin, M., & Wang, H. (2008). A regional climate model study of how biomass burning aerosol impacts land-atmosphere interactions over the Amazon. Journal of Geophysical Research: Atmospheres, 113(D14).

228. Zhao, L., Lee, X. & Liu, S. (2013). Correcting surface solar radiation of two data assimilation systems against FLUXNET observations in North America. Journal of Geophysical Research: Atmospheres 118. 9552–9564.

229. Zhao, L., Lee, X., Smith, R. B., & Oleson, K. (2014). Strong contributions of local background climate to urban heat islands. Nature, 511(7508), 216-219.

230. Zhou, Q., Flores, A., Glenn, N. F., Walters, R. & Han, B. (2017). A machine learning approach to estimation of downward solar radiation from satellite-derived data products: An application over a semi-arid ecosystem in the US. Plos one 12, e0180239.

Appendices

Appendix A

Developing a Global Dataset of Surface Urban Heat Islands

A.1 Abstract

We develop a new algorithm, the simplified urban-extent (SUE) algorithm, to estimate the surface urban heat island (UHI) intensity at a global scale. We implement the SUE algorithm on the Google Earth Engine platform using Moderate Resolution Imaging Spectroradiometer (MODIS) images to calculate the UHI intensity for over 9500 urban clusters using over 15 years of data, making this one of the most comprehensive characterizations of the surface UHI to date. The results from this algorithm are validated against previous multi-city studies to demonstrate the suitability of this method. The dataset created is then filtered for elevation differentials and percentage of urban area and used to estimate the diurnal, monthly, and long-term variability in the surface UHI in different climate zones. The global mean surface UHI intensity is 0.85 °C during daytime and 0.55 °C at night. Cities in arid climate show distinct diurnal and seasonal patterns, with higher surface UHI during nighttime (compared to daytime) and two peaks throughout the year. The diurnal variability in surface UHI is highest for equatorial climate zone (0.88 °C) and lowest for arid zone (0.53 °C). The seasonality is highest in the snow climate zone and lowest for equatorial climate zone. While investigating the change in the surface UHI over a decade and a half, we find a consistent increase in the daytime surface UHI in the urban clusters of the warm temperate climate zone (0.04 °C per decade) and snow climate zone (0.05 °C per decade). Only arid climate zones show a statistically significant increase in the nighttime surface UHI intensity (0.03 °C per decade). Globally, the change is mainly seen during the daytime (0.03 °C per decade). Finally, the importance of vegetation differential between urban and rural areas on the spatiotemporal variability is examined. Vegetation has a strong control on the seasonal variability of the surface UHI and may also partly control the long-term variability. The complete UHI data is available on this website, where the user can query the UHI of an urban cluster through a simple interface.

A.2   Introduction

The urban heat island (UHI) effect refers to the positive temperature difference between an urban area and its hinterland, and it is one of the most well-known consequences of urbanization on local climate (Souch and Grimmond, 2006). It has been an active area of research in urban climatology since it was first observed a century back by Luke Howard (Howard, 1833). Traditionally, it was defined as the air temperature difference between the urban zone and its surroundings, known as the canopy UHI, and was studied using in-situ weather stations or mobile measurements (Voogt, 2007). The advent of satellite data has allowed us to define a new kind of urban heat island, known as the surface UHI, which is the difference in land surface temperature (LST) between the urban area and its surrounding non-urban area (Rao, 1972). Canopy and surface UHI intensities are similar at the annual scale, but may have different diurnal and seasonal variabilities (Cui and De Foy, 2012, Chakraborty et al., 2017).

Urbanization changes the surface energy budget by modifying albedo, reducing evaporative cooling via replacement of vegetated surfaces with built-up surfaces, increasing heat storage due to the higher heat capacity of urban structures, and changing dissipation of heat via modulation of thermal roughness and urban spatial configuration (Goward, 1981, Taha, 1997, Arnfield, 2003, Connors et al., 2013, Zhao et al., 2014, Debbage & Shepherd, 2015). For heavily polluted cities in arid regions, dust particles can trap long-wave radiation and increase the nighttime UHI intensity (Cao et al., 2016). Other major determinants of the UHI intensity mentioned in the literature are synoptic conditions, city size, precipitation, humidity, cloud cover, and coastal feedback (Santamouris, 2015).

Studies quantifying the magnitude of the UHI effect have been performed for hundreds of cities around the world (Oke, 1979, Arnfield, 2003, Santamouris, 2015). Traditionally, such studies are done on a city-by-city basis, which can lead to inconsistencies due to

differences in data collection processes, sensor types, and other methodological considerations. A systematic critique of the UHI literature (Stewart, 2011) found that roughly half of the UHI studies lacked robustness. Some important issues were: not controlling for weather factors, lack of information on site meta data and instrumentation, lack of accounting for temporal variability during mobile surveys, inconsistency in defining both urban and rural measurement locations, and disregarding the effect of scale.

The use of satellite data has reduced the inconsistency in measurement techniques by allowing a standardized data collection approach that can be implemented for multiple cities. Previously, Tran et al. (2006) and Imhoff et al. (2010) used satellite data to investigate the surface UHI of 18 Asian megacities and 38 highly populated US cities, respectively. Systematic studies have also been performed on the UHI intensity of cities in Europe (Schwarz et al., 2011, Zhou et al., 2013). A recent study investigated the diurnality and seasonality of the surface UHI in the 84 largest cities in India (Shastri et al., 2017). The principal works done on multiple cities at the global scale are by Peng et al. (2011), who analyzed the UHI of 419 largest cities using 5 years of MODIS AQUA LST data and Clinton & Gong (2013), who investigated the global pattern of the UHI intensity for 2010.

For both canopy and surface UHI studies, one persistent issue is the definition of the rural station (for canopy UHI) or the boundary between the urban and rural area (for surface UHI) (Martin-Vide et al., 2015). Nearby rural areas are affected by advection from the urban core. However, if the rural station is too far away, local weather changes might be more important than the impact of land use changes. A recent study in China found that the footprint of the UHI can be twice or thrice the area of the city (Zhou et al., 2015). This is much higher than the area of the fixed buffer zones normally used in global UHI studies (Clinton & Gong, 2013). The study also demonstrated that for closely located cities, the effect of advection from other cities could also have an impact on the UHI intensity.

Smaller urban areas have generally been overlooked in the existing UHI literature,

which disproportionately focuses on large mega-cities. Moreover, the temporal and seasonal variability of the UHI intensity has not been investigated at a global scale. So in this study, we map the daytime and nighttime surface UHI for all urban areas currently detectable via MODIS-based spectral classification of land use using over 15 years of observed data. Buffer-based analyses of the UHI intensity are common in the literature and it is hard to choose a fixed buffer width that is reasonable for all the cities across the globe. So we develop a new algorithm, the simplified urban-extent algorithm (SUE), that can be used to automatically calculate the UHI intensity at a global scale. The algorithm is implemented on Google Earth Engine, a cloud-based platform for planetary-scale data archiving and geospatial analysis (Gorelick et al., 2017). We estimate the surface UHI intensity for almost 9500 distinct urban clusters and estimate the diurnal, seasonal, and annual pattern of the UHI intensity for each climate zone. Many of the factors that influence the UHI intensity, like urban albedo, longwave trapping by the urban canyon, surface roughness, etc. do not show significant seasonal or temporal variations, given the relatively constant nature of urban areas. The main varying characteristic is vegetation cover, which changes throughout the year, as well as between years. Given the focus on the seasonal and temporal variability of the UHI in the present study, we examine how vegetation controls this dynamic globally, and for different climate zones.

The major research questions investigated in the present study are:

- How well does the newly designed SUE algorithm replicate the known characteristics of the surface UHI effect?

- How does the mean, diurnal, and seasonal patterns of the UHI compare for urban clusters in different climate zones?

- How has the UHI intensity changed in the last decade and a half, both globally and for each climate zone?

- How strongly does vegetation control the seasonal and temporal variability of the surface UHI?

Section A.3 describes the SUE algorithm developed for this study. Section A.4 shows the comparison of the results with those obtained from previous multi-city studies. Section A.5 shows the general results as well as the diurnal, seasonal, and annual variability of the surface UHI for urban clusters in different climate zones. Section A.6 examines how vegetation controls the spatiotemporal variability of the UHI and discusses the advantages and disadvantages of the SUE algorithm.

A.3   Methodology

A.3.1   The Simplified Urban-Extent (SUE) Algorithm

In this study, we define the surface UHI as the difference in LST of the urban pixels and the non-urban pixels within each urban extent, which we call the simplified urban-extent (SUE) algorithm. First, the MODIS-derived LST data from TERRA (MOD11A2) and AQUA (MYD11A2) satellites, available at 1 km x 1 km resolution, are pre-processed, with only the clear-sky pixels with average LST error of less than or equal to 3 K being selected for further analysis. The quality-controlled datasets are then used to estimate the LST at 0130, 1030, 1330, and 2230 local time (LT). Data from 2000 to 2017 (18 years) are used from the TERRA platform, while data from 2002 to 2017 (16 years) are used from AQUA.

The urban extent data are from Natural Earth (2018). It is a combination of the global urban land database by Schneider et al., 2009, Schneider et al., 2010 and the Oak Ridge National Laboratory's LandScan population database (Dobson et al., 2000). The urban data are based on MODIS measurements for February 2001 to February 2002 and is de-

fined using the C4.5 decision tree algorithm (Quinlan, 1993). This dataset has already been validated, with an overall accuracy of 93%, using a Landsat-based map of 140 urban areas in different ecoregions, and for different levels of population and economic development (Schneider et al., 2010). These global urban data are intersected with Thiessen polygons derived from the LandScan population points to create the urban land database; the results are in vector format on the Natural Earth website (2018). The urban units are closed polygons around contiguous urban agglomerations. Fig. A.1 shows an example of one such urban unit consisting of multiple urban areas. The advantage of using this dataset is that it is based on a consistent algorithm implemented on the MODIS land use satellite product and bounds the global hot spots of human habitation.

Figure A.1 shows the steps used to estimate the surface UHI of each urban cluster. Firstly, the global LST and MODIS LU/LC data (at 500 m x 500 m resolution) for 2013 (MCD12Q1) are clipped to the urban extent dataset. Then, two subsets are created, one for urban land use (in red in Fig. A.1) and another for all land use other than urban and water based on the land use data. The water pixels are removed since the high specific heat capacity of water would lead to an overestimation of the UHI intensity during the daytime and an underestimation during nighttime. After subsetting, the spatial mean of the LST for both subsets are calculated for each urban cluster and their difference is the surface UHI for that cluster. Before taking the spatial means, the subsetted LST pixels are automatically resampled to 500 m x 500 m grids to match the resolution of the LU/LC data. When calculating the surface UHI for separate years, the same extent shape is applied to all years, though the subsetting is done using the MODIS LU/LC data for that particular year. Since the MODIS LU/LC data are only available till 2013, the 2013 data are also used for the years 2014 to 2017. Unless otherwise stated, the daytime UHI is derived from the mean of LST values at 1030 and 1330 LT, while the nighttime UHI is based on the mean of the LST at 0130 and 2230 LT. The same method is used to find the difference in
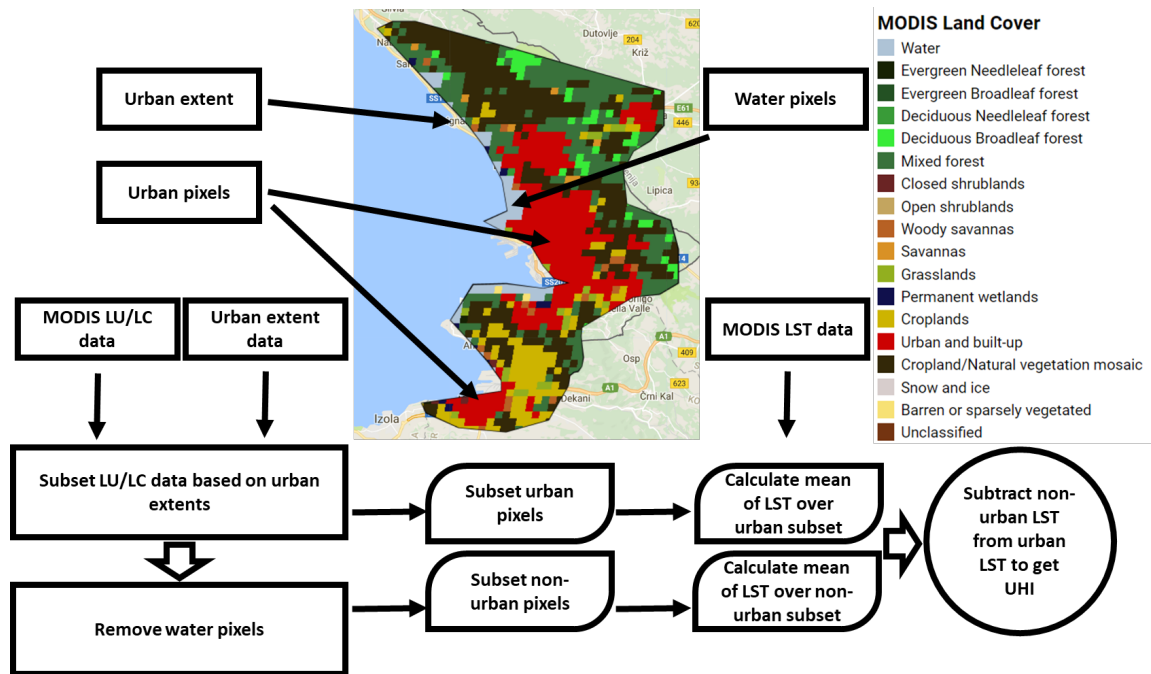
Figure A.1: Sequence of steps used to estimate the surface UHI for each urban cluster. First, a subset of the MODIS LU/LC data are created based on the the urban extent dataset. Two subsets of this data are created; one for urban land use, and another for non-urban, non-water land use. The mean of the LST over these LU/LC pixels gives the urban and rural temperatures, respectively. Finally, the difference between these two is the calculated surface UHI. The figure also shows one example of urban units used in the present study, along with the MODIS LU/LC dataset used to create the subsets.

Enhanced Vegetation Index (EVI) (ΔEVI), a proxy for green vegetation density, between the urban and rural pixels using the AQUA 16-day EVI dataset available at 250 m x 250 m resolution (MYD13Q1) for the same time period.

Evidently, the algorithm, in its current form, does not work for the clusters that are entirely urban or rural. This is especially true for small clusters (with area< 3 km^2) with very few pixels. We remove the clusters with no rural pixels. After removing these from the original dataset of 12022 separate clusters, we are left with 9483 urban clusters. Since the difference in elevation between the urban and rural pixels can influence the UHI intensity, the dataset was further filtered to only include those clusters with a mean elevation difference of less than 50 m. For this, we use the Global Multi-resolution Terrain Elevation Data

2010 (GMTED2010), which combines terrain elevation data from multiple sources and is available at 7 arc seconds (roughly 30 m at the equator) (Danielson and Gesch, 2011). Finally, to further constrain the variability in the ratio of urban to rural pixels for each cluster, only the clusters with at least 10% urban area are considered. The surface UHI is then calculated using all the available data after quality control (from 2000 to 2017 for TERRA and from 2002 to 2017 for AQUA). For the summer surface UHI, data for June, July, and August are considered for the Northern Hemisphere and December, January and February for the Southern Hemisphere. For winter, June, July, and August are considered for the Southern Hemisphere and December, January and February for the Northern Hemisphere. The final dataset consists of 7374 urban clusters comprising 760600 km^2 with 38.78% of the total area (294960 km^2) being urban with a mean elevation difference of 4.46 m between urban and rural pixels. This is similar to the area analyzed by Clinton & Gong (2013), though we use a new algorithm and 16 years of data versus the one year (2010) used in that study. The multiple years of data allow us to characterize the long-term variability of the surface UHI and get better uncertainty estimates of the seasonal trend and annual values.

A.3.2 Latitudinal pattern of the surface UHI

The zonal characteristics of the UHI at a global scale are first investigated. To do this, the Earth is divided into 5° latitudinal increments and the mean and standard error of the UHI intensity are computed for each increment. Some urban clusters lie on the boundary between two latitudinal increments and this would lead to double counting. To avoid this, the centroid of each urban cluster is determined before grouping into the latitudinal increments. Peng et al. (2011) characterized the latitudinal variability of the surface UHI difference between summer and winter using MODIS AQUA data for the 419 largest cities. For the purpose of algorithm validation, this is also done with the 419 largest urban clusters

in the present study (subsection A.4).

A.3.3 Climatic Variability of the Surface UHI

While zonal characteristics can give an overview of the global surface UHI characteristics, it cannot account for any forcing other than the latitudinally varying incoming solar radiation. There is some evidence that the surface UHI intensity is influenced by the background climate of the city (Zhao et al., 2014). Zonal characterization cannot account for differences in background climate since there may be multiple climate zones in one latitudinal increment. Thus, in the present study, the surface UHI characteristics are separately investigated for each climate zone.

The updated Koppen–Geiger classification data for 1901–2100 are used, based on Rubel and Kottek (2010). The Koppen-Geiger classification divides the world into 5 major climate zones: equatorial, arid, warm temperate, snow, and polar (Fig. A.2**a**). Similar to the latitudinal classification, the centroids of the urban clusters are used for grouping to minimize double counting using an XY tolerance of 500 m on ArcMap. There are 762 urban clusters in the equatorial climate zone, 1136 in the arid climate zone, 3968 in the warm temperate climate zone, 1499 in the snow climate zone. The latitudinal variation of the urban clusters for each climate zone is in Fig. A.2**b**, the distribution of the area of urban clusters is in Fig. A.3, and the distribution of the percentage of urban pixels in each cluster is in Fig. A.4. All the urban clusters in the polar climate zone are filtered out since the elevation difference between the rural and urban pixels is >50 m in all these clusters. The total number of urban clusters in all climate zone, when added, is 7374, which is 9 less than the total number of clusters in the global dataset. This is because the climate zone vector used in the grouping process do not enclose the position of some of the urban centroids. In addition, several urban clusters are double counted as they are in two or more climate zones at once; a result of the XY tolerance used while grouping. Since the sample
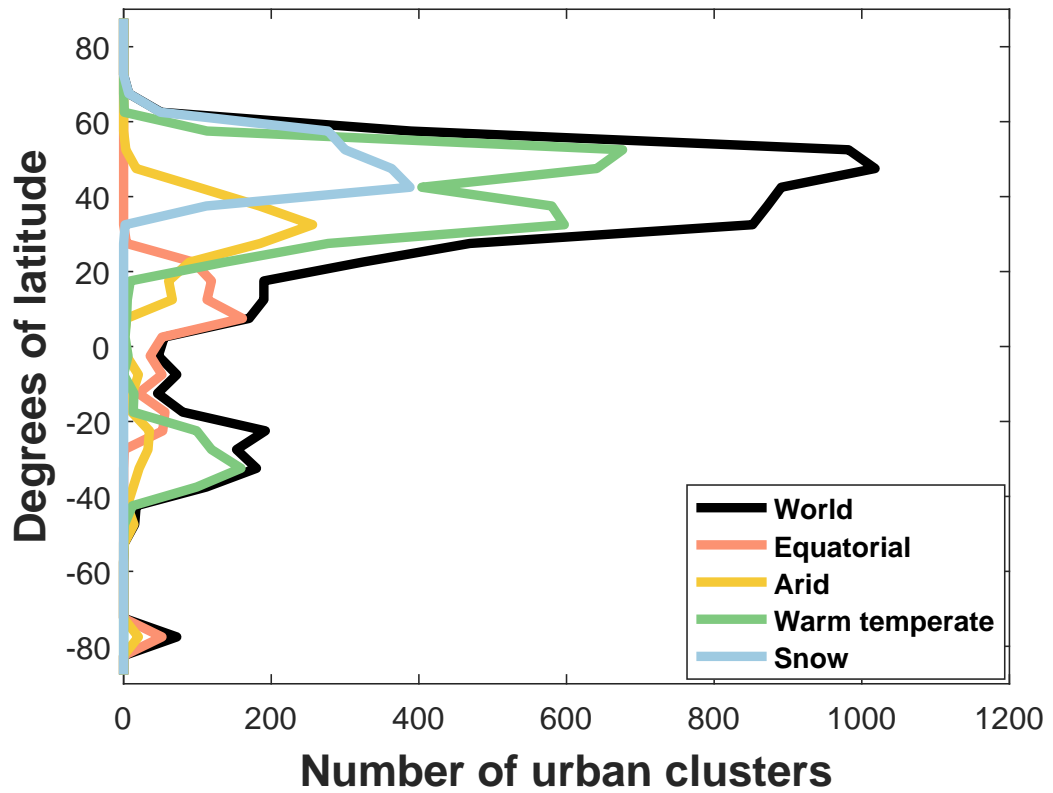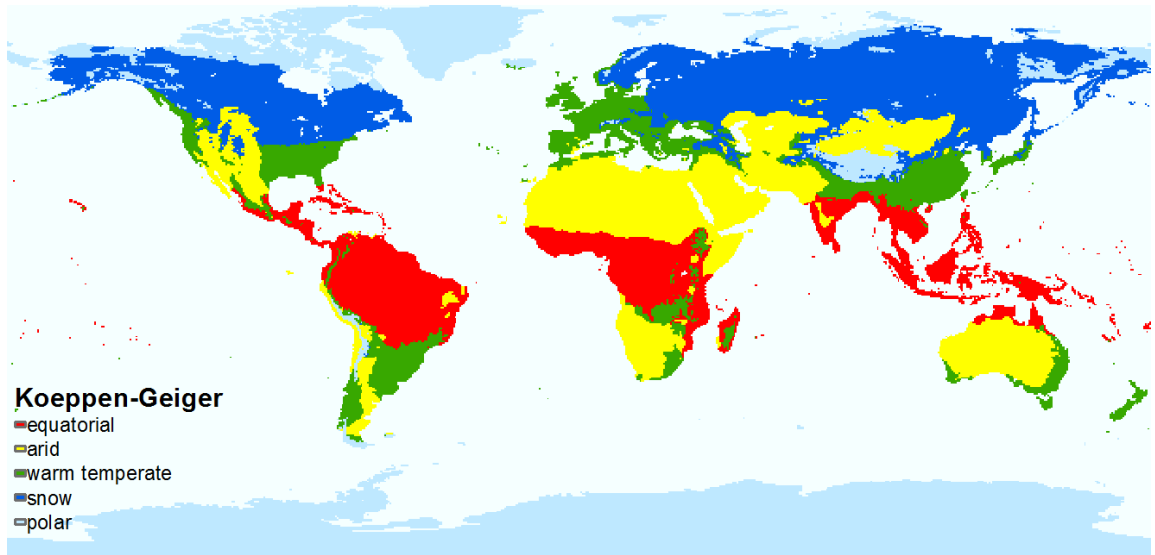
Figure A.2: The major 5 climate zones as defined by the Koppen-Geiger climate classification and the latitudinal variation of the urban clusters for the world and each climate zone

Table A.1: Summary of surface UHI characteristics (mean $\pm$ standard deviation) for the largest 419 urban clusters compared to the largest 419 cities considered by Peng et al.(2011).

Source	TERRA (present study)	AQUA (present study)	Peng et al.
Annual day (°C)	1.11 $\pm$ 1.05	1.50 $\pm$ 1.26	1.50 $\pm$ 1.20
Annual night (°C)	0.89 $\pm$ 0.44	0.80 $\pm$ 0.44	1.10 $\pm$ 0.50
Summer day (°C)	1.62 $\pm$ 1.47	2.03 $\pm$ 1.64	1.90 $\pm$ 1.50
Summer night (°C)	1.05 $\pm$ 0.45	0.90 $\pm$ 0.41	1.00 $\pm$ 0.05
Winter day (°C)	0.64 $\pm$ 0.77	0.96 $\pm$ 1.00	1.10 $\pm$ 1.20
Winter night (°C)	0.86 $\pm$ 0.61	0.78 $\pm$ 0.61	1.00 $\pm$ 0.70

size is large, these small discrepancies are trivial.

A.4 Validation of Results

Peng et al. (2011) used the city-clustering algorithm by Rozenfeld et al. (2008) to define the urban areas at a fine scale. Then, they estimated the surface UHI as the difference in LST between the city core and its rural hinterland using MODIS AQUA data. In contrast, the SUE algorithm developed in the present study uses the difference in the mean LST of the urban pixels and the mean LST of the non-urban pixels within the same urban extent to define the surface UHI. To validate the accuracy of SUE at estimating the surface UHI versus the method used by Peng et al. (2011), the surface UHI intensities from AQUA for the 419 largest urban clusters in the dataset (same as the number of cities studied by Peng et al. (2011) were calculated. The surface UHI intensities for TERRA were also calculated for comparison. The daytime and nighttime surface UHI intensities (mean $\pm$ standard deviation) for annual, summer and winter for both methods are shown in Table A.1. The results from the SUE algorithm are in line with the results from the city-clustering algorithm, especially for daytime. During nighttime, the SUE algorithm slightly underestimates the surface UHI (around 27% underestimation for annual nighttime surface UHI), while wintertime UHI intensity is biased low for both daytime and nighttime.
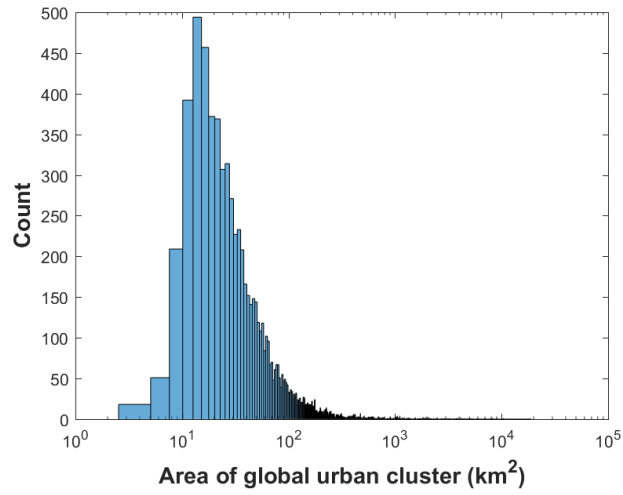
(a) World
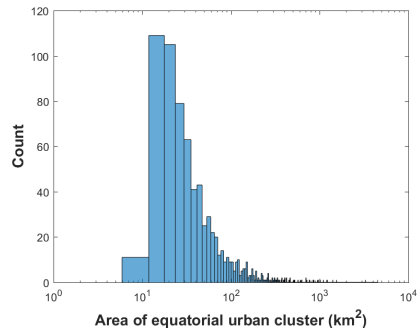
(b) Equatorial climate zone
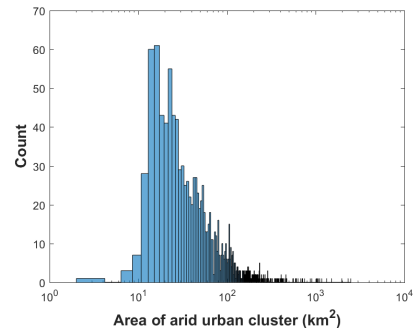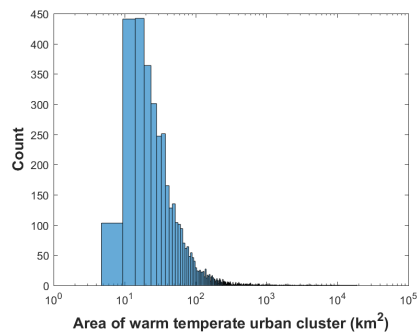
(c) Arid climate zone

(d) Warm temperate climate zone
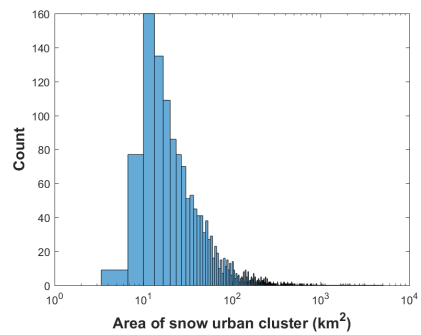
(e) Snow climate zone

Figure A.3: Distribution of the area of the urban clusters for the world and each climate zone.
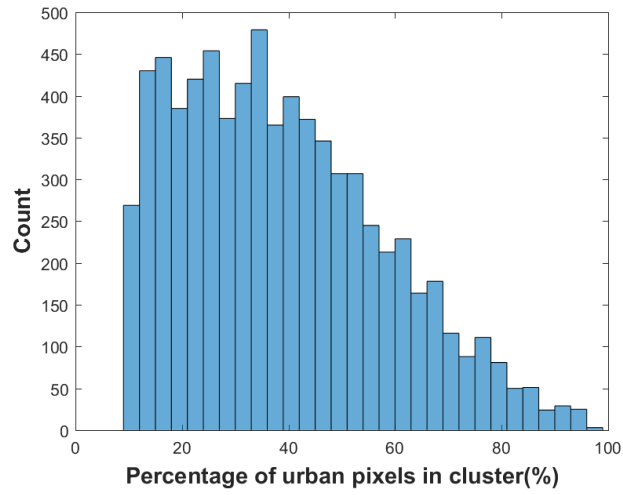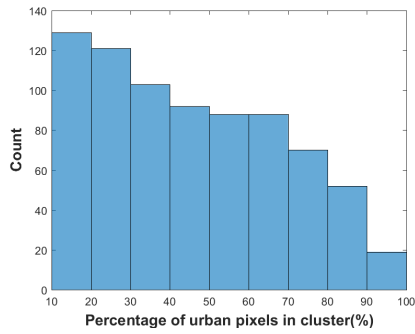
(a) World

(b) Equatorial climate zone
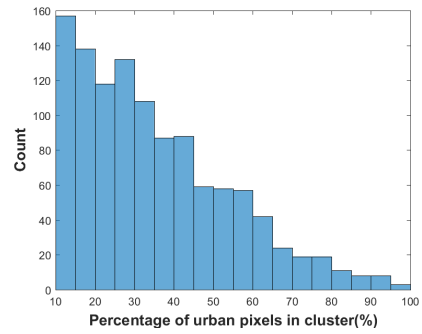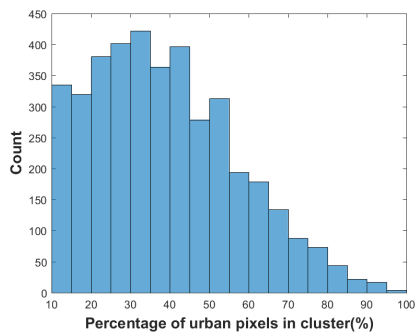
(c) Arid climate zone

(d) Warm temperate climate zone
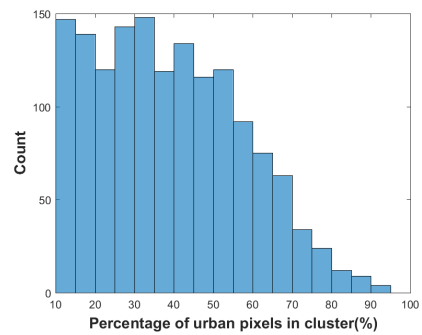
(e) Snow climate zone

Figure A.4: Distribution of the percentage of urban area in each cluster for the world and each climate zone.

The study by Peng et al. (2011) did not show any major seasonality for the nighttime surface UHI, with annual, winter time and summertime mean values being very close. On the contrary, the present study shows that the summertime UHI is the highest and the winter time UHI is the lowest, and the annual mean UHI is between those two values. This is consistent with the observations for the 419 largest cities derived from the TERRA dataset. The seasonality of the UHI is discussed in more detail in section A.5.5.

The slight deviation from the previous values may not only be due to the different methodologies. The present study uses 16 years (from 2002 to 2017) of data for AQUA compared to 6 years of data (from 2003 to 2008) used in Peng et al. (2011). Moreover, the largest 419 urban clusters are not same as the largest 419 cities. Many of the larger urban clusters are created from contiguous cities. Thus, the 419 largest urban clusters incorporate more area than the 419 largest cities used in Peng et al. (2011). Moreover, in the present study, MODIS pixels with an error greater than 3 K are removed before the final analyses.

The latitudinal variation of the AQUA-derived surface UHI differences between summer and winter for the 419 largest urban clusters is compared with the pattern seen from the methodology used by Peng et al. (2011) in Fig. A.5. The study by Peng et al. (2011) used 15 latitudinal increments to find the variation, whereas we use 20 latitudinal increments of 5° width. Overall, both methods show very similar patterns. For daytime, the values from the present study have a less pronounced latitudinal variability. Otherwise, the peaks and troughs are roughly replicated by our methodology. The only exception is the opposite trend seen for 20° South latitude. For nighttime, the patterns from the two algorithms are even more similar in magnitude and latitudinal variability.

Clinton & Gong (2013) also calculated the surface UHI for all global urban areas for 2010 using 5 - and 10-km buffers. We compared the 2010 data from the present study with the results of that study (Table A.2). The UHI values found here are very similar to the

(a) Daytime   **(b)** Nighttime
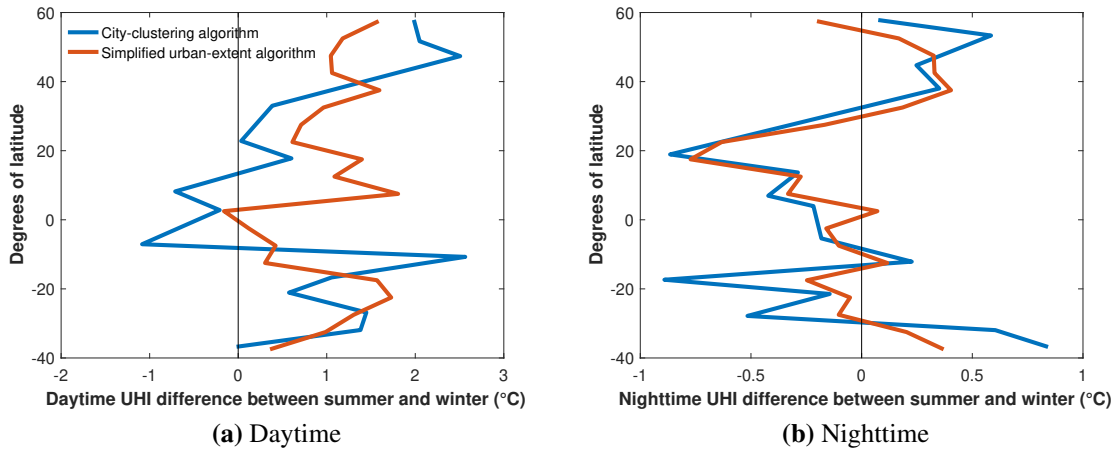
Figure A.5: Comparison of latitudinal variation in difference between summer and winter surface UHI intensity from the city-clustering algorithm-based definition and the SUE algorithm for **a** daytime and **b** nighttime. The black vertical line represents the zero value.

Table A.2: Summary of surface UHI characteristics (mean $\pm$ standard deviation) for the all urban areas compared to the results from Clinton & Gong (2013)

Local time	Present study (SUE)	Clinton & Gong (5 km buffer)	Clinton & Gong (10 km buffer)
0130 LT	0.51 ± 0.47	0.60 ± 0.90	0.70 ± 1.00
1030 LT	0.73 ± 0.86	0.70 ± 1.40	1.00 ± 1.60
1330 LT	1.00 ± 1.08	0.90 ± 1.60	1.10 ± 1.80
2230 LT	0.60 ± 0.47	0.60 ± 0.90	0.80 ± 1.00

values calculated using 5-km buffers and lower than those calculated using 10-km buffers.

The standard deviations of the UHI values are lower in the present study.

The results of present study are in agreement with the results of the buffer-based analysis for large cities and all cities. Thus, we are confident that the SUE algorithm is a viable alternative to buffer-based characterizations of surface UHI intensity.

A.5 Results

A.5.1 Global Patterns

Figure A.6 shows the global map of the mean surface UHI for daytime and nighttime derived from MODIS satellite measurements. The global mean surface UHI intensity is 0.85 °C for daytime and 0.55 °C for nighttime. The majority (87%) of the urban clusters show a positive daytime surface UHI, with 44% showing values greater than 1.00 °C. During nighttime, 93% of the urban clusters show positive UHI intensities, but only 13% show value greater than 1.00 °C. The urban clusters with negative surface UHI are concentrated in the dry and desert areas, namely the Arabian Desert in the Middle East, the Chihuahuan Desert in southern US and Mexico, the Thar Desert along the border of India and Pakistan, the Kalahari Desert in southern Africa, and the Patagonian Desert in the southern part of South America. The nighttime surface UHI intensities are generally lower than the daytime values. Daytime UHI is influenced by more factors like the difference in evaporative cooling and surface roughness between urban and rural areas, anthropogenic heat flux, and thermal inertia of built-up structures (Zhao et al., 2014). In contrast, nighttime UHI is primarily influenced by heat storage from the daytime, and anthropogenic heat flux. This explains why the temperature differential is higher during the day than at night.

When the UHI derived from AQUA and TERRA are analyzed separately, the data from AQUA shows higher values during daytime and lower values during nighttime. Table A.3 summarizes the surface UHI intensity from the global dataset from both TERRA and AQUA platforms. The annual daytime surface UHI intensity is greater than the nighttime intensity for both TERRA and AQUA. The daytime and nighttime summer surface UHI intensities are larger than their corresponding winter time components. The daytime intensity for summer are over twice the UHI intensity for winter for both TERRA and

213

(a) Daytime

(b) Nighttime
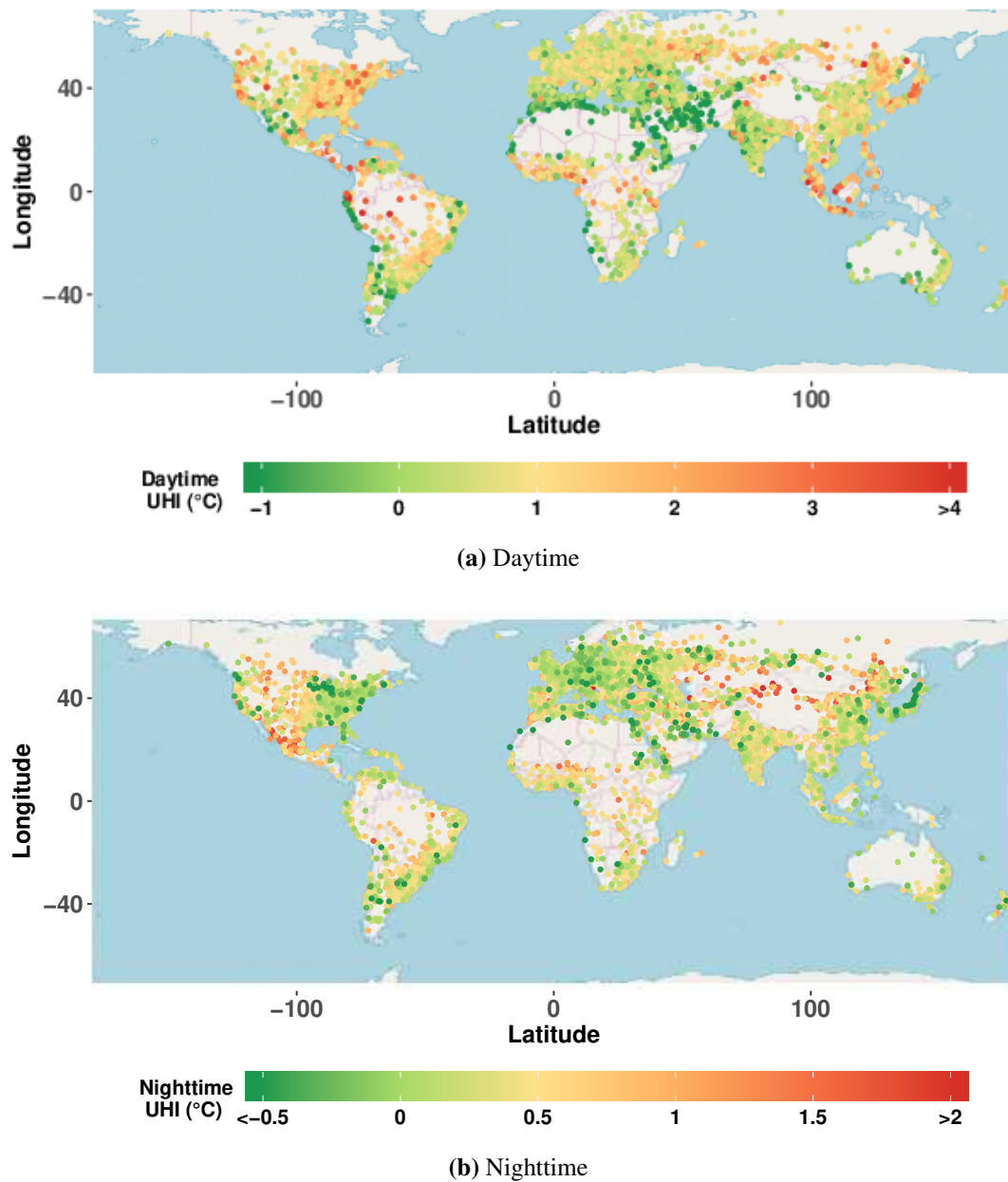
Figure A.6: Global map of mean surface UHI for 7374 urban clusters estimated using the SUE algorithm. The daytime value is the mean of the UHI intensity at 1030 LT derived from TERRA (2001-2017) and the UHI intensity at 1330 LT derived from AQUA (2003-2017). The nighttime value is the mean of the UHI intensity at 2230 LT derived from TERRA and the UHI intensity at 0130 LT derived from AQUA.

AQUA. For nighttime, the seasonal difference is less pronounced. The daytime surface UHI is larger than the nighttime surface UHI for all cases. Paired t-tests were performed between all daytime and nighttime datasets and they were found to be statistically significant with $p<0.01$ for all cases.

Table A.3: Summary of global surface UHI characteristics, where the sample size is 7374. Differences in daytime and nighttime UHI intensities are statistically significant ($p<0.01$) for all cases.

Period	Local time	Mean	Standard deviation	1st quartile	2nd quartile	3rd quartile
Annual	0130 LT	0.51	0.44	0.25	0.50	0.75
	1030 LT	0.71	0.82	0.30	0.74	1.17
	1330 LT	1.00	1.04	0.44	1.02	1.59
	2230 LT	0.59	0.44	0.32	0.56	0.84
Summer	0130 LT	0.57	0.44	0.30	0.55	0.82
	1030 LT	1.12	1.19	0.45	1.18	1.87
	1330 LT	1.44	1.42	0.61	1.51	2.36
	2230 LT	0.69	0.46	0.40	0.67	0.96
Winter	0130 LT	0.50	0.54	0.19	0.44	0.75
	1030 LT	0.35	0.59	0.09	0.35	0.63
	1330 LT	0.53	0.79	0.13	0.52	0.92
	2230 LT	0.57	0.54	0.24	0.50	0.84

A.5.2 Latitudinal Patterns

Figure A.7 shows the latitudinal variation in the surface UHI for daytime and nighttime. The solid lines show the mean surface UHI intensities for each 5° latitudinal increments, while the shaded portions represent the standard error from the mean. The daytime and
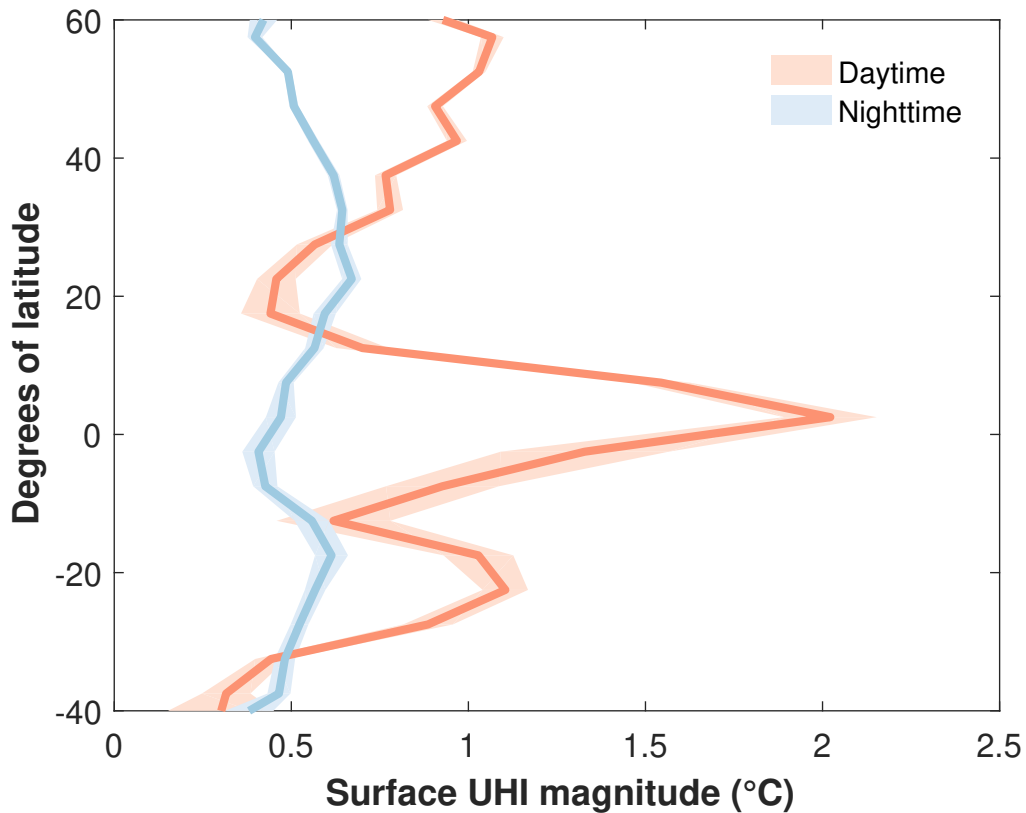
Figure A.7: Latitudinal variation in surface UHI intensity. The solid lines are for mean values, while the shaded portions represent the standard error. The daytime and nighttime intensities are consolidated values from TERRA and AQUA platforms.

nighttime surface UHI intensities show distinct patterns. For daytime, there are pronounced positive surface UHI intensities around the equator, at 20° South, and between 40° and 60° North. Compared to the daytime UHI, the nighttime UHI shows lesser latitudinal variability. There is a pronounced nighttime UHI at 30° North and around 10° South. At around 25° North and 30° South, the daytime and nighttime UHI intensities flip, i.e. the nighttime surface UHI is greater than the daytime intensity. These latitudes are predominantly arid and cities in arid climate show higher nighttime surface UHI intensity (refer section A.5.3). This reversal of the UHI diurnality in desert cities has been observed in previous studies (Imhoff et al., 2010, Zhang et al., 2010, Lazzarini et al., 2013).

A.5.3 Variations Across Climate Zones

Figure A.8 shows the mean and standard error of the daytime and nighttime surface UHI categorized into the Koppen-Geiger climate zones. For daytime, the highest surface UHI is for the equatorial urban clusters, followed by snow, warm temperate, and arid. Arid urban clusters, in particular, have nearly zero daytime UHI. This pattern is consistent at both 1030 LT and at 1330 LT. For nighttime, arid urban clusters have the highest UHI intensity. The urban clusters in equatorial, warm temperate and snow climate zones all show very similar surface UHI intensities. The daytime surface UHI is greater than the nighttime surface UHI for all climate zones other than the arid. Paired t-tests confirm that the difference between the daytime and nighttime UHI intensity is statistically significant (p<0.01) for all climate zones.

(a) AQUA   (b) TERRA
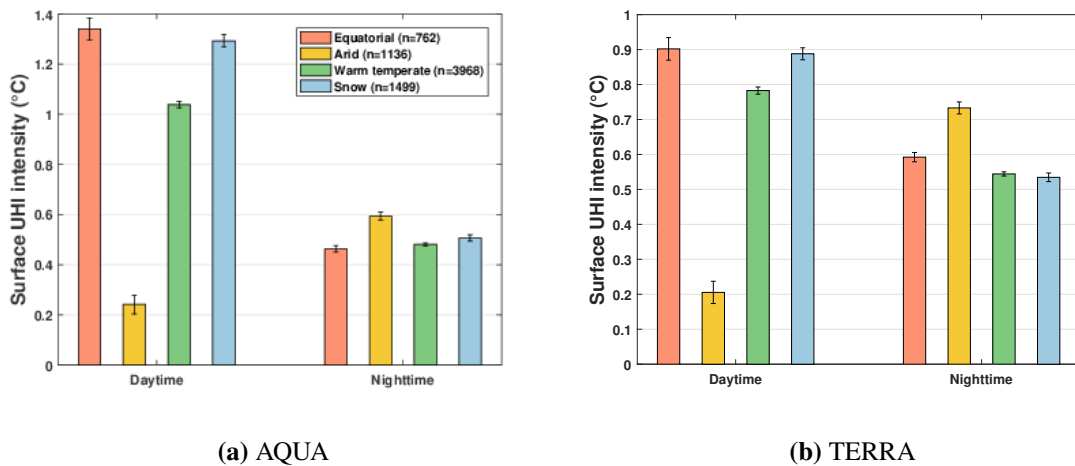
Figure A.8: Global daytime and nighttime surface UHI intensities (mean $\pm$ standard error) for each climate zone.

A.5.4 Diurnality

The daytime and nighttime measurements from TERRA and AQUA were combined to calculate the diurnality of the surface UHI intensity for the world and for each climate
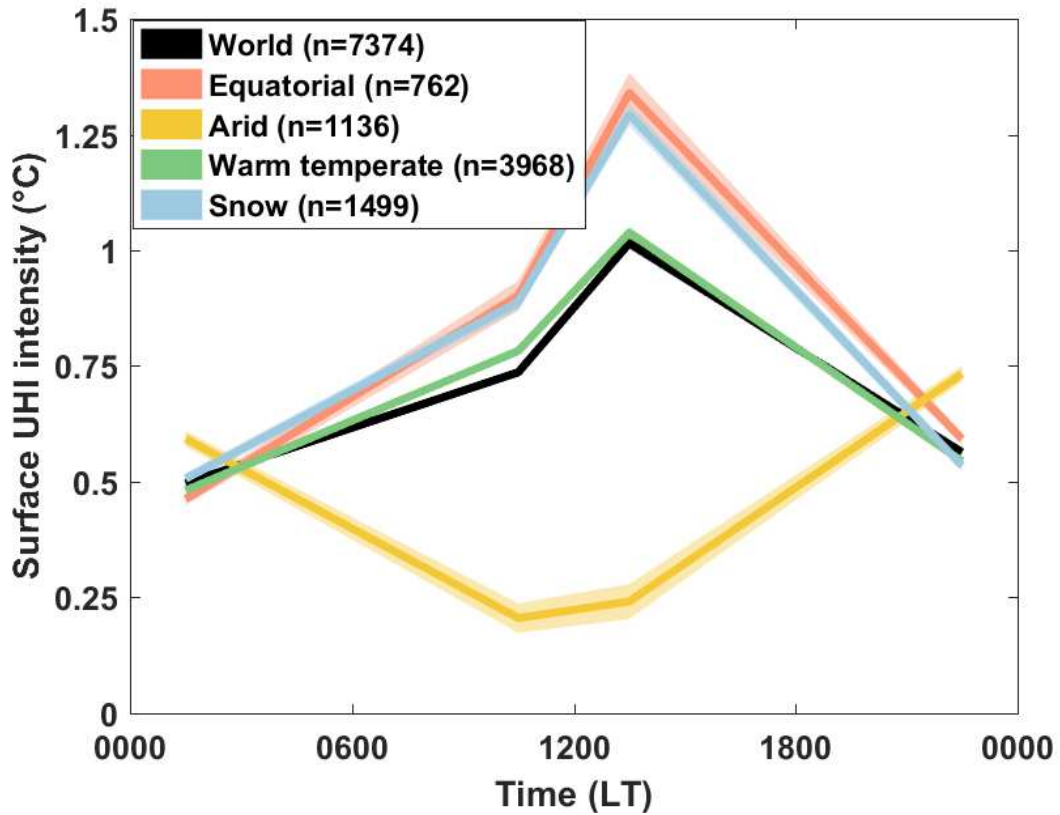
Figure A.9: Diurnality of the surface UHI for the world and each climate zone. The solid lines represent the mean value, while the shaded areas represent the standard errors.

zone. In Fig. A.9, the solid lines represent the mean of the diurnal variation, while the shaded regions show the one standard error from the mean. As discussed previously, globally, the surface UHI intensity is higher during the day than at night, which has been seen in previous studies (Peng et al., 2011, Clinton & Gong, 2013). The present study shows that this diurnality is consistent across all the climate zones except the arid zone. Among equatorial, warm temperate, and snow urban clusters, the UHI intensity is highest at 1330 LT and lowest at 0130 LT. For the arid zone, the highest surface UHI intensity is at 2230 LT and the lowest is at at 1030 LT.

The diurnal range of the surface UHI – the difference between the maximum and minimum surface UHI intensities – is highest for the equatorial urban clusters (0.88 °C), fol-
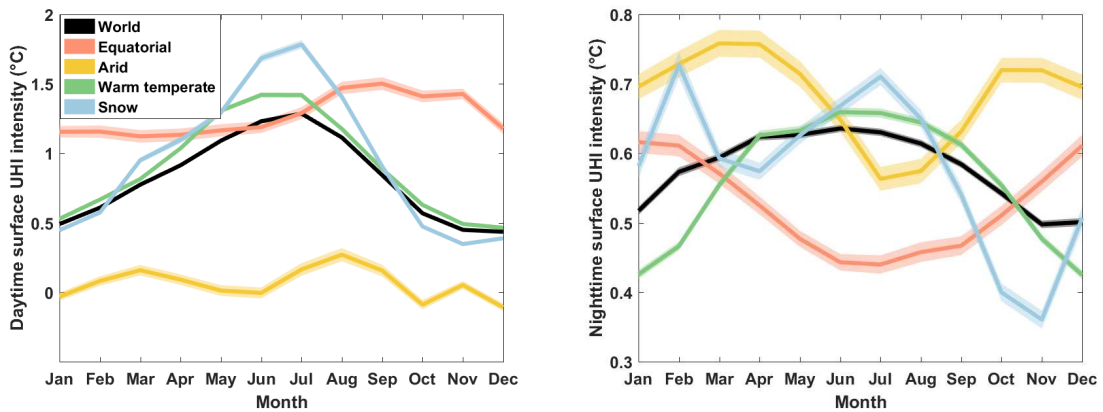
Figure A.10: Seasonal variability in global daytime and nighttime surface UHI intensities for each climate zone. The solid lines represent the mean value, while the shaded areas represent the standard errors.

lowed by 0.79 °C for snow, 0.56 °C for warm temperate, and 0.53 °C for arid. Overall, the diurnal range of the surface UHI is 0.52 °C. The standard error of UHI intensity is very low because of the large sample size.

A.5.5 Seasonal Variability

The monthly means and standard errors of the surface UHI intensity for each of the 12 months of the year are presented in Fig. A.10. Globally, the daytime surface UHI shows higher values during the boreal summer, with the highest intensities in July (1.29 ± 0.01 °C) and the lowest values in December 0.43 ± 0.01 °C.

When the data are divided into climate zones, all of them do not show the same pattern. The warm temperate and snow urban clusters show comparable patterns with low values during the boreal winter and high values during boreal summer. For daytime, the maximum surface UHI intensities for the warm temperate and snow urban clusters are during the boreal summer (1.43 ± 0.02 °C in June for warm temperate; 1.78 ± 0.03 °C in July for snow) and the lowest values are in boreal autumn (0.46 ± 0.01 °C in December for warm temperate; 0.35 ± 0.01 in November °C for snow). The daytime surface UHI intensity in

the equatorial and arid zones show distinct patterns. For the arid urban clusters, there is hardly any seasonality compared to the other climate zones. Moreover, the daytime surface UHI intensities are close to zero for most of the year. The daytime surface UHI in the equatorial climate zone shows the opposite pattern to the warm temperate and snow climate zones, with the highest values during boreal autumn and the lowest values during boreal spring.

The seasonality of the global nighttime surface UHI is similar to the daytime pattern with June highs and November lows (Fig. A.10 **b**). The nighttime surface UHI of the warm temperate climate zone shows high values during boreal summer (July) and low values in boreal autumn (December). Like the daytime case, the seasonality of the monthly surface UHI is atypical for equatorial and arid zone. The arid zone again shows two peaks during the year, one in March and another in October. The minimum surface UHI in the arid urban clusters is in July. The equatorial zone shows the highest surface UHI intensity in boreal winter (January) and the minimum in boreal summer (July). For nighttime, urban clusters in the snow climate zone also show two peaks during the year, one in February and another in July. The lowest nighttime intensity for this climate zone is in November.

The maximum daytime surface UHI intensity in all climate zones other than equatorial are in and around boreal summer. Eighty nine percent of the urban clusters considered in the present study are in the Northern Hemisphere. Moreover, most of the urban clusters in the Southern Hemisphere are in the Tropics, which show very little seasonality. Since the energy imbalance due to urban land use (due to changes in albedo, thermal mass, evapotranspiration, etc.) is a function of the magnitude of incoming solar radiation, it makes sense that the surface UHI is highest when the Northern Hemisphere receives the highest net radiation. When the dataset is separated into hemispheres, the seasonal variation is identical in the Northern Hemisphere and reverses for the Southern Hemisphere (Fig. A.11). For the Southern Hemisphere, the peak daytime surface UHI intensity is shifted

(a) Northern Hemisphere

(b) Southern Hemisphere

(c) Northern Hemisphere

(d) Southern Hemisphere
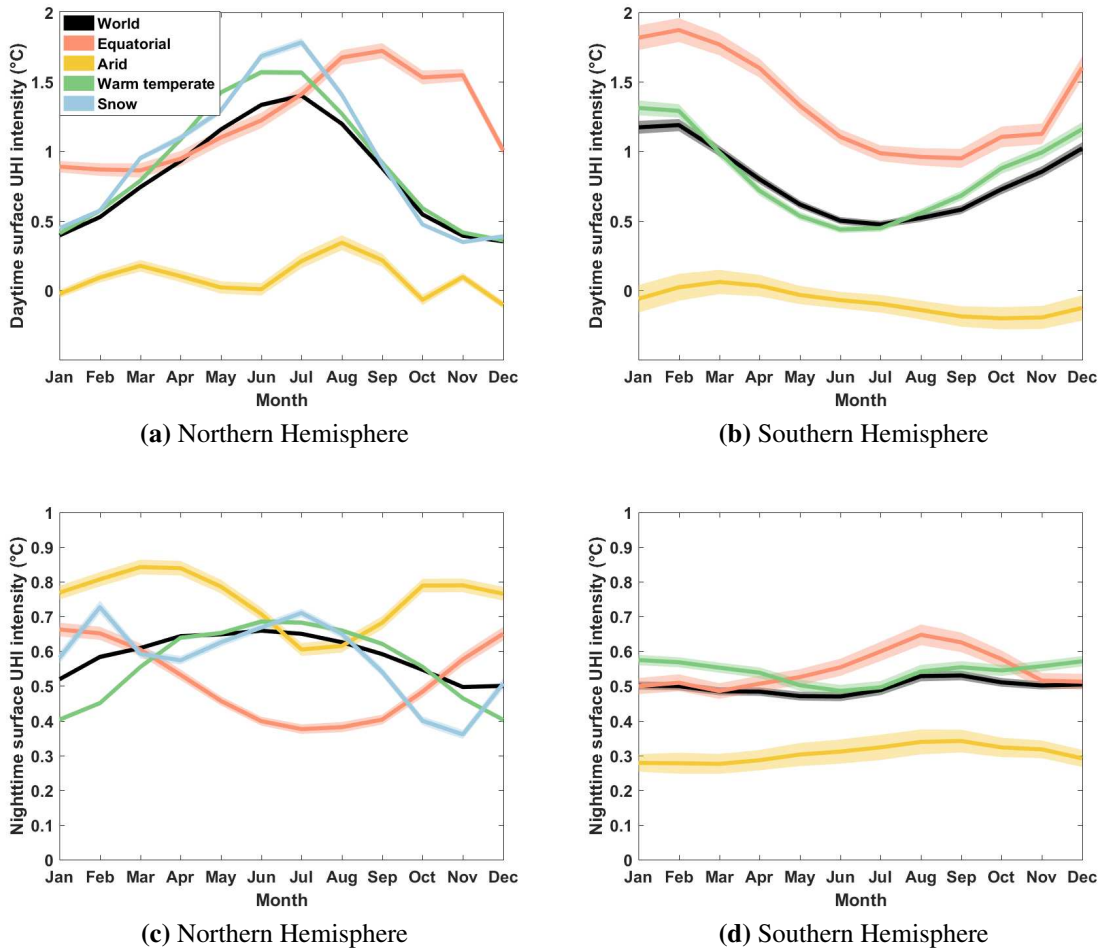
Figure A.11: Seasonal variation in daytime and nighttime surface UHI magnitudes for each climate zone from consolidated TERRA and AQUA measurements for the Northern and Southern Hemispheres. The solid lines represent the mean value, while the shaded areas represent the standard errors.

towards the austral summer for all the climate zones. Nighttime surface UHI shows very little seasonal variation in the Southern Hemisphere.

The global inter-seasonal range of the daytime UHI – the difference between the maximum and minimum mean monthly daytime surface UHI intensities during the 12-month cycle – is 0.85 °C. The highest seasonality in the daytime surface UHI is 1.44 °C for urban clusters in the snow climate zone, followed by warm temperate zone (0.95°C). Inter-seasonal range of daytime surface UHI 0.38 °C for both equatorial and arid climate zone.

The inter-seasonal range of the global nighttime UHI is very low (0.14 °C). A recent multi-city study showed that many urban centers in India show a negative surface UHI during daytime during the hot period (Shastri et al., 2017). This dampens the seasonality of the daytime UHI in the equatorial climate zone. The snow urban clusters show the highest inter-seasonal range of nighttime UHI intensity (0.37 °C), followed by warm temperate (0.23 °C), arid (0.19 °C), and equatorial (0.18 °C).

Very few studies have investigated the seasonality of the UHI on a month-by-month basis for multiple cities (Debbage & Shepherd, 2015). Clinton & Gong (2013) looked at the time of maximum and minimum surface UHI intensity for cities around the globe, though they did it only for 2010. This is the first study to characterize the seasonality of the surface UHI at a global scale using all available MODIS observations.

A.5.6 Long-Term Trend

Figure A.12 shows the temporal variability in the annual UHI from 2003 to 2017 based on aggregated data from TERRA and AQUA. The change per decade for each case, along with its 95% confidence interval, is mentioned in the figure. Globally, the daytime surface UHI shows a positive temporal trend, with an increase of around 0.03 ± 0.02 °C per decade. In comparison, the nighttime surface UHI intensities have remained practically unchanged (-0.00 ± 0.01 °C per decade). The increase in the daytime UHI intensity is highest for the snow urban clusters (0.05 ± 0.03 °C per decade) and lowest in the arid zone (-0.03 ± 0.01 °C per decade).

For nighttime, the surface UHI intensity does not show any significant change (with 95% confidence), except for urban clusters in the arid zone, which show an increasing trend (0.03 ± 0.01 °C per decade). Daytime surface UHI intensity has decreased significantly in arid urban clusters over the last decade and a half. This makes sense because urban clusters in arid climate are cooler than their surroundings (Zhao et al., 2014) and

222
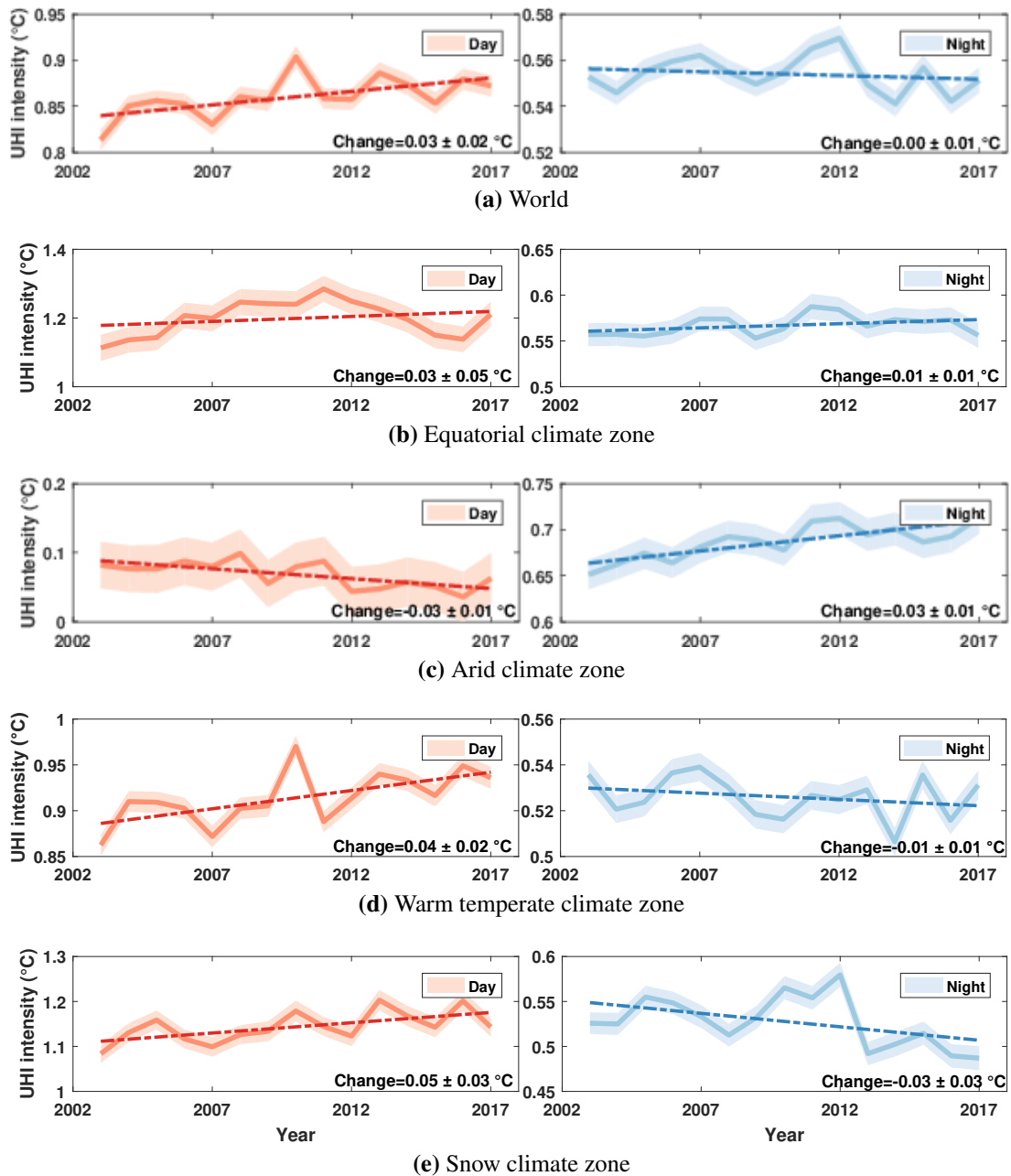
Figure A.12: Temporal variability in annual daytime and nighttime surface UHI intensities from 2003 to 2017. The solid lines represent the mean values, while the shaded areas represent the standard errors. The dashed line represents the trend for best linear fit and the change in the surface UHI intensity per decade (mean $\pm$ 95% confidence interval) is mentioned on each plot.

expansion of these areas over time would intensify these urban cool islands. The daytime UHI intensity change over the warm temperate zone, which includes the majority of urban clusters in Europe and North America, is also positive. The present study is the first investigation of how the surface UHI has changed over the last decade and a half on a global scale and for each climate zone using observed data.

In comparison to the changes found here, the global land temperature anomalies have increased at the rate of 0.30 °C per decade from 2003 to 2017 (NOAA, 2018). It should be noted that since the surface UHI is calculated in reference to non-urban land use, the changes in UHI intensity found in the present study is in addition to the increase in surface temperature due to global climate change. In comparison, deforestation shows a much stronger effect, though the strength and sign of change depends on the latitude (Lee et al., 2011). A recent study using MODIS LST products from 2003 to 2013 found an increase in average surface temperature at the rate of 0.28 °C per decade in equatorial regions, a maximum cooling of 0.55 °C per decade in boreal regions, and a warming of up to 0.32 °C per decade in temperate regions (Li et al., 2016).

Previously, two such studies (Fischer et al., 2012, Oleson, 2012) have analyzed the difference in urban and rural response to climate change using global climate models, i.e. the change in the UHI intensity. Depending on the climate change scenario used (best to worst), the UHI either stayed the same or slightly reduced compared to the present day scenario. However, these studies did not take urban expansion into consideration, which could be influencing the changes observed in the present study.

A.6 Discussion

A.6.1 Vegetation Control on the Surface UHI Intensity

Several previous studies have shown that difference in vegetation between the urban and rural areas strongly modulates the surface UHI intensity via differential evaporative cooling of urban versus rural surfaces. This has been seen when comparing surface UHI of multiple cities (Peng et al., 2011, Clinton & Gong, 2013), as well as when comparing the seasonal surface UHI trend of individual cities (Qiao et al., 2013, Chakraborty et al., 2017). Similarly, in the present study, when the dataset is divided into increasing ΔEVI quartiles, the daytime surface UHI intensity decreases (Fig. A.13). This is particularly true for global, equatorial, arid, and warm temperate cases. For the snow urban clusters, daytime surface UHI increases slightly for the highest ΔEVI bin. This is because these cities are primarily in the northern latitudes, where vegetation control is less dominant. Similarly, there is no consistent association between nighttime UHI and ΔEVI since, mechanistically, impact of vegetation on surface temperature is dominant during daytime.
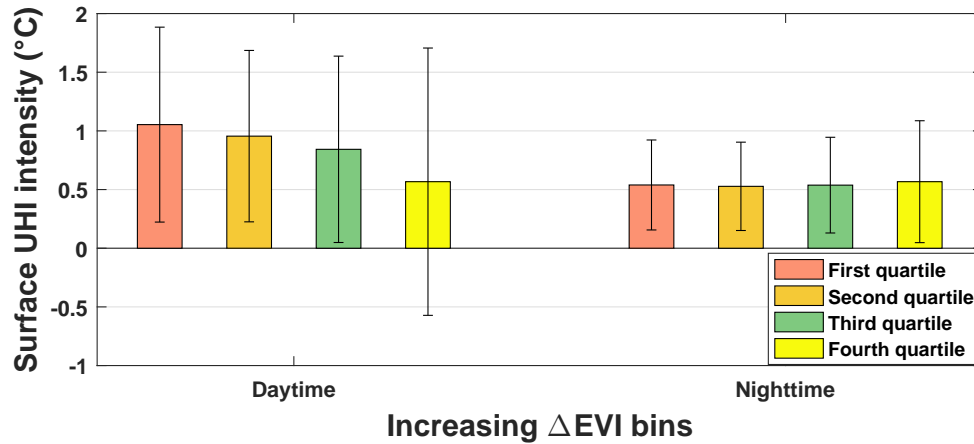
(a) World
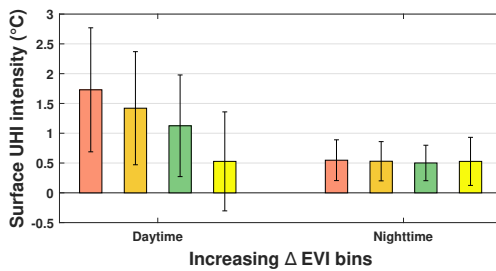
(b) Equatorial climate zone
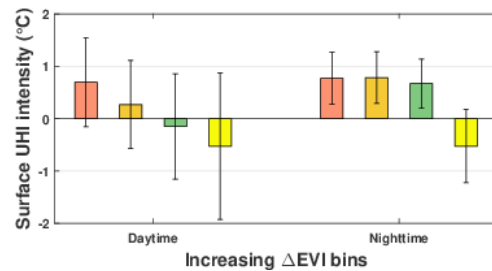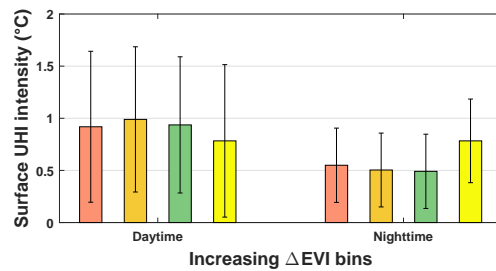
(c) Arid climate zone

(d) Warm temperate climate zone
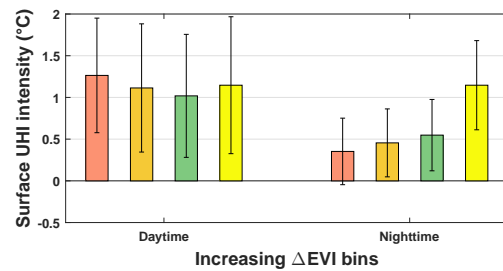
(e) Snow climate zone

Figure A.13: Daytime and nighttime surface UHI intensity (mean $\pm$ standard deviation) for increasing urban-rural EVI difference bins.

We examine how the seasonality of the ΔEVI modulates the seasonal variability of the surface UHI. The monthly ΔEVI accounts for 95% of the variance in the monthly daytime UHI at a global scale (Fig. A.14). Similar strong correlations are found for urban clusters in warm temperate (r^2=0.94) and snow (r^2=0.84) climate zones. The correlations are not

statistically significant (p >0.01) for urban clusters in equatorial and arid zones. This is partly because the seasonal variability is lowest in these climate zones as they are nearer to the equator. Moreover, vegetation is not a strong determinant of the daytime UHI in the arid zone and the equatorial region is strongly influenced by other factors, like cloudiness, monsoonal rainfall, etc., which can impact the UHI intensity.
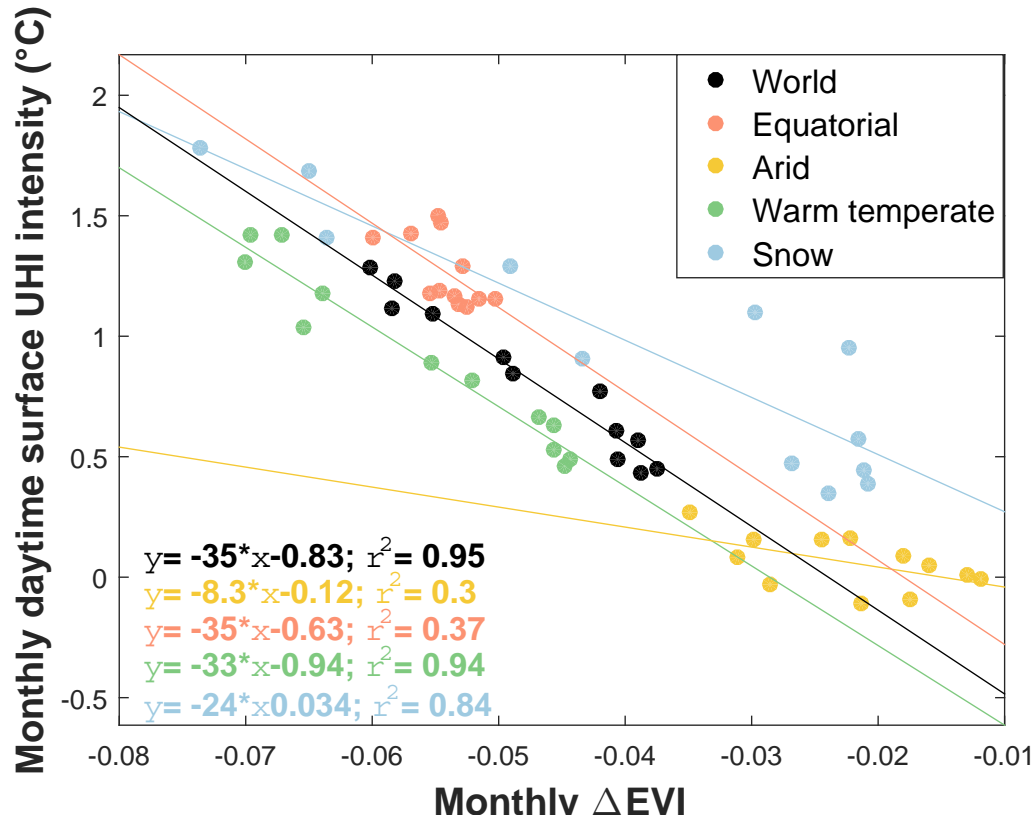
Figure A.14: Association between monthly daytime surface UHI intensity and monthly ΔEVI for all urban clusters, and urban clusters in each climate zone.

The rural EVI shows a stronger seasonal cycle than the urban EVI for all climate zones other than equatorial, which modulates the differential evaporative cooling between urban and rural areas, and thus, the daytime UHI intensity (Fig. A.15). The nighttime surface UHI shows a much weaker association with the ΔEVI, suggesting that it is not strongly controlled by the vegetation differential between urban and rural surfaces, as also found in a previous study (Peng et al., 2011). For nighttime, the association is only statistically

significant for the world and warm temperate climate zones (Fig. A.16).
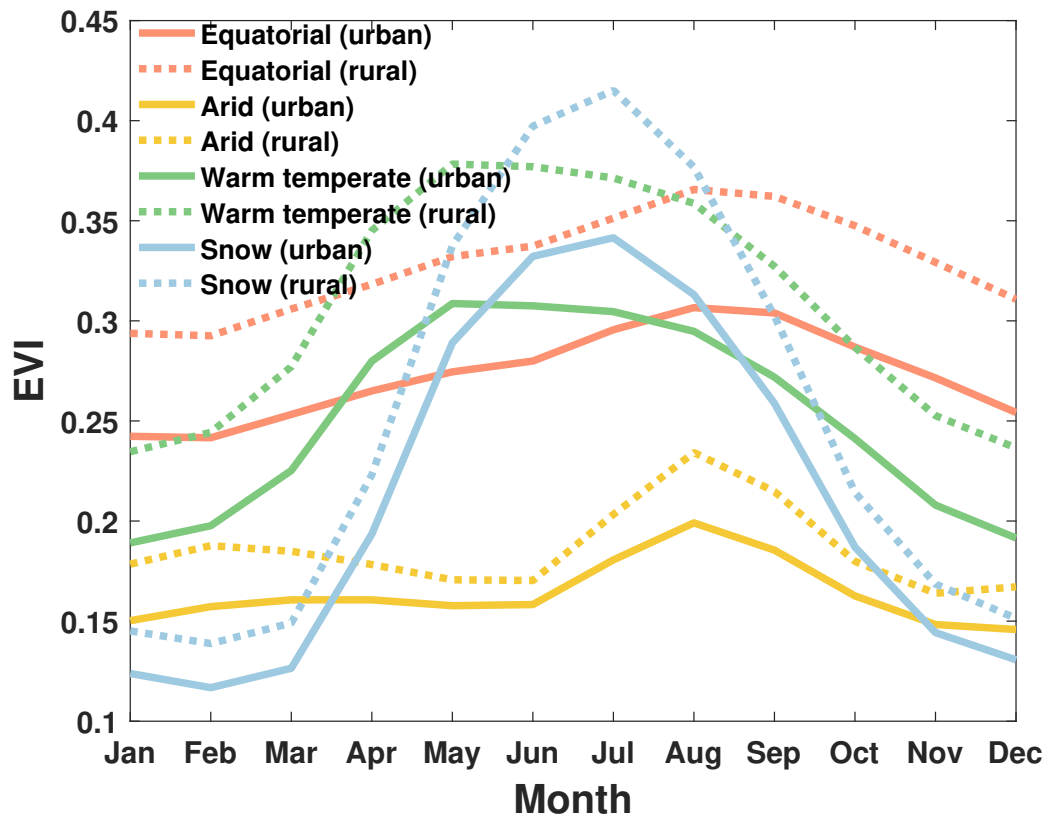
Figure A.15: Seasonal variation in urban and rural EVI for the world and each climate zone from 16-day AQUA measurements.
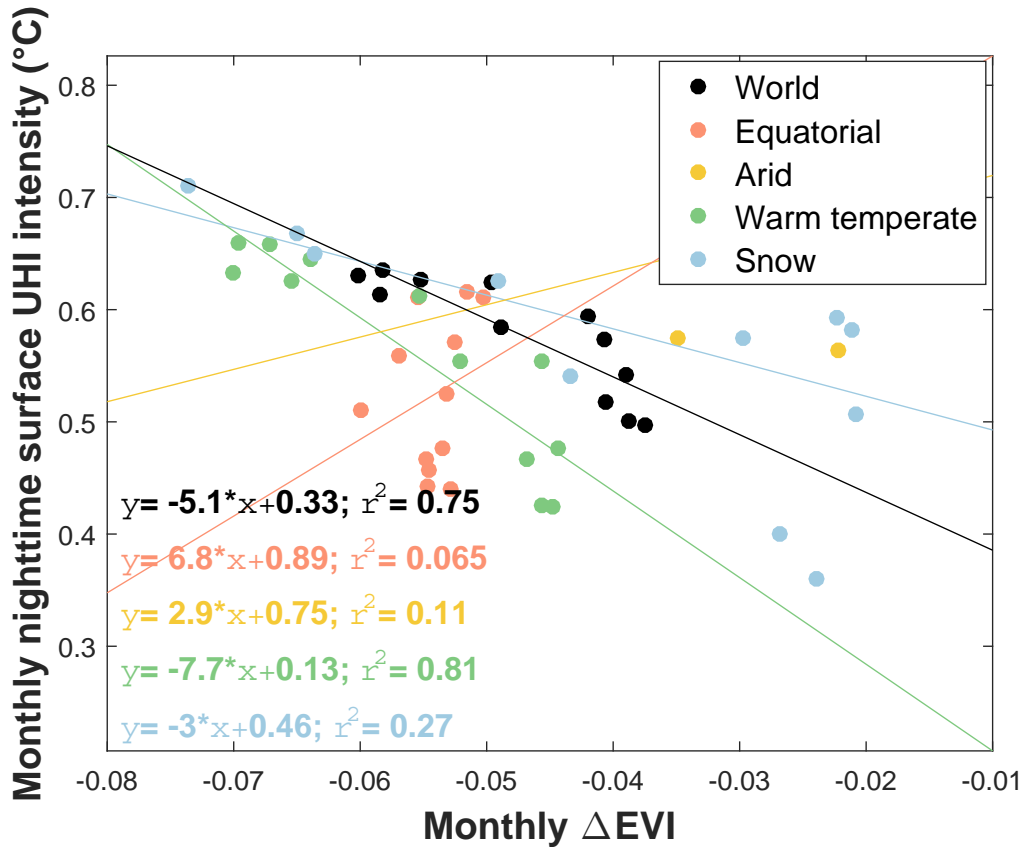
Figure A.16: Association between monthly nighttime surface UHI intensity and monthly ΔEVI for all urban clusters, and urban clusters in each climate zone.

Similar correlations were attempted between the yearly daytime and nighttime surface UHI intensities and the yearly ΔEVI values (Fig. A.17 and A.18). The relationships are much weaker, except for the arid zone. Temporal analyses of the urban and rural EVI over 16 years show that the rate of change of urban EVI per decade is lower than the corresponding change in the rural EVI (Fig. A.19). Globally, the urban EVI has remained the same while the rural EVI has increased slightly. However, these results are near the detection limit of MODIS.
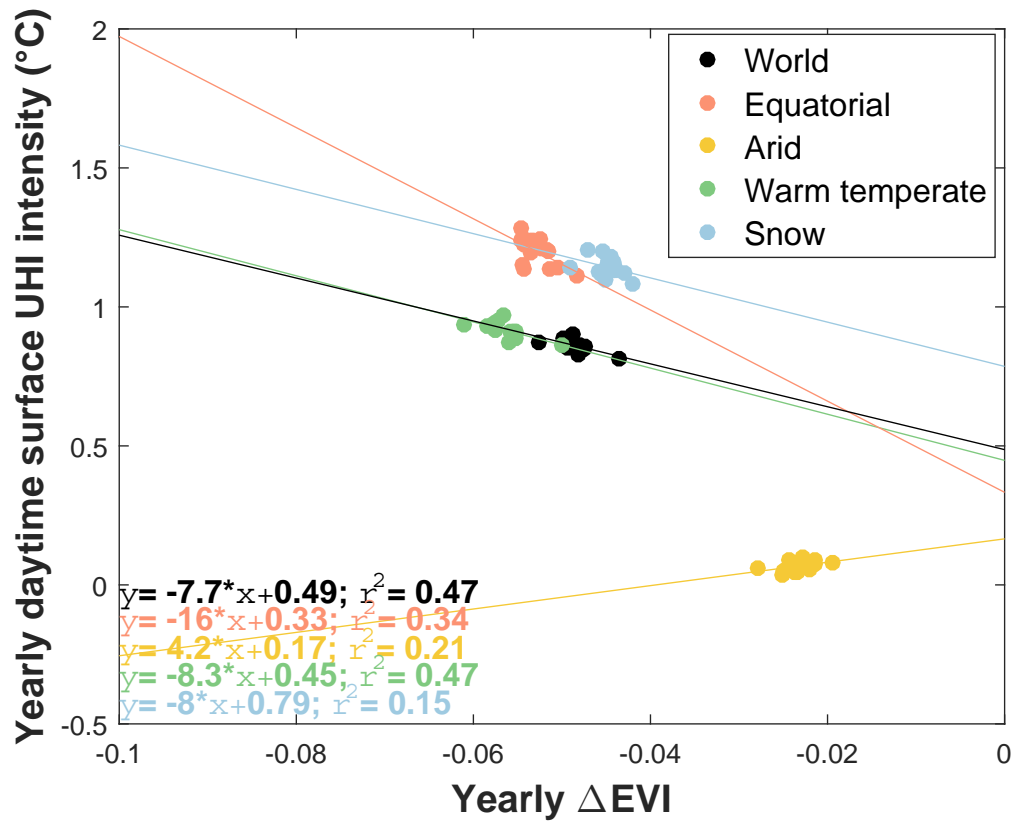
Figure A.17: Association between yearly (2003-2017) surface UHI intensity and monthly ΔEVI for all urban clusters, and urban clusters in each climate zone.
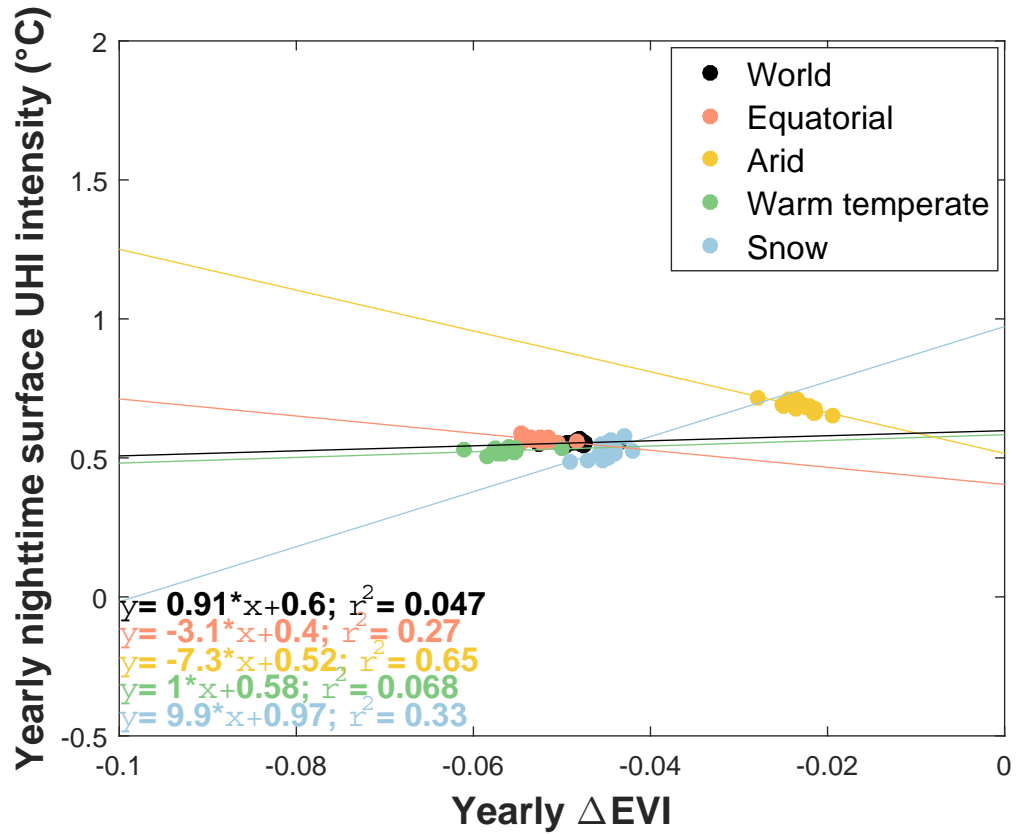
Figure A.18: Association between yearly (2003-2017) surface UHI intensity and monthly ΔEVI for all urban clusters, and urban clusters in each climate zone.

(a) World

(b) Equatorial climate zone

(c) Arid climate zone

(d) Warm temperate climate zone

(e) Snow climate zone
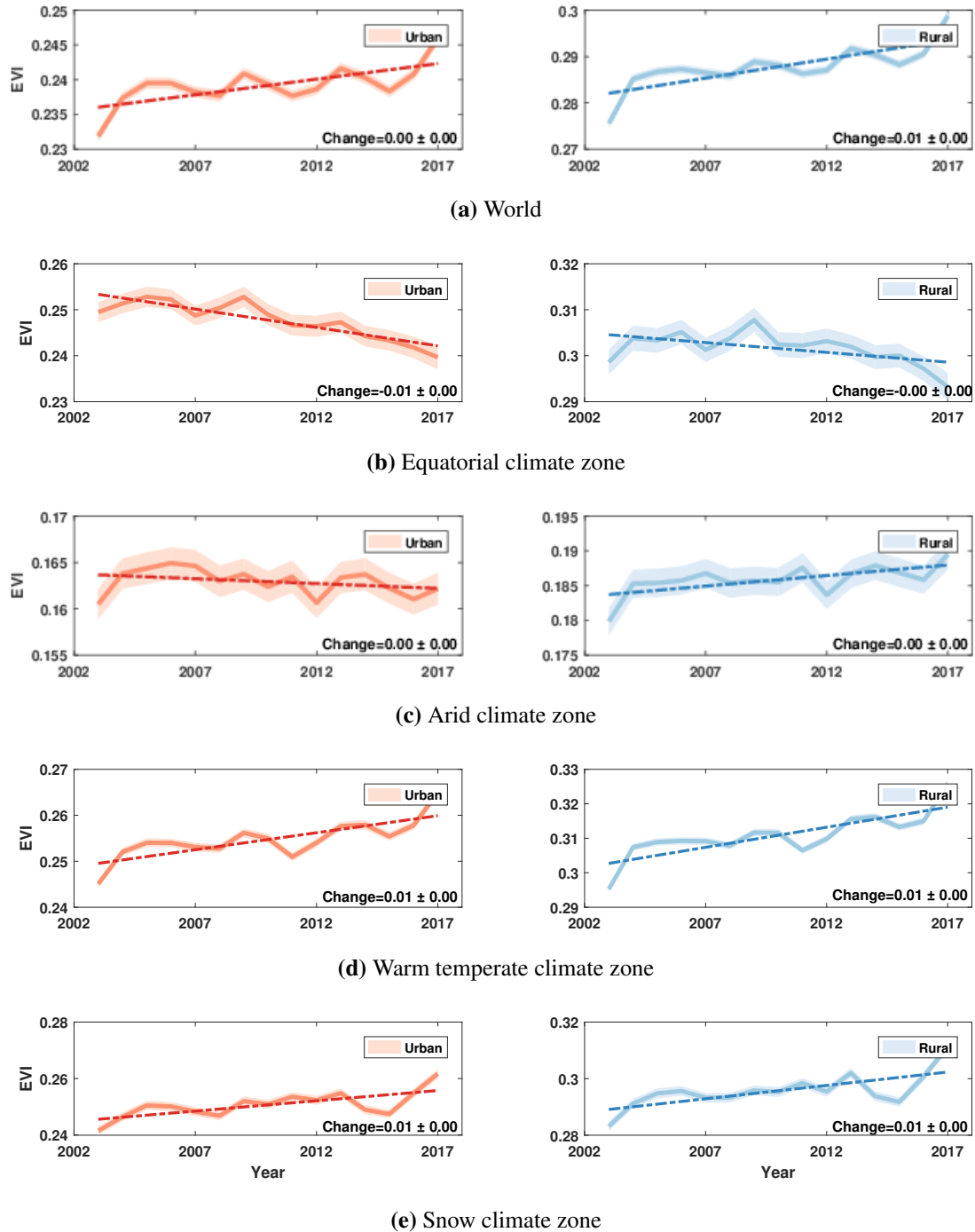
Figure A.19: Temporal variability in annual urban and rural EVI from 2003 to 2017. The solid lines represent the mean values, while the shaded areas represent the standard errors. The dashed line represents the trend for best linear fit and the change in EVI per decade (mean $\pm$ 95% confidence interval) is mentioned on each plot.

A.6.2 Advantages of the SUE Algorithm

One major advantage of the SUE algorithm is that it can be automated to estimate the surface UHI intensity at a global scale. We do not need to explicitly define a buffer around an urban area to implement this algorithm. Instead, we use the urban boundaries as the units of calculation, with the spectral classification of remotely sensed data being used to separate the urban and rural pixels. The choice of a buffer around an urban area can be arbitrary. Moreover, studies on individual cities sometimes use administrative boundaries to define the urban area, which are usually not related to the physical characteristics of urban land use. In comparison, the rural area in the Natural Earth dataset used in this iteration of the SUE algorithm is the non built-up pixels of human inhabited regions of Earth. Thus, the surface UHI, as defined in this study, is the temperature change experience by people as they move into built-up areas.

Since the footprint of the UHI varies significantly and can be up to 3.9 times the city area for nighttime, the choice of the rural pixel can significantly affect the calculated UHI intensity (Zhou et al., 2015). In many cities, especially developing cities, the city is surrounded by satellite towns with their own urban influence. This lack of standardization of the urban and rural area in the context of the UHI effect was also pointed out by Stewart and Oke (2009). The SUE algorithm, as implemented in this study, merges many of these satellite towns by using urban clusters, which is one step towards standardization.

A.6.3 Limitations of the Study

While the SUE algorithm, as used in this study, solves a few methodological issues in the existing UHI literature, it has limitations mainly due to the datasets used in the present study. The urban extent database used in the present study is based on satellite observations from 2001-2002. Urban areas have grown since then, especially Asian and African cities,

which have experienced tremendous urban sprawl in the last decade. The urban pixels of the MODIS MCD12Q1 raster data have also remained same since 2002 (Li et al., 2017). In addition, due to the nature of the urban extent data used in the study, some MODIS urban pixels transcend the urban extents, leading to a reduction of urban data points for some clusters. Given the large number of data points, this does not cause widespread biases at the global or regional scale. Since we do not use explicit buffers around the urban areas, the rural reference sprawls in an anisotropic manner, which could create biases in the estimated surface UHI for individual cities. Buffer-based estimates of surface UHI of coastal cities have the same problem, with the data from the buffer over the water pixels not being used as a part of the rural reference. In addition to the anisotropy in the rural reference, the percentage of urban clusters within each pixel varies significantly (Fig. A.4), from 10% to roughly 98%. Caution should be exercised when comparing the surface UHI of individual clusters because of this disparity in the percentage of urban area between different clusters.

These are mostly issues with the datasets used, not the SUE algorithm itself. New, more recent urban datasets, if available, can be used in conjunction with the SUE algorithm to create updated maps of the surface UHI.

While MODIS data products are relatively accurate over homogeneous terrain, their accuracy decreases substantially over heterogeneous surfaces, for instance, urban areas. To control for this, we have only considered the pixels with less than 3 K uncertainty. We initially tried using only pixels with uncertainty of less than 1 K. However, doing so removes the majority of urban pixels. It should be noted that this uncertainty is an issue with all satellite-based observations of UHI intensity.

In addition to the uncertainty of the urban pixels, the MODIS thermal band used for LST retrieval is constrained to clear sky conditions. The impact of cloud contaminated pixels could significantly alter the estimated UHI intensity. While we have considered

only clear sky pixels in our calculations, the frequency of cloudy pixels is a function of season and may impact our estimates of the UHI intensity due to biases in sampling. It is important to keep these uncertainties in mind while interpreting the results of this study.

A.7   Conclusions

A new algorithm (SUE) is designed to study the surface UHI at a global scale. The study validates a few well-known surface UHI characteristics, like latitudinal variability and the annual, summertime, and wintertime intensity. The algorithm extends the analysis by using a complete urban extent dataset and all available MODIS satellite observations. Most important is the analysis of multiple years of data to reduce uncertainties in surface UHI estimates and investigating long-term variability of the surface UHI.

Globally, the daytime surface UHI is higher than the nighttime UHI, with the summer season showing the highest values compared to winter. The urban extent dataset is divided into climate zones using the Koppen-Geiger climate classification system to investigate the differences in the diurnal, seasonal, and long-term variability in the surface UHI for the first time using a consistent methodology. All climate zones other than arid show higher daytime surface UHI intensities, with snow urban clusters showing the highest diurnal range and maximum daytime values. There are significant differences in the seasonality of the surface UHI for different climate zones, in particular for arid and equatorial urban clusters. The long-term variability in the surface UHI is investigated using yearly land use classes from MODIS. A consistent increase is seen in the surface UHI intensity for urban clusters, particularly for daytime, indicating a temporal redistribution of heat due to urbanization.

Finally, we investigate the importance of vegetation in controlling the surface UHI intensity. Vegetation is a strong modulator of the seasonal variability of the surface UHI,

and may also affect the long-term changes observed in this study. Since the difference in vegetation between the urban and rural area is a strong predictor of the surface UHI intensity, increased urban vegetation can be used to dampen UHI intensity in cities prone to heat stress. In particular, seasonal urban irrigation has the potential to mitigate high UHI during the hot season.

This study demonstrates that the urban clusters in different background climates show distinct diurnal, seasonal, and long-term variability using a globally consistent dataset for the first time. Our results indicate that background climate should be taken into consideration for city-specific UHI mitigation policies, as well as when planning new cities and expanding existing urban areas.

A.8 References

1. Arnfield, A. J. (2003). Two decades of urban climate research: a review of turbulence, exchanges of energy and water, and the urban heat island. International Journal of Climatology: a Journal of the Royal Meteorological Society, 23(1), 1-26.

2. Cao, C., Lee, X., Liu, S., Schultz, N., Xiao, W., Zhang, M., & Zhao, L. (2016). Urban heat islands in China enhanced by haze pollution. Nature Communications, 7(1), 1-7.

3. Chakraborty, T., & Lee, X. (2018). Global UHI data table. Dataset on Mendeley. https://doi.org/10.17632/h9pfd42fv9.1#file-9cb9f20e-b16e-4b1f-914e-bbb12cf29916.

4. Chakraborty, T., Sarangi, C., & Tripathi, S. N. (2017). Understanding diurnality and inter-seasonality of a sub-tropical urban heat island. Boundary-Layer Meteorology, 163(2), 287-309.

5. Clinton, N., & Gong, P. (2013). MODIS detected surface urban heat islands and sinks: Global locations and controls. Remote Sensing of Environment, 134, 294-304.

6. Connors, J. P., Galletti, C. S., & Chow, W. T. (2013). Landscape configuration and urban heat island effects: assessing the relationship between landscape characteristics and land surface temperature in Phoenix, Arizona. Landscape ecology, 28(2), 271-283.

7. Cui, Y. Y., & De Foy, B. (2012). Seasonal variations of the urban heat island at the surface and the near-surface and reductions due to urban vegetation in Mexico City. Journal of Applied Meteorology and Climatology, 51(5), 855-868.

8. Danielson, J. J., & Gesch, D. B. (2011). Global multi-resolution terrain elevation data 2010 (GMTED2010) (p. 26). US Department of the Interior, US Geological Survey.

9. Debbage, N., & Shepherd, J. M. (2015). The urban heat island effect and city contiguity. Computers, Environment and Urban Systems, 54, 181-194.

10. Dobson, J. E., Bright, E. A., Coleman, P. R., Durfee, R. C., & Worley, B. A. (2000). LandScan: a global population database for estimating populations at risk. Photogrammetric engineering and remote sensing, 66(7), 849-857.

11. Fischer, E. M., Oleson, K. W., & Lawrence, D. M. (2012). Contrasting urban and rural heat stress responses to climate change. Geophysical research letters, 39(3).

12. Gorelick, N., Hancher, M., Dixon, M., Ilyushchenko, S., Thau, D., & Moore, R. (2017). Google Earth Engine: Planetary-scale geospatial analysis for everyone. Remote sensing of Environment, 202, 18-27.

13. Goward, S. N. (1981). Thermal behavior of urban landscapes and the urban heat island. Physical Geography, 2(1), 19-33.

14. Howard, L. (1833). The climate of London: deduced from meteorological observations made in the metropolis and at various places around it (Vol. 3). Harvey and Darton, J. and A. Arch, Longman, Hatchard, S. Highley & R. Hunter.

15. Imhoff, M. L., Zhang, P., Wolfe, R. E., & Bounoua, L. (2010). Remote sensing of the urban heat island effect across biomes in the continental USA. Remote sensing of environment, 114(3), 504-513.

16. Kelso, N. V., & Patterson, T. (2018) Urban areas: Cultural vector (1:10m). http://www.naturalearthdata.com/downloads/10m-cultural-vectors/10murban-area/.

17. Lazzarini, M., Marpu, P. R., & Ghedira, H. (2013). Temperature-land cover interactions: The inversion of urban heat island phenomenon in desert city areas. Remote Sensing of Environment, 130, 136-152.

18. Lee, X., Goulden, M. L., Hollinger, D. Y., Barr, A., Black, T. A., Bohrer, G., ... & Zhao, L. (2011). Observed increase in local cooling effect of deforestation at higher latitudes. Nature, 479(7373), 384-387.

19. Li, X., Messina, J. P., Moore, N. J., Fan, P., & Shortridge, A. M. (2017). MODIS land cover uncertainty in regional climate simulations. Climate Dynamics, 49(11), 4047-4059.

20. Li, Y., Zhao, M., Mildrexler, D. J., Motesharrei, S., Mu, Q., Kalnay, E., ... & Wang, K. (2016). Potential and actual impacts of deforestation and afforestation on land surface temperature. Journal of Geophysical Research: Atmospheres, 121(24), 14-372.

21. Martin-Vide, J., Sarricolea, P., & Moreno-García, M. C. (2015). On the definition of urban heat island intensity: the "rural" reference. Frontiers in Earth Science, 3, 24.

22. NOAA (2018). NOAA national centers for environmental information, climate at a glance: Global time series URL http://www.ncdc.noaa.gov/cag/.

23. Oke, T. R., & TR, O. (1979). Review of urban climatology 1973-1976.

24. Oleson, K. (2012). Contrasts between urban and rural climate in CCSM4 CMIP5 climate change scenarios. Journal of Climate, 25(5), 1390-1412.

25. Peng, S., Piao, S., Ciais, P., Friedlingstein, P., Ottle, C., Breon, F. M., ... & Myneni, R. B. (2012). Surface urban heat island across 419 global big cities. Environmental science & technology, 46(2), 696-703.

26. Qiao, Z., Tian, G., & Xiao, L. (2013). Diurnal and seasonal impacts of urbanization on the urban thermal environment: a case study of Beijing using MODIS data. ISPRS Journal of Photogrammetry and Remote Sensing, 85, 93-101.

27. Quinlan, J. R. (1993). C4. 5: programs for machine learning. Elsevier.

28. Rao, P. K. (1972). Remote sensing of urban" heat islands" from an environmental satellite. Bulletin of the American meteorological society, 53(7), 647-648.

29. Rozenfeld, H. D., Rybski, D., Andrade, J. S., Batty, M., Stanley, H. E., & Makse, H. A. (2008). Laws of population growth. Proceedings of the National Academy of Sciences, 105(48), 18702-18707.

30. Rubel, F., & Kottek, M. (2010). Observed and projected climate shifts 1901-2100 depicted by world maps of the Köppen-Geiger climate classification. Meteorologische Zeitschrift, 19(2), 135.

31. Santamouris, M. (2015). Analyzing the heat island magnitude and characteristics in one hundred Asian and Australian cities and regions. Science of the Total Environment, 512, 582-598.

32. Schneider, A., Friedl, M. A., & Potere, D. (2009). A new map of global urban extent from MODIS satellite data. Environmental research letters, 4(4), 044003.

33. Schneider, A., Friedl, M. A., & Potere, D. (2010). Mapping global urban areas using MODIS 500-m data: New methods and datasets based on 'urban ecoregions'. Remote Sensing of Environment, 114(8), 1733-1746.

34. Schwarz, N., Lautenbach, S., & Seppelt, R. (2011). Exploring indicators for quantifying surface urban heat islands of European cities with MODIS land surface temperatures. Remote Sensing of Environment, 115(12), 3175-3186.

35. Shastri, H., Barik, B., Ghosh, S., Venkataraman, C., & Sadavarte, P. (2017). Flip flop of day-night and summer-winter surface urban heat island intensity in India. Scientific reports, 7(1), 1-8.

36. Souch, C., & Grimmond, S. (2006). Applied climatology: urban climate. Progress in physical geography, 30(2), 270-279.

37. Stewart, I. D., & Oke, T. R. (2009). A new classification system for urban climate sites. Bulletin of the American Meteorological Society, 90(7), 922-923.

38. Stewart, I. D. (2011). A systematic review and scientific critique of methodology in modern urban heat island literature. International Journal of Climatology, 31(2), 200-217.

39. Taha, H. (1997). Urban climates and heat islands: albedo, evapotranspiration, and anthropogenic heat. Energy and buildings, 25(2), 99-103.

40. Tran, H., Uchihama, D., Ochi, S., & Yasuoka, Y. (2006). Assessment with satellite data of the urban heat island effects in Asian mega cities. International journal of applied Earth observation and Geoinformation, 8(1), 34-48.

41. Voogt, J. (2007, July). How researchers measure urban heat islands. In United States Environmental Protection Agency (EPA), State and Local Climate and Energy Program, Heat Island Effect, Urban Heat Island Webcasts and Conference Calls.

42. Zhang, P., Imhoff, M. L., Wolfe, R. E., & Bounoua, L. (2010). Characterizing urban heat islands of global settlements using MODIS and nighttime lights products. Canadian Journal of Remote Sensing, 36(3), 185-196.

43. Zhao, L., Lee, X., Smith, R. B., & Oleson, K. (2014). Strong contributions of local background climate to urban heat islands. Nature, 511(7508), 216-219.

44. Zhou, B., Rybski, D., & Kropp, J. P. (2013). On the statistics of urban heat island intensity. Geophysical research letters, 40(20), 5486-5491.

45. Zhou, D., Zhao, S., Zhang, L., Sun, G., & Liu, Y. (2015). The footprint of urban heat island effect in China. Scientific reports, 5(1), 1-11.

Appendix B

Examining Atmosphere-Biosphere Interactions in the Indo-Gangetic Basin During the COVID-19 Lockdowns

B.1 Abstract

The COVID-19 lockdowns drastically reduced human activity, emulating a controlled experiment on human-land-atmosphere coupling. Here using a fusion of satellite and reanalysis products, we examine this coupling through changes in the surface energy budget during the lockdown (1st April to 15th May 2020) in the Indo-Gangetic Basin, one of the world's most populated and polluted regions. During the lockdown, the reduction ($>10\%$) in columnar air pollution compared to a 5-year baseline, expected to increase incoming solar radiation, was counteracted by a $\approx 30\%$ enhancement in cloud cover, causing little change in available energy at the surface. More importantly, the delay in winter crop harvesting during the lockdown increased surface vegetation cover, causing almost half the regional cooling via evapotranspiration. Since this cooling was higher for rural areas, the daytime surface urban heat island (SUHI) intensity increased (by 0.20 to 0.41 K) during a period of reduced human activity. Our study provides strong observational evidence of the influence of agricultural activity on rural climate in this region and its indirect impact on the SUHI intensity.

B.2 Introduction

Human-induced changes in the Earth's surface climate have traditionally been difficult to constrain (Pielke et al., 2002; Lawrence et al., 2016), particularly since these changes typically occur at time scales similar to natural decadal perturbations. In contrast, the COVID-19 lockdowns – the restrictions placed by various governing bodies as a response to the COVID-19 pandemic in 2020 – caused unprecedented slowdown in human activity (Rutz et al., 2020), were short in duration, and yet intense enough to produce measurable effects. They can thus serve as natural experiments on the anthropogenic control on sur-

face climate. An ideal study area to explore the results of this perturbation experiment is the Indo-Gangetic Basin (IGB), one of the most densely populated regions on the planet with high levels of air pollution (Dey et al., 2011). Covering the majority of North India, the IGB has a subtropical monsoon climate, and is a global hot spot for land-atmosphere coupling (Koster et al., 2004). From late March to end of May, a countrywide lockdown was imposed in India as a response to COVID-19. This lockdown strictly restricted people's movement outside their homes, suspended educational, industrial, and hospitality services, and limited all transportation systems (Government of India, 2020).

Being both heavily cultivated and rapidly urbanizing (Seto et al., 2012; Siderius et al., 2014), the IGB is strongly influenced by anthropogenic changes in land use and land cover (Sarangi et al., 2018; Barton et al., 2019). Human influence on surface climate is distinct for urban and rural areas. Urbanization modifies the biophysical properties of the surface due to replacement of natural vegetation with built-up structures. Consequently, cities are characterized by higher temperatures compared to their surroundings – the urban heat island (UHI) effect (Oke, 1982). The UHI is commonly calculated as the temperature difference between the city and a non-standard rural area around the city. Rural areas are influenced by land use and land management practices, which is primarily due to agriculture in this region.

The reduction in atmospheric aerosols during the lockdown (up to 45% reduction for some Indian states) is well-documented (Ranjan et al., 2020) and, all else remaining constant, would increase incoming surface radiation. Since urban and rural areas may have different levels of pollution, this radiative forcing change can impact the UHI intensity (Cao et al., 2016; Li et al., 2018). However, the UHI, and surface climate in general, is also modulated by non-radiative pathways (Zhao et al., 2014). The lockdown restrictions delayed crop harvesting (Rawal et al., 2020), which would maintain high vegetation cover and can enhance latent heat flux (λE), a non-radiative pathway of surface heat dissipation.

Previous studies have noted that the seasonality of the UHI in this region is influenced by the variability in surface vegetation in the rural area (Chakraborty et al., 2019; Venter et al., 2020). Agricultural influence on surface climate in this region is not well-captured by LSMs due to inaccurate representation of vegetation properties and the poorly constrained influence of irrigation on the hydrological cycle (Chakraborty et al., 2019; Barton et al., 2019). Thus, beyond the widely studied changes in atmospheric composition (Venter et al., 2020; Quere et al., 2020), the lockdowns provide a unique opportunity to ask broader questions about human-land-atmosphere interactions in the IGB. For example, the role of these interactions in modulating the ensuing South Asian monsoon circulations is critical to the livelihood of over a billion people dependent on this region (Turner et al., 2019).

Here we examine the changes in the surface temperature in the IGB during the lockdown with a focus on the UHI, allowing us to separate human influence on urban and rural surface climate, particularly due to air pollution and land use. First, using a suite of satellite observations, we isolate changes in atmospheric and surface properties over urban areas and their rural periphery. Second, since satellite observations are restricted by the presence of clouds and do not directly provide estimates of the surface energy budget, we use a reanalysis dataset to gain a mechanistic understanding of the observed perturbations in rural surface climate.

B.3   Materials and Methods

B.3.1   Urban-Rural Delineations for Region of Interest

We only consider the Indian portion of the IGB (Fig. B.1a; ≈ 50000 km^2), to avoid uncertainties arising from variations in lockdown periods in other countries. An urban cluster database was developed for this region by generating polygons covering continuous groups

of high-density urban pixels from the Global Human Settlement Index (GHSL) for 2015 (Pesaresi et al., 2013). The corresponding normalized rural reference (roughly equal to area of urban cluster) for each of these clusters was created using an iterative buffering procedure with a step size of 300 m. Our methodology generates 1420 urban-rural delineations for the region.
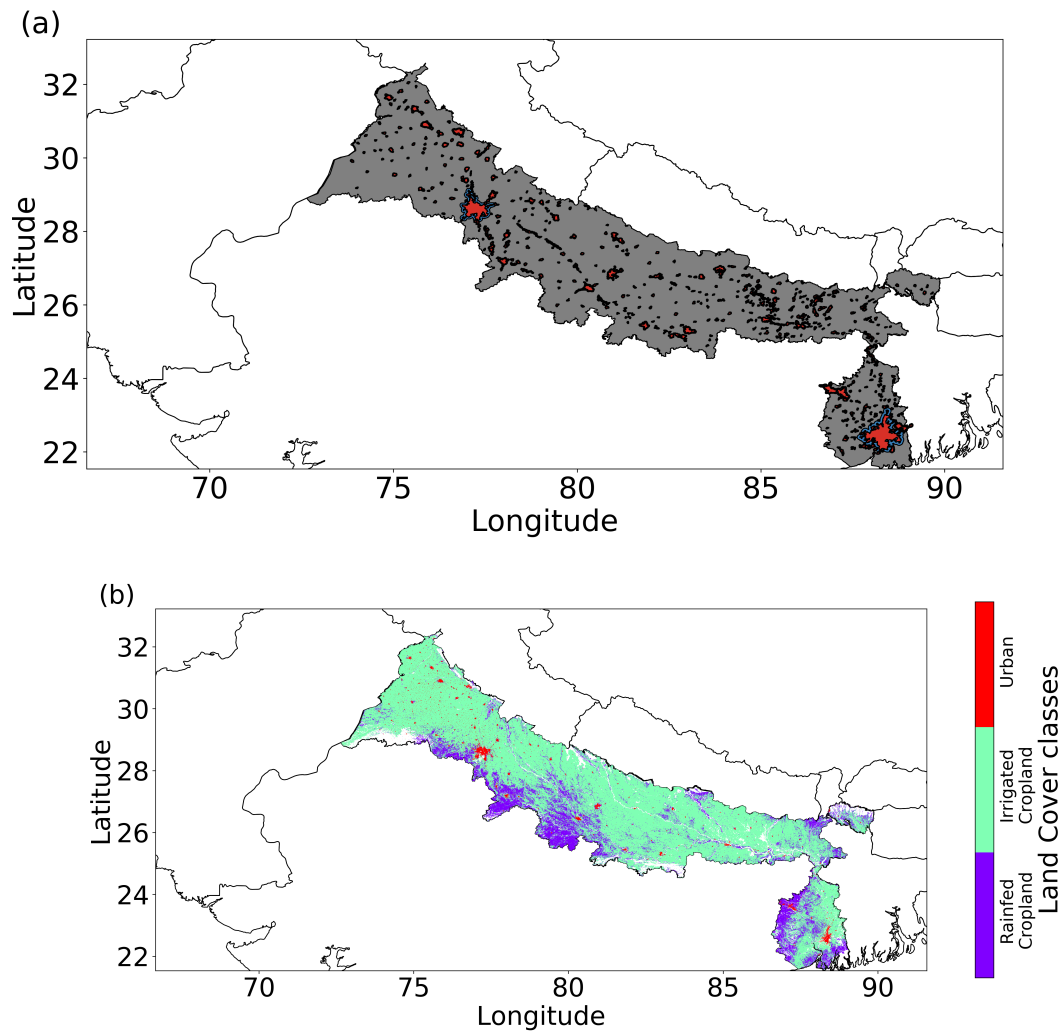
Figure B.1: Map of study area. The black polygon in sub-figure **a** show the Indo-Gangetic Basin (IGB). The generated urban clusters are in red, while their corresponding normalized rural buffers are shown in blue. Sub-figure **b** shows the distribution of three relevant land cover categories for the IGB from the European Space Agency Climate Change Initiative land cover dataset for 2018.

B.3.2 Satellite Observations

Multiple satellite-derived products were used to extract urban-rural differentials in relevant variables (details in Table B.1), including Land Surface Temperature (LST) for calculating surface UHI (SUHI; Wain et al., 2007), reflectance data from Moderate Resolution Imaging Spectroradiometer (MODIS) to estimate surface vegetation (Pagano et al., 1993), and metrics of air pollution, including aerosol optical depth (AOD) from MODIS (Remer et al., 2006) and individual pollutant estimates from the Sentinel-5P TROPOspheric Monitoring Instrument (TROPOMI) sensor (Veefkind et al., 2012). We also extract cloud fraction (CF) from Sentinel-5P since clouds strongly affect the radiative budget and can be higher over cities (Theeuwes et al., 2019). Finally, the Black-Sky Albedo (BSA) and White-Sky Albedo (WSA), the reflectivity of the surface for direct beam and diffuse radiation, respectively, were extracted from MODIS (Strahler et al., 1999). These can be combined to derive total surface albedo (α), which is known to vary between urban and rural areas (Rizwan et al., 2008). Although the MODIS observations are daily, the multi-day (see Table B.1) composites are used to reduce cloud contamination (Chakraborty et al., 2020).

The normalized difference vegetation index (NDVI) is a proxy for green vegetation (Jouse et al., 1973) and used here to estimate the impact of the lockdown on surface vegetation cover. We calculate NDVI from the NIR (near infra-red) and RED bands of the 8-day composite MODIS surface reflectance product, available for 1 km x 1 km grids (Table B.1), as:

$$\mathrm{NDVI} = \frac{\mathrm{NIR} - \mathrm{RED}}{\mathrm{NIR} + \mathrm{RED}} \tag{B.1}$$

The lockdown in India started from midnight March 24th and continued in a limited capacity till June 7th. To remove the noise from the transition periods, we considered April 1st to May 15th, 2020 to be the lockdown case. The 5-year (2015-2019) mean of

the data from April 1st to May 15th was treated as the baseline (only April 1st to May 15th, 2019 for TROPOMI due to data unavailability). Since the satellite observations are relatively coarse (see Table B.1), only urban clusters with an area of above 10 km^2 were considered. This threshold, along with cloud screening, leaves 382 clusters for the MODIS and Sentinel-derived CF data (Fig. B.2) and 302 clusters for the Sentinel-derived air pollutant data.
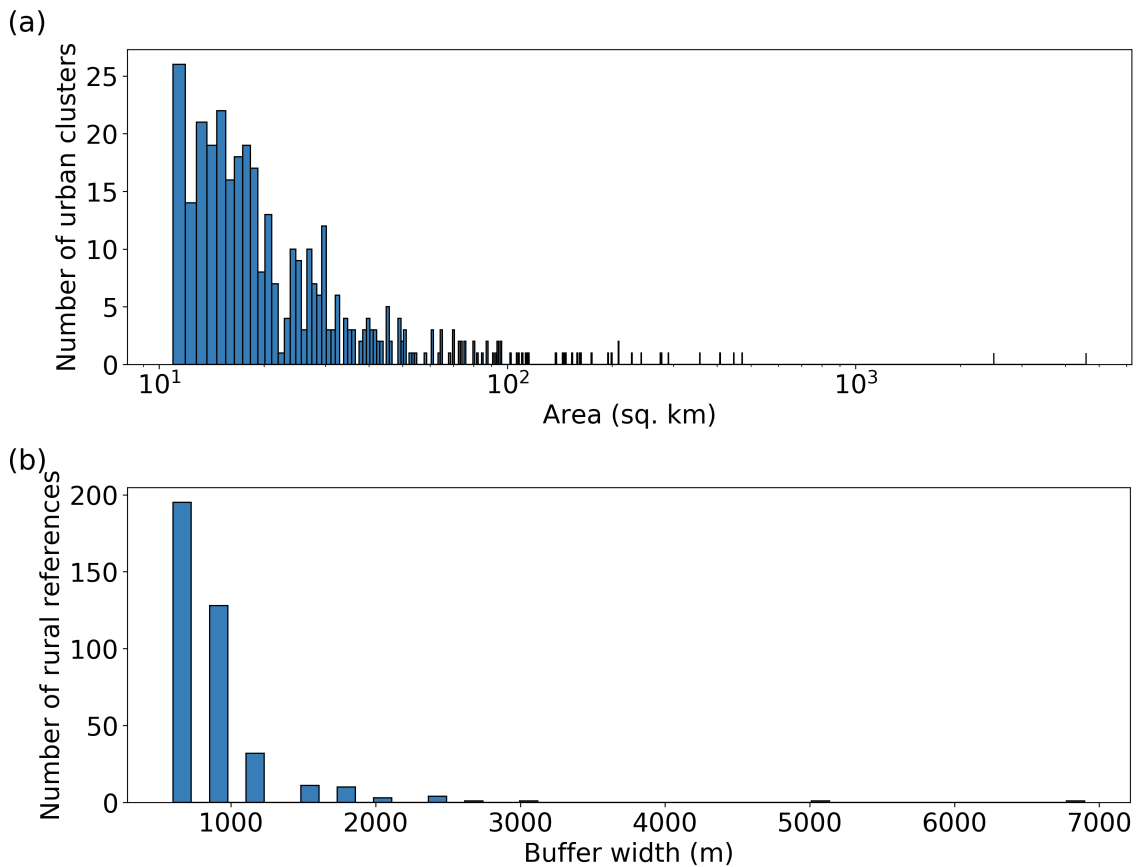
Figure B.2: Distribution of urban and rural units of calculations used in the study. Sub-figure **a** shows the density plot of the urban clusters with areas greater than 1 km^2 used in the study after cloud screening of the data. Sub-figure **b** shows the distribution of the buffer widths used to calculate the rural references following the integration procedure used to minimize area difference between urban areas and their references.

Urban and rural means of all the variables of interest were extracted after regridding to 300 m ESA CCI grids using the Google Earth Engine platform (Gorelick et al., 2017). The

urban values were calculated as the spatial means of all the urban pixels, as defined by the European Space Agency Climate Change Initiative (ESA CCI) land cover data (Bontemps et al., 2013), within an urban cluster. The corresponding rural values are the spatial means of the non-urban, non-water pixels (from the ESA data) in the rural references. The urban-rural differential in LST is the SUHI, while for the other variables, we use the subscript $_{urb-rur}$. We also calculate the averages of each variable (and their differences) weighted by the urban cluster areas. Since larger urban areas are known to have higher SUHI intensity, area weighing gives us regional mean SUHI (versus the urban cluster mean SUHI).

Table B.1: Summary of satellite products used in the present study.

Satellite product	Time of Interest	Variable(s) of interest	Temporal resolution	Spatial resolution	Reference
MODIS Land Surface Temperature (LST) product (MYD11A2 v006)	2015-2020	Daytime and nighttime LST from Aqua	8-day	1000 m	(Wan, 2006)
MODIS surface reflectance product (MYD09A1 v006)	2015-2020	Reflectances in the near-infrared and red bands	8-day	500 m	(Pagano & Durham, 1993)
MODIS global albedo (α) product (MCD43A3 v006)	2015-2020	Black Sky Albedo (BSA) and White Sky Albedo (WSA)	16-day	500 m	(Strahler et al., 1999)
MODIS Aerosol Optical Depth (AOD) product (MCD19A2.006)	2015-2020	AOD	Daily	1000 m	(Remer et al., 2006)
Sentinel-5P TROPOMI	2019-2020	Nitrogen Dioxide (NO_2), Sulphur Dioxide (SO_2), Ozone (O_3), Carbon Monoxide (CO), Formaldehyde (HCHO), Methane (CH_4), and Cloud Fraction (CF)	2-day	1000 m (downscaled)	(Veefkind et al., 2012)
European Space Agency Climate Change Initiative (ESA CCI) land cover data	2018	Land cover	Yearly	300 m	(Bontemps et al., 2013)

B.3.3   Reanalysis Data

The MERRA-2 reanalysis assimilates bias-corrected satellite observations of aerosols and provides estimates of the aerosol direct radiative effect, making it ideal for studying the impacts of the COVID-19 lockdowns. Though MERRA-2 also includes estimates of k_d, inter-reanalysis evaluations show that it significantly underestimates k_d compared to other products (Chakraborty & Lee, 2021). Thus, MERRA-2 data were not used to calculate α.

Instead, MERRA-2 was used to get all-sky estimates of perturbations in the surface and atmospheric variables (since satellites only provide clear-sky estimates) and to diagnose reasons for perturbations in the rural LST. The MERRA-2 variables were based on hourly data from 12:30 pm to 2:30 pm local time, corresponding to the 1:30 pm MODIS Aqua overpass.

B.3.4 Statistical Analysis

We used two reanalysis products - the European Centre for Medium-Range Weather Forecasts (ECMWF) Reanalysis 5 (ERA5; Hersbach et al., 2020), available at $0.25°\text{x}0.25°$, and the Modern-Era Retrospective analysis for Research and Applications, Version 2 (MERRA-2; Gelaro et al., 2017), available at $0.5°\text{x}0.625°$. The 5-year (2015-2019) mean of the diffuse fraction (k_d) of the ERA5 reanalysis was used to calculate α from BSA and WSA (Qu et al., 2015) using the equation:

$$\alpha = k_\text{d}\text{WSA} + (1 - k_\text{d})\text{BSA} \tag{B.2}$$

For each case, the centroid of the urban and rural polygons was located and k_d was extracted for the ERA5 grid containing it, similar to (Chakraborty et al., 2020).

To examine reasons for any potential SUHI change, we considered the temporal changes (Δ, variable value during the lockdown minus value of the reference period) in $\text{AOD}_\text{urb−rur}$, $\text{NDVI}_\text{urb−rur}$, $\alpha_\text{urb−rur}$, and $\text{CF}_\text{urb−rur}$ as the predictors. For robustness, we used two methods –linear regressions and random forest (RF) regression. For the linear regressions, we considered each of these four predictors ($\Delta\text{AOD}_\text{urb−rur}$, $\Delta\text{NDVI}_\text{urb−rur}$, $\Delta\alpha_\text{urb−rur}$, and $\Delta\text{CF}_\text{urb−rur}$) and all their combinations and subsets. Since the relationships between the predictors and ΔSUHI are not necessarily linear, we also checked the consistency of our results using RF regressions. RF regressions use ensembles of decision trees to detect

non-linear relationships and are less sensitive to outliers than parametric linear models (Breiman, 2001). To prevent overfitting, we trained the models using 70% of the data and checked the model accuracy using the remaining data. The training and accuracy assessment were repeated 50 times with different random splits of training and validation data (Xu et al., 2001). The signal can be hard to separate from the noise in the satellite observations when examining small perturbations. Thus, we also correlate the variables after binning the data into 5 percentile bins, assuming that this noise is random and contributes to the unexplained variance within bins.

B.3.5 Intrinsic Biophysical Mechanism

Since the statistical analyses using satellite observations are primarily for hypothesis generation and do not reveal the physical mechanisms for the SUHI increase, we employed the theory of Intrinsic Biophysical Mechanism (IBPM; Lee et al., 2011; Zhao et al., 2014; Cao et al., 2016; Chakraborty & Lee, 2019a), implemented using the MERRA-2 variables (Chakraborty & Lee, 2019a), to diagnose and quantify the reasons for the change in the LST_{rur} in the region. Conceptually, the total LST change (ΔLST) due to a forcing agent is the sum of the changes in the blending height temperature (ΔBHT), where the blending height is the height at which surface heterogeneity has negligible impact on atmospheric variables (Mahrt, 2000), and the local temperature response (ΔT):

$$\Delta\mathrm{LST} = \Delta T + \Delta\mathrm{BHT} \qquad (B.3)$$

ΔBHT is the results of atmospheric factors while ΔT is the surface response to atmospheric forcing. According to the IBPM theory, the local temperature response is:

$$\Delta T = \frac{\lambda_0}{1+f}\Delta K_{\downarrow}(1-\alpha) + \frac{\lambda_0}{1+f}\Delta L + \frac{-\lambda_0}{(1+f)^2}(R_n^* - G)\Delta f_1$$
$$+ \frac{-\lambda_0}{(1+f)^2}(R_n^* - G)\Delta f_2 + \frac{\lambda_0}{1+f}\Delta G \quad \text{(B.4)}$$

The terms on the right-hand side of Eq. B.4, from left to right, are the contributions to ΔT from shortwave radiative forcing, longwave radiative forcing, energy redistribution through evaporation, energy redistribution through convection, and change in ground heat flux. Here $\Delta K_{\downarrow}$ is the change in incoming shortwave radiation, ΔL is the change in absorbed longwave radiation, and ΔG is the change in ground heat flux. Since the net radiation R_n is dependent on LST (through the $L_{\uparrow}$ term), we define an apparent net radiation (R_n^*) that is not a function of the land surface by replacing LST with BHT.

$$R_n^* = K\downarrow(1-\alpha) + L\downarrow(1-\epsilon) - \epsilon\sigma\text{BHT}^4 \quad \text{(B.5)}$$

where ϵ is the surface emissivity and σ is the Stefan Boltzmann constant (5.67×10^{-8} kg s^{-3} K^{-4}). λ_0 is the temperature sensitivity due to longwave feedback and is given by:

$$\lambda_0 = \frac{1}{4\epsilon\sigma\text{LST}^3} \quad \text{(B.6)}$$

and f is a factor denoting energy redistribution through non-radiative pathways like convection and evaporation, which can be calculated using the diagnostic equation:

$$f = \frac{\lambda_0}{\text{LST} - \text{BHT}}(R_n^* - G) - 1 \quad \text{(B.7)}$$

The change in f due to evaporative (Δf_1) and convection (Δf_2) can be calculated from:

$$\Delta f_1 = -f \frac{\Delta \beta}{\beta(1+\beta)} \tag{B.8}$$

$$\Delta f_2 = -f \frac{\Delta r_a}{r_a} \tag{B.9}$$

where β is the Bowen ratio ($\frac{H}{\lambda E}$), where H is the sensible heat flux and λE is the latent heat flux, and r_a is the aerodynamic resistance, formulated as:

$$r_a = \frac{\rho C_p (\mathrm{LST} - \mathrm{BHT})}{H} \tag{B.10}$$

Here ρ is the air density, while C_p is the specific heat capacity of air at constant pressure. All the perturbation terms were calculated from the MERRA-2 reanalysis as the difference between the 5-year baseline and the lockdown period. f and λ_0 were calculated for the baseline period, while β, r_a, and λ_0 are the averages of the two periods. Since f cannot have a negative value, the grids with $f \lesssim 0$ were excluded from the analysis. The implementation of the IBPM method using MERRA-2 data used here is an extension of the methodology employed in (Chakraborty & Lee, 2019a).

B.4 Results

B.4.1 Changes in Urban-Rural Differentials During Lockdown

The daytime SUHI increased (non-weighted mean from 0.23 K to 0.43 K; area-weighted mean from 0.56 K to 0.97 K) during the COVID-19 lockdown period compared to the 5-year baseline (Fig. B.3 and Fig. B.4), with 67% or 257 of the 382 urban clusters showing an increase (Fig. B.5). In contrast, the nighttime ΔSUHI was statistically insignificant (p-value > 0.01). Daytime LST decreased during the lockdown (compared to baseline),

though the mean decrease over rural locations was greater (-1.96 K non-weighted; -1.55 K weighted) compared to that over urban regions (-1.76 K non-weighted; -1.14 K weighted).
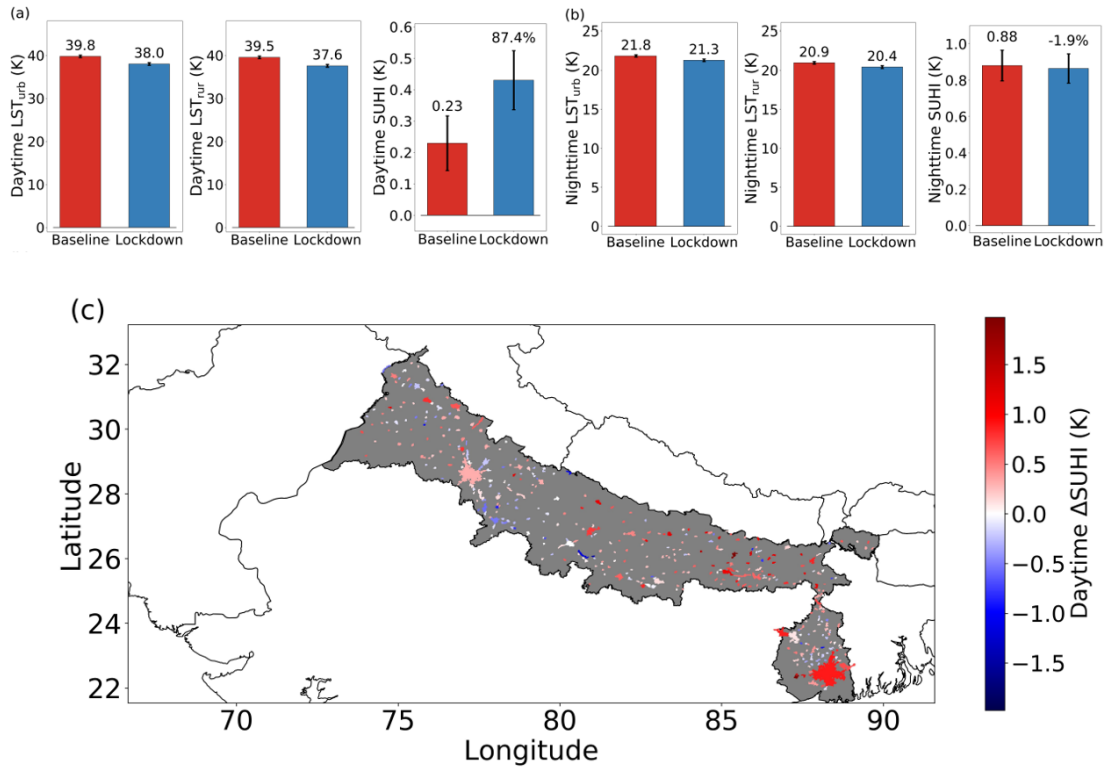
Figure B.3: Perturbations to land surface temperature (LST) and surface urban heat island (SUHI) intensity. Sub-figures **a** and **b** show the mean (not weighted by urban cluster area) land surface temperature (LST) and surface urban heat island (SUHI) for urban clusters and their rural references for the baseline period, as well as their perturbed values during the lockdown period, for daytime and nighttime, respectively. The values above the bars show the mean values (percentage change during lockdown period for SUHI) and the error bars represent the 95% confidence interval of the mean. The changes shown here are summarized in Table B.2. Sub-figure **c** shows a map of the urban clusters in the region of interest and the change in their spatial mean daytime SUHI during the lockdown compared to the five year baseline.

Table B.2: Summary (mean, 95% confidence intervals of mean) of satellite-derived estimates of the main variables of interest for urban clusters and their rural references. The spatial mean of each urban (and corresponding rural) polygon is treated as a sample point.

Variable (unit)	Satellite Observations	
	Baseline	Lockdown
Daytime surface urban heat island (K)	(0.23, 0.14, 0.32)	(0.43, 0.34, 0.52)
Nighttime surface urban heat island (K)	(0.88, 0.8, 0.97)	(0.86, 0.78, 0.94)
Urban normalized difference vegetation index	(0.3, 0.29, 0.31)	(0.34, 0.33, 0.34)
Rural normalized difference vegetation index	(0.32, 0.31, 0.33)	(0.37, 0.36, 0.38)
Urban aerosol optical depth	(0.53, 0.53, 0.54)	(0.5, 0.49, 0.51)
Rural aerosol optical depth	(0.54, 0.53, 0.55)	(0.51, 0.5, 0.52)
Urban surface albedo	(0.155, 0.154, 0.157)	(0.151, 0.15, 0.153)
Rural surface albedo	(0.164, 0.162, 0.165)	(0.159, 0.158, 0.16)
Urban cloud fraction	(0.107, 0.102, 0.111)	(0.146, 0.14, 0.151)
Rural cloud fraction	(0.106, 0.102, 0.111)	(0.145, 0.14, 0.15)
Urban daytime surface temperature (K)	(312.9, 312.6, 313.2)	(311.2, 310.8, 311.5)
Rural daytime surface temperature (K)	(312.7, 312.4, 313.0)	(310.7, 310.4, 311.1)
Urban nighttime surface temperature (K)	(295.0, 294.8, 295.1)	(294.4, 294.3, 294.6)
Rural nighttime surface temperature (K)	(294.1, 293.9, 294.3)	(293.6, 293.4, 293.7)
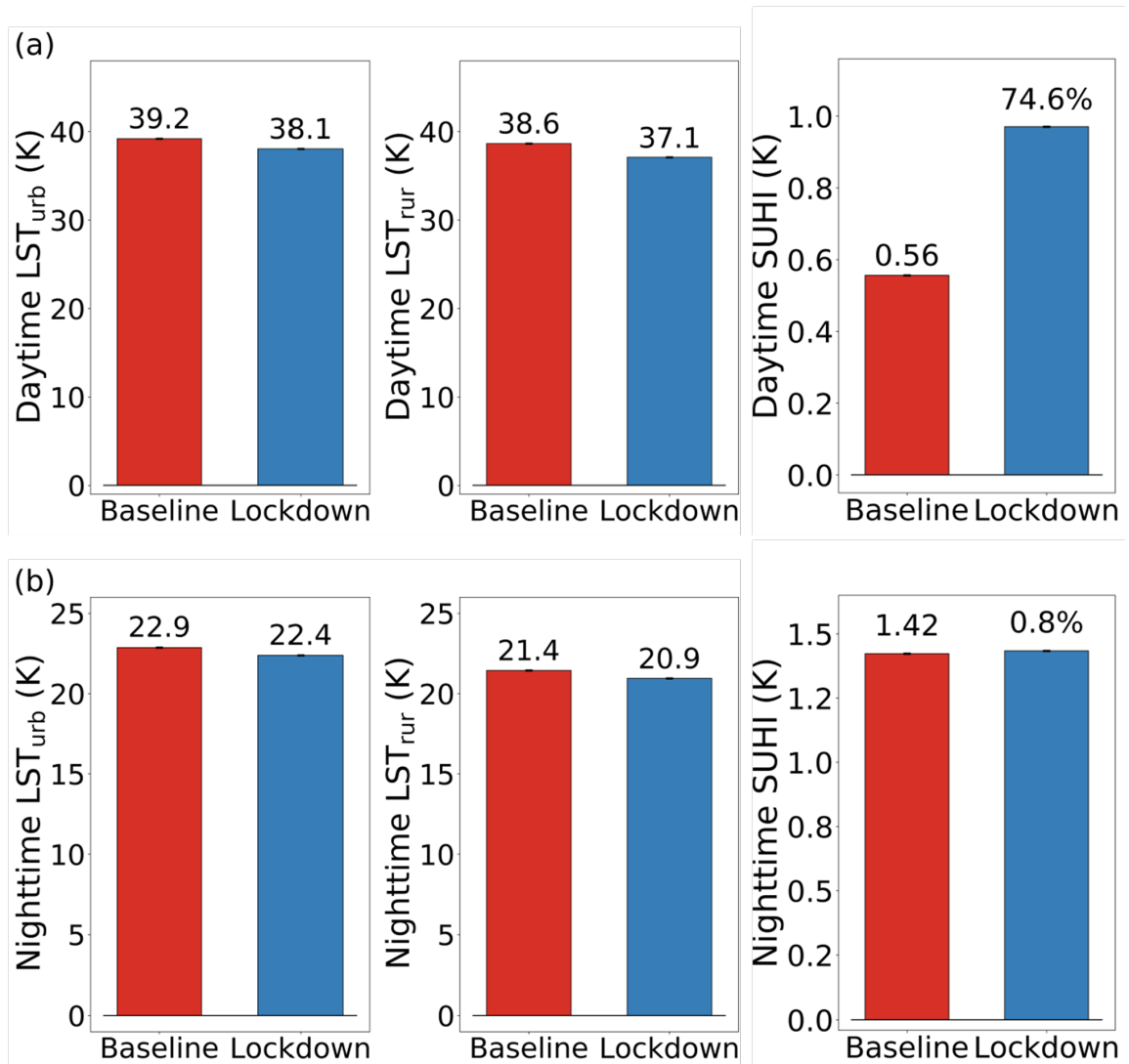
Figure B.4: Perturbations to land surface temperature (LST) and surface urban heat island (SUHI) intensity. Sub-figures **a** and **b** show the mean (weighted by urban cluster area) land surface temperature (LST) and surface urban heat island (SUHI for urban clusters and their rural references for the baseline period, as well as their perturbed values during the lockdown period, for daytime and nighttime, respectively. The values above the bars show the mean values (percentage change during lockdown period for SUHI) and the error bars represent the 95% confidence interval of the area-weighted mean.
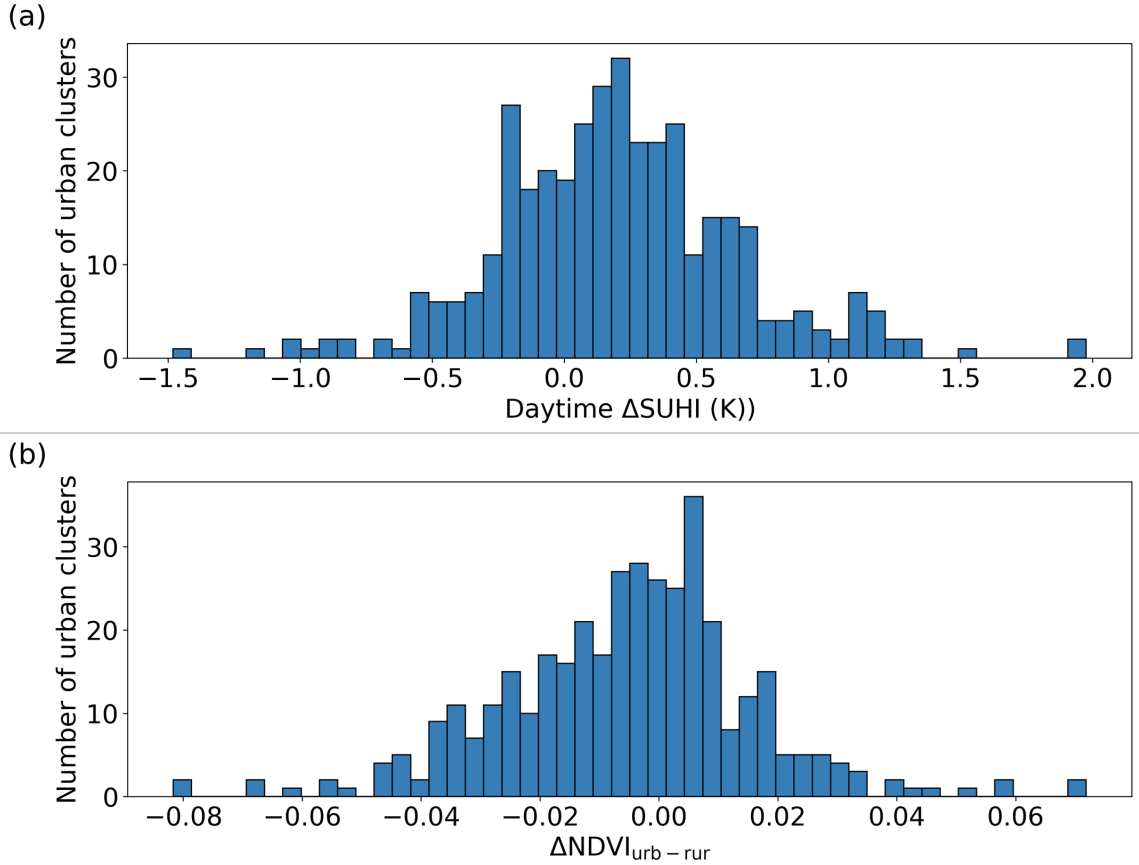
Figure B.5: Distribution of **a** daytime ΔSUHI and **b** ΔNDVI$_{\text{urb}-\text{rur}}$ among the urban clusters used in the study.

To explain this differential perturbation in daytime LST$_{\text{urb}}$ and LST$_{\text{rur}}$, we consider major atmospheric (CF and AOD) and surface (NDVI and α) factors that impact the SUHI. The air quality over both urban and rural locations improved during the lockdown. This reduced air pollution is evident from both MODIS-derived AOD ($\approx$5-6% decrease; Figs 2a and S5a) and individual air pollutants measured by TROPOMI ($\approx$14% and $\approx$19% decrease in urban NO$_2$ and SO$_2$, respectively; Fig. B.8). AOD decreases in roughly 67% of the urban clusters (increasing in others) and for most non-urban grids in the IGB (Fig. B.9a). The small magnitude of MODIS-derived AOD$_{\text{urb}-\text{rur}}$ could be due to the large contributions from natural dust and biomass burning aerosols, as well as occurrence of turbulently mixed deep boundary layers, in this region during this period (Sarangi et al.,

2016). Moreover, there was a surprisingly large (>36% for non-weighted; >43% for weighted) increase in CF during the lockdown (Fig. B.6d and Fig. B.7d), though some regions show a decrease (Fig. B.9b).
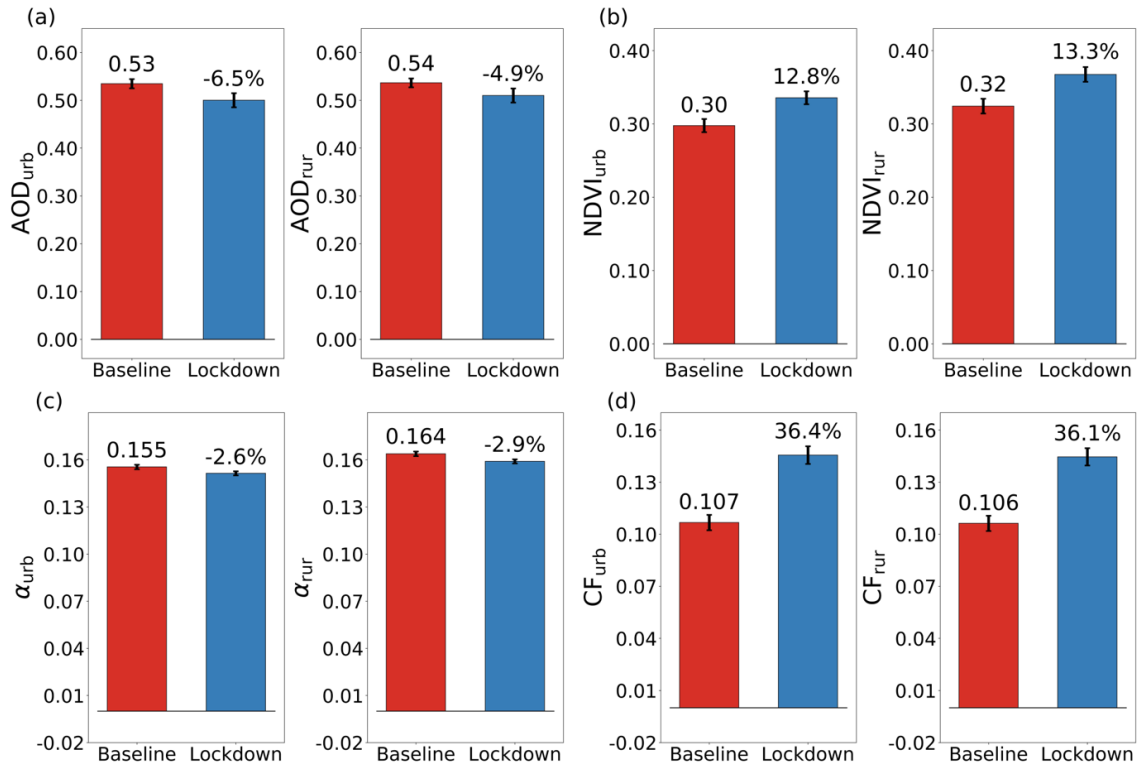
Figure B.6: Changes in major surface and atmospheric factors. Sub-figures **a–d** show the mean (not weighted by urban cluster area) aerosol optical depth (AOD), normalized difference vegetation index (NDVI), surface albedo (α), and cloud fraction (CF) for urban clusters and their rural references for the baseline period, as well as their perturbed values during the lockdown. The values above the bars show the mean values for the baseline period (2015–2019 baseline for everything other than CF; 2019 baseline for CF) and the percentage change from that value. The error bars represent the 95% confidence interval of the mean. The changes shown here are summarized in Table B.2.

We find large (>12%) increases in NDVI during the lockdown period. These increases are generally higher in rural references (13.3% or 0.043) than in urban areas (12.8% or 0.038; Fig. B.6b), with $\Delta NDVI_{urb-rur}$ being negative in ≈59% of the urban clusters (Figs B.5b, B.9a, and B.10a). The positive $\Delta NDVI_{rur}$ (Fig. B.10b) is consistent with the impact of the lockdown on agricultural activity, which is the predominant land use for ≈88% of
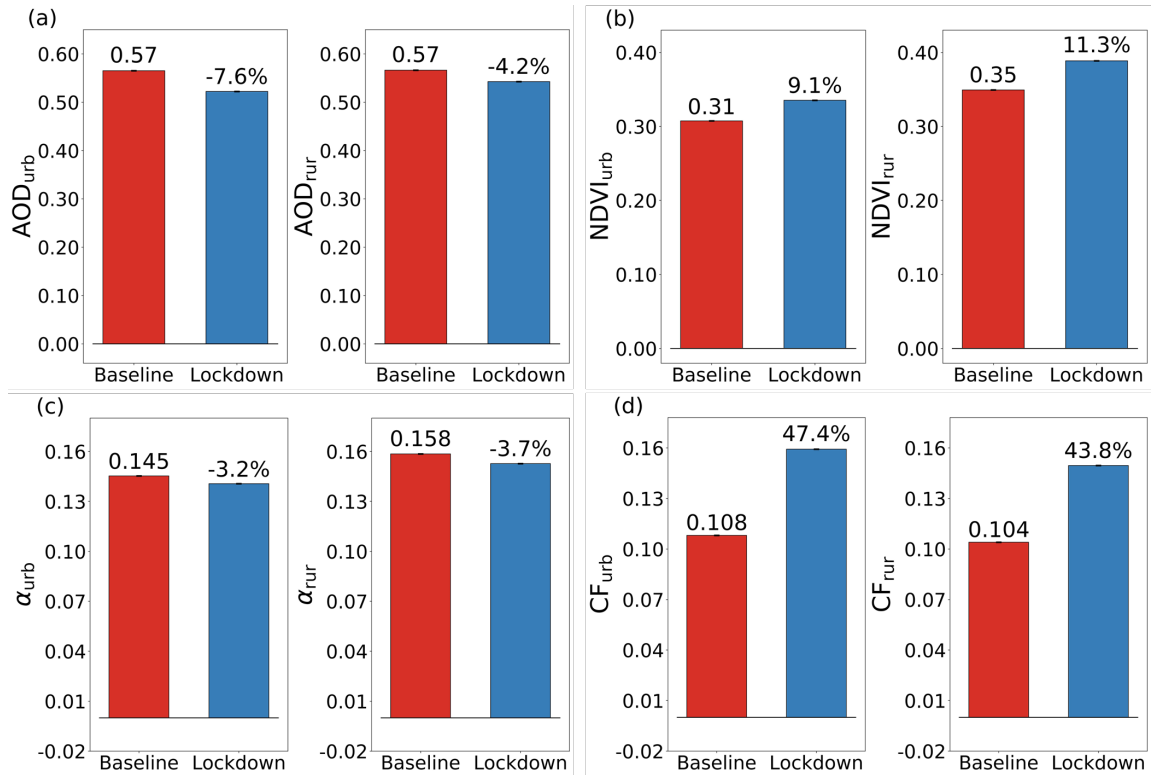
Figure B.7: Changes in major surface and atmospheric factors. Sub-figures **a**, **b**, **c**, and **d** show the mean (weighted by urban cluster area) Aerosol Optical Depth (AOD), normalized difference vegetation index (NDVI), surface albedo (α), and cloud fraction (CF) for urban clusters and their rural references for the baseline period, as well as their perturbed values during the lockdown. The values above the bars show the mean values for the baseline period (2015-2019 baseline for everything other than CF; 2019 baseline for CF) and the percentage change from that value. The error bars represent the 95% confidence interval of the area-weighted mean. The values shown here are also summarized in Table B.2.

this area according to the ESA CCI data (Fig. B.2b). The lockdown overlapped with the harvesting season for rabi (winter) crops, which, together with the drier conditions during this period, reduces surface vegetation during regular years, as can be seen from the moving average of MODIS-derived 8-day $NDVI_{rur}$ in Figure 3c. The delay in harvesting activity (Rawal et al., 2020) may have temporally shifted this normal drop in $NDVI_{rur}$, contributing to surface greening compared to the baseline (Fig. B.11c). The $\Delta NDVI_{rur}$ is higher than the inter-annual standard deviation of $NDVI_{rur}$ during this period, also demonstrated by the largest standardized anomalies of the year during the lockdown. Most of IGB shows this surface greening, with $\Delta NDVI_{rur}$, ranging from -0.01 (5th percentile) to 0.11 (95th percentile), as well as a reduction in LST_{rur} (Figs B.11a and B.11b) from -4.3 K (5th percentile) to 0.4 K (95th percentile), with the SUHI increasing compared to baseline (Fig. B.11d). Simultaneously, α decreased in both urban (-2.6%) and rural (-2.9%) areas (Figs B.6c and B.7c). Paired two-sample t-tests confirm that all the satellite-observed changes in the variables, other than that for nighttime SUHI, are statistically significant (p-value $<$ 0.01). The 95% confidence intervals for the mean of each variable are in Table B.2.

B.4.2 Attribution of Daytime SUHI Enhancement

Previous studies have shown relationships between $AOD_{urb-rur}$ and SUHI (Cao et al., 2016; Li et al., 2018). Here we find almost no associations between the perturbations in the two during the lockdown period (Fig. B.14a; $r^2 = 0.02$ for cluster; not statistically significant for binned). Similarly, $AOD_{urb-rur}$ and daytime SUHI are not well-correlated during the baseline and lockdown periods (Fig. B.12b; $r^2 \approx 0$). However, $\Delta NDVI_{urb-rur}$ shows a relatively strong inverse relationship with $\Delta SUHI$ (Fig. B.14b; $r^2 = 0.16$ for cluster; 0.76 for binned). Given the generally higher $\Delta NDVI_{rur}$, the pause in human activity in the rural area may have contributed to the enhanced daytime SUHI. This impact of urban-rural vegetation differentials on SUHI is consistent with previous studies
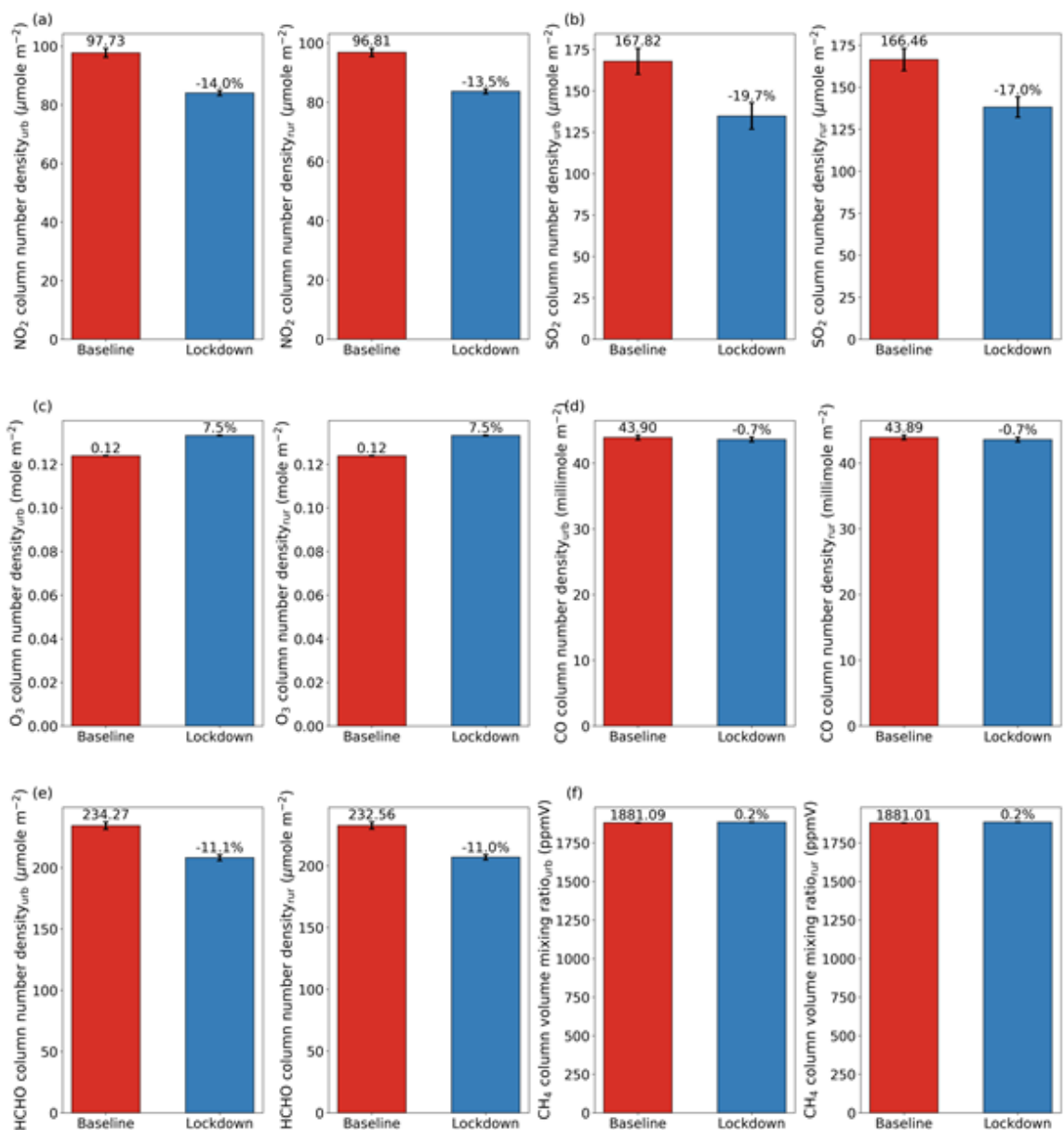
Figure B.8: Sub-figures **a**, **b**, **c**, **d**, **e**, and **f** show the mean (weighted by urban cluster area) Nitrogen Dioxide (NO_2), Sulphur Dioxide (SO_2), Ozone (O_3), Carbon Monoxide (CO), Formaldehyde (HCHO), and Methane (CH_4) concentrations for urban clusters and their rural references for the 2019 baseline, as well as their perturbed values during the lockdown. The values above the bars show the mean values for the baseline period and the percentage change from that value. The error bars represent the 95% confidence interval of the mean.
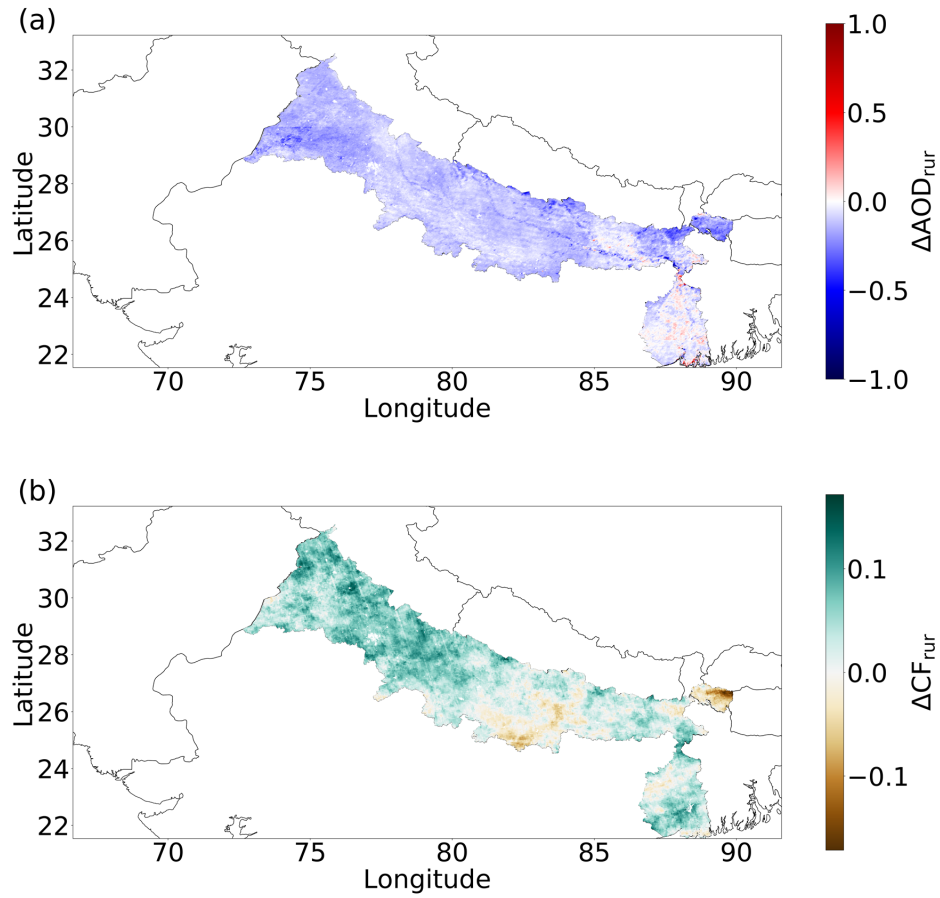
Figure B.9: Regional changes in aerosols and clouds. Sub-figures **a** and **b** show maps of the changes in rural aerosol optical depth (AOD$_{rur}$) and cloud fraction (CF$_{rur}$) during the lockdown compared to the baseline (5-year for AOD and 1-year for CF).
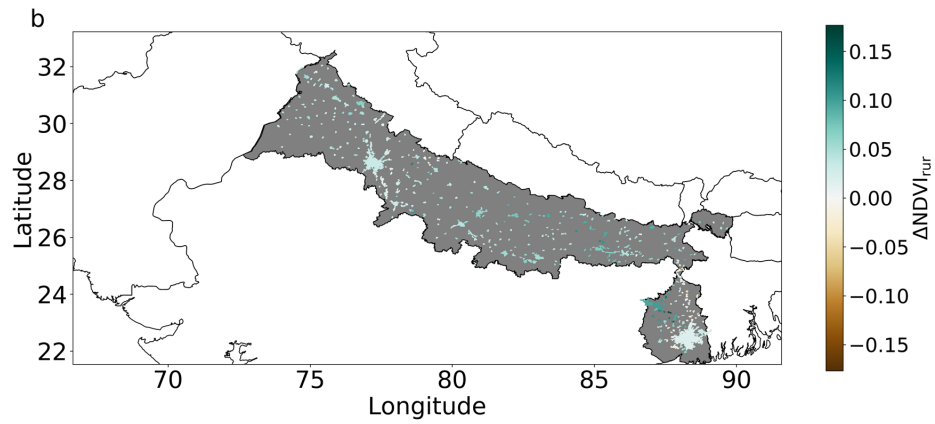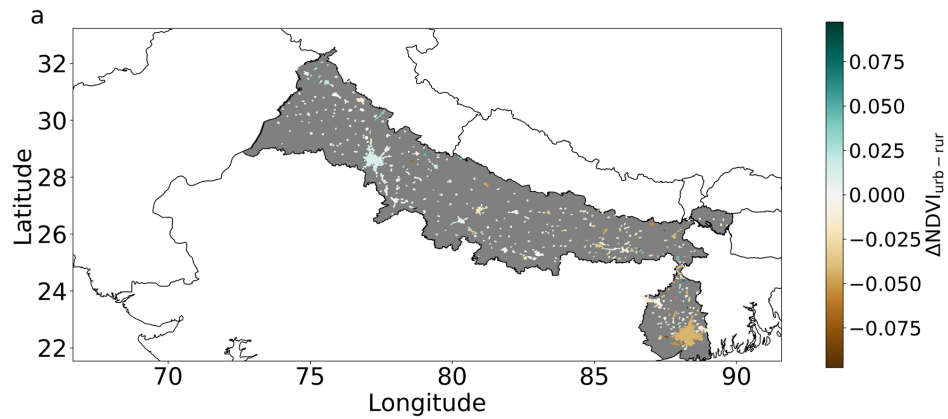
Figure B.10: Map of the urban clusters in the region of interest and the change in their **a** spatial mean urban-rural differential in NDVI ($\Delta\text{NDVI}_{\text{urb}-\text{rur}}$) and **b** spatial mean rural NDVI ($\Delta\text{NDVI}_{\text{rur}}$) during the lockdown compared to the 5-year baseline.

(Peng et al., 2012; Chakraborty & Lee, 2019b) and is corroborated by the relatively strong associations between $NDVI_{urb-rur}$ and daytime SUHI for the two periods (Fig. B.12a). Although $\Delta\alpha_{urb-rur}$ shows a positive relationship with ΔSUHI (r2 = 0.05 for cluster; 0.52 for binned), this relationship is not physically possible in isolation, since a higher α implies lower absorption of solar insolation by the surface, and thus, lower ΔSUHI. Since α and NDVI are correlated (Fig. B.13), the positive relationship between $\Delta\alpha_{urb-rur}$ and ΔSUHI may be a statistical artifact of the relatively higher $NDVI_{rur}$. Neither $CF_{urb-rur}$ and daytime SUHI intensity, nor their perturbations from the baseline to the lockdown, are correlated (Figs B.14d and B.12c).
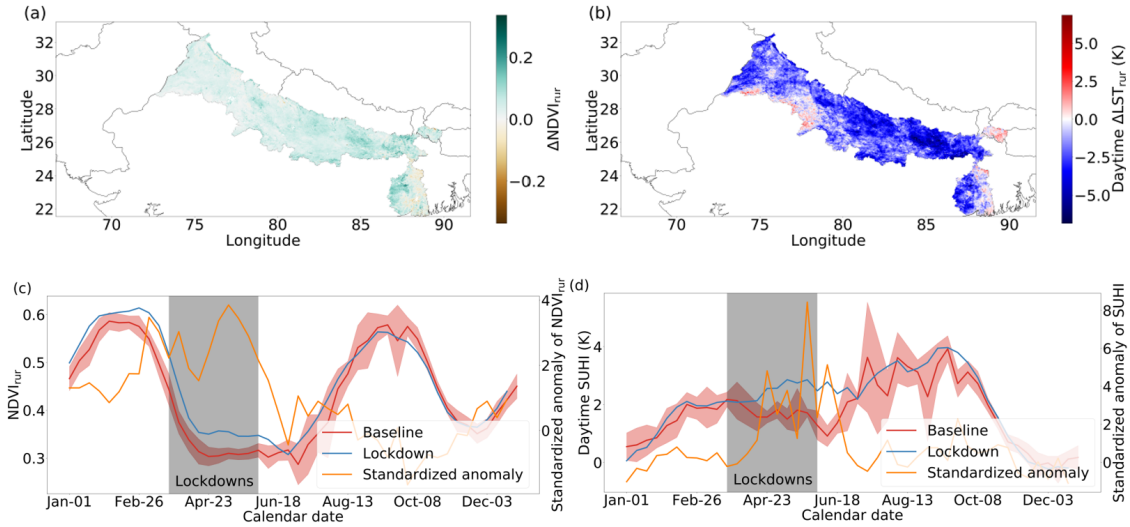
Figure B.11: Contributions of different pathways to regional land surface temperature (LST) change. Sub-figure **a** shows contributions of all pathways, namely shortwave radiative forcing, longwave radiative forcing, evaporation, convection, and ground heat storage to the total calculated local temperature change (ΔT) in the Indo-Gangetic Basin during the lockdown compared to the five year baseline. The corresponding ΔT, ΔLST, and change in blending height temperature (ΔBHT) in MERRA-2 are also shown. The standard errors are displayed in all cases. Sub-figure **b** shows the correlations between the MERRA-2 grid-averaged leaf are index (LAI) and the corresponding ΔT from MERRA-2, the calculated ΔT using the IBPM framework, and the contributions to ΔT through the evaporative pathway and convective pathways. Each data point corresponds to a grid cell average. The lines of best fit are shown and the corresponding equations (including confidence bounds for the slopes of the lines, sample sizes, and p-values) are annotated. Values that are outside the 1–99 percentile of the total diagnosed local temperature change are considered outliers and not shown in the scatter plot.

Figure B.12: Correlations between surface urban heat islands (SUHI) and the urban-rural differentials in **a** normalized difference vegetation index ($NDVI_{urb-rur}$), **b** Aerosol Optical Depth ($AOD_{urb-rur}$), **c** cloud fraction ($CF_{urb-rur}$), and **d** surface albedo ($\alpha_{urb-rur}$) respectively, for all urban clusters during the lockdown (in blue) and 5-year baseline period (in red). The lines of best fit and coefficients of correlation are shown.

We use multiple linear and RF regressions to provide further statistical robustness to our findings (Table B.3). In general, $\Delta NDVI_{urb-rur}$ explains the largest portion of the variability in $\Delta SUHI$ (Adjusted R^2=0.15), followed by $\Delta \alpha_{urb-rur}$, $\Delta AOD_{urb-rur}$, and $CF_{urb-rur}$. The permutation importance scores from the RF models also support the primary control of $\Delta NDVI_{urb-rur}$ on $\Delta SUHI$ (Table B.3).

Table B.3: Summary of data-driven examination of the control of the urban-rural differentials on the change in SUHI using multiple linear and random forest (RF) regressions. For the linear regressions, the combination of variables that lead to the highest adjusted R^2 is listed for increasing subset size. For the RF regression, both the mean and standard deviation of the permutation feature importance scores and r^2(based on the 50 random training/validation splits) are noted.

Linear Regressions		Random Forest Regressions		
Model	Adjusted R^2	Feature	Importance Scores	r^2
ΔSUHI=0.14-9.76ΔNDVI$_{\text{urb-rur}}$	0.15	ΔNDVI$_{\text{urb-rur}}$	0.82 ± 0.08	
ΔSUHI=0.13-9.07ΔNDVI$_{\text{urb-rur}}$+23.54$\Delta\alpha_{\text{urb-rur}}$	0.18	$\Delta\alpha_{\text{urb-rur}}$	0.46 ± 0.07	0.09 ± 0.10
ΔSUHI=0.12-8.70ΔNDVI$_{\text{urb-rur}}$+24.08$\Delta\alpha_{\text{urb-rur}}-1.36\Delta$AOD$_{\text{urb-rur}}$	0.19	ΔAOD$_{\text{urb-rur}}$	0.27 ± 0.04	
ΔSUHI=0.12-8.67ΔNDVI$_{\text{urb-rur}}$+24.08$\Delta\alpha_{\text{urb-rur}}-1.39\Delta$AOD$_{\text{urb-rur}}-3.61\Delta$CF$_{\text{urb-rur}}$	0.19	ΔCF$_{\text{urb-rur}}$	0.21 ± 0.03	

The percentage changes in the atmospheric variables (AOD and CF) are higher over urban areas compared to the rural areas during the lockdown period and the surface properties (NDVI and α) change more for rural areas (Figs B.6 and B.7). Although 2020 was already wetter than regular years (Kumar et al., 2017), a further reduction in AOD over the study area may have perturbed the regional circulation and thermodynamics (Lau et al., 2006; Bollasina et al., 2011), creating an environment conducive to more cloud formation. It may also be possible that the lower aerosol loading reduced the cloud-burning effect (Ackerman et al., 2000), thus increasing CF. Finally, the surface greening could also enhance CF (Teuling et al., 2017). We expect a greater decrease in AOD over urban clusters to correspond to an increase in $K_\downarrow$, which can enhance SUHI intensity. However, our statistical analysis does not support this hypothesis. Instead, the observed positive ΔSUHI is associated with the higher vegetation cover over rural areas. This control of vegetation cover on LST is further corroborated by the negative correlations between LST and NDVI for the urban and rural units (Fig. B.15). The relatively weaker correlations for the cluster-level data in Fig. B.14b compared to Figs B.12a and B.15 (and previous studies (Peng et
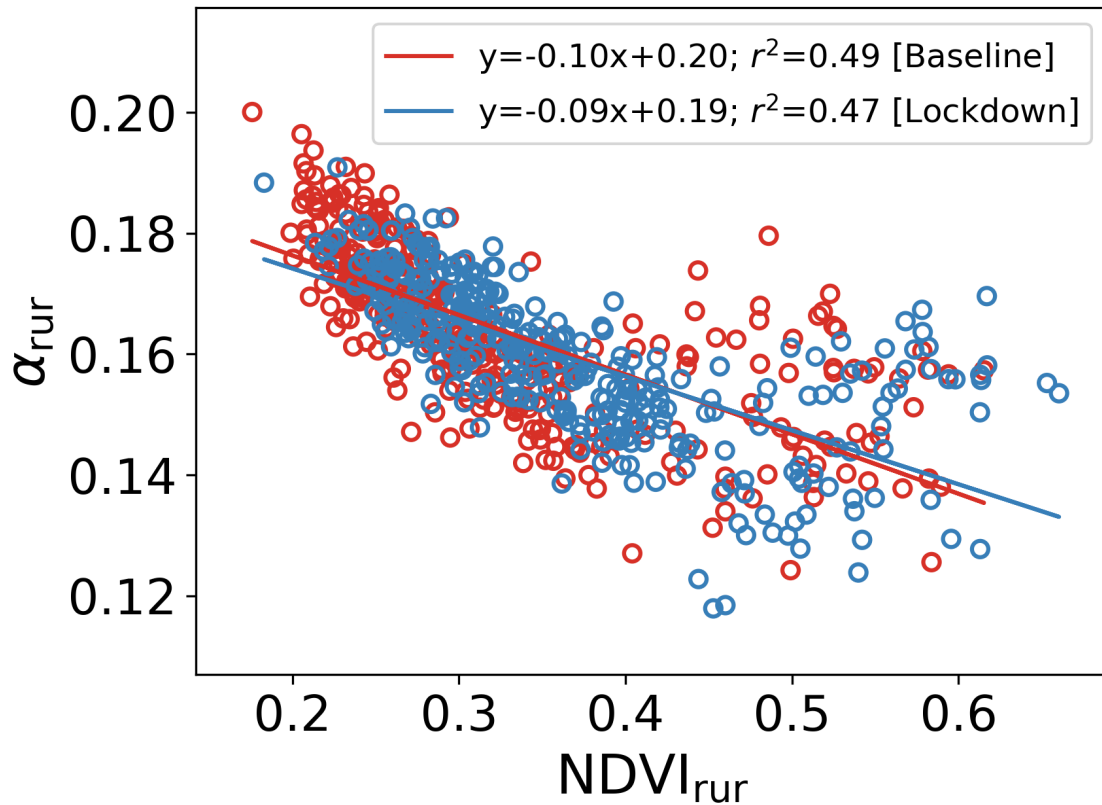
Figure B.13: Correlations between surface albedo (α) and normalized difference vegetation index (NDVI), for rural references during the lockdown (in blue) and for the 5-year baseline period (in red). The lines of best fit and coefficients of correlation are shown.

al., 2012; Chakraborty & Lee, 2019b, Yue et al., 2007)) is because we are dealing with differences of differences in Fig. B.14b during a time of the year with low expected SUHI intensities (Fig. B.14d), making the signal hard to isolate from the noise.
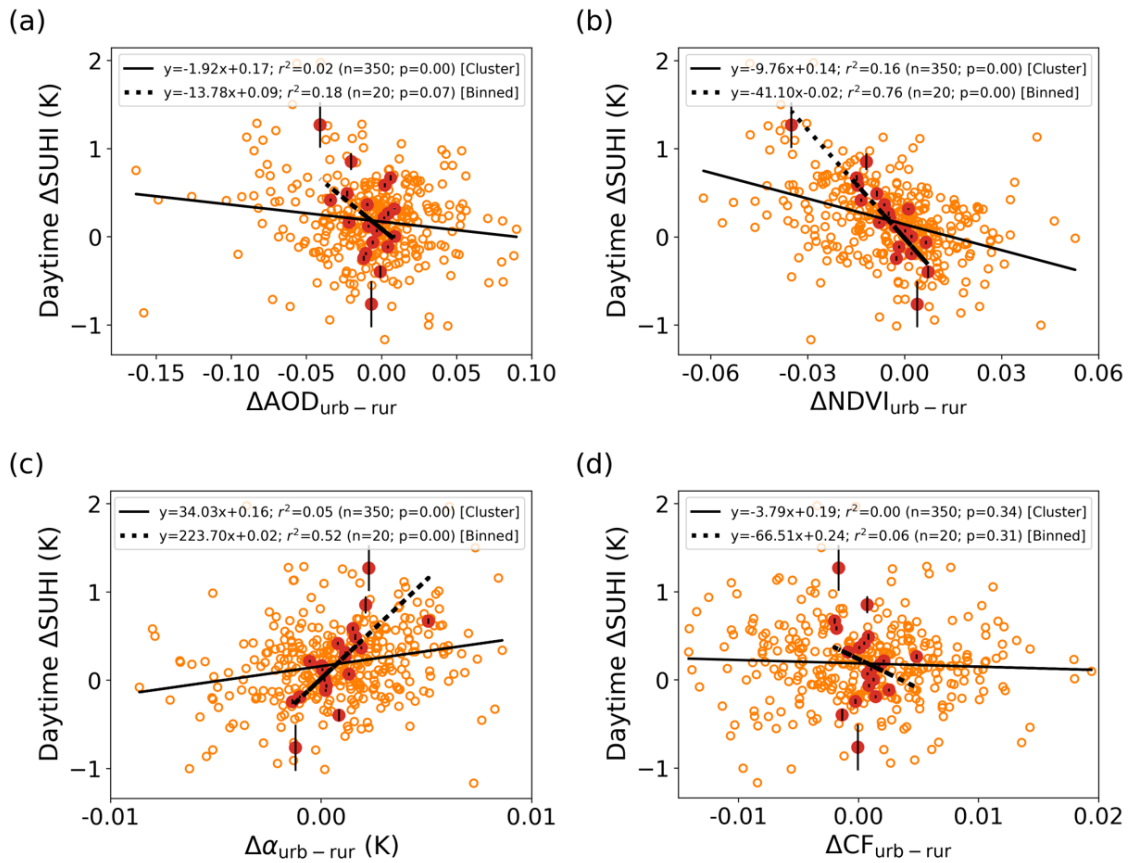
Figure B.14: Statistical examination of daytime surface urban heat island (SUHI) enhancement. Sub-figures **a–d** show the correlations between daytime change in surface urban heat island (SUHI) (ΔSUHI) during the lockdown compared to the five year baseline and the respective change in urban–rural differential in aerosol optical depth ($\Delta\text{AOD}_{\text{urb}-\text{rur}}$), normalized difference vegetation index ($\Delta\text{NDVI}_{\text{urb}-\text{rur}}$), surface albedo ($\Delta\alpha_{\text{urb}-\text{rur}}$), and cloud fraction ($\Delta\text{CF}_{\text{urb}-\text{rur}}$), respectively. Each data point for the raw case (in orange) corresponds to an urban cluster. The lines of best fit are shown, and their corresponding equations (along with their sample sizes and p-values) are annotated. Values that are outside the 1–99 percentiles of the change in the predictor variables are considered outliers and not shown in these scatter plots. Correlations (in red) are also shown after binning every 5th percentile of ΔSUHI and the corresponding changes in the predictors. The vertical black lines show the standard deviation of ΔSUHI in each bin.
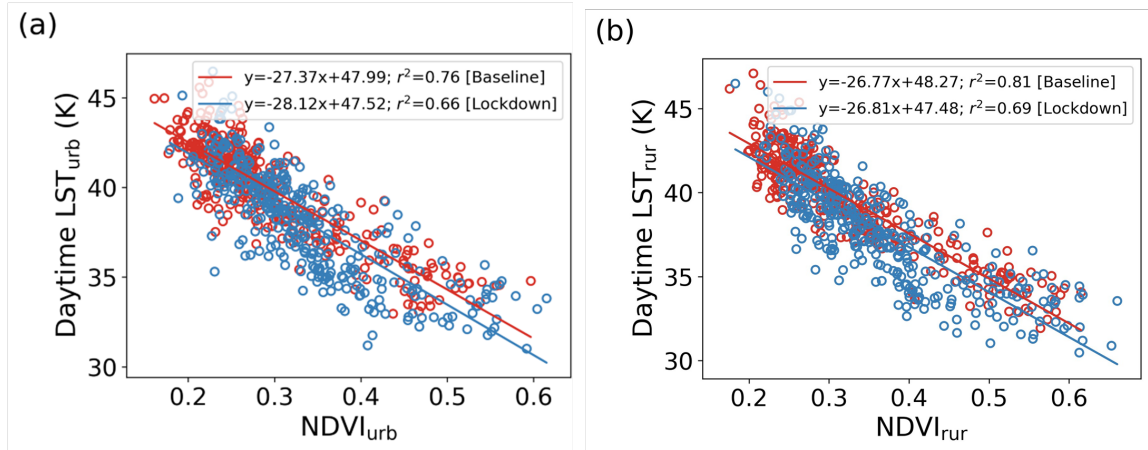
Figure B.15: Correlations between land surface temperature (LST) and normalized difference vegetation index (NDVI), for **a** urban clusters and **b** rural references during the lockdown (in blue) and for the 5-year baseline period (in red). The lines of best fit and coefficients of correlation are shown.

B.4.3 Perturbations to Rural Background Surface Climate

The lack of large-scale continuous observations of meteorological variables in urban areas makes diagnosing these patterns for all-sky conditions difficult using in-situ observations. Instead, we use the MERRA-2 reanalysis, which is observationally constrained by ground-level measurements of surface meteorology and satellite measurements of columnar AOD, and physically constrained by the model components (Gelaro et al., 2017). MERRA-2 primarily represents the rural background since it does not incorporate urban land cover. Since, as suggested by the satellite-derived NDVI and α (Fig. B.6), urban surfaces changed less than rural surfaces during the lockdown, the reanalysis data can be used to generate mechanistic insights about the SUHI enhancement.

The MERRA-2 reanalysis captures the direction of the changes in the region during the lockdown compared to satellite observations (Table B.4). Although the midday aerosol direct radiative effect in MERRA-2 decreases by almost 25% (from -78.4±12.6 W m^{-2} to -58.7±13.3 W m^{-2}) during the lockdown, with the potential to increase $K_\downarrow$ by 19.8±5.1

W m^{-2}, we find an overall reduction in $K_\downarrow$ (-10.5±39.8 W m^{-2}). This decrease in $K_\downarrow$ is due to the compensating effect of increased cloudiness during the lockdown, as well as the higher water vapor content in the atmospheric column, as seen from the higher near-surface relative humidity (Table B.4). Overall, the total absorbed energy by the surface decreases slightly (-10.4±32 W m^{-2}) during the lockdown despite the negative $\Delta\text{AOD}_{\text{rur}}$.

Separating the contributions from both radiative and non-radiative pathways that can change LST reveals large evaporative cooling (-1.79±0.05 K) during this period (Fig. B.16a), which is expected if vegetation cover increased. The diagnosed and MERRA-2 calculated ΔT are similar in magnitude (-1.29 K versus -1.22 K) and in spatial distribution (Fig. B.16b). MERRA-2 uses prescribed vegetation, with identical leaf area index (LAI; regional mean = $\approx$0.79) for the two periods. However, since it is constrained by observed surface meteorology, it captures the decrease in Bowen ratio – the ratio of sensible heat flux (H) and λE – during midday (from 2.87±3.02 for baseline to 1.24±0.76 during the lockdown; Table B.4), which is an expected impact of surface greening. The higher precipitation, latent heat, cloud cover, and relative humidity point to a more intense hydrological cycle during the lockdown compared to regular years (Table B.4).

Table B.4: Regional midday (1:30 pm local time) values (mean ± standard deviation) of relevant variables for the baseline, the lockdown, and their corresponding changes from both the MERRA-2 reanalysis and the satellite observations.

Variable (unit)	MERRA-2 Reanalysis			Satellite Observations		
	Baseline	Lockdown	Change	Baseline	Lockdown	Change
Aerosol optical depth	0.54±0.09	0.44±0.09	-0.1±0.02	0.54±0.11	0.49±0.12	-0.05±0.07
Cloud fraction	0.18±0.05	0.23±0.1	0.05±0.08	0.1±0.05	0.14±0.05	0.04±0.04
Surface temperature (K)	317.4±5	313.5±5.1	-3.9±1.4	313.2±4	311.2±4.2	-2±1.4
Air temperature (K)	311.2±3.6	308.1±3.7	-3.1±1	NA	NA	NA
Relative humidity (%)	18.1±8.2	24.8±7.1	6.7±3.6	NA	NA	NA
Precipitation (mm day^{-1})	0.83±3.2	1.20±3	0.37±0.8	NA	NA	NA
Wind speed (m s^{-1})	4.73±0.7	4.14±0.6	-0.59±0.5	NA	NA	NA
All-sky incident shortwave radiation (W m^{-2})	815.1±56.8	804.6±58.4	-10.5±39.8	NA	NA	NA
Clear-sky incident shortwave radiation (W m^{-2})	867.4±41	880.1±38.9	-12.7±3.7	NA	NA	NA
Clear, clean-sky Incident shortwave radiation (W m^{-2})	949.5±31.4	942.3±28.5	-7.2±3.5	NA	NA	NA
Shortwave aerosol radiative forcing (W m^{-2})	-78.5±12.6	-58.7±13.3	19.8±5.1	NA	NA	NA
All-sky incoming longwave radiation (W m^{-2})	398.9±21.2	396.5±18	-2.4±4.8	NA	NA	NA
Clear, clean-sky incoming longwave radiation (W m^{-2})	390.8±22.5	388.9±21.1	-1.9±4	NA	NA	NA
Clear-sky longwave aerosol radiative forcing (W m^{-2})	4.6±0.8	2.8±0.6	-1.8±0.4	NA	NA	NA
Black-sky albedo	NA	NA	NA	0.164±0.02	0.158±0.182	-0.006±0.008
White-sky albedo	NA	NA	NA	0.181±0.021	0.176±0.019	-0.005±0.009
Surface albedo	0.151±0.02	0.152±0.02	-0.001±0	NA	NA	NA
Normalized difference vegetation index	NA	NA	NA	0.31±0.13	0.35±0.12	0.04±0.04
Sensible heat flux (W m^{-2})	309.5±55	246.4±53.1	-63.1±38.4	NA	NA	NA
Latent heat flux (W m^{-2})	107.7±67.1	198.1±67.2	90.4±39.2	NA	NA	NA
Bowen ratio	2.87±3.02	1.24±0.76	-1.63±2.35	NA	NA	NA

The satellite-observed negative $\Delta NDVI_{urb-rur}$ suggests that the increase in evaporative cooling during the lockdown was more for rural areas compared to urban areas. This would be true even if $NDVI_{urb}$ and $NDVI_{rur}$ had changed identically, since urban areas are generally more moisture-limited. Figure 5b shows the correlations of ΔT from MERRA-2, the IBPM calculations, and contributions due to evaporation and convection with LAI.

The negative correlations between LAI and ΔT demonstrate a stronger cooling response during the lockdown over more densely vegetated surfaces. Here the lowest LAI grids represent relatively urbanized areas. The increasing positive temperature response through the convective pathway with LAI suggests that this is a negative feedback to the evaporative cooling (Gerken et al., 2019). This convective feedback can be understood either in terms of energy conservation or through evaporation-induced near-surface stability. A relative increase in λE under similar (or reduced) available energy requires a corresponding decrease in H. Alternatively, the additional evaporative cooling of the surface compared to the blending height renders the lower atmosphere relatively stable compared to the baseline period, impeding the dissipation of available energy via H.

Overall, ΔT is almost a third of ΔLST, with the other two-thirds attributable to atmospheric factors, including AOD and CF (Fig. B.16a). The IBPM results show that the sum of the evaporative cooling and its convective feedback accounted for roughly 79% of the midday ΔT, while the evaporative cooling alone accounted for roughly 46% of the corresponding ΔLST (of -3.92 K). The land contribution to ΔLST found here is probably a lower bound estimate since there is strong coupling between the land and the atmosphere. For instance, enhanced surface evaporation due to the increase in vegetation cover would also increase low level cloudiness through condensation feedback (Ban-Weiss et al., 2011), lowering both BHT and LST. A similar theoretical diagnosis is not possible for the urban surfaces explicitly since the MERRA-2 land cover dataset does not consider urban areas. Nonetheless, these results can explain the SUHI increase, as the implicit assumption is that the surface characteristics of the rural areas changed more than those of the urban areas during the lockdown period, which is reasonable given the time scale.
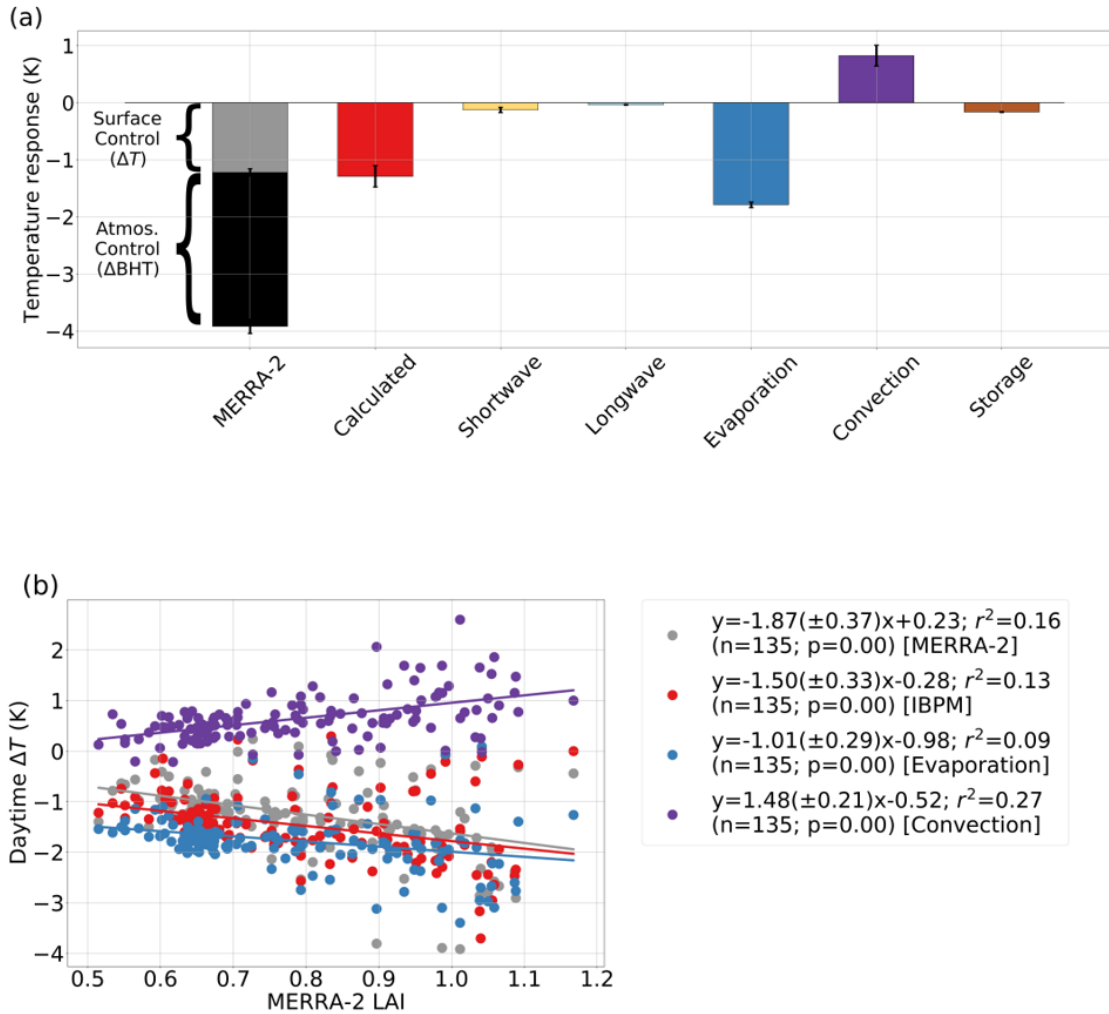
Figure B.16: Contributions of different pathways to regional land surface temperature (LST) change. Sub-figure **a** shows contributions of all pathways, namely shortwave radiative forcing, longwave radiative forcing, evaporation, convection, and ground heat storage to the total calculated local temperature change (ΔT) in the Indo-Gangetic Basin during the lockdown compared to the five year baseline. The corresponding ΔT, ΔLST, and change in blending height temperature (ΔBHT) in MERRA-2 are also shown. The standard errors are displayed in all cases. Sub-figure **b** shows the correlations between the MERRA-2 grid-averaged leaf are index (LAI) and the corresponding ΔT from MERRA-2, the calculated ΔT using the IBPM framework, and the contributions to ΔT through the evaporative pathway and convective pathways. Each data point corresponds to a grid cell average. The lines of best fit are shown and the corresponding equations (including confidence bounds for the slopes of the lines, sample sizes, and p-values) are annotated. Values that are outside the 1–99 percentile of the total diagnosed local temperature change are considered outliers and not shown in the scatter plot.

B.5 Discussion and Conclusions

The UHI effect is traditionally viewed as an outcome of the replacement of the natural landscape by built-up structures. The consequences of this land cover change are simpler to define in the abstract than to measure in practice. While cities modify their local climate as they expand, the UHI intensity is usually quantified using snapshot measurements in the urban area and for some rural reference. For the SUHI, how to define this rural reference remains a contentious issue (Peng et al., 2012; Martin et al., 2015; Martin-Vide et al., 2015; Li et al., 2019). Generally, the urban-rural delineations are more clearly constructed for less sprawling cities with very little land management surrounding the city centers. Here we show an example of a region of the world with high human intervention in both urban and rural areas, the interruption of which leads to the seemingly counter-intuitive enhancement of the SUHI during a period of low human activity. Thus, the COVID-19 lockdown period illustrates the importance of the rural reference on the SUHI intensity during a perturbation scenario, the relevance of which has previously only been examined for the mean climate state in this region (Chakraborty et al., 2017; Kumar et al., 2017; Shastri et al., 2017).

Our results can help contextualize a larger current discussion in the urban climate community on the utility of the UHI as a metric to examine urban public health (Manoli et al., 2020b; Martilli et al., 2020b; Manoli et al. 2020c). The UHI intensity is the impact of urbanization on local temperature (Manoli et al. 2020a). However, urban heat stress is dependent on the absolute temperature, or more accurately, a combination of temperature, humidity, and other factors (Lemonsu et al., 2015). As such, the relevance of UHI for urban public health can be misleading during certain times because enhancement in UHI intensity does not necessarily imply similar enhancement in heat stress (or even temperature) in urban areas. In agreement, Martilli et al. (2020a) argues that mitigating the UHI

should not be the goal when addressing the public health consequences of urbanization. In theory, one can reduce the UHI intensity by increasing the rural temperature, which does not change the potential heat stress in the urban area. Here we see something similar occurring, with the SUHI increasing due to rural areas cooling down more than the urban core between the baseline and the lockdown periods, rather than due to an increase in urban temperature. However, this is only the temporal perspective. From the spatial perspective, it is also true that residents moving from rural to urban regions in the IGB were exposed to higher temperatures than they would have had they remained in rural areas. This separation of the temporal and spatial perspectives is critical to reconciling the debate in the community. The criticisms of UHI as a metric primarily pertain to the total impact of temperature on human health in urban areas. In contrast, since the UHI is an abstract isolation of the contribution to that temperature from urbanization, it remains theoretically important, assuming we establish a more consistent definition of the rural reference to facilitate accurate inter-urban comparisons.

Lastly, our finding demonstrates the importance of human-land-atmosphere coupling on the regional climate over South Asia as a whole. Agricultural practices in this region strongly control the vegetation phenology of the croplands, modulating how energy is partitioned and dissipated from the surface through non-radiative means (Fig. B.11c). As seen here, the importance of these non-radiative components on the LST is apparent, even when input energy to the system is relatively stable, providing large-scale observational evidence of previously modeled results (Ban-Weiss et al., 2011). Over 88% of the landmass in North India is agricultural (Fig. B.1b). Therefore, an increase in surface vegetation due to agriculture can lead to large regional cooling, modify cloud formation, and lower tropospheric stability. Moreover, enhanced evaporative cooling over the Indian landmass during the monsoon onset period (as seen here) can also perturb the land-sea thermal gradient - a major driver of monsoonal wind circulation (Roxy et al., 2015). Our

278

study puts forth important observational evidence of human-induced control on surface climate, which strengthens the need for the ongoing efforts to explicitly include these in earth system models to better predict long-term climate change (Beckage et al., 2018; Donges et al., 2020). For the UHI, the inclusion of human dynamics can help constrain its future estimates, since urban and rural areas are expected to change differently in future scenarios (Oleson, 2012).

Although our two-pronged approach using satellite observations and reanalysis product demonstrates the consistency of these perturbations, a few uncertainties remain. First, since 2020 was wetter than the baseline years (Table B.4), the NDVI perturbations seen during lockdown may not have been solely due to the well-documented delay in harvesting in this region (Rawal et al., 2020). The lockdown-induced anthropogenic pause could influence the natural variability, cloud cover, and rainfall (Latha et al., 2021; Timmerman et al., Under Review), and in turn also affect the NDVI/LST. Regardless, the large, standardized anomaly in $NDVI_{rur}$ during the lockdown, seen in Fig. B.11c, strongly suggests that the lockdown played a role. The higher $\Delta NDVI_{rur}$ (compared to $\Delta NDVI_{urb}$) and $\Delta SUHI$ is also see when using 18-year (2003-2019) baseline from MODIS Aqua measurements (Figs B.17a and B.17b). Moreover, NDVI differences are seen at urban-to-urban periphery scale (5-30 km), which is much smaller than the inherent spatial scale of the anticipated natural variability. Second, since the perturbations are small in magnitude, sensor noise could account for some of the variability. Our results are qualitatively replicated when we calculate the relevant variables from the MODIS Terra satellite (Figs B.17c and B.17d), which has a different sensor and equatorial overpass time ($\approx$10:30 am), indicating that the perturbations are robust and cannot be just random noise from one sensor. Third, since our study deals with regional changes using coarse satellite observations, we neither examine the perturbations for individual urban clusters, which can vary from the mean changes (Figs B.5a and B.5b), nor characterize intra-urban distributions. Some of these limitations

can be addressed with the development of better parameterized models for this region with explicit irrigation schemes, which can clearly isolate the impact of the agricultural cycle on regional climate.
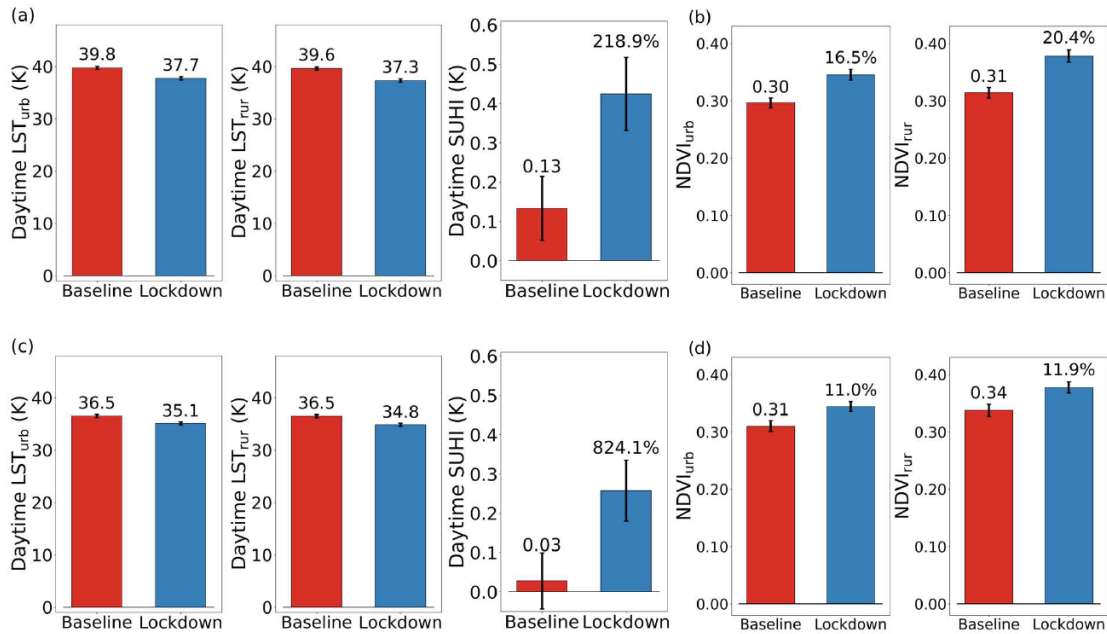
Figure B.17: Sensitivity of changes in normalized differences vegetation index (NDVI), land surface temperature (LST), and surface urban heat island (SUHI) to baseline and sensor selection. Sub-figures **a** and **b**, show the mean NDVI and LST for urban clusters and their rural references for an 18-year (2003-2019) baseline period, as well as their perturbed values during the lockdown. Sub-figures **c** and **d** are similar, but based on measurements from the Terra satellite and using 5-year (2015-2019) baseline. The error bars represent the 95% confidence interval of the mean.

B.6 References

1. Ackerman, A. S., Toon, O. B., Stevens, D. E., Heymsfield, A. J., Ramanathan, V., & Welton, E. J. (2000). Reduction of tropical cloudiness by soot. Science, 288(5468), 1042-1047.

2. Ban-Weiss, G. A., Bala, G., Cao, L., Pongratz, J., & Caldeira, K. (2011). Climate forcing and response to idealized changes in surface latent and sensible heat. Environmental Research Letters, 6(3), 034032.

3. Barton, E. J., Taylor, C. M., Parker, D. J., Turner, A. G., Belušić, D., Böing, S. J., ... & Mitra, A. K. (2020). A case-study of land–atmosphere coupling during monsoon onset in northern India. Quarterly Journal of the Royal Meteorological Society, 146(731), 2891-2905.

4. Beckage, B., Gross, L. J., Lacasse, K., Carr, E., Metcalf, S. S., Winter, J. M., ... & Hoffman, F. M. (2018). Linking models of human behaviour and climate alters projected climate change. Nature Climate Change, 8(1), 79-84.

5. Bollasina, M. A., Ming, Y., & Ramaswamy, V. (2011). Anthropogenic aerosols and the weakening of the South Asian summer monsoon. science, 334(6055), 502-505.

6. Bontemps, S., Defourny, P., Radoux, J., Van Bogaert, E., Lamarche, C., Achard, F., ... & Arino, O. (2013, September). Consistent global land cover maps for climate modelling communities: current achievements of the ESA's land cover CCI. In Proceedings of the ESA living planet symposium, Edimburgh (pp. 9-13).

7. Breiman, L. (2001). Random forests. Machine learning, 45(1), 5-32.

8. Cao, C., Lee, X., Liu, S., Schultz, N., Xiao, W., Zhang, M., & Zhao, L. (2016).

Urban heat islands in China enhanced by haze pollution. Nature Communications, 7(1), 1-7.

9. Chakraborty, T. & Lee, X. (2021). Large Differences in Diffuse Solar Radiation Among Current-Generation Reanalysis and Satellite-Derived Products. Journal of Climate.

10. Chakraborty, T., & Lee, X. (2019a). Land cover regulates the spatial variability of temperature response to the direct radiative effect of aerosols. Geophysical Research Letters, 46(15), 8995-9003.

11. Chakraborty, T., & Lee, X. (2019b). A simplified urban-extent algorithm to characterize surface urban heat islands on a global scale and examine vegetation control on their spatiotemporal variability. International Journal of Applied Earth Observation and Geoinformation, 74, 269-280.

12. Chakraborty, T., Hsu, A., Manya, D., & Sheriff, G. (2019). Disproportionately higher exposure to urban heat in lower-income neighborhoods: A multi-city perspective. Environmental Research Letters, 14(10), 105003.

13. Chakraborty, T., Hsu, A., Manya, D., & Sheriff, G. (2020). A spatially explicit surface urban heat island database for the United States: Characterization, uncertainties, and possible applications. ISPRS Journal of Photogrammetry and Remote Sensing, 168, 74-88.

14. Chakraborty, T., Sarangi, C., & Tripathi, S. N. (2017). Understanding diurnality and inter-seasonality of a sub-tropical urban heat island. Boundary-Layer Meteorology, 163(2), 287-309.

15. Chakraborty, T., Sarangi, C., Krishnan, M., Tripathi, S. N., Morrison, R., & Evans, J.

(2019). Biases in model-simulated surface energy fluxes during the Indian monsoon onset period. Boundary-Layer Meteorology, 170(2), 323-348.

16. Dey, S., & Di Girolamo, L. (2011). A decade of change in aerosol properties over the Indian subcontinent. Geophysical Research Letters, 38(14).

17. Donges, J. F., Heitzig, J., Barfuss, W., Wiedermann, M., Kassel, J. A., Kittel, T., ... & Lucht, W. (2020). Earth system modeling with endogenous and dynamic human societies: the copan: CORE open World–Earth modeling framework. Earth System Dynamics, 11(2), 395-413.

18. Gelaro, R., McCarty, W., Suárez, M. J., Todling, R., Molod, A., Takacs, L., ... & Zhao, B. (2017). The modern-era retrospective analysis for research and applications, version 2 (MERRA-2). Journal of climate, 30(14), 5419-5454.

19. Gerken, T., Ruddell, B. L., Yu, R., Stoy, P. C., & Drewry, D. T. (2019). Robust observations of land-to-atmosphere feedbacks using the information flows of FLUXNET. Npj Climate and Atmospheric Science, 2(1), 1-10.

20. Gorelick, N., Hancher, M., Dixon, M., Ilyushchenko, S., Thau, D., & Moore, R. (2017). Google Earth Engine: Planetary-scale geospatial analysis for everyone. Remote sensing of Environment, 202, 18-27.

21. Guidelines, Ministry of Home Affairs, Government of India
https://www.mha.gov.in/sites/default/files/Guidelines.pdf (2020), Accessed 27th Dec 2020

22. Hersbach, H., Bell, B., Berrisford, P., Hirahara, S., Horányi, A., Muñoz-Sabater, J., ... & Thépaut, J. N. (2020). The ERA5 global reanalysis. Quarterly Journal of the Royal Meteorological Society, 146(730), 1999-2049.

23. Koster, R. D., Dirmeyer, P. A., Guo, Z., Bonan, G., Chan, E., Cox, P., ... & Yamada, T. (2004). Regions of strong coupling between soil moisture and precipitation. Science, 305(5687), 1138-1140.

24. Kumar, R., Mishra, V., Buzan, J., Kumar, R., Shindell, D., & Huber, M. (2017). Dominant control of agriculture and irrigation on urban heat island in India. Scientific reports, 7(1), 1-10.

25. Latha, R., Murthy, B. S., Sandeepan, B. S., Bhanage, V., Rathod, A., Tiwari, A., ... & Singh, S. (2021). Propagation of cloud base to higher levels during Covid-19-Lockdown. Science of The Total Environment, 759, 144299.

26. Lau, K. M., Kim, M. K., & Kim, K. M. (2006). Asian summer monsoon anomalies induced by aerosol direct forcing: the role of the Tibetan Plateau. Climate dynamics, 26(7-8), 855-864.

27. Lawrence, D. M., Hurtt, G. C., Arneth, A., Brovkin, V., Calvin, K. V., Jones, A. D., ... & Shevliakova, E. (2016). The Land Use Model Intercomparison Project (LUMIP) contribution to CMIP6: rationale and experimental design. Geoscientific Model Development, 9(9), 2973-2998.

28. Le Quéré, C., Jackson, R. B., Jones, M. W., Smith, A. J., Abernethy, S., Andrew, R. M., ... & Peters, G. P. (2020). Temporary reduction in daily global CO_2 emissions during the COVID-19 forced confinement. Nature Climate Change, 10(7), 647-653.

29. Lee, X., Goulden, M. L., Hollinger, D. Y., Barr, A., Black, T. A., Bohrer, G., ... & Zhao, L. (2011). Observed increase in local cooling effect of deforestation at higher latitudes. Nature, 479(7373), 384-387.

30. Lemonsu, A., Viguie, V., Daniel, M., & Masson, V. (2015). Vulnerability to heat

waves: Impact of urban expansion scenarios on urban heat island and heat stress in Paris (France). Urban Climate, 14, 586-605.

31. Li, H., Meier, F., Lee, X., Chakraborty, T., Liu, J., Schaap, M., & Sodoudi, S. (2018). Interaction between urban heat island and urban pollution island during summer in Berlin. Science of the total environment, 636, 818-828.

32. Li, K., Chen, Y., Wang, M., & Gong, A. (2019). Spatial-temporal variations of surface urban heat island intensity induced by different definitions of rural extents in China. Science of The Total Environment, 669, 229-247.

33. Mahrt, L. (2000). Surface heterogeneity and vertical structure of the boundary layer. Boundary-Layer Meteorology, 96(1), 33-62.

34. Manoli, G., Fatichi, S., Bou-Zeid, E., & Katul, G. G. (2020a). Seasonal hysteresis of surface urban heat islands. Proceedings of the National Academy of Sciences, 117(13), 7082-7089.

35. Manoli, G., Fatichi, S., Schläpfer, M., Yu, K., Crowther, T. W., Meili, N., ... & Bou-Zeid, E. (2019b). Magnitude of urban heat islands largely explained by climate and population. Nature, 573(7772), 55-60.

36. Manoli, G., Fatichi, S., Schläpfer, M., Yu, K., Crowther, T. W., Meili, N., ... & Zeid, E. B. (2020c). Reply to Martilli et al.(2020): Summer average urban-rural surface temperature differences do not indicate the need for urban heat reduction.

37. Martilli, A., Krayenhoff, E. S., & Nazarian, N. (2020a). Is the urban heat island intensity relevant for heat mitigation studies?. Urban Climate, 31, 100541.

38. Martilli, A., Roth, M., Chow, W. T., Demuzere, M., Lipson, M., Krayenhoff, E. S., ... & Hart, M. A. (2020b). Summer average urban-rural surface temperature

differences do not indicate the need for urban heat reduction.

39. Martin, P., Baudouin, Y., & Gachon, P. (2015). An alternative method to characterize the surface urban heat island. International journal of biometeorology, 59(7), 849-861.

40. Martin-Vide, J., Sarricolea, P., & Moreno-García, M. C. (2015). On the definition of urban heat island intensity: the "rural" reference. Frontiers in Earth Science, 3, 24.

41. Oke, T. R. (1982). The energetic basis of the urban heat island. Quarterly Journal of the Royal Meteorological Society, 108(455), 1-24.

42. Oleson, K. (2012). Contrasts between urban and rural climate in CCSM4 CMIP5 climate change scenarios. Journal of Climate, 25(5), 1390-1412.

43. Pagano, T. S., & Durham, R. M. (1993, August). Moderate resolution imaging spectroradiometer (MODIS). In Sensor Systems for the Early Earth Observing System Platforms (Vol. 1939, pp. 2-17). International Society for Optics and Photonics.

44. Peng, S., Piao, S., Ciais, P., Friedlingstein, P., Ottle, C., Breon, F. M., ... & Myneni, R. B. (2012). Surface urban heat island across 419 global big cities. Environmental science & technology, 46(2), 696-703.

45. Pesaresi, M., Huadong, G., Blaes, X., Ehrlich, D., Ferri, S., Gueguen, L., ... & Zanchetta, L. (2013). A global human settlement layer from optical HR/VHR RS data: Concept and first results. IEEE Journal of Selected Topics in Applied Earth Observations and Remote Sensing, 6(5), 2102-2131.

46. Pielke Sr, R. A., Marland, G., Betts, R. A., Chase, T. N., Eastman, J. L., Niles, J. O., ... & Running, S. W. (2002). The influence of land-use change and landscape

dynamics on the climate system: relevance to climate-change policy beyond the radiative effect of greenhouse gases. Philosophical Transactions of the Royal Society of London. Series A: Mathematical, Physical and Engineering Sciences, 360(1797), 1705-1719.

47. Qu, Y., Liang, S., Liu, Q., He, T., Liu, S., & Li, X. (2015). Mapping surface broadband albedo from satellite observations: A review of literatures on algorithms and products. Remote Sensing, 7(1), 990-1020.

48. Ranjan, A. K., Patra, A. K., & Gorai, A. K. (2020). Effect of lockdown due to SARS COVID-19 on aerosol optical depth (AOD) over urban and mining regions in India. Science of the Total Environment, 745, 141024.

49. Rawal, V., Kumar, M., Verma, A., & Pais, J. (2020). COVID-19 lockdown: Impact on agriculture and rural economy. Society for Social and Economic Research.

50. Remer, L. A., Tanré, D., Kaufman, Y. J., Levy, R., & Mattoo, S. (2006). Algorithm for remote sensing of tropospheric aerosol from MODIS: Collection 005. National Aeronautics and Space Administration, 1490.

51. Rizwan, A. M., Dennis, L. Y., & Chunho, L. I. U. (2008). A review on the generation, determination and mitigation of Urban Heat Island. Journal of environmental sciences, 20(1), 120-128.

52. Rouse, J. W., Haas, R. H., Schell, J. A., Deering, D. W., & Harlan, J. C. (1974). Monitoring the vernal advancement and retrogradation (green wave effect) of natural vegetation. NASA/GSFC Type III Final Report, Greenbelt, Md, 371.

53. Roxy, M. K., Ritika, K., Terray, P., Murtugudde, R., Ashok, K., & Goswami, B. N. (2015). Drying of Indian subcontinent by rapid Indian Ocean warming and a weakening land-sea thermal gradient. Nature communications, 6(1), 1-10.

54. Rutz, C., Loretto, M. C., Bates, A. E., Davidson, S. C., Duarte, C. M., Jetz, W., ... & Cagnacci, F. (2020). COVID-19 lockdown allows researchers to quantify the effects of human activity on wildlife. Nature Ecology & Evolution, 4(9), 1156-1159.

55. Sarangi, C., Tripathi, S. N., Mishra, A. K., Goel, A., & Welton, E. J. (2016). Elevated aerosol layers and their radiative impact over Kanpur during monsoon onset period. Journal of Geophysical Research: Atmospheres, 121(13), 7936-7957.

56. Sarangi, C., Tripathi, S. N., Qian, Y., Kumar, S., & Ruby Leung, L. (2018). Aerosol and urban land use effect on rainfall around cities in Indo-Gangetic Basin from observations and cloud resolving model simulations. Journal of Geophysical Research: Atmospheres, 123(7), 3645-3667.

57. Seto, K. C., Güneralp, B., & Hutyra, L. R. (2012). Global forecasts of urban expansion to 2030 and direct impacts on biodiversity and carbon pools. Proceedings of the National Academy of Sciences, 109(40), 16083-16088.

58. Shastri, H., Barik, B., Ghosh, S., Venkataraman, C., & Sadavarte, P. (2017). Flip flop of day-night and summer-winter surface urban heat island intensity in India. Scientific reports, 7(1), 1-8.

59. Siderius, C., Hellegers, P. J. G. J., Mishra, A., van Ierland, E. C., & Kabat, P. (2014). Sensitivity of the agroecosystem in the Ganges basin to inter-annual rainfall variability and associated changes in land use. International Journal of Climatology, 34(10), 3066-3077.

60. Strahler, A. H., Muller, J., Lucht, W., Schaaf, C., Tsang, T., Gao, F., ... & Barnsley, M. J. (1999). MODIS BRDF/albedo product: algorithm theoretical basis document version 5.0. MODIS documentation, 23(4), 42-47.

61. Teuling, A. J., Taylor, C. M., Meirink, J. F., Melsen, L. A., Miralles, D. G., Van Heerwaarden, C. C., ... & de Arellano, J. V. G. (2017). Observational evidence for cloud cover enhancement over western European forests. Nature communications, 8(1), 1-7.

62. Theeuwes, N. E., Barlow, J. F., Teuling, A. J., Grimmond, C. S. B., & Kotthaus, S. (2019). Persistent cloud cover over mega-cities linked to surface heat release. npj Climate and Atmospheric Science, 2(1), 1-6.

63. Timmermann, A., Lee, S. S., Chu, J. E., Chung, E. S., & Lee, J. Y. (Under Review). COVID-19-related drop in anthropogenic aerosol emissions in China and corresponding cloud and climate effects.

64. Turner, A. G., Bhat, G. S., Martin, G. M., Parker, D. J., Taylor, C. M., Mitra, A. K., ... & New, B. (2020). Interaction of convective organization with monsoon precipitation, atmosphere, surface and sea: The 2016 INCOMPASS field campaign in India. Quarterly Journal of the Royal Meteorological Society, 146(731), 2828-2852.

65. Veefkind, J. P., Aben, I., McMullan, K., Förster, H., De Vries, J., Otter, G., ... & Levelt, P. F. (2012). TROPOMI on the ESA Sentinel-5 Precursor: A GMES mission for global observations of the atmospheric composition for climate, air quality and ozone layer applications. Remote sensing of environment, 120, 70-83.

66. Venter, Z. S., Aunan, K., Chowdhury, S., & Lelieveld, J. (2020). COVID-19 lockdowns cause global air pollution declines. Proceedings of the National Academy of Sciences, 117(32), 18984-18990.

67. Wan, Z. (2006). MODIS land surface temperature products users' guide. ICESS, University of California.

68. Xu, Q. S., & Liang, Y. Z. (2001). Monte Carlo cross validation. Chemometrics and Intelligent Laboratory Systems, 56(1), 1-11.

69. Yue, W., Xu, J., Tan, W., & Xu, L. (2007). The relationship between land surface temperature and NDVI with remote sensing: application to Shanghai Landsat 7 ETM+ data. International journal of remote sensing, 28(15), 3205-3226.

70. Zhao, L., Lee, X., Smith, R. B., & Oleson, K. (2014). Strong contributions of local background climate to urban heat islands. Nature, 511(7508), 216-219.